# From Migmatites to Granitoids: Transport Mechanisms, Timescales, and Melt Source

Inaugural dissertation
of the Faculty of Science,
University of Bern

presented by

Hugo Dominguez

Supervisors of the doctoral thesis:
Prof. Dr. Pierre Lanari
Dr. Nicolas Riel

Institute of Geological Sciences
University of Bern

# From Migmatites to Granitoids: Transport Mechanisms, Timescales, and Melt Source

Inaugural dissertation
of the Faculty of Science,
University of Bern

presented by

Hugo Dominguez

Supervisors of the doctoral thesis:
Prof. Dr. Pierre Lanari
Dr. Nicolas Riel

Institute of Geological Sciences
University of Bern

Accepted by the Faculty of Science.

Bern, November 18, 2024

The Dean
Prof. Dr. Jean-Louis Reymond

# LICENSE

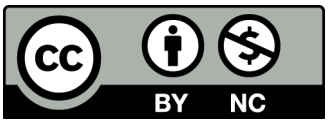

# Abstract

Melting processes in the continental crust are responsible for crust formation and recycling, and play an important role in heat transport. A better understanding of these processes can shed light on crustal differentiation and continental growth throughout the Earth's history. This thesis focuses on three major key aspects of the link between the melt source and crustal-derived granitoid plutons: (i) the mechanisms involved in melt transport, (ii) the timescales of melting and emplacement of melt, and (iii) the compositional and reactional link between the melt source and crustal-derived granitoids. Numerical models are an essential tool for investigating melting processes, where the processes of interest often occur on time- and length-scales inaccessible to direct observation. However, constraints from the natural rock record are also needed to compare models with observations. Therefore, this thesis aims to develop and extend new numerical methods to study melting processes while keeping a focus on natural systems. In particular, the El Oro complex, in Ecuador, is used as a natural laboratory to provide constraints on melting processes from a geological point of view. This metamorphic complex is a tilted section of a paleo-crust that provides a clear exposure from the source of melting to crustal-derived granitoid plutons.

In terms of numerical models, two-phase flow approach offers the possibility of dynamically modelling the interaction between the melt and the rock. Currently, this approach is mainly used to model the mechanical interactions between the melt and the host rock. To obtain a fully reactive transport model, phase reactions and melt/rock interactions are required. The first part of this thesis investigates how to numerically couple a purely mechanical two-phase flow model with chemical interactions, focusing on chemical advection. I show that the weighted essentially non-oscillatory (WENO) algorithm is the best suited for this problem, with good accuracy and performance.

In a second part, I investigate the timescales of melting and emplacement by producing and interpreting geochronological and trace element data from zircons of the El Oro complex. Both the melting source and the end-product granitoids are analysed using laser ablation inductively coupled plasma mass spectrometry (LA-ICP-MS). I show the interest of collecting large datasets of zircon analyses per sample, to not only assign a geological age, but for investigating the duration of melting processes. I propose that in the El Oro complex, the total duration of the deep crustal melting event and pluton emplacement are similar and long-lived ($\sim$20 Myr). I propose that multiple short magmatic pulses are responsible for the apparent long duration of plutons in the El Oro complex, alternating with longer periods of lower magmatic activity. I also show evidence of open system behaviour in migmatites and how the combinaison of trace element data with geochronology to decipher melting processes.

In the final part of this thesis, I explore the potential of coupling a crustal thermal model with phase equilibrium modelling. I apply this multi-layered model to the El Oro complex. This model allows the volume of melt extracted to be predicted, as well as melt composition and residual composition at the crustal scale. The novelty of this approach is that all these variables can be studied through time, a crucial variable missing phase equilibrium modelling studies. Different models are constructed to test different scenarios and the results confirm that the volume of melt produced from the base of the metamorphic sequence of the El Oro complex is compatible with the volume of pluton currently observed in the sequence. In addition, I show that mixing with a mafic component is required to reconcile the predicted compositions of the melt from the model with the observed composition of the El Oro complex granitoids.

This work highlights the value of developing and applying numerical models to better understand melting processes in the continental crust. It also emphasises the importance of constraining these models with natural data and observations. In particular, time is a critical variable that must be accurately constrained and compared with model predictions. Further development and refinement of these models, together with a better understanding of the duration and timescale of crustal melting, is essential to gain a deeper insight into these processes. This thesis aims to demonstrate the potential of this approach.

# Acknowledgements

First of all, I would like to thank my supervisors, Pierre Lanari and Nicolas Riel. Pierre, thank you for giving me the complete freedom and the opportunity to explore very different topics during my PhD. You know that I love to get lost in the details, and you gave me the chance to do so to my full satisfaction (and sometimes my own demise). Thank you for always being available to listen to me talk for hours about equations and for dealing with my stubbornness. I know now that listening more to your suggestions would have saved me often a lot of time. Thank you for teaching me to be more optimistic about my research and to not be afraid of testing things. And finally, thank you for letting me get so much free food during my PhD, that was a real pleasure. I am happy to be officially your first PhD student and I am sure that supervision will seem easy for all the PhD students that will follow after working with me. Nicolas, thank you for introducing me to the world of numerical modelling and mushroom picking. Thank you for welcoming me to Mainz and to convince me to give up on Python to embrace Julia. I don't know many people who would be happy to fix bugs at 11 pm, but you are one of them. Thank you for introducing me to MAGEMin and letting me destroy it a few times with interesting pull requests. I look forward to work more closely (in the geographical sense) with you in the coming years.

Thank you to all the colleagues at the institute of Bern, from which I learned a lot and that made these four years fly. Thank you to Jörg Hermann, Daniela Rubatto and Thomas Pettke, to name some of the big names from Bern, for teaching me a lot of things during group meetings and discussions. Thank you to Thomas Aebi, Stephan Brechbühl and Nadine Lötscher for their technical expertise and for using their skills for making my thin sections. Thank you to Marina Beutler, Ursula Kuonen, Sarah Antenen for always helping me with the administrative side of my PhD. Many thanks also goes to Jean-François Moyen, for not only accepting to review my thesis, but also for introducing me to Archean geology some years ago, bringing me to an Archean craton in South Africa in the middle of my master semester and for forwarding an email about a PhD position four years ago. Thank you to Gary Stevens for teaching me the joy of petrology and for giving me the opportunity to learn what it means to do research before starting this PhD.

Finally, some further special mentions and thanks, in no particular order, to the people I have met over these four years: first, Jacob Forshaw, for being my flatmate, colleague and friend for almost three years. I am glad that you decided that your room was good enough for your stay in Bern and not just a temporary solution. I already miss our carbonara and film nights. Thank you for your support in the last years of this PhD. Thank you also for introducing me to the wisdom of the elders and proving time and again that everything has been already done in the 70's. Next, Dr Coralie Vesin (aka Vésin), for being my office mate and French friend for these four years. Our friendship has been very important to me in some crucial moments of these four years. I look forward to resuming our puzzle and French movies night. You managed to finish your PhD before me, but I am catching up. To Mona Lüder, thank you for your unconditional support over the past few months and your patience with me. Thank you for always bringing cakes in times of need and for always being there for me. I look forward to spending more time with you again. To Renée Tamblyn, for proving to me that you can have a grandmother's first name and still be a cool person. Thank you for introducing me to geochronology and for always being optimistic and supportive of my work. To our hectic laser sessions. I am still convinced that focusing on mercury in zircons is the way forward even though you always refused to measure it accurately. To Thorsten Markmann, for being there to teach me the German way, for reminding me why I stopped playing basketball by constantly obliterating me and for being my PhD brother under the same supervisor. To Mahyra Tedeschi, for introducing me to the world of migmatites and your beautiful country. To Philip Hartmeier, for sharing my enthusiasm for programming, maths and One Piece. Good luck with your PhD, I now know the full experience. To Jiahui Liu and Qian Zhang (her husband), for the hectic dumpling sessions and for the great time we spent together. To Michelle Ulrich, for introducing me to some martial arts and for being so Swiss. Thanks also goes to my different office mates in the office 116 over the years: Julien

Reynes, Thomas Bovay, Luca Pacchiega, Sara Nerone. To Déborah Harlet, for our Mario Kart and Koh Lanta evenings. And to all the people who have shared some memorable times with me over the years, from Bern or elsewhere: Scott Jess, Catarina Da Paz, Timi Schmidt, Bennet Schuster, Robert Webster, Weijia Zhan, Shan Grémion, Maxime Daviray, Romain Poirier, Léo Marconato, Victor Klaba, Quentin Millard, Marin Laurent, Maude Chenudet, Clémence Rouillon, to name but a few. And, of course, a special mention to the people I have forgotten in this non-exhaustive list. Last but not least, a huge thank you to my family who have always supported me over the years and continue to do so.

# Contents

Chapter I

# Introduction

Modern active melting processes are relatively rare at the scale of the continental crust, as they require enormous amounts of energy, and are typically found along current converging plate boundaries (Barbarin, 1999; Bea, 2012; Clark et al., 2011; Henk et al., 2000; Wells, 1980). Nevertheless, these processes are crucial for crust formation and recycling, as well as for heat transport and crustal differentiation (Hawkesworth et al., 2010; Jaupart & Mareschal, 2010; Korenaga, 2018; Sawyer et al., 2011; Sighinolfi & Gorgoni, 1978; Vielzeuf et al., 1990; Wells, 1981). The end products of these processes, namely granitoid rocks, are a major component of the continental crust and contribute to its low density, which enables the long-term stability and preservation of the continents on Earth (Rudnick & Gao, 2003; Taylor & McLennan, 2009). Two end member mechanisms have been proposed to explain the formation of granitoids: (i) fractionation and differentiation of mantle-derived magmas, with chemical contribution from the crust (e.g Dessimoz et al., 2012; Hildreth & Moorbath, 1988; Jagoutz & Klein, 2018; Jagoutz et al., 2009; Tuttle & Bowen, 1958), and (ii) partial melting and melt segregation of continental crustal rocks (e.g. Chappell & White, 1974; Clemens & Stevens, 2012; Clemens & Vielzeuf, 1987). Both mechanisms are supported by strong geological evidence, although the dominance of one mechanism over the other depends on the geological setting, for example whether subduction or collision is dominant. As these two processes are end members, hybrid granitoid suites are probably the most common (e.g. Jacob et al., 2021). Thus, an important debate is not how granitoid suites generally form, but rather which mechanism is dominant on the scale of Earth history, which one is responsible for recycling and/or producing continental crust, and in which geological settings do they occur (e.g. Moyen et al., 2021; Moyen et al., 2017).

To try to answer these questions, it is important to have a good understanding of various processes related to melt generation, transport and emplacement. Studying granitoids alone may not be sufficient, as most granitic melts tend to evolve towards the granitic minimum composition (e.g. Bonin et al., 2020; Johannes & Holtz, 1996), meaning that different processes can lead to similar end products. Also, granitoids may be more accurately viewed as mixtures of cumulus phases or crystal mushes, from which liquids may have been extracted and subsequently erupted as dacites or rhyolites (e.g. Bachmann, 2004). Therefore, a better understanding of the mechanisms leading to melt extraction and segregation, and obtaining constraints not only from the end product of melting processes, but also from the source of melt and intermediate products, is key. This thesis focuses on the processes involved in the formation of crustal-derived granitic melts, from partial melting to melt transport and emplacement within the crust.

Migmatites are rocks found in medium- to high-grade metamorphic terranes that exhibit heterogeneity from the microscopic to the macroscopic scale. They are rocks that have undergone partial melting and often consist of two petrographically distinct parts: (i) the paleosome, which is considered to be the part of the protolith that hasn't melted, and (ii) the neosome, which is interpreted to be the result of partial melting and subsequent melt crystallisation. The neosome typically contains pale quartzofeldspathic or feldspathic minerals and darker sections enriched in ferromagnesian minerals. In some cases, partial melting does not produce distinct light and dark zones, but instead alters the mineralogy, microstructure, and grain size (Sawyer, 2008). Migmatites show evidence of melt segregation and transport, where melt segregation here describes the motion of the melt relative to the solid at the grain scale, whereas melt transport, or melt ascent, implies motion of the melt beyond the grain scale (e.g. Allibone & Norris, 1992; Johannes, 1988; Sawyer, 1994). The migmatites of interest for this thesis are the ones produced during regional metamorphism, as opposed to the migmatites formed in contact aureoles. Such migmatites, formed in the upper amphibolite to lower granulite facies, have been identified as a melt source and their association with granitoids is now well established (e.g. Patiño Douce & Johnston, 1991; Solar & Brown, 2001). However, the study of migmatites is complex. Because the melt is mobile, they are better described as a dynamic open system where melt can be extracted but also injected, and back reaction of melt with the host rock can be considerable (e.g. Hasalová et al., 2008; Kriegsman, 2001). Furthermore, preserved outcrops of migmatite can be seen as the last geological snapshot involving melting before the system froze, which can make it difficult to decipher the details of their formation.

Finally, the study of the link and relationship between migmatites and large granitoid plutons is best achieved in a crustal section where both rock types are exposed and a clear co-genetic link can be established. However, continuous exposures of granitoid systems from migmatite sources to granitoid plutons are rarely observed (e.g. Martini et al., 2019; Reichardt & Weinberg, 2012). This is because melting typically occurs deep

in the continental crust, close to the heat source, whereas most plutons are emplaced in the middle to upper crust, where the transition from ductile to brittle rheology occurs (Sawyer et al., 2011). As a result, most of what is known about melting processes is derived from the integration of different and often geographically unlinked geological systems.

This thesis focuses on three different key aspects of the link between the formation of migmatites and crustal-derived granitoid plutons: (i) the mechanisms involved for melt transport, (ii) the timescale of melting and emplacement of melt, and (iii) the compositional and reactional link between metapelitic migmatites and crustal-derived granitoids. These aspects are investigated using different approaches: numerical modelling, geochemistry and geochronology, and natural data and observations. In particular, the geological object of interest in this thesis is the El Oro complex, Ecuador. This metamorphic complex is a tilted section of a paleo-crust that provides a clear exposure from migmatites to crustal-derived granitoid plutons (e.g. Riel et al., 2013; Riel et al., 2014).

## 1. Mechanisms of melt transport in crustal-melting dominated system and the potential of two-phase flow modelling

The mechanisms involved in melt transport remain largely unconstrained, especially in the lower to middle crust, where the ductile regime predominates, and is probably the least understood aspect of migmatitisation and melting processes at present (Brown, 2013; Brown, 1994; Cruden & Weinberg, 2018; Sawyer, 1994, 2001; Vanderhaeghe, 2009). A wide range of mechanisms have been proposed, reflecting the different approaches used to study these processes, the diversity observed in the geological record, but also the complexity of the problem. The challenges in studying these mechanisms arise from the complex rheology involved, where a solid, stiffer matrix interacts with a weaker, liquid phase. This makes the partially molten crust a highly dynamic, non-linear system with time-dependent behaviour characterised by shifts in deformation mechanisms and redistribution of melt. Such mechanisms in the lower to middle crust include diking, diapirism, shear channeling and pervasive flow (Brown, 1994; Cruden & Weinberg, 2018; Grout, 1945; Hasalová et al., 2008; Ramberg, 1970). It is likely that more than one of these mechanisms may be operating simultaneously and that gradual changes from one to the other may occur throughout a system's history.

As natural samples in geochemical and petrological studies represent only the end product of the melting processes (Brown, 2013; Clemens et al., 2022; Johnson et al., 2021), numerical modelling offers an attractive complementary approach by allowing the study of these processes at different spatial and temporal scales. Ultimately, the different transport mechanisms noted above can be modelled using the continuum formulation of two-phase flow, which describes the physical behaviour of a silicate melt percolating through and interacting with a tectonically deforming host rock, and can be viewed as different end members (Dohmen & Schmeling, 2021; Keller et al., 2013). A two-phase flow formalism was first developed to describe the ascent of basaltic melt in the asthenosphere and lithosphere for a low melt fraction, using viscous creep of the host rock as the main deformation mechanism (e.g. Bercovici et al., 2001; Drew, 1971; Fowler, 1985; McKenzie, 1984; Sleep, 1974). In this view, the main drivers of melt segregation and transport are the compaction/decompaction of the rock matrix and the relative buoyancy of the melt compared to the host rock. This formulation has been shown to generate porosity waves (Barcilon & Richter, 1986; Scott & Stevenson, 1984, 1986; Spiegelman, 1993a, 1993b) and has been successfully used to model melt transport at mid-oceanic ridges and above subduction zones (e.g. Bessat et al., 2022; Cagnioncle et al., 2007; Katz, 2010; Spiegelman & McKenzie, 1987).

However, the applicability of these assumptions has been questioned for migmatites, as the timescales of compaction/decompaction may be too long relative to the timescales of regional metamorphism when applied to granitic melt (Sawyer, 1994; Vigneresse et al., 1996; Wickham, 1987). This is mainly due to one observation: granitic melts can be up to 3 to 8 orders of magnitude more viscous than basaltic melts at the same temperatures, depending on the water content considered (Clemens & Petford, 1999; Giordano et al., 2008). The lower temperatures typically considered for migmatites, between 650 and 900°C, also contribute to producing a more viscous melt compared to mantle-derived melt. This implies a lower viscosity contrast between the host rock and the melt, which reduces the efficiency of compaction and decompaction processes.

In addition, dehydration-melting reactions and water-fluxed melting produce a significant amount of melt, and the assumption of a low melt-fraction is not always met, as demonstrated by the common occurrence of diatexites. This has led to the widespread idea of the importance of a melt connectivity transition, associated with a certain amount of melt volume fraction that would be required to achieve melt connectivity and allow weakening of the host rock (e.g. Rosenberg & Handy, 2005; Vigneresse et al., 1996). The development of two-phase flow formulations incorporating more complex rheology and the extension of the formulations to higher melt-fractions may then be required to model these systems. Recently, new formulations have been developed to include visco-elasto-plastic regimes, extending the range of possible mechanisms for melt transport (Connolly & Podladchikov, 2007; Keller et al., 2013; Yarushina et al., 2015). Also, some formulations have recently been expanded to apply to moderate or even high melt fractions, going beyond the Darcy's law assumption, and further reducing the number of approximations used (Keller & Suckale, 2019; Schmeling et al., 2019; Wong & Keller, 2023). This opens up the potential to model the transport of melt in crustal melting settings in a dynamic way at the crustal scale, from the migmatites to the plutons, at the cost of additional complexity in the formulations (e.g. Schmeling et al., 2023). Finally, an important layer of additional complexity that is not considered in these formulations is phase reactions and chemical transport, which is the final step to achieve a fully multiphase multicomponent reactive transport model (Oliveira et al., 2018). Several studies have investigated the impact of reactive melt transport (e.g. Aharonov et al., 1997; Bouilhol et al., 2011; Jackson et al., 2005; Omlin et al., 2017; Riel et al., 2019), showing the potential of such an approach. With the incorporation of phase reactions and chemical transport, this opens up the potential of being able to compare the rock record with such models, as migmatites and crustal-derived granitoids are both ultimately the product of melt-producing metamorphic reactions.

However, numerical models of a fully non-linear coupled system of increasing complexity implies increasing uncertainty, as more parameters are added to the model and more complex interactions take place. It is therefore important to reduce as much as possible the inevitable numerical errors introduced during the coupling. An evaluation is needed to find the best way to couple chemical transport with the mechanical formulation of two-phase flow before it can be applied to a geological object, and before hypotheses about melt transport mechanisms can be tested. This will be investigated in Chapter II of this thesis.

## 2. Timescales of crustal melting and pluton emplacement

Our understanding of the timescales and durations of crustal melting and granitoid plutons has improved greatly in recent decades. This is mainly due to improved precision in geochronology, now often combined with in situ trace element measurements and isotopic analyses, particularly using zircon. Combined with cathodoluminescence imaging to distinguish different growth zones and populations, this approach has been successful and zircon has been widely used in both metamorphic and igneous communities to constrain the timing and conditions of melting processes. It has been shown to be a robust tool for unravelling the complex history of granitoid plutons and migmatites, with the caveat of accepting its various limitations (e.g. Kohn et al., 2015; Rubatto, 2017; Schmitt et al., 2023, and references therein).

For plutons, this new generation of high spatial resolution data has significantly advanced the view that magma reservoirs are incrementally constructed zones within the crust, where melt, crystals, and volatiles are unevenly distributed both spatially and temporally (Cashman et al., 2017; Kemp et al., 2007; Wotzlaw et al., 2013). The achievement of unprecedented high precision in thermal ionisation mass spectrometry (TIMS) zircon geochronology, with accuracies better than 0.1% on $^{206}Pb/^{238}U$ dates (e.g. Schaltegger et al., 2015; Schoene & Baxter, 2017), has shown that pluton assembly could be accomplished between ca. 100 thousand years up to a few million years (Coleman et al., 2004; Matzel et al., 2006; Michel et al., 2008; Samperton et al., 2015; Schoene et al., 2012; Wotzlaw et al., 2013). The different timescales of different plutons, when compared, show a positive correlation with the size of the pluton considered, which has been interpreted to show that plutonic magmatic fluxes appear to be comparable from one geological context to another (De Saint Blanquat et al., 2011). This has led to the view that magma transfer, and therefore pluton emplacement, occurs on shorter timescales compared to tectonic rates (e.g. Annen, 2011; De Saint Blanquat et al., 2011; Petford et al.,

2000; Van Zalinge et al., 2022). It is important to note, however, that most of these studies have focused on continental and oceanic arcs and intraplate continental environments, where granitoids are primarily formed by mixing of mantle-derived and crustal magmas (e.g. Szymanowski et al., 2015, and previous references). In comparison, fewer studies have been carried out using this type of approach on purely crustal-derived granitoids, such as peraluminous granitoids (Farina et al., 2014; Farina et al., 2018).

The timescales considered for deep crustal melting are different. This is because, apart from the initial composition of the protolith, the primary controls on dehydration-reaction driven partial melting in a rock are the metamorphic conditions and, in particular, the temperature. As such, it is mainly controlled by tectonic processes and geodynamics, and mainly depends on the duration of prograde metamorphism (Winter, 2014). As a consequence, typical timescales are closer to tectonic rates, on the order of tens of millions of years for regional metamorphism, but can be smaller depending on the heat source and the geological setting considered (e.g. Gordon et al., 2008; Gordon et al., 2010; Harris et al., 2004; Rubatto et al., 2001, 2013; Weinberg, 2016).

This difference in timescale is an important observation that needs to be addressed. This would be best achieved by comparing both crustal-derived granitoids and their source. Few studies report the studies of both granitoid plutons and migmatites, their potential source (e.g. Couzinié et al., 2021; Li et al., 2022; Reichardt & Weinberg, 2012). Chapter III of this thesis will focus on this question and approach using mainly geochronology and trace element data of zircon from the El Oro complex, Ecuador.

## 3. Melting reactions in high-grade metapelites and their link with crustal-derived granitoids

Metapelites are metamorphosed clastic clay-rich sedimentary rocks. They are widely studied because they are common and develop a distinctive suite of index minerals that can be used to qualitatively estimate the *P*–*T* conditions in both subsolidus and suprasolidus rocks (Bucher & Grapes, 2011). The reactions involving melting in the absence of a free aqueous fluid are well known. Melting occurs by incongruent melting reactions involving dehydration of micas. The main reactions involve the breakdown of two micas: muscovite and biotite. At pressure higher than 0.5 GPa, the breakdown of muscovite occurs first, at 650–750°C and with a small *P* dependence. The breakdown of biotite occurs at higher *T*, 750–850°C, with a stronger *P* dependence. Muscovite breakdown typically produces peritectic aluminosilicates and K-feldspar in addition to melt, whereas biotite breakdown often produces garnet, orthopyroxene and/or cordierite (Breton & Thompson, 1988; Clemens & Wall, 1981; Dyck et al., 2020; Gardien et al., 1995; Thompson & Algor, 1977; Thompson & Tracy, 1979). Both reactions produce a peraluminous granitic melt, compatible with sedimentary-derived (S-type) granitoid compositions (Chappell & White, 1974, 2001; Patiño Douce & Johnston, 1991; Solar & Brown, 2001), and such peritectic minerals are commonly observed in migmatites derived from metapelites, consistent with these *P*–*T* dependant reactions (Sawyer, 2008).

However, the link between the melt produced in metapelitic migmatites and S-type granitoid plutons, especially in terms of composition, is not so simple. The chemical variation observed in such plutons, in terms of major, minor, trace and isotopic compositions is significant (e.g. Brown, 2013; Brown & Pressley, 1999; Clemens & Stevens, 2012; Villaros, Stevens, Moyen, & Buick, 2009). This variation cannot be explained solely by the variation in the melt chemistry produced during the progress of the melting reactions in the source (Montel & Vielzeuf, 1997; Patiño Douce & Johnston, 1991; Sawyer, 1996). As such, multiple hypotheses have been proposed over the years to explain this range, such as compositional variations in the protolith of the source at the crustal scale, contamination from a mantle-derived source, entrapment of restite/peritectic minerals, fractional crystallisation or contamination from wall-rocks during emplacement (e.g. Breaks & Moore, 1992; Chappell et al., 1987; Clemens & Stevens, 2012; Collins, 1996; Gray, 1990; Johannes et al., 2003; Stevens et al., 2007; Villaros, Stevens, & Buick, 2009).

A popular approach to test these hypotheses is phase equilibrium modelling. This approach has emerged in the last decades as a powerful tool to model phase reactions and predict stable phase assemblages at equilibrium conditions. In particular, frameworks and tools have been developed to tackle the challenges of

models involving melt, such as simulating open-system behaviour with melt extraction steps along a *P–T* path (Johnson et al., 2021; Mayne, Stevens, Moyen, & Johnson, 2020). This led to recent studies exploring different hypotheses with variations in bulk rock compositions, and different extraction and entrapments scenarios with melt extraction (e.g. Koblinger & Pattison, 2017; Mayne, Stevens, & Moyen, 2020; Schwindinger et al., 2019). Chapter IV of this thesis aims to extend this approach by coupling phase equilibrium modelling with thermal modelling at the crustal scale. This approach provides new insights into the relationship between the melt source and the final product, both in terms of composition and melt volume. In addition, these variables can be studied through time, a crucial variable missing in phase equilibrium modelling studies. This approach is applied to the El Oro complex, in Ecuador, similarly to Chapter III.

## 4. Outline of the thesis

This thesis aims to provide a better understanding of the processes linking crustal melting and crustal-derived granitoid plutons. In addition to the present introduction (Chapter I) and a conclusion summarising the main findings (Chapter V), this thesis is divided into three main chapters, each of which focuses on a specific aspect of melting processes: (i) the mechanisms of melt transport, (ii) the timescales of melting processes, and (iii) the compositional relationship between migmatites and crustal-derived granitoid plutons. Chapter II focuses purely on numerical modelling, while Chapter III and Chapter IV are studies applied to the locality of the El Oro complex, in Ecuador. These last two chapters are the present outcomes of a mission of more than 1 month of field work carried out in the El Oro complex during the work of this thesis. During this mission, more than 100 samples were collected, which will also be used for future projects. A brief description of each of the main chapters is given bellow.

**Chapter II: Modelling chemical advection during magma ascent**

This chapter focuses on finding the best numerical approach to combine chemical advection with two-phase flow modelling. The first part of the chapter describes four algorithms commonly used in different fields for modelling advection. The second part studies the coupling between these different algorithms with a two-phase flow code. The main result of this chapter is that one algorithm, the weighted essentially non-oscillatory (WENO) scheme, performs the best in terms of mass conservation and is the best compromise between numerical diffusion and performance. This opens the way to perform more accurate reactive transport modelling in the crust. This manuscript was published in August 2024 in the journal *Geoscientific Model Development*.

**Chapter III: Melting dynamics and pluton formation in the continental crust: a zircon geochronology and trace element study of the El Oro complex, Ecuador**

This chapter studies mainly the time relationship between metapelitic migmatites and a S-type granitoid pluton, the Marcabelí pluton, in the El Oro complex, Ecuador. It also aims at improving the time constraints on the regional metamorphic event of interest. U–Pb geochronology on zircon is combined with trace element data using LA-ICP-MS from both migmatites and granitoids. U–Pb geochronology on titanite of the potential heat source is also performed. This chapter shows that the Marcabelí pluton is a long-lived pluton with a total duration of emplacement similar to the metamorphic melting event in the migmatites. The results are interpreted as showing that not continuous but multiple pulses of magma are recorded over a period of time of more than 20 Myr in the pluton. In addition, this chapter highlights the appeal of measuring both U–Pb and trace element data to discriminate population, and gaining insight into melt processes, such as open system behaviour in migmatites. This manuscript is in preparation for submission to the journal *Contributions to Mineralogy and Petrology*.

**Chapter IV: Coupling thermal and phase equilibrium modelling to investigate time constraints in melting processes**

This chapter studies the chemical relationships between the same geological objects as Chapter III: the metapelitic migmatites and the S-type granitoid pluton preserved as the Marcabelí pluton of the El Oro complex. New bulk chemical data are introduced and two new 1D crustal thermal models are developed to account for the new geochronological constraints obtained from Chapter III. One of the 1D thermal models is then coupled with phase equilibrium modelling to study the melt produced by partial melting in the crust. Different models are tested and the compositions and volumes of melt produced are compared with the natural data of the El Oro complex. This chapter shows the potential of combining phase equilibrium modelling with thermal models to obtain time constraints on phase reactions during regional metamorphism, to perform mass balance assessments and to compare complex models with natural observations. This manuscript is in preparation for submission to *Journal of Metamorphic Geology*.

# References


Aharonov, E., Spiegelman, M., & Kelemen, P. (1997). Three-dimensional flow and reaction in porous media: Implications for the Earth's mantle and sedimentary basins. *Journal of Geophysical Research: Solid Earth*, *102*(B7), 14821–14833. https://doi.org/10.1029/97JB00996 (cit. on p. 4).

Allibone, A. H., & Norris, R. J. (1992). Segregation of leucogranite microplutons during syn-anatectic deformation: An example from the Taylor Valley, Antarctica. *Journal of Metamorphic Geology*, *10*(4), 589–600. https://doi.org/10.1111/j.1525-1314.1992.tb00107.x (cit. on p. 2).

Annen, C. (2011). Implications of incremental emplacement of magma bodies for magma differentiation, thermal aureole dimensions and plutonism–volcanism relationships. *Tectonophysics*, *500*(1–4), 3–10. https://doi.org/10.1016/j.tecto.2009.04.010 (cit. on p. 4).

Bachmann, O. (2004). On the Origin of Crystal-poor Rhyolites: Extracted from Batholithic Crystal Mushes. *Journal of Petrology*, *45*(8), 1565–1582. https://doi.org/10.1093/petrology/egh019 (cit. on p. 2).

Barbarin, B. (1999). A review of the relationships between granitoid types, their origins and their geodynamic environments. *Lithos*, *46*(3), 605–626. https://doi.org/10.1016/S0024-4937(98)00085-1 (cit. on p. 2).

Barcilon, V., & Richter, F. M. (1986). Nonlinear waves in compacting media. *Journal of Fluid Mechanics*, *164*, 429–448. https://doi.org/10.1017/S0022112086002628 (cit. on p. 3).

Bea, F. (2012). The sources of energy for crustal melting and the geochemistry of heat-producing elements. *Lithos*, *153*, 278–291. https://doi.org/10.1016/j.lithos.2012.01.017 (cit. on p. 2).

Bercovici, D., Ricard, Y., & Schubert, G. (2001). A two-phase model for compaction and damage: 1. General Theory. *Journal of Geophysical Research: Solid Earth*, *106*(B5), 8887–8906. https://doi.org/10.1029/2000JB900430 (cit. on p. 3).

Bessat, A., Pilet, S., Podladchikov, Y. Y., & Schmalholz, S. M. (2022). Melt Migration and Chemical Differentiation by Reactive Porosity Waves. *Geochemistry, Geophysics, Geosystems*, *23*(2). https://doi.org/10.1029/2021GC009963 (cit. on p. 3).

Bonin, B., Janoušek, V., & Moyen, J.-F. (2020). Chemical variation, modal composition and classification of granitoids. *Geological Society, London, Special Publications*, *491*(1), 9–51. https://doi.org/10.1144/SP491-2019-138 (cit. on p. 2).

Bouilhol, P., Connolly, J. A., & Burg, J.-P. (2011). Geological evidence and modeling of melt migration by porosity waves in the sub-arc mantle of Kohistan (Pakistan). *Geology*, *39*(12), 1091–1094. https://doi.org/10.1130/G32219.1 (cit. on p. 4).

Breaks, F. W., & Moore, J. M. (1992). The Ghost Lake batholith, Superior Province of northwestern Ontario: A fertile, S-type, peraluminous granite-rare-element pegmatite system. *Canadian Mineralogist*, *30*, 835–835 (cit. on p. 5).

Breton, N. L., & Thompson, A. B. (1988). Fluid-absent (dehydration) melting of biotite in metapelites in the early stages of crustal anatexis. *Contributions to Mineralogy and Petrology*, *99*(2), 226–237. https://doi.org/10.1007/BF00371463 (cit. on p. 5).

Brown, M. (2013). Granite: From genesis to emplacement. *Geological Society of America Bulletin*, *125*(7–8), 1079–1113. https://doi.org/10.1130/B30877.1 (cit. on pp. 3, 5).

Brown, M., & Pressley, R. (1999). Crustal melting in nature: Prosecuting source processes. *Physics and Chemistry of the Earth, Part A: Solid Earth and Geodesy*, *24*(3), 305–316. https://doi.org/10.1016/S1464-1895(99)00034-4 (cit. on p. 5).

Brown, M. (1994). The generation, segregation, ascent and emplacement of granite magma: The migmatite-to-crustally-derived granite connection in thickened orogens. *Earth-Science Reviews*, *36*(1–2), 83–130. https://doi.org/10.1016/0012-8252(94)90009-4 (cit. on p. 3).

Bucher, K., & Grapes, R. (2011). Metamorphism of Pelitic Rocks (Metapelites). In K. Bucher & R. Grapes (Eds.), *Petrogenesis of Metamorphic Rocks* (pp. 257–313). Springer. https://doi.org/10.1007/978-3-540-74169-5_7 (cit. on p. 5).

Cagnioncle, A.-M., Parmentier, E. M., & Elkins-Tanton, L. T. (2007). Effect of solid flow above a subducting slab on water distribution and melting at convergent plate boundaries. *Journal of Geophysical Research: Solid Earth*, *112*(B9), 2007JB004934. https://doi.org/10.1029/2007JB004934 (cit. on p. 3).

Cashman, K. V., Sparks, R. S. J., & Blundy, J. D. (2017). Vertically extensive and unstable magmatic systems: A unified view of igneous processes. *Science*, *355*(6331), eaag3055. https://doi.org/10.1126/science.aag3055 (cit. on p. 4).

Chappell, B., & White, A. (1974). Two contrasting granite types. *Pacific Geology*, *8*, 173–174 (cit. on pp. 2, 5).

Chappell, B., & White, A. (2001). Two contrasting granite types: 25 years later. *Australian Journal of Earth Sciences*, *48*(4), 489–499. https://doi.org/10.1046/j.1440-0952.2001.00882.x (cit. on p. 5).

Chappell, B., White, A., & Wyborn, D. (1987). The Importance of Residual Source Material (Restite) in Granite Petrogenesis. *Journal of Petrology*, *28*(6), 1111–1138. https://doi.org/10.1093/petrology/28.6.1111 (cit. on p. 5).

Clark, C., Fitzsimons, I. C. W., Healy, D., & Harley, S. L. (2011). How Does the Continental Crust Get Really Hot? *Elements*, *7*(4), 235–240. https://doi.org/10.2113/gselements.7.4.235 (cit. on p. 2).

Clemens, J., & Petford, N. (1999). Granitic melt viscosity and silicic magma dynamics in contrasting tectonic settings. *Journal of the Geological Society*, *156*(6), 1057–1060 (cit. on p. 3).

Clemens, J., Bryan, S. E., Stevens, G., Mayne, M. J., & Petford, N. (2022). How are silicic volcanic and plutonic systems related? Part 2: Insights from phase-equilibria, thermodynamic modelling and textural evidence. *Earth-Science Reviews*, *235*, 104250. https://doi.org/10.1016/j.earscirev.2022.104250 (cit. on p. 3).

Clemens, J., & Stevens, G. (2012). What controls chemical variation in granitic magmas? *Lithos*, *134–135*, 317–329. https://doi.org/10.1016/j.lithos.2012.01.001 (cit. on pp. 2, 5).

Clemens, J., & Vielzeuf, D. (1987). Constraints on melting and magma production in the crust. *Earth and Planetary Science Letters*, *86*(2–4), 287–306. https://doi.org/10.1016/0012-821X(87)90227-5 (cit. on p. 2).

Clemens, J., & Wall, V. J. (1981). Origin and crystallization of some peraluminous (S-type) granitic magmas. *The Canadian Mineralogist*, *19*(1), 111–131 (cit. on p. 5).

Coleman, D. S., Gray, W., & Glazner, A. F. (2004). Rethinking the emplacement and evolution of zoned plutons: Geochronologic evidence for incremental assembly of the Tuolumne Intrusive Suite, California. *Geology*, *32*(5), 433. https://doi.org/10.1130/G20220.1 (cit. on p. 4).

Collins, W. (1996). Lachlan Fold Belt granitoids: Products of three-component mixing. *Earth and Environmental Science Transactions of the Royal Society of Edinburgh*, *87*(1–2), 171–181 (cit. on p. 5).

Connolly, J. A. D., & Podladchikov, Y. Y. (2007). Decompaction weakening and channeling instability in ductile porous media: Implications for asthenospheric melt segregation. *Journal of Geophysical Research*, *112*(B10), B10205. https://doi.org/10.1029/2005JB004213 (cit. on p. 4).

Couzinié, S., Bouilhol, P., Laurent, O., Marko, L., & Moyen, J.-F. (2021). When zircon drowns: Elusive geochronological record of water-fluxed orthogneiss melting in the Velay dome (Massif Central, France). *Lithos*, *384–385*, 105938. https://doi.org/10.1016/j.lithos.2020.105938 (cit. on p. 5).

Cruden, A., & Weinberg, R. (2018). Mechanisms of magma transport and storage in the lower and middle crust—magma segregation, ascent and emplacement. *Volcanic and igneous plumbing systems*, 13–53 (cit. on p. 3).

De Saint Blanquat, M., Horsman, E., Habert, G., Morgan, S., Vanderhaeghe, O., Law, R., & Tikoff, B. (2011). Multiscale magmatic cyclicity, duration of pluton construction, and the paradoxical relationship between tectonism and plutonism in continental arcs. *Tectonophysics*, *500*(1–4), 20–33. https://doi.org/10.1016/j.tecto.2009.12.009 (cit. on p. 4).

Dessimoz, M., Müntener, O., & Ulmer, P. (2012). A case for hornblende dominated fractionation of arc magmas: The Chelan Complex (Washington Cascades). *Contributions to Mineralogy and Petrology*, *163*(4), 567–589. https://doi.org/10.1007/s00410-011-0685-5 (cit. on p. 2).

Dohmen, J., & Schmeling, H. (2021). Magma ascent mechanisms in the transition regime from solitary porosity waves to diapirism. *Solid Earth*, *12*(7), 1549–1561. https://doi.org/10.5194/se-12-1549-2021 (cit. on p. 3).

Drew, D. A. (1971). Averaged Field Equations for Two-Phase Media. *Studies in Applied Mathematics*, *50*(2), 133–166. https://doi.org/10.1002/sapm1971502133 (cit. on p. 3).

Dyck, B., Waters, D. J., St-Onge, M. R., & Searle, M. P. (2020). Muscovite dehydration melting: Reaction mechanisms, microstructures, and implications for anatexis. *Journal of Metamorphic Geology*, *38*(1), 29–52. https://doi.org/10.1111/jmg.12511 (cit. on p. 5).

Farina, F., Stevens, G., Gerdes, A., & Frei, D. (2014). Small-scale Hf isotopic variability in the Peninsula pluton (South Africa): The processes that control inheritance of source 176Hf/177Hf diversity in S-type granites. *Contributions to Mineralogy and Petrology*, *168*(4), 1065. https://doi.org/10.1007/s00410-014-1065-8 (cit. on p. 5).

Farina, F., Dini, A., Davies, J. H., Ovtcharova, M., Greber, N. D., Bouvier, A.-S., Baumgartner, L., Ulianov, A., & Schaltegger, U. (2018). Zircon petrochronology reveals the timescale and mechanism of anatectic magma formation. *Earth and Planetary Science Letters*, *495*, 213–223. https://doi.org/10.1016/j.epsl.2018.05.021 (cit. on p. 5).

Fowler, A. C. (1985). A mathematical model of magma transport in the asthenosphere. *Geophysical & Astrophysical Fluid Dynamics*, *33*(1–4), 63–96. https://doi.org/10.1080/03091928508245423 (cit. on p. 3).

Gardien, V., Thompson, A. B., Grujic, D., & Ulmer, P. (1995). Experimental melting of biotite + plagioclase + quartz ± muscovite assemblages and implications for crustal melting. *Journal of Geophysical Research: Solid Earth*, *100*(B8), 15581–15591. https://doi.org/10.1029/95JB00916 (cit. on p. 5).

Giordano, D., Russell, J. K., & Dingwell, D. B. (2008). Viscosity of magmatic liquids: A model. *Earth and Planetary Science Letters*, *271*(1–4), 123–134. https://doi.org/10.1016/j.epsl.2008.03.038 (cit. on p. 3).

Gordon, S. M., Whitney, D. L., Teyssier, C., Grove, M., & Dunlap, W. J. (2008). Timescales of migmatization, melt crystallization, and cooling in a Cordilleran gneiss dome: Valhalla complex, southeastern British Columbia. *Tectonics*, *27*(4), 2007TC002103. https://doi.org/10.1029/2007TC002103 (cit. on p. 5).

Gordon, S. M., Bowring, S. A., Whitney, D. L., Miller, R. B., & McLean, N. (2010). Time Scales of Metamorphism, Deformation, and Crustal Melting in a Continental Arc, North Cascades USA. *Geological Society of America Bulletin*, *122*(7–8), 1308–1330. https://doi.org/10.1130/B30060.1 (cit. on p. 5).

Gray, C. M. (1990). A strontium isotopic traverse across the granitic rocks of southeastern Australia: Petrogenetic and tectonic implications. *Australian Journal of Earth Sciences*. https://doi.org/10.1080/08120099008727931 (cit. on p. 5).

Grout, F. F. (1945). Scale models of structures related to batholiths. *Am. Jour. Sci*, *243*, 260–284 (cit. on p. 3).

Harris, N. B. W., Caddick, M., Kosler, J., Goswami, S., Vance, D., & Tindle, A. G. (2004). The pressure–temperature–time path of migmatites from the Sikkim Himalaya. *Journal of Metamorphic Geology*, *22*(3), 249–264. https://doi.org/10.1111/j.1525-1314.2004.00511.x (cit. on p. 5).

Hasalová, P., Štípská, P., Powell, R., Schulmann, K., Janoušek, V., & Lexa, O. (2008). Transforming mylonitic metagranite by open-system interactions during melt flow. *Journal of Metamorphic Geology*, *26*(1), 55–80. https://doi.org/10.1111/j.1525-1314.2007.00744.x (cit. on pp. 2, 3).

Hawkesworth, C., Dhuime, B., Pietranik, A., Cawood, P., Kemp, A., & Storey, C. (2010). The generation and evolution of the continental crust. *Journal of the Geological Society*, *167*(2), 229–248 (cit. on p. 2).

Henk, A., Von Blanckenburg, F., Finger, F., Schaltegger, U., & Zulauf, G. (2000). Syn-convergent high-temperature metamorphism and magmatism in the Variscides: A discussion of potential heat sources. *Geological Society, London, Special Publications*, *179*(1), 387–399. https://doi.org/10.1144/GSL.SP.2000.179.01.23 (cit. on p. 2).

Hildreth, W., & Moorbath, S. (1988). Crustal contributions to arc magmatism in the Andes of Central Chile. *Contributions to Mineralogy and Petrology*, *98*(4), 455–489. https://doi.org/10.1007/BF00372365 (cit. on p. 2).

Jackson, M., Gallagher, K., Petford, N., & Cheadle, M. (2005). Towards a coupled physical and chemical model for tonalite–trondhjemite–granodiorite magma formation. *Lithos*, *79*(1–2), 43–60. https://doi.org/10.1016/j.lithos.2004.05.004 (cit. on p. 4).

Jacob, J.-B., Moyen, J.-F., Fiannacca, P., Laurent, O., Bachmann, O., Janoušek, V., Farina, F., & Villaros, A. (2021). Crustal melting vs. fractionation of basaltic magmas: Part 2, Attempting to quantify mantle and crustal contributions in granitoids. *Lithos*, *402–403*, 106292. https://doi.org/10.1016/j.lithos.2021.106292 (cit. on p. 2).

Jagoutz, O., Burg, J.-P., Hussain, S., Dawood, H., Pettke, T., Iizuka, T., & Maruyama, S. (2009). Construction of the granitoid crust of an island arc part I: Geochronological and geochemical constraints from the plutonic Kohistan (NW Pakistan). *Contributions to Mineralogy and Petrology*, *158*(6), 739–755. https://doi.org/10.1007/s00410-009-0408-3 (cit. on p. 2).

Jagoutz, O., & Klein, B. (2018). On the importance of crystallization-differentiation for the generation of $SiO_2$-rich melts and the compositional build-up of arc (and continental) crust. *American Journal of Science*, *318*(1), 29–63. https://doi.org/10.2475/01.2018.03 (cit. on p. 2).

Jaupart, C., & Mareschal, J.-C. (Eds.). (2010). Global energy budget. Crust, mantle and core. *Heat Generation and Transport in the Earth*, 232–260. https://doi.org/10.1017/CBO9780511781773.009 (cit. on p. 2).

Johannes, W. (1988). What controls partial melting in migmatites? *Journal of Metamorphic Geology*, *6*(4), 451–465. https://doi.org/10.1111/j.1525-1314.1988.tb00433.x (cit. on p. 2).

Johannes, W., Ehlers, C., Kriegsman, L. M., & Mengel, K. (2003). The link between migmatites and S-type granites in the Turku area, southern Finland. *Lithos*, *68*(3–4), 69–90. https://doi.org/10.1016/S0024-4937(03)00032-X (cit. on p. 5).

Johannes, W., & Holtz, F. (1996). *Petrogenesis and Experimental Petrology of Granitic Rocks* (P. J. Wyllie, A. E. Goresy, W. Von Engelhardt, & T. Hahn, **typeredactors**Vol. 22). Springer Berlin Heidelberg. https://doi.org/10.1007/978-3-642-61049-3 (cit. on p. 2).

Johnson, T., Yakymchuk, C., & Brown, M. (2021). Crustal melting and suprasolidus phase equilibria: From first principles to the state-of-the-art. *Earth-Science Reviews*, *221*, 103778. https://doi.org/10.1016/j.earscirev.2021.103778 (cit. on pp. 3, 6).

Katz, R. F. (2010). Porosity-driven convection and asymmetry beneath mid-ocean ridges. *Geochemistry, Geophysics, Geosystems*, *11*(11), 2010GC003282. https://doi.org/10.1029/2010GC003282 (cit. on p. 3).

Keller, T., May, D. A., & Kaus, B. J. P. (2013). Numerical modelling of magma dynamics coupled to tectonic deformation of lithosphere and crust. *Geophysical Journal International*, *195*(3), 1406–1442. https://doi.org/10.1093/gji/ggt306 (cit. on pp. 3, 4).

Keller, T., & Suckale, J. (2019). A continuum model of multi-phase reactive transport in igneous systems. *Geophysical Journal International*, *219*(1), 185–222. https://doi.org/10.1093/gji/ggz287 (cit. on p. 4).

Kemp, A. I. S., Hawkesworth, C. J., Foster, G. L., Paterson, B. A., Woodhead, J. D., Hergt, J. M., Gray, C. M., & Whitehouse, M. J. (2007). Magmatic and Crustal Differentiation History of Granitic Rocks from Hf-O Isotopes in Zircon. *Science*, *315*(5814), 980–983. https://doi.org/10.1126/science.1136154 (cit. on p. 4).

Koblinger, B. M., & Pattison, D. R. M. (2017). Crystallization of Heterogeneous Pelitic Migmatites: Insights from Thermodynamic Modelling. *Journal of Petrology*, *58*(2), 297–326. https://doi.org/10.1093/petrology/egx017 (cit. on p. 6).

Kohn, M. J., Corrie, S. L., & Markley, C. (2015). The fall and rise of metamorphic zircon. *American Mineralogist*, *100*(4), 897–908. https://doi.org/10.2138/am-2015-5064 (cit. on p. 4).

Korenaga, J. (2018). Crustal evolution and mantle dynamics through Earth history. *Philosophical Transactions of the Royal Society A: Mathematical, Physical and Engineering Sciences*, *376*(2132), 20170408 (cit. on p. 2).

Kriegsman, L. M. (2001). Partial melting, partial melt extraction and partial back reaction in anatectic migmatites. *Lithos*, *56*(1), 75–96. https://doi.org/10.1016/S0024-4937(00)00060-8 (cit. on p. 2).

Li, Y., Xie, H., Dong, C., Wang, S., & Wan, Y. (2022). Zircon evolution from migmatite to crustally-derived granite: A case study of late Neoarchean migmatite in the Yishan area, western Shandong, North China Craton. *Gondwana Research*, *112*, 82–104. https://doi.org/10.1016/j.gr.2022.09.008 (cit. on p. 5).

Martini, A., Bitencourt, M. D. F., Weinberg, R. F., De Toni, G. B., & Lauro, V. N. (2019). From migmatite to magma - crustal melting and generation of granite in the Camboriú Complex, south Brazil. *Lithos*, *340–341*, 270–286. https://doi.org/10.1016/j.lithos.2019.05.017 (cit. on p. 2).

Matzel, J. E., Bowring, S. A., & Miller, R. B. (2006). Time scales of pluton construction at differing crustal levels: Examples from the Mount Stuart and Tenpeak intrusions, North Cascades, Washington. *Geological Society of America Bulletin*, *118*(11–12), 1412–1430. https://doi.org/10.1130/B25923.1 (cit. on p. 4).

Mayne, M. J., Stevens, G., & Moyen, J.-F. (2020). A phase equilibrium investigation of selected source controls on the composition of melt batches generated by sequential melting of an average metapelite. *Geological*

*Society, London, Special Publications*, *491*(1), 223–241. https://doi.org/10.1144/SP491-2018-121 (cit. on p. 6).

Mayne, M. J., Stevens, G., Moyen, J.-F., & Johnson, T. (2020). Performing process-oriented investigations involving mass transfer using Rcrust: A new phase equilibrium modelling tool. *Geological Society, London, Special Publications*, *491*(1), 209–221. https://doi.org/10.1144/SP491-2018-85 (cit. on p. 6).

McKenzie, D. (1984). The Generation and Compaction of Partially Molten Rock. *Journal of Petrology*, *25*(3), 713–765. https://doi.org/10.1093/petrology/25.3.713 (cit. on p. 3).

Michel, J., Baumgartner, L., Putlitz, B., Schaltegger, U., & Ovtcharova, M. (2008). Incremental growth of the Patagonian Torres del Paine laccolith over 90 k.y. *Geology*, *36*(6), 459. https://doi.org/10.1130/G24546A.1 (cit. on p. 4).

Montel, J.-M., & Vielzeuf, D. (1997). Partial melting of metagreywackes, Part II. Compositions of minerals and melts. *Contributions to Mineralogy and Petrology*, *128*(2–3), 176–196. https://doi.org/10.1007/s004100050302 (cit. on p. 5).

Moyen, J.-F., Janoušek, V., Laurent, O., Bachmann, O., Jacob, J.-B., Farina, F., Fiannacca, P., & Villaros, A. (2021). Crustal melting vs. fractionation of basaltic magmas: Part 1, granites and paradigms. *Lithos*, *402–403*, 106291. https://doi.org/10.1016/j.lithos.2021.106291 (cit. on p. 2).

Moyen, J.-F., Laurent, O., Chelle-Michou, C., Couzinié, S., Vanderhaeghe, O., Zeh, A., Villaros, A., & Gardien, V. (2017). Collision vs. subduction-related magmatism: Two contrasting ways of granite formation and implications for crustal growth. *Lithos*, *277*, 154–177. https://doi.org/10.1016/j.lithos.2016.09.018 (cit. on p. 2).

Oliveira, B., Afonso, J. C., Zlotnik, S., & Diez, P. (2018). Numerical modelling of multiphase multicomponent reactive transport in the Earth's interior. *Geophysical Journal International*, *212*(1), 345–388. https://doi.org/10.1093/gji/ggx399 (cit. on p. 4).

Omlin, S., Malvoisin, B., & Podladchikov, Y. Y. (2017). Pore Fluid Extraction by Reactive Solitary Waves in 3-D: Reactive Porosity Waves. *Geophysical Research Letters*, *44*(18), 9267–9275. https://doi.org/10.1002/2017GL074293 (cit. on p. 4).

Patiño Douce, A. E., & Johnston, A. D. (1991). Phase equilibria and melt productivity in the pelitic system: Implications for the origin of peraluminous granitoids and aluminous granulites. *Contributions to Mineralogy and Petrology*, *107*(2), 202–218. https://doi.org/10.1007/BF00310707 (cit. on pp. 2, 5).

Petford, N., Cruden, A. R., McCaffrey, K. J. W., & Vigneresse, J.-L. (2000). Granite magma formation, transport and emplacement in the Earth's crust. *Nature*, *408*(6813), 669–673. https://doi.org/10.1038/35047000 (cit. on p. 4).

Ramberg, H. (1970). Model studies in relation to plutonic bodies. *Mechanism of igneous intrusion* (cit. on p. 3).

Reichardt, H., & Weinberg, R. F. (2012). The dike swarm of the Karakoram shear zone, Ladakh, NW India: Linking granite source to batholith. *Geological Society of America Bulletin*, *124*(1–2), 89–103. https://doi.org/10.1130/B30394.1 (cit. on pp. 2, 5).

Riel, N., Guillot, S., Jaillard, E., Martelat, J.-E., Paquette, J.-L., Schwartz, S., Goncalves, P., Duclaux, G., Thebaud, N., Lanari, P., Janots, E., & Yuquilema, J. (2013). Metamorphic and geochronogical study of the Triassic El Oro metamorphic complex, Ecuador: Implications for high-temperature metamorphism in a forearc zone. *Lithos*, *156–159*, 41–68. https://doi.org/10.1016/j.lithos.2012.10.005 (cit. on p. 3).

Riel, N., Bouilhol, P., van Hunen, J., Cornet, J., Magni, V., Grigorova, V., & Velic, M. (2019). Interaction between mantle-derived magma and lower arc crust: Quantitative reactive melt flow modelling using STyx. *Geological Society, London, Special Publications*, *478*(1), 65–87. https://doi.org/10.1144/SP478.6 (cit. on p. 4).

Riel, N., Martelat, J.-E., Guillot, S., Jaillard, E., Monié, P., Yuquilema, J., Duclaux, G., & Mercier, J. (2014). Fore arc tectonothermal evolution of the El Oro metamorphic province (Ecuador) during the Mesozoic. *Tectonics*, *33*(10), 1989–2012. https://doi.org/10.1002/2014TC003618 (cit. on p. 3).

Rosenberg, C. L., & Handy, M. R. (2005). Experimental deformation of partially melted granite revisited: Implications for the continental crust. *Journal of Metamorphic Geology*, *23*(1), 19–28. https://doi.org/10.1111/j.1525-1314.2005.00555.x (cit. on p. 4).

Rubatto, D. (2017). Zircon: The Metamorphic Mineral. *Reviews in Mineralogy and Geochemistry*, *83*(1), 261–295. https://doi.org/10.2138/rmg.2017.83.9 (cit. on p. 4).

Rubatto, D., Chakraborty, S., & Dasgupta, S. (2013). Timescales of crustal melting in the Higher Himalayan Crystallines (Sikkim, Eastern Himalaya) inferred from trace element-constrained monazite and zircon chronology. *Contributions to Mineralogy and Petrology*, *165*(2), 349–372. https://doi.org/10.1007/s00410-012-0812-y (cit. on p. 5).

Rubatto, D., Williams, I. S., & Buick, I. S. (2001). Zircon and monazite response to prograde metamorphism in the Reynolds Range, central Australia. *Contributions to Mineralogy and Petrology*, *140*(4), 458–468. https://doi.org/10.1007/PL00007673 (cit. on p. 5).

Rudnick, R. L., & Gao, S. (2003). Composition of the continental crust. *Treatise on Geochemistry*, *3*, 659. https://doi.org/10.1016/B0-08-043751-6/03016-4 (cit. on p. 2).

Samperton, K. M., Schoene, B., Cottle, J. M., Brenhin Keller, C., Crowley, J. L., & Schmitz, M. D. (2015). Magma emplacement, differentiation and cooling in the middle crust: Integrated zircon geochronological–geochemical constraints from the Bergell Intrusion, Central Alps. *Chemical Geology*, *417*, 322–340. https://doi.org/10.1016/j.chemgeo.2015.10.024 (cit. on p. 4).

Sawyer, E. W. (1994). Melt segregation in the continental crust. *Geology*, *22*(11), 1019. https://doi.org/10.1130/0091-7613(1994)022<1019:MSITCC>2.3.CO;2 (cit. on pp. 2, 3).

Sawyer, E. W. (1996). Melt segregation and magma flow in migmatites: Implications for the generation of granite magmas. *Earth and Environmental Science Transactions of The Royal Society of Edinburgh*, *87*(1–2), 85–94. https://doi.org/10.1017/S0263593300006507 (cit. on p. 5).

Sawyer, E. W. (2001). Melt segregation in the continental crust: Distribution and movement of melt in anatectic rocks. *Journal of Metamorphic Geology*, *19*(3), 291–309. https://doi.org/10.1046/j.0263-4929.2000.00312.x (cit. on p. 3).

Sawyer, E. W., Cesare, B., & Brown, M. (2011). When the Continental Crust Melts. *Elements*, *7*(4), 229–234. https://doi.org/10.2113/gselements.7.4.229 (cit. on pp. 2, 3).

Sawyer, E. W. (2008). *Atlas of migmatites*. NRC research press. (Cit. on pp. 2, 5).

Schaltegger, U., Schmitt, A., & Horstwood, M. (2015). U–Th–Pb zircon geochronology by ID-TIMS, SIMS, and laser ablation ICP-MS: Recipes, interpretations, and opportunities. *Chemical Geology*, *402*, 89–110. https://doi.org/10.1016/j.chemgeo.2015.02.028 (cit. on p. 4).

Schmeling, H., Marquart, G., Weinberg, R., & Kumaravel, P. (2023). Dynamic Two-Phase Flow Modeling of Melt Segregation in Continental Crust: Batholith Emplacement Versus Crustal Convection, With Implications for Magmatism in Thickened Plateaus. *Geochemistry, Geophysics, Geosystems*, *24*(5), e2023GC010860. https://doi.org/10.1029/2023GC010860 (cit. on p. 4).

Schmeling, H., Marquart, G., Weinberg, R., & Wallner, H. (2019). Modelling melting and melt segregation by two-phase flow: New insights into the dynamics of magmatic systems in the continental crust. *Geophysical Journal International*, *217*(1), 422–450. https://doi.org/10.1093/gji/ggz029 (cit. on p. 4).

Schmitt, A., Sliwinski, J., Caricchi, L., Bachmann, O., Riel, N., Kaus, B., Cisneros De Léon, A., Cornet, J., Friedrichs, B., Lovera, O., Sheldrake, T., & Weber, G. (2023). Zircon age spectra to quantify magma evolution. *Geosphere*, *19*(4), 1006–1031. https://doi.org/10.1130/GES02563.1 (cit. on p. 4).

Schoene, B., & Baxter, E. F. (2017). Petrochronology and TIMS. *Reviews in Mineralogy and Geochemistry*, *83*(1), 231–260. https://doi.org/10.2138/rmg.2017.83.8 (cit. on p. 4).

Schoene, B., Schaltegger, U., Brack, P., Latkoczy, C., Stracke, A., & Günther, D. (2012). Rates of magma differentiation and emplacement in a ballooning pluton recorded by U–Pb TIMS-TEA, Adamello batholith, Italy. *Earth and Planetary Science Letters*, *355–356*, 162–173. https://doi.org/10.1016/j.epsl.2012.08.019 (cit. on p. 4).

Schwindinger, M., Weinberg, R. F., & Clos, F. (2019). Wet or dry? The difficulty of identifying the presence of water during crustal melting. *Journal of Metamorphic Geology*, *37*(3), 339–358. https://doi.org/10.1111/jmg.12465 (cit. on p. 6).

Scott, D. R., & Stevenson, D. J. (1984). Magma solitons. *Geophysical Research Letters*, *11*(11), 1161–1164. https://doi.org/10.1029/GL011i011p01161 (cit. on p. 3).

Scott, D. R., & Stevenson, D. J. (1986). Magma ascent by porous flow. *Journal of Geophysical Research: Solid Earth*, *91*(B9), 9283–9296. https://doi.org/10.1029/JB091iB09p09283 (cit. on p. 3).

Sighinolfi, G., & Gorgoni, C. (1978). Chemical evolution of high-grade metamorphic rocks — Anatexis and remotion of material from granulite terrains. *Chemical Geology*, *22*, 157–176. https://doi.org/10.1016/0009-2541(78)90029-3 (cit. on p. 2).

Sleep, N. H. (1974). Segregation of Magma from a Mostly Crystalline Mush. *Geological Society of America Bulletin*, *85*(8), 1225. https://doi.org/10.1130/0016-7606(1974)85<1225:SOMFAM>2.0.CO;2 (cit. on p. 3).

Solar, G. S., & Brown, M. (2001). Petrogenesis of migmatites in Maine, USA: Possible source of peraluminous leucogranite in plutons? *Journal of Petrology*, *42*(4), 789–823 (cit. on pp. 2, 5).

Spiegelman, M. (1993a). Flow in deformable porous media. Part 1 Simple analysis. *Journal of Fluid Mechanics*, *247*, 17–38. https://doi.org/10.1017/S0022112093000369 (cit. on p. 3).

Spiegelman, M. (1993b). Flow in deformable porous media. Part 2 Numerical analysis – the relationship between shock waves and solitary waves. *Journal of Fluid Mechanics*, *247*, 39–63. https://doi.org/10.1017/S0022112093000370 (cit. on p. 3).

Spiegelman, M., & McKenzie, D. (1987). Simple 2-D models for melt extraction at mid-ocean ridges and island arcs. *Earth and Planetary Science Letters*, *83*(1–4), 137–152. https://doi.org/10.1016/0012-821X(87)90057-4 (cit. on p. 3).

Stevens, G., Villaros, A., & Moyen, J.-F. (2007). Selective peritectic garnet entrainment as the origin of geochemical diversity in S-type granites. *Geology*, *35*(1), 9. https://doi.org/10.1130/G22959A.1 (cit. on p. 5).

Szymanowski, D., Ellis, B. S., Bachmann, O., Guillong, M., & Phillips, W. M. (2015). Bridging basalts and rhyolites in the Yellowstone–Snake River Plain volcanic province: The elusive intermediate step. *Earth and Planetary Science Letters*, *415*, 80–89. https://doi.org/10.1016/j.epsl.2015.01.041 (cit. on p. 5).

Taylor, S. R., & McLennan, S. M. (2009). *Planetary crusts: Their composition, origin and evolution*. Cambridge university press. (Cit. on p. 2).

Thompson, A. B., & Algor, J. R. (1977). Model systems for anatexis of pelitic rocks: I. Theory of melting reactions in the system KAlO2-NaAlO2-Al2O3-SiO2-H2O. *Contributions to Mineralogy and Petrology*, *63*, 247–269 (cit. on p. 5).

Thompson, A. B., & Tracy, R. J. (1979). Model systems for anatexis of pelitic rocks: II. Facies series melting and reactions in the system CaO-KAlO2-NaAlO2-Al2O3-SiO2-H2O. *Contributions to Mineralogy and Petrology*, *70*(4), 429–438 (cit. on p. 5).

Tuttle, O. F., & Bowen, N. L. (1958). Origin of granite in the light of experimental studies in the system NaAlSi3O8–KAlSi3O8–SiO2–H2O (cit. on p. 2).

Van Zalinge, M. E., Mark, D. F., Sparks, R. S. J., Tremblay, M. M., Keller, C. B., Cooper, F. J., & Rust, A. (2022). Timescales for pluton growth, magma-chamber formation and super-eruptions. *Nature*, *608*(7921), 87–92. https://doi.org/10.1038/s41586-022-04921-9 (cit. on p. 5).

Vanderhaeghe, O. (2009). Migmatites, granites and orogeny: Flow modes of partially-molten rocks and magmas associated with melt/solid segregation in orogenic belts. *Tectonophysics*, *477*(3–4), 119–134. https://doi.org/10.1016/j.tecto.2009.06.021 (cit. on p. 3).

Vielzeuf, D., Clemens, J. D., Pin, C., & Moinet, E. (1990). Granites, Granulites, and Crustal Differentiation. In D. Vielzeuf & Ph. Vidal (Eds.), *Granulites and Crustal Evolution* (pp. 59–85). Springer Netherlands. https://doi.org/10.1007/978-94-009-2055-2_5 (cit. on p. 2).

Vigneresse, J. L., Barbey, P., & Cuney, M. (1996). Rheological Transitions During Partial Melting and Crystallization with Application to Felsic Magma Segregation and Transfer. *Journal of Petrology*, *37*(6), 1579–1600. https://doi.org/10.1093/petrology/37.6.1579 (cit. on pp. 3, 4).

Villaros, A., Stevens, G., & Buick, I. S. (2009). Tracking S-type granite from source to emplacement: Clues from garnet in the Cape Granite Suite. *Lithos*, *112*(3–4), 217–235. https://doi.org/10.1016/j.lithos.2009.02.011 (cit. on p. 5).

Villaros, A., Stevens, G., Moyen, J.-F., & Buick, I. S. (2009). The trace element compositions of S-type granites: Evidence for disequilibrium melting and accessory phase entrainment in the source. *Contributions to Mineralogy and Petrology*, *158*(4), 543–561. https://doi.org/10.1007/s00410-009-0396-3 (cit. on p. 5).

Weinberg, R. F. (2016). Himalayan leucogranites and migmatites: Nature, timing and duration of anatexis. *Journal of Metamorphic Geology*, *34*(8), 821–843. https://doi.org/10.1111/jmg.12204 (cit. on p. 5).

Wells, P. (1980). Thermal models for the magmatic accretion and subsequent metamorphism of continental crust. *Earth and Planetary Science Letters*, *46*(2), 253–265. https://doi.org/10.1016/0012-821X(80)90011-4 (cit. on p. 2).

Wells, P. (1981). Accretion of continental crust: Thermal and geochemical consequences. *Philosophical Transactions of the Royal Society of London. Series A, Mathematical and Physical Sciences*, *301*(1461), 347–357 (cit. on p. 2).

Wickham, S. M. (1987). The segregation and emplacement of granitic magmas. *Journal of the Geological Society*, *144*(2), 281–297. https://doi.org/10.1144/gsjgs.144.2.0281 (cit. on p. 3).

Winter, J. D. (2014). *Principles of igneous and metamorphic petrology* (2. ed., Pearson new internat. ed). Pearson Education. (Cit. on p. 5).

Wong, Y.-Q., & Keller, T. (2023). A unified numerical model for two-phase porous, mush and suspension flow dynamics in magmatic systems. *Geophysical Journal International*, *233*(2), 769–795. https://doi.org/10.1093/gji/ggac481 (cit. on p. 4).

Wotzlaw, J.-F., Schaltegger, U., Frick, D. A., Dungan, M. A., Gerdes, A., & Günther, D. (2013). Tracking the evolution of large-volume silicic magma reservoirs from assembly to supereruption. *Geology*, *41*(8), 867–870. https://doi.org/10.1130/G34366.1 (cit. on p. 4).

Yarushina, V. M., Podladchikov, Y. Y., & Connolly, J. A. D. (2015). (De)compaction of porous viscoelastoplastic media: Solitary porosity waves. *Journal of Geophysical Research: Solid Earth*, *120*(7), 4843–4862. https://doi.org/10.1002/2014JB011260 (cit. on p. 4).

# Modelling chemical advection during magma ascent

Hugo Dominguez[1], Nicolas Riel[2], Pierre Lanari[1, 3]

[1] Institute of Geological Sciences, University of Bern, Baltzerstrasse 3, 3012 Bern, Switzerland
[2] Institute of Geosciences, Johannes Gutenberg University, 55099 Mainz, Germany
[3] Institute of Earth Sciences, University of Lausanne, Géopolis, 1015 Lausanne, Switzerland

 Published in *Geoscientific Model Development*:
https://doi.org/10.5194/gmd-17-6105-2024

## Abstract

Modelling magma transport requires robust numerical schemes for chemical advection. Current numerical schemes vary in their ability to be mass conservative, computationally efficient, and accurate. This study compares four of the most commonly used numerical schemes for advection: an upwind scheme, a weighted essentially non-oscillatory (WENO-5) scheme, a semi-Lagrangian (SL) scheme, and a marker-in-cell (MIC) method. The behaviour of these schemes is assessed using the passive advection of two different magmatic compositions. This is coupled in 2D with the temporal evolution of a melt anomaly that generates porosity waves. All algorithms, except the upwind scheme, are able to predict the melt composition with reasonable accuracy, but none of them is fully mass conservative. However, the WENO-5 scheme shows the best mass conservation. In terms of total running time and when multithreaded, the upwind, SL, and WENO-5 schemes show similar performance, while the MIC scheme is the slowest due to reseeding and removal of markers. The WENO-5 scheme has a reasonable total run time, has the best mass conservation, is easily parallelisable, and is therefore best suited for this problem.


## 1. Introduction

Mechanisms of magma ascent and emplacement within the lithosphere and upper asthenosphere remain largely unconstrained (e.g. Connolly & Podladchikov, 2007a; Katz et al., 2022). Studies have attempted to address this problem using techniques ranging from geophysical measurements of the present-day lithosphere to geochemical analysis of the rock record. However, geophysical studies are hampered by indirect measurements, and natural samples in geochemical studies represent only the end-product of the melting processes (Brown, 2013; Clemens et al., 2022; Johnson et al., 2021). Comparatively, numerical modelling allows investigation of these processes at a range of scales in space and time (e.g. Katz & Weatherley, 2012; Keller et al., 2013).

To numerically model such open systems, it is necessary to be able to describe the chemical and physical processes responsible for magma ascent in a rock. At low melt fractions and in the absence of externally applied stress, the physical processes are based on the continuum formulation of two-phase flow. It takes into account the concurrent mechanisms of rock matrix compaction and buoyancy of partial melt in an interconnected porous network (e.g. McKenzie, 1984; Scott & Stevenson, 1984). This formulation is based on mass and momentum conservation, and an appropriate set of constitutive relationships. In addition, conservation of energy needs to be ensured to link mechanical to chemical processes (e.g. Katz, 2008). Chemical processes, such as phase reactions, can be considered using thermodynamics and/or kinetics and relate the equilibration of the melt with the hosting rock (e.g. Bessat et al., 2022; Omlin et al., 2017). They contribute to the transport dynamics by changing rock properties, such as density, viscosity, porosity, and permeability (Aharonov et al., 1995a; Jha et al., 1994; Keller & Katz, 2016). However, the amount of melt interacting with the rock is also modulated by transport mechanisms (Aharonov et al., 1995b; Kelemen et al., 1997; Spiegelman & Kenyon, 1992). Therefore, the development of integrated models that successfully describe the complex interaction between reaction and transport is key to understanding melting and melt extraction at all scales.

Numerous numerical studies have investigated reactive melt transport. It has been shown that melts that partially crystallise or dissolve the host rock could be a viable mechanism for channelling flow and creating heterogeneities in the mantle in the context of mid-ocean ridges (Aharonov et al., 1997; Spiegelman et al., 2001) and sub-arc magmatism (Bouilhol et al., 2011). Concerning lower-crust melting, this approach has mainly been used to understand the processes of chemical differentiation and the compositional range of melts in mafic systems (e.g. Jackson et al., 2005; Riel et al., 2019; Solano et al., 2012).

One challenge of reactive melt transport modelling is the advection of the melt composition through its ascent. This part, which is mathematically well understood, being described by a mass balance equation, is numerically challenging (e.g. LeVeque, 1992). This is mainly due to the fact that most numerical models are based on a Eulerian frame of reference, where the discretised space is fixed in space and in time. In contrast, transport is by essence better defined from a Lagrangian perspective, where the observer follows the particles of fluid as they move. In addition, two-phase flow models are at least 2D problems due to the formation of channels (e.g. Barcilon & Lovera, 1989; Connolly & Podladchikov, 2007a) and to the fact that

mass cannot be transported efficiently in 1D in the melt (Jordan et al., 2018). This brings a limitation to the resolution of the models and hence requires accurate advection schemes.

This study compares four numerical schemes applied to the problem of the advection of magmatic composition: an upwind scheme, a weighted essentially non-oscillatory (WENO) scheme, a semi-Lagrangian (SL) scheme, and a marker-in-cell (MIC) method. This selection provides a representation of the different approaches to solving advection problems that are commonly used in a wide range of applications. We assess the performance of each scheme in terms of accuracy, mass conservation, and computational time. A 2D model coupling chemical advection with a two-phase flow solver is then used to evaluate which algorithm is best suited for this problem.

# 2. Governing equations

Chemical transport in two-phase flow systems is described by the four mass conservation equations of the system (e.g. Aharonov et al., 1997). The first two equations describe the conservation of the total mass of the solid and the liquid:

$$\frac{\partial\left[(1-\phi)\rho_{\mathrm{s}}\right]}{\partial t} = -\nabla\cdot\left[(1-\phi)\vec{v}_{\mathrm{s}}\rho_{\mathrm{s}}\right], \tag{1}$$

$$\frac{\partial(\phi\rho_{\mathrm{f}})}{\partial t} = -\nabla\cdot\left(\phi\vec{v}_{\mathrm{f}}\rho_{\mathrm{f}}\right), \tag{2}$$

where f and s represent the fluid and solid phases, $t$ is the time (in s), $\phi$ is the fluid-filled porosity, $\rho$ is the density of the respective phase ($\mathrm{kg\,s^{-3}}$), $\vec{v}$ is the velocity of the respective phase ($\mathrm{m\,s^{-1}}$). The last two equations express the conservation of each chemical component within the solid and fluid phases:

$$\begin{aligned}\frac{\partial\left[(1-\phi)\rho_{\mathrm{s}}C_e^{\mathrm{s}}\right]}{\partial t} = \nabla\cdot\big[&D_e^{\mathrm{s}}(1-\phi)\rho_{\mathrm{s}}\nabla C_e^{\mathrm{s}} \\ &-(1-\phi)\vec{v}_{\mathrm{s}}\rho_{\mathrm{s}}C_e^{\mathrm{s}}\big],\end{aligned} \tag{3}$$

$$\frac{\partial\left(\phi\rho_{\mathrm{f}}C_e^{\mathrm{f}}\right)}{\partial t} = \nabla\cdot\left(\mathbf{D}_{\mathbf{e}}^{\mathbf{f}}\phi\rho_{\mathrm{f}}\nabla C_e^{\mathrm{f}} - \phi\vec{v}_{\mathrm{f}}\rho_{\mathrm{f}}C_e^{\mathrm{f}}\right), \tag{4}$$

where $C_e$ is the mass fraction of the chemical component $e$ in the respective phase, $D_e^{\mathrm{s}}$ is the solid diffusion coefficient of the chemical component $e$ (in $\mathrm{m^2\,s^{-1}}$), and $\mathbf{D_e^f}$ is the hydrodynamic dispersion tensor of the chemical component $e$ in the fluid ($\mathrm{m^2\,s^{-1}}$). These four equations assume no mass transfer due to reactions between the solid and the liquid phases.

## 2.1. Simplifications

In this study, the advection of the chemical components transported by the liquid phase is considered, and the diffusion term in Eqs. (3) and (4) is neglected. Since $\rho_{\mathbf{s}}$ is assumed to be constant and the host rock has a fixed composition, Eq. (3) is omitted.

Subtracting Eq. (2) in Eq. (4), and dividing by $\rho_{\mathrm{f}}$ and $\phi$ yields

$$\frac{\partial C_e^{\mathrm{f}}}{\partial t} = -\vec{v}_{\mathrm{f}}\nabla\cdot C_e^{\mathrm{f}}. \tag{5}$$

Equation (5) is formally equivalent to Eq. (4) without the dispersion term. Moreover, Eq. (4) is written in conservative form, whereas Eq. (5) is expressed in Lagrangian or non-conservative form. Equation (5) removes the time dependence on $\phi$ and is linear. It is a common form used in the reactive transport modelling community (e.g. Carrera et al., 2022).

An expression for $\vec{v}_{\mathrm{f}}$ can be derived by coupling Eqs. (1) and (2) to the momentum conservation equations (e.g. Bercovici et al., 2001; McKenzie, 1984). These are usually solved before Eq. (5) ; a description of the system used in this study is provided below in section 5.1.

# 3. Numerical methods

Solving an advection equation using a linear Eulerian scheme leads to high numerical diffusion for first-order schemes, such as the upwind scheme (Courant et al., 1952), and to oscillations on sharp gradients for higher-order schemes (LeVeque, 2002). The latter effect is described by Godunov's theorem (Godunov & Bohachevsky, 1959). This theorem states that linear Eulerian schemes with an order of accuracy greater than 1 cannot preserve the monotonicity of the solution for sharp gradients, discontinuities, or shocks. This has led to extensive developments in the design of high-order Eulerian non-linear schemes that can achieve high accuracy without bringing oscillations. Examples of such developments are the essentially non-oscillatory (ENO) methods (Harten et al., 1987) that later led to WENO schemes (Liu et al., 1994). These schemes are based on the idea of using a non-linear adaptive procedure to automatically choose the locally smoothest stencil, and early examples of appli-

cations include the modelling of shocks appearing in acoustics (e.g. Grasso & Pirozzoli, 2000) or solving the Hamilton-Jacobi equations (e.g. Jiang & Peng, 2000).

Another approach is to use schemes closer to the Lagrangian perspective, such as the MIC (or alternatively named marker-and-cell) method (e.g. Gerya & Yuen, 2003a; Harlow et al., 1955). It consists of tracking individual particles on a Lagrangian frame and reinterpolating them when needed on a Eulerian stationary grid. This approach has the advantage of producing little numerical diffusion, being uncondionally stable and has been extensively used in geodynamic models (e.g. Duretz et al., 2011; Gerya, 2019; van Keken et al., 1997).

Finally, there are intermediate methods, such as semi-Lagrangian methods, trying to take advantages from both Eulerian and Lagrangian schemes (McDonald, 1984; Robert, 1981). These schemes look at different particles at each time step, considering only particles whose final trajectories correspond to the position of grid nodes. This has the advantage of only considering a number of particles equal to the resolution of the Eulerian grid and is computationally efficient. They are also unconditionally stable but have issues with mass conservation (Chandrasekar, 2022). They were first developed for atmospheric modelling (e.g. Robert, 1981; Staniforth & Côté, 1991) and later successfully used in the plasma modelling community (e.g. Sonnendrücker et al., 1999).

To solve for Eq. (5) in the context of two-phase flow, we implemented and tested four different advection schemes that are representative of the approaches described above: an upwind scheme, a WENO scheme, an SL scheme and a MIC method.

## 3.1. Upwind scheme

The upwind scheme is among the simplest algorithms for solving an advection equation on a Eulerian grid (e.g. LeVeque, 1992). It is explicit and first order in space and in time. It consists of using a spatially biased stencil that depends on the direction of the flow (Fig. 1).

### 3.1.1. Spatial discretisation

Using a first-order spatially biased stencil, Eq. (5) can be approximated for one chemical element and in 1D as

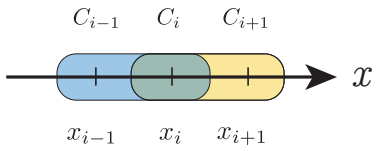


**Figure 1:** Spatial stencil of the upwind scheme in 1D. The blue box is the valid stencil for positive velocities and the yellow box for negative velocities.

$$\begin{aligned} \frac{\partial C_i}{\partial t} + v_{\mathrm{f},i}\frac{C_i^n - C_{i-1}^n}{\Delta x} = 0 \quad \text{for} \quad v_{\mathrm{f},i} > 0, \\ \frac{\partial C_i}{\partial t} + v_{\mathrm{f},i}\frac{C_{i+1}^n - C_i^n}{\Delta x} = 0 \quad \text{for} \quad v_{\mathrm{f},i} < 0, \end{aligned} \tag{6}$$

where $i$ is a spatial index in the $x$ direction, $\Delta x$ is the constant grid spacing, and $v_{f,i}$ is the $x$ component of the fluid velocity.

### 3.1.2. Temporal discretisation

Combined with the first-order forward Euler method, we retrieve the classical upwind scheme from Eq. (6):

$$\begin{aligned} \frac{C_i^{n+1} - C_i^n}{\Delta t} + v_{\mathrm{f},i}\frac{C_i^n - C_{i-1}^n}{\Delta x} = 0 \quad \text{for} \quad v_{\mathrm{f},i} > 0, \\ \frac{C_i^{n+1} - C_i^n}{\Delta t} + v_{\mathrm{f},i}\frac{C_{i+1}^n - C_i^n}{\Delta x} = 0 \quad \text{for} \quad v_{\mathrm{f},i} < 0, \end{aligned} \tag{7}$$

where $\Delta t$ is the time step.

It can also be rewritten in a more compact form:

$$C_i^{n+1} = C_i^n - \Delta t \left[ v_{\mathrm{f},i}^+ \left( \frac{C_i^n - C_{i-1}^n}{\Delta x} \right) + v_{\mathrm{f},i}^- \left( \frac{C_{i+1}^n - C_i^n}{\Delta x} \right) \right], \tag{8}$$

where

$$\begin{aligned} v_{\mathrm{f},i}^+ &= \max(v_{\mathrm{f},i}, 0), \\ v_{\mathrm{f},i}^- &= \min(v_{\mathrm{f},i}, 0). \end{aligned}$$

This scheme is well-known to produce a lot of numerical diffusion and is bounded by the following Courant–Friedrichs–Lewy (CFL) condition for $p$ dimensions:

$$\Delta t \left( \sum_{j=1}^{p} \frac{\left| v_{\mathrm{f}_j} \right|}{\Delta x_j} \right) \leq Co_{\max} = 1,$$

where $Co_{\max}$ is the maximum Courant ($Co$) number (e.g. Hirsch, 2007). In addition, it is not mass conservative for non-constant $v_{\mathrm{f}}$, especially for divergent flow.

## 3.2. Weighted essentially non-oscillatory scheme

Weighted essentially non-oscillatory schemes were developed by Liu et al. (1994). The reader can refer to Shu (2009) for a comprehensive review of the development of WENO schemes and Pawar and San (2019) for implementations using Julia.

They are high-order schemes able to resolve sharp gradients, produce little numerical diffusion but also follow the same CFL condition as the upwind scheme. The key idea behind them is to use a non-linear adaptive procedure to automatically choose the locally smoothest stencil. This allows WENO schemes to dispose of oscillations when advecting sharp gradients.

We use a fifth-order-in-space finite-difference approach for non-conservative problems, referenced as WENO-5 hereafter.

### 3.2.1. Spatial discretisation

Equation (5) can be discretised in space using the WENO-5 scheme similarly to the upwind scheme, in 1D, for one chemical element and for a single grid point such as

$$\frac{\partial C_i}{\partial t} + v^+_{f,i}\left(\frac{C^L_{i+\frac{1}{2}} - C^L_{i-\frac{1}{2}}}{\Delta x}\right) + v^-_{f,i}\left(\frac{C^R_{i+\frac{1}{2}} - C^R_{i-\frac{1}{2}}}{\Delta x}\right) = 0, \tag{9}$$

where

$$\begin{aligned} C^L_{i+\frac{1}{2}} &= w^L_0\left(\frac{1}{3}C_{i-2} - \frac{7}{6}C_{i-1} + \frac{11}{6}C_i\right) + \\ &\quad w^L_1\left(-\frac{1}{6}C_{i-1} + \frac{5}{6}C_i + \frac{1}{3}C_{i+1}\right) + \\ &\quad w^L_2\left(\frac{1}{3}C_i + \frac{5}{6}C_{i+1} - \frac{1}{6}C_{i+2}\right), \\ C^R_{i-\frac{1}{2}} &= w^R_0\left(-\frac{1}{6}C_{i-2} + \frac{5}{6}C_{i-1} + \frac{1}{3}C_i\right) + \\ &\quad w^R_1\left(\frac{1}{3}C_{i-1} + \frac{5}{6}C_i - \frac{1}{6}C_{i+1}\right) + \\ &\quad w^R_2\left(\frac{11}{6}C_i - \frac{7}{6}C_{i+1} + \frac{1}{3}C_{i+2}\right). \end{aligned}$$

Here, $C^L_{i-\frac{1}{2}}$ and $C^R_{i+\frac{1}{2}}$ are omitted to avoid redundancy. They can be obtained by shifting the index by -1 and 1, respectively.

**Table 1:** Optimal weights for WENO-5 scheme

| $d_k$ | $k$=0 | $k$=1 | $k$=2 |
|---|---|---|---|
| $d^L_k$ | 0.1 | 0.6 | 0.3 |
| $d^R_k$ | 0.3 | 0.6 | 0.1 |

The non-linear weights $w$ are defined as

$$w^L_k = \frac{\alpha_k}{\alpha_0+\alpha_1+\alpha_2}, \quad \alpha_k = \frac{d^L_k}{(\beta_k+\epsilon)^2}, \quad k = 0,1,2,$$
$$w^R_k = \frac{\alpha_k}{\alpha_0+\alpha_1+\alpha_2}, \quad \alpha_k = \frac{d^R_k}{(\beta_k+\epsilon)^2}, \quad k = 0,1,2.$$

The values of the optimal weights $d^L_k$ and $d^R_k$ are given in Table 1. $\epsilon$ represents the machine epsilon, the relative approximation error due to rounding in floating-point arithmetic, and is used to avoid division by zero.

Smoothness indicators $\beta$ are equal to

$$\begin{aligned} \beta_0 &= \frac{13}{12}\left(C_{i-2} - 2C_{i-1} + C_i\right)^2 + \frac{1}{4}\left(C_{i-2} - 4C_{i-1} + 3C_i\right)^2, \\ \beta_1 &= \frac{13}{12}\left(C_{i-1} - 2C_i + C_{i+1}\right)^2 + \frac{1}{4}\left(C_{i-1} - C_{i+1}\right)^2, \\ \beta_2 &= \frac{13}{12}\left(C_i - 2C_{i+1} + C_{i+2}\right)^2 + \frac{1}{4}\left(3C_i - 4C_{i+1} + 3C_{i+2}\right)^2. \end{aligned}$$

The WENO-5 scheme requires, in 1D, a stencil of five points biased towards the left for positive velocities and five points biased towards the right for negative velocities as shown in Fig. 2. This commonly requires two ghost points on each side of the model to apply the boundary conditions. To extend this scheme to 2D, two new terms can be added to (9) for the new positive and negative component of $v_f$. The expressions of $C$ at half points of the new index can be derived using the same formulae as in 1D for the new direction.

### 3.2.2. Temporal discretisation

Weighted essentially non-oscillatory schemes are not stable using the standard forward Euler time integration method (Wang & Spiteri, 2007). The most commonly used discretisation is the third-order strong stability preserving (SSP) explicit Runge–Kutta method (e.g. Ghosh & Baeder, 2012; Jiang & Shu, 1996). Strong stability preserving schemes are used to fully capture discontinuous solutions and are therefore well-suited for solving hyperbolic partial differential equations (Gottlieb et al., 2001).

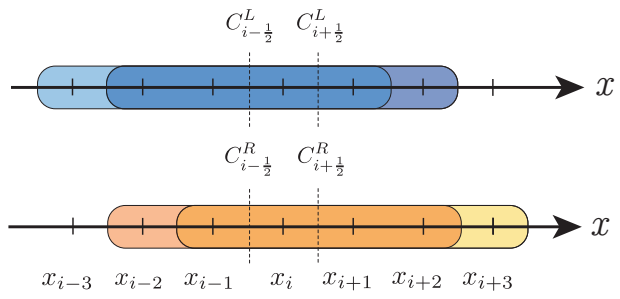


**Figure 2:** Spatial stencil of the WENO-5 scheme in 1D. $C^L$ is used for positive velocities and $C^R$ for negative velocities. The blue boxes are valid stencils for positive velocities, and the yellow and orange boxes are valid for negative velocities.

The third-order SSP Runge–Kutta for Eq. (5) for one chemical element can be written as

$$\begin{aligned} C_i^1 &= C_i^n - \Delta t L(C_i^n), \\ C_i^2 &= \frac{3}{4}C_i^n + \frac{1}{4}\left[C_i^1 - \Delta t L\left(C_i^1\right)\right], \\ C_i^{n+1} &= \frac{1}{3}C_i^n + \frac{2}{3}\left[C_i^2 - \Delta t L\left(C_i^2\right)\right], \end{aligned}$$

with $L$ being the spatial discretisation operator:

$$L(C_i) = v_{\mathrm{f},i}^{+}\left(\frac{C^L_{i+\frac{1}{2}} - C^L_{i-\frac{1}{2}}}{\Delta x}\right) + v_{\mathrm{f},i}^{-}\left(\frac{C^R_{i+\frac{1}{2}} - C^R_{i-\frac{1}{2}}}{\Delta x}\right).$$

With this formulation, the WENO-5 scheme is fifth order in space and third order in time.

## 3.3. Semi-Lagrangian schemes

Semi-Lagrangian schemes take a different approach than classical Eulerian methods and are related to tracer-based advection schemes. Semi-Lagrangian schemes aim to use the best of Lagrangian and Eulerian methods by solving the problem for particles whose trajectories pass through a fixed grid at the end of each time step, rather than recording the full history of individual particles. They are therefore unconditionally stable. Two steps are usually required to implement SL schemes: trajectory tracing and interpolation back to the grid. In this study, a backward-in-time SL scheme is used for the trajectory tracing and the quasi-monotone scheme developed by Bermejo and Staniforth (1992) for the interpolation.

### 3.3.1. Trajectory tracing

The advantage of backward-in-time SL schemes is that the interpolant is defined from the Eulerian grid. In the case of a regular grid, this reduces the complexity of the implementation and the numerical cost of the interpolation function, since the interpolant is defined on a regular grid. From a particle point of view, the goal is to retrieve the position of the particle at time $t_n$ for which the position corresponds to a grid point at time $t_{n+1}$. Using Eq. (5) for one chemical element and in 1D, the following ordinary differential equation has to be solved:

$$\frac{dx}{dt} = v_{\mathrm{f}}(x,t). \tag{10}$$

Knowing $x(t_{n+1}) = x_i$, where $i$ is a grid point, $x(t_n) = x_d$, where $d$ is a departure point that needs to be found. In most practical cases, the velocity field varies greatly in time and in space between each time-step, especially for porosity waves, so it is not easy to determine $x_d$. A common approach to accurately determine $x_d$ is to use a linear multistep method such as the implicit mid-point scheme (Robert (1981)):

$$\frac{x_i - x_d}{\Delta t} = v_{\mathrm{f}}\left(\frac{x_i + x_d}{2}, t_{n+\frac{1}{2}}\right), \tag{11}$$

where $v_f$ at time $t_{n+\frac{1}{2}}$ is obtained by taking the mean between the velocity at $n$ and $n+1$. The assumption behind the mid-point rule is that the velocity remains constant at the mid-point value during each time step. This ensures that each trajectory is linear, with the mid-point being the average of the positions of its endpoints (Fig. 3). This method is a second-order accurate trajectory method in both space and time.

Equation (11) must be solved implicitly because $x_d$ is present on both sides of the equation and therefore requires iterations. It can be achieved for $r$ iterations in this form:

$$x_d^{r+1} = x_i - \Delta t v_{\mathrm{f}}\left(\frac{x_i + x_d^r}{2}, t_{n+\frac{1}{2}}\right). \tag{12}$$

A minimum of three iterations while using linear interpolation has been shown to be sufficient in most cases (e.g. McDonald, 1984).

### 3.3.2. Interpolation

In most cases, $x_d$ does not correspond to a grid node (see Fig. 3). In this case, interpolation is required to retrieve the value of the unknown at $x_d$:

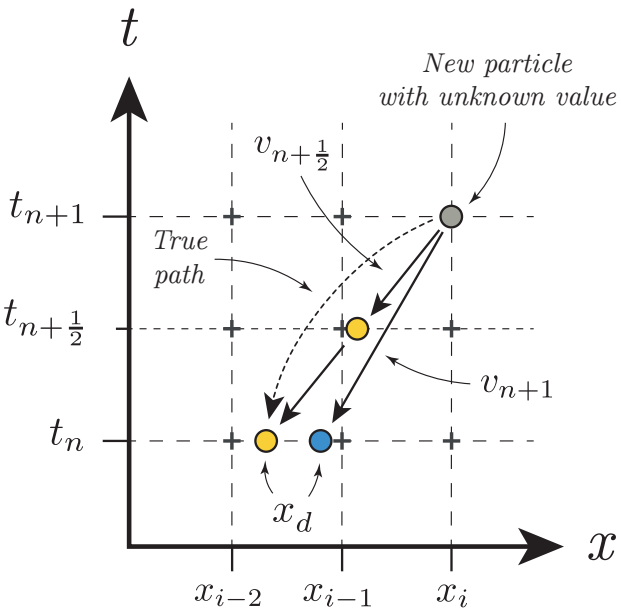


**Figure 3:** Summary of trajectory tracing for backward semi-Lagrangian schemes. The aim is to find the value of the advected quantity at the position $x_i$ and at the time step $t_{n+1}$. The blue particle uses the velocity at $n+1$. The yellow particle shows the mid-point method, using an approximation of the velocity at $n+\frac{1}{2}$. The value of the particle at position $x_d$ can then be interpolated at $t_n$ to obtain the value at $x_i$ at $t_{n+1}$.

$$C(x_d, t) = \mathcal{L}\left[C(x_{i_k}), t\right],$$

where $\mathcal{L}$ is an interpolation operator and $x_{i_k}$ represents the nodes of the cell containing $x_d$.

Commonly, cubic interpolants are used as they offer a good compromise between performance and accuracy (e.g. Chandrasekar, 2022) and require in 1D four grid points $x_{i_k}$ per particle. Cubic B-splines are used in this study. Godunov's theorem still applies to linear SL schemes, and since cubic interpolation is third order in space, it introduces oscillations and overshoots for high gradients. To overcome this limitation, quasi-monotone (QM) SL schemes were developed by Bermejo and Staniforth (1992). The term QM means that the scalar field values cannot exceed the range of the previous time step, but can still develop wiggles inside that range. Quasi-monotonicity is equivalent to the notion of essentially non-oscillatory (Bermejo, 2001). A disadvantage of this method is an increased numerical diffusion, especially for a high $Co$ number. A maximum $Co$ number of 1.5 is generally used (e.g. Smith, 2000).

To implement quasi-monotone semi-Lagrangian (QMSL) schemes, let us define $C^-$ and $C^+$ as the minimum and maximum scalar values of the nodes of the cell containing $x_d$ and $C^H$ as the high-order non-monotone interpolant, here a cubic spline. Then, a local clipping can be applied at the end of each time step:

$$C^M(x_d, t) = \begin{cases} C^+(x_d, t) & \text{if} \quad C^H(x_d, t) > C^+(x_d, t) \\ C^-(x_d, t) & \text{if} \quad C^H(x_d, t) < C^-(x_d, t) \\ C^H(x_d, t) & \text{otherwise,} \end{cases} \tag{13}$$

where $C^M$ is the quasi-monotone interpolant. Equation (13) can be rewritten in a more compact way:

$$C^M(x_d, t) = \min\left\{\max\left[C^-(x_d, t), C^H(x_d, t)\right], C^+(x_d, t)\right\}.$$

Formally, this formulation is equivalent to a linear combination between a high-order interpolant and a first-order (monotone) interpolant (Bermejo, 2001).

## 3.4. Marker-in-cell schemes

Marker-in-cell schemes share the same ambition as SL schemes, such as being unconditionally stable, but are closer to Lagrangian schemes. They record the complete history of individual particles, called markers and interpolate their values on a fixed grid. This approach has the advantage of greatly reducing numerical diffusion and making MIC schemes unconditionally stable. In addition to trajectory tracing and interpolation, the MIC schemes require markers to be generated within the domain of the model.

### 3.4.1. Initial marker generation and reseeding of particles

The number of markers per cell required can vary depending on the complexity of the problem, here 5 markers per cell dimension and effectively 25 in 2D. This is generally sufficient to achieve good accuracy (e.g. Gerya, 2019). The initial value in each marker can then be directly derived from the initial conditions or obtained by linear interpolation from the initial conditions of the Eulerian grid.

For highly divergent flows or sometimes strongly stretching flows, it is necessary to regenerate or remove markers during the simulation. For highly divergent flows, this is because particles will accumulate in zones with negative divergence values and create a gap in zones with positive divergence values. For highly stretching flow, increases or gaps in the density of the markers can be induced by preferential

flow in a particular direction. For reseeding, a non-conservative strategy similar to Keller et al. (2013) is used. If the marker density per cell is less than 25% of the initial density, new markers are generated and assigned the value of the nearest marker. The old markers are discarded after this step. For marker accumulation, the marker density cannot exceed twice the initial density. If it does, a quarter of the markers are discarded at random.

### 3.4.2. Trajectory tracing

The goal of trajectory tracing for MIC schemes is to determine the position of each marker at the next time step. The same equation as Eq. 10 is solved. However, compared to backward SL where the final position is known, the unknown in this case is the position of the arrival point at $t^{n+1}$. Also, the common way to solve this equation for MIC schemes is not using a linear multistep method such as the implicit mid-point scheme, but rather Runge–Kutta schemes (Gerya, 2019). Using a second-order Runge–Kutta scheme, it consists of four steps. Interpolating $v_f$ at $t_n$ at the departure point $x_d$ of the markers, finding the position of the markers at $t_{n+\frac{1}{2}}$ using $v_f$ at $t_n$, reinterpolating the velocity at this new position, and using this new velocity to compute the arrival point $x_a$ of the markers at $t_{n+1}$ from $t_n$.

Since classical interpolants do not retain the physical properties of the velocity field, such as its divergence, a simple bilinear interpolation may lead to unphysical clustering of markers on the timescale of a numerical model. To address this issue, Pusok et al. (2017) explored different interpolants and showed the advantages of using the LinP interpolation scheme (Gerya, 2019). The LinP interpolation scheme is an empirical relationship that combines two linear interpolants defined at the sides and at the centre of each cell. It is defined as

$$v_\mathrm{f}(x,t) = A\mathcal{L}\left[v_\mathrm{f}(x_\mathrm{side},t)\right] + (1-A)\mathcal{L}\left[v_\mathrm{f}(x_\mathrm{centre},t)\right],$$

with $A$ a constant commonly equal to $2/3$, $\mathcal{L}$ a linear interpolant, and $x_\mathrm{side}$ and $x_\mathrm{centre}$ the position of the sides and centre of the cell containing the marker.

Using this definition, we can rewrite the four steps of the second-order Runge–Kutta scheme in mathematical notation with four equations:

$$\begin{aligned} v_\mathrm{f}(x_d,t_n) &= A\mathcal{L}\left[v_\mathrm{f}(x_\mathrm{side},t_n)\right] + \\ &\quad (1-A)\mathcal{L}\left[v_\mathrm{f}(x_\mathrm{centre},t_n)\right], \\ x_h &= x_d + \frac{1}{2}\Delta t v_\mathrm{f}(x_d,t_n), \\ v_\mathrm{f}(x_h,t_n) &= A\mathcal{L}\left[v_\mathrm{f}(x_\mathrm{side},t_n)\right] + \\ &\quad (1-A)\mathcal{L}\left[v_\mathrm{f}(x_\mathrm{centre},t_n)\right], \\ x_a &= x_d + \Delta t v_\mathrm{f}(x_h,t_n), \end{aligned} \tag{15}$$

with $x_h$ the intermediate position of the marker. Solving these four equations successively to obtain a value for $x_a$ with this method is second order in space but only first order in time, as only the velocity at $t_n$ is used.

### 3.4.3. Interpolation

After calculating the position of the markers, it is necessary to interpolate back on the Eulerian grid and/or to update the values of the markers from the Eulerian grid depending on the problem being solved. The step of updating the markers is not described in detail here, as it is not used in this study, but involves a simple interpolant when a regular grid is used. This step is more complex for updating the advected field on the Eulerian grid because the markers are not uniformly distributed for a non-trivial velocity field. Therefore, contrary to SL schemes, interpolation is performed on an unstructured grid as it is based on the position of the markers. In most cases, linear interpolants are used because they prevent oscillations, and the marker densities are high enough to prevent numerical diffusion. In this study, a weighted-distance-averaging linear interpolant is used (Gerya, 2019):

$$\begin{aligned} w(x_m,t_{n+1}) &= 1 - \frac{\Delta x_m}{\Delta x}, \\ C(x_i,t_{n+1}) &= \frac{\sum_{i=1}^{m} C(x_m,t_{n+1})\, w(x_m,t_{n+1})}{\sum_{i=1}^{m} w(x_m,t_{n+1})}, \end{aligned}$$

where $x_m$ is the position of a marker $m$, $\Delta x_m$ is the distance between a marker $m$ and the grid point $i$, and $w$ is the weight of a marker $m$. All markers found in the cells surrounding grid point $i$ are used for interpolation, as in Gerya and Yuen (2003b). The relationship between the markers and the grid in 2D is summarised in Fig. 4. One disadvantage of this interpolant is that it is prone to race conditions in shared memory systems, as it involves two sums, which require the use of atomic operations to parallelise the

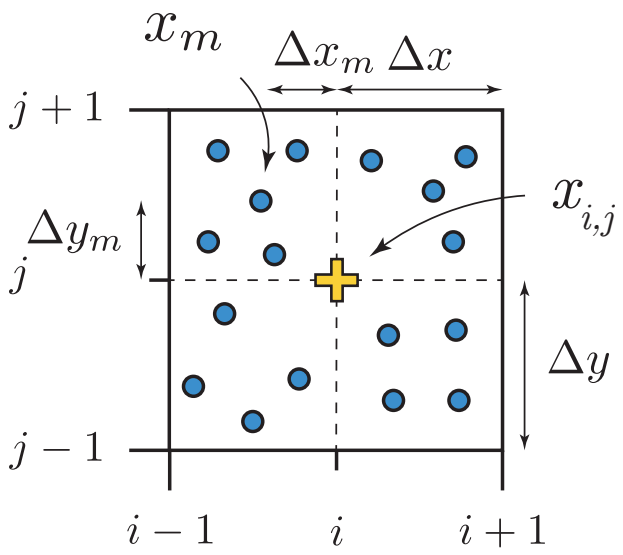


**Figure 4:** Sketch showing the geometric relationship in 2D between a point $x_{i,j}$ of the Eulerian grid and the markers $x_m$ used for the interpolation on a regular grid. The value at the point $x_{i,j}$ is interpolated from the markers $x_m$ contained inside the four neighbouring cells. $x_{i,j}$ is fixed in time and in space, whereas the position of the markers $x_m$ are time-dependent.

implementation.

## 4. Numerical tests

To test the four advection schemes, two different numerical tests are performed in 2D: the pure rotation of a cylinder and the advection through a more complex velocity field mimicking a convection cell. In both cases, the domain is a square of size $1.0 \times 1.0$ with a constant spacing of $\Delta x = \Delta y = 0.005$ for a resolution of $201 \times 201$ nodes. The radius of the cylinder is $24\Delta x$ with a mass fraction of 1.0 and is centred at coordinates $(0.25\ ,\ 0.25)$. The initial conditions for both tests are shown in Fig. 5.

For the first test, the time increment is $\Delta t = 400$ with $\omega = \pi \times 10^{-5}$, so it takes 500 time steps to make a full revolution. The velocity is defined as $\vec{v} = (-\omega(y - 0.5)\ ,\ \omega(x - 0.5))$, so the rotation is anti-clockwise, and the centre of it is at coordinates $(0.5\ ,\ 0.5)$. The $Co$ numbers inside the cylinder range between 0.45 and 0.8. The test is stopped after two revolutions. For the second test, $\vec{v}$ is defined as $\vec{v} = (-2\pi \times sin(\pi x) \times cos(\pi y)\ ;\ 2\pi \times cos(\pi x) \times sin(\pi y))$. The time increment $\Delta t$ is fixed by constraining the $Co$ number to be 0.7 for a total time of 0.8 and 1016 time steps. At half of the total time, the opposite sign of $\vec{v}$ is taken as the new value of $\vec{v}$, such that the analytical solution of the problem corresponds to the initial conditions.

To compare and quantify the results of the different schemes, the following quantities were monitored: the mass conservation ($M$), the total error ($E_{\text{tot}}$), the maximum value of the final mass fraction ($\max(C_{\text{f}})$), and the minimum elapsed computational time of one time step after 10000 runs, with one thread and with 24 threads.

The mass conservation is defined as

$$M = \frac{\sum_{k=1}^{K} \left(C_{\text{f}}^{k}\right)}{\sum_{k=1}^{K} \left(C_{0}^{k}\right)}, \tag{16}$$

where $k$ is a 2D grid point index, $K$ is the total number of grid points, $C_{\text{f}}^{k}$ is the final mass fraction at index $k$, and $C_{0}^{k}$ is the initial mass fraction at index $k$.

The total error in the scheme is defined as the mean square error:

$$E_{\text{tot}} = \frac{1}{K} \sum_{k=1}^{K} \left(C_{0}^{k} - C_{\text{f}}^{k}\right)^{2}.$$

The results for both tests are reported in Table 2 and in Figs. 6 and 7 for the four different schemes. Both tests show the strong numerical diffusion of the upwind scheme and its high $E_{tot}$ due to its first order in time and space. The WENO-5 scheme shows no oscillation and a good accuracy, being fifth order in space and third in time in both tests, with a small mass loss in the second test. The QMSL is not mass conservative for both problems. It shows a relatively good accuracy, being third order in space and second in time; is monotone; but shows deformation of the original cylinder at the end of the second test. Finally, for both tests, the MIC scheme is mass conservative and monotone and shows the best accuracy with almost no numerical diffusion. These simple tests highlight the properties of each scheme but use a velocity field that is divergence-free and without sharp variations. Coupling with a two-phase flow system is therefore necessary to assert which scheme is the more suitable in this case.

## 5. Coupling chemical advection and two-phase flow

Solving Eq. (5) for concrete cases implies having an expression for $v_{\text{f}}$ at each time step. In this section,

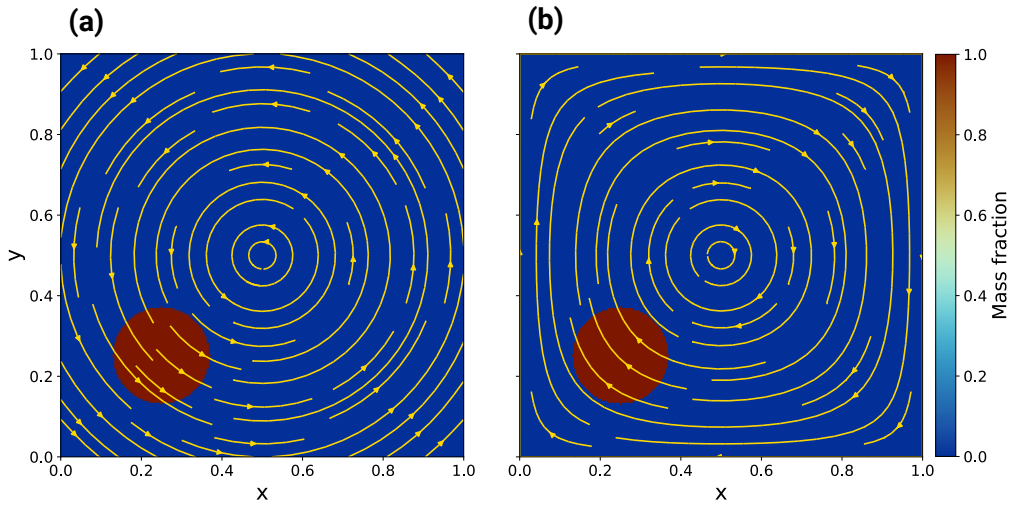


**Figure 5:** Initial conditions for the two numerical tests. The yellow arrows show the velocity fields of the tests. (a) Rotation of a cylinder. (b) Convection of a circular anomaly.

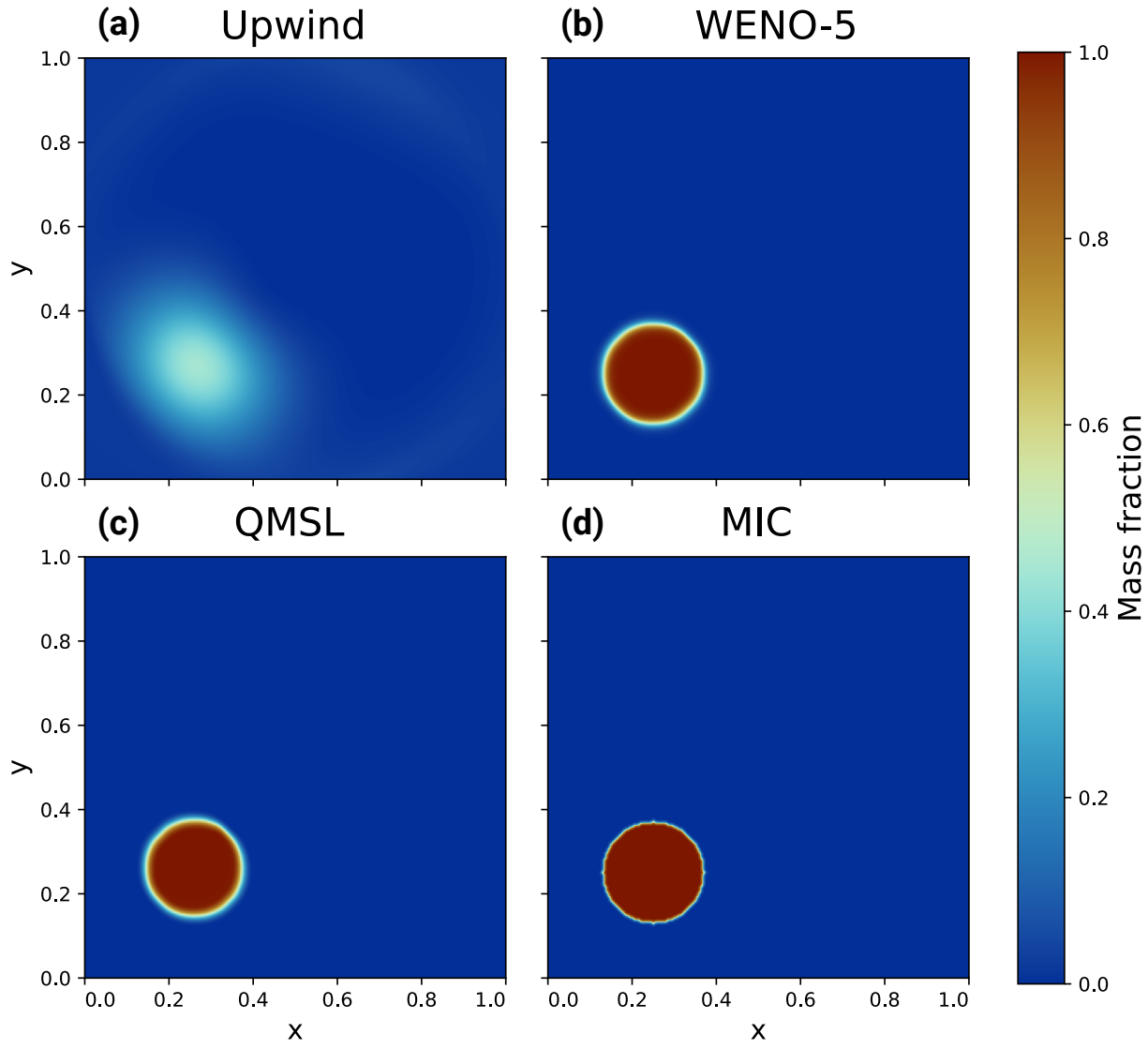


**Figure 6:** Results of the rotational test after two revolutions for the upwind, WENO-5, QMSL, and MIC schemes (a)-(d). Note that the upwind scheme was run with $\Delta t = 80$ due to stability issues.

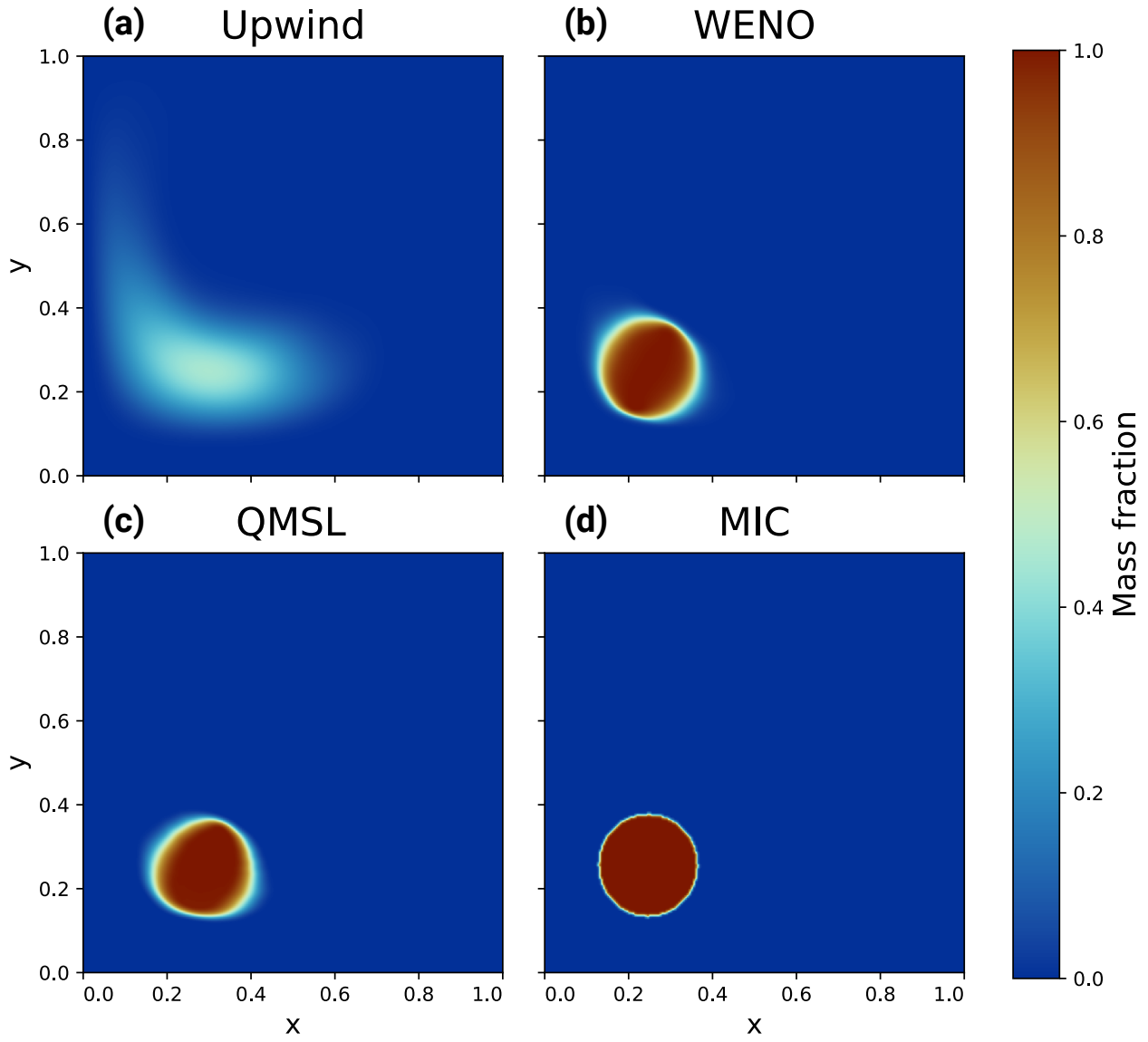


**Figure 7:** Results of the convection test after a total time of 0.8 for the upwind, WENO-5, QMSL, and MIC schemes (a)-(d). The velocity field was reversed at half of the total time so that the anomaly returns to its initial position.

**Table 2:** Results of the two numerical tests for four advection schemes. The running time for the MIC does not include the reseeding and removal step of markers.

| | Rotational test | | | Convection test | | | Running time of one time step [ms] | |
|---|---|---|---|---|---|---|---|---|
| Numerical schemes | $M$ | $E_{\text{tot}}$ | $\max(C)$ | $M$ | $E_{\text{tot}}$ | $\max(C)$ | Single-threaded | Multithreaded (24) |
| Upwind | 1.000 | $14.92\times10^{-3}$ | 0.700 | 1.000 | $24.17\times10^{-3}$ | 0.454 | 0.545 | 0.122 |
| WENO-5 | 1.000 | $1.57\times10^{-3}$ | 1.000 | 0.997 | $3.39\times10^{-3}$ | 1.008 | 14.882 | 1.767 |
| QMSL | 0.963 | $2.51\times10^{-3}$ | 1.000 | 1.003 | $7.73\times10^{-3}$ | 1.003 | 17.710 | 3.320 |
| MIC | 1.000 | $0.32\times10^{-3}$ | 1.000 | 1.000 | $2.39\times10^{-3}$ | 1.000 | 145.091 | 16.959 |

Eq. (5) is coupled to a transport model based on two-phase flow formalism. This transport model is used to model magma ascent in a porous solid phase. The main mechanism of transport is decompaction weakening, buoyancy, and failure and combines the formulations of Connolly and Podladchikov (2007b) and Vasilyev et al. (1998). It considers a compressible viscoelastic matrix with incompressible solid grains and an incompressible fluid phase, and it neglects the effect of shear stresses on fluid flow and compaction.

## 5.1. Two-phase flow formulation

In the case of a laminar fluid flow, conservation of momentum for the fluid can be expressed using Darcy's law:

$$\phi(\vec{v}_\mathrm{f} - \vec{v}_\mathrm{s}) = -\frac{k(\phi)}{\mu_\mathrm{f}}(\nabla P_\mathrm{f} + \rho_\mathrm{f}\vec{g}), \tag{17}$$

with $P_\mathrm{f}$ the fluid pressure (in Pa), $k$ the permeability ($\mathrm{m}^2$), a function of the filled porosity or melt fraction $\phi$, $\mu_\mathrm{f}$ the fluid viscosity (Pa s), and $\vec{g}$ the gravity vector ($\mathrm{m\,s^{-2}}$).

The relation between permeability and the filled porosity is assumed to follow the Kozeny–Carman law (Carman, 1939; Costa, 2006):

$$k = a\phi^3,$$

where $a$ is a proportionality constant.

The effective pressure $P_e$ is defined as the difference between lithostatic pressure and fluid pressure:

$$P_e = P_\mathrm{lith} - P_\mathrm{f}, \tag{18}$$

with $P_\mathrm{lith}$ the lithostatic pressure or the vertical load (in Pa). Substituting Eq. (18) in Eq. (17) and assuming constant rock density, we obtain

$$\phi(\vec{v}_\mathrm{f} - \vec{v}_\mathrm{s}) = \frac{k(\phi)}{\mu_\mathrm{f}}\left(\nabla P_e + \Delta\rho\vec{g}\right). \tag{19}$$

Considering the solid phase as a Maxwell body, we introduce rheology as the sum of viscous and poroelastic deformation:

$$\nabla \cdot \vec{v}_\mathrm{s} = -\frac{P_e}{\zeta(\phi, P_e)} - \phi^b \beta_\phi \frac{\partial P_e}{\partial t}, \tag{20}$$

where $\zeta$ is the volume viscosity of the rock (in Pa s), $b$ a constant, and $\beta_\phi$ the pore compressibility modulus ($\mathrm{Pa^{-1}}$). The terms on the right-hand side represent viscous and poroelastic deformation. Equation (20) is valid on the basis that shear stress is neglected.

The volume viscosity $\zeta$ is defined as a function of $\phi$ and $P_e$:

$$\zeta = \frac{\mu_\mathrm{s}}{\phi^m}\left[\frac{1}{R} - H\left(P_e\right)\left(\frac{1}{R} - 1\right)\right],$$

with $\mu_\mathrm{s}$ the shear viscosity of the rock (in Pa s), $m$ a constant, and $R$ the decompaction weakening factor defined as the inverse of the $R$ factor in Connolly and Podladchikov (2007b). $H(P_e)$ is originally defined as the Heaviside function but is here approximated by a hyperbolic tangent function as similarly done by Räss et al. (2018).

We approximate here $\beta_\phi$ as the inverse of $G$, the shear modulus of the rock (in Pa):

$$\beta_\phi \approx \frac{1}{G}.$$

This is valid for cylindrical pores, as described by Yarushina et al. (2015).

Summing up the right-hand sides of Eqs. (1) and (2) describing mass conservation and neglecting the change in densities, we obtain the total volumetric flux of material. Applying the divergence operator, we can derive

$$\nabla \cdot [\vec{v}_\mathrm{s} + \phi(\vec{v}_\mathrm{f} - \vec{v}_\mathrm{s})] = 0. \tag{21}$$

We can then substitute Eqs. (19) and (20) in Eq. (21) to obtain

$$\frac{P_e}{\zeta(\phi, P_e)} + \frac{\phi^b}{G}\frac{\partial P_e}{\partial t} = \nabla \cdot \left[\frac{k(\phi)}{\mu_\mathrm{f}}\left(\nabla P_e + \Delta\rho\vec{g}\right)\right]. \tag{22}$$

In addition, developing Eq. (1) with the assumption that $\phi$ is much smaller than unity, and substituting with Eq. (20) yields

$$\frac{\partial \phi}{\partial t} = -\frac{P_e}{\zeta(\phi, P_e)} - \frac{\phi^b}{G}\frac{\partial P_e}{\partial t}. \tag{23}$$

Equation (22) can be seen as the mass conservation equation of the system, relating the flux densities of the solid and fluid phases. Equation (23) relates the evolution of porosity with the deformation of the solid phase. Solving these two coupled equations for $P_e$ and $\phi$ allows the calculation of $\vec{v}_\mathrm{s}$ and $\vec{v}_\mathrm{f}$ from Eqs. (20) and (19) at each time step, making the link with Eq. (5).

## 5.2. Non-dimensionalisation and numerical approach

To mitigate numerical errors, a dimensionless scaling of the system is applied. The scaling variables are defined in Table 3. Using the scaling variables with Eqs. (19), (20), (22) and (23) and rearranging, we obtain the dimensionless system of equations:

$$\frac{\partial p}{\partial t_c} = \frac{1}{\varphi^b De} \times \left( \nabla \cdot \left[ \varphi^n \left( \nabla p + 1 \right) \right] - \frac{\varphi p}{\frac{1}{R} - H(p)\left(\frac{1}{R} - 1\right)} \right), \tag{24}$$

$$\frac{\partial \varphi}{\partial t_c} = - \left[ \frac{\varphi p}{\frac{1}{R} - H(p)\left(\frac{1}{R} - 1\right)} + \varphi^b De \frac{\partial p}{\partial t_c} \right], \tag{25}$$

$$\nabla \cdot \vec{u_s} = \frac{\partial \varphi}{\partial t_c}, \tag{26}$$

$$\vec{u_f} = \varphi^{n-1} \left( \nabla p + 1 \right) + \vec{u_s}, \tag{27}$$

where $\varphi$, $p$, $t_c$, $\vec{u_s}$, and $\vec{u_f}$ are the dimensionless porosity, the dimensionless effective pressure, the dimensionless time, the dimensionless solid velocity, and the dimensionless fluid velocity, respectively. The Deborah number $De$ is formally the ratio of the relaxation time to the observation time (Reiner, 1964), and here it characterises the ratio between viscous and elastic deformation. In the limit of small porosities, $\vec{u_s}$ can be neglected and only eqs. (24), (25), and (27) are here solved.

Equations (24) and (25) are strongly coupled and highly stiff due to the non-linearity of the system and require an efficient numerical solver. DifferentialEquations.jl (Rackauckas & Nie, 2017), a robust ordinary differential equation (ODE) solver package, was used. This package has the advantage of simplicity, both in concept and in coding, and allows arbitrary orders of accuracy in time to be easily tested using different ODE solvers.

Equations (24) and (25) are first discretised in space using finite differences on a uniform Cartesian grid in 2D and then integrated in time using the trapezoidal rule with the second-order backward difference formula (TR-BDF2) scheme, an implicit scheme suitable for highly stiff problems (Bank et al., 1985) using DifferentialEquations.jl. It uses adaptive time-stepping and the Newton-Raphson method as a non-linear solver, using forward automatic differentiation to compute the Jacobian matrix (Revels et al., 2016). Knowing $\varphi$ and $p$, (27) is then solved to compute $\vec{u_f}$ at each time step. The boundary conditions are periodic in all directions for all models. The system is then dimensionalised back.

## 5.3. Application to magmatic system

To assess the behaviour of the four advection schemes coupled with a two-phase flow system, we model the ascent of a magmatic anomaly. The spatial domain is a 2D regular grid of 450 by 900 m, and the total physical time is 1.5 Myr. The initial melt fraction distribution is defined using the following 2D Gaussian function:

$$\phi = \phi_0 + \phi_{\max} \times \exp\left( - \frac{(x - x_0)^2 + (z - z_0)^2}{\sigma^2} \right),$$

with $\phi_0$ the background porosity defined as 0.1%, $\phi_{\max}$ the maximum porosity defined as 5%, and $x_0$ and $z_0$, the centre of the anomaly. The standard deviation $\sigma$ of the Gaussian is 30 m. All physical parameters and corresponding scaling variables used are reported in Table 3. The evolution of porosity is shown in Fig. 8. All models were performed on a single computer with an Intel Xeon Gold 6128 processor and 128 GB of RAM using Julia version 1.10.2. All models were computed on a CPU with multithreading using 24 threads.

The melt fraction is associated with two different arbitrary chemical compositions: a basaltic composition for the background melt fraction and an andesitic composition for the anomaly, corresponding to a circle with a radius of 60 m. The aim is not to model a realistic magmatic system, but to investigate how the advection schemes can numerically affect the predictions of the model. The two compositions are reported in Table 4. No feedback between the melt compositions and the physical properties of the melt was considered, to prevent the advection schemes from influencing on the two-phase flow. In real settings, the effect of melt composition on melt viscosity and density is not negligible for these conditions. The maximum time step allowed for the two-phase flow is constrained by the $Co$ number associated with the melt velocity. Its maximum value allowed for the upwind and the WENO-5 schemes is 0.7, but a value of 0.7 and 1.5 for the QMSL and the MIC schemes were both used to take advantage of the extended stability of these schemes. The results for the evolution of the silica content in the melt are shown in Fig. 9 for the

**Table 3:** Parameters and corresponding scaling variables used in the models. Definitions of the scaling variables are from McKenzie (1984) and Connolly and Podladchikov (1998).

| Parameter | Symbol | Definition | Value | Unit |
|---|---|---|---|---|
| Melt viscosity | $\mu_f$ | | 100 | Pa s |
| Rock shear viscosity | $\mu_s$ | | $10^{19}$ | Pa s |
| Density contrast between solid and melt | $\Delta\rho$ | | 500 | kg m$^{-3}$ |
| Weakening parameter | $R$ | | 100 | |
| Shear modulus | $G$ | | $3.5 \times 10^9$ | Pa |
| Background porosity | $\phi_0$ | | $10^{-3}$ | |
| Permeability constant | $a$ | | $10^{-7}$ | m$^2$ |
| Background permeability | $k_0$ | | $a\,\phi_0$ | m$^2$ |
| Exponent for bulk viscosity term | $m$ | | 1 | |
| Exponent for poroelastic term | $b$ | | 1 | |
| Gravity acceleration | $g$ | | 9.80665 | m s$^{-2}$ |
| Characteristic porosity | $\phi^*$ | $\phi_0$ | $10^{-3}$ | |
| Characteristic viscous compaction length | $L^*$ | $\sqrt{\frac{\mu_s k_0}{\phi_0 \mu_f}}$ | 100 | m |
| Characteristic effective pressure | $P_e^*$ | $L^* \Delta\rho g$ | 490332.5 | Pa |
| Characteristic fluid flux | $q_f^*$ | $\frac{\mu_f}{\phi_0} \Delta\rho g L^*$ | $4.9 \times 10^{-12}$ | m s$^{-1}$ |
| Characteristic time | $t^*$ | $\frac{L^*}{q_f^*}$ | 0.65 | Myr |
| Deborah number | $De$ | $\beta_\phi P_e^*$ | $1.4 \times 10^{-5}$ | |

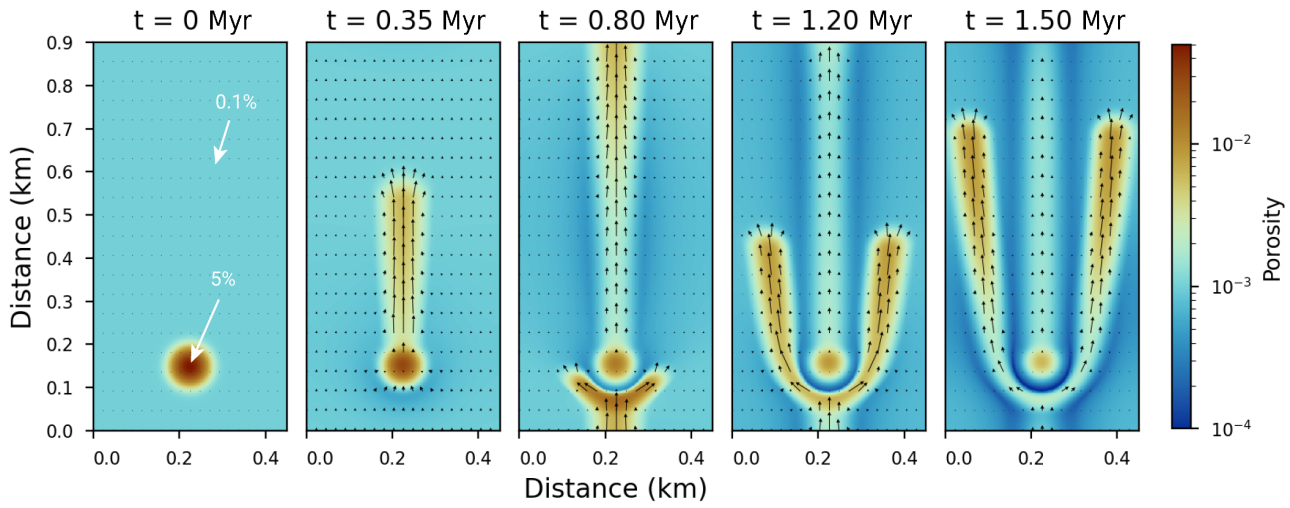


**Figure 8:** Reference evolution of the porosity in a 2D model from an initial Gaussian anomaly, which forms porosity waves. The superimposed vector field shows the melt velocity. Periodic boundaries are applied on all sides. The initial porosity anomaly is a Gaussian function with a maximum value of 5%. The background porosity is 0.1%. The spatial resolution of the grid is 300×600. The physical parameters used are listed in Table 3. The melt velocity is scaled by relative magnitude.

**Table 4:** Melt compositions (in wt%) used in the models. 1: Recalculated from Giordano and Dingwell (2003). 2: Recalculated from Neuville et al. (1993).

| Oxide (wt%) | Basalt[1] | Andesite[2] |
|---|---|---|
| $SiO_2$ | 48.32 | 59.87 |
| $TiO_2$ | 1.65 | 0.82 |
| $Al_2O_3$ | 16.72 | 16.93 |
| FeO(T) | 10.41 | 5.28 |
| MgO | 5.31 | 3.28 |
| CaO | 10.75 | 5.70 |
| $Na_2O$ | 3.85 | 3.76 |
| $K_2O$ | 1.99 | 1.36 |
| $H_2O$ | 1.00 | 3.00 |

*Co* number of 0.7 and for the four algorithms at a resolution of 500x1000.

As there is no analytical solution to this particular problem, it is not possible to directly calculate the numerical error in the different advection schemes. Nevertheless, we can compute the mass conservation of the advected quantities. The total mass of the melt composition is conserved, as it is re-normalized to 100% at each time step. This is a constant-sum constraint and is characteristic of compositional data (Aitchison, 1982). However, it is not necessarily the case for each individual oxide. In that light, similar to Eq. (16), we monitor the mass conservation of each individual oxide $M_{\text{ox}}$ in the melt at each time step:

$$M_{\text{ox}} = \frac{\sum_{k=1}^{K} \left(\phi^k C_{\text{ox}}^k\right)}{\sum_{k=1}^{K} \left(\phi_0^k C_{\text{ox}_0}^k\right)},$$

where $\phi^k$ and $\phi_0^k$ are the current and initial porosity at index $k$, and $C_{\text{ox}}^k$ and $C_{\text{ox}_0}^k$ the current and initial composition of the oxide of interest in the melt at the index $k$.

The melt fraction $\phi$ is conserved through the models, as Eqs. (24) and (25) are solved using a conservative discretisation. Therefore, $M_{\text{ox}}$ only monitors the effects of the advection schemes for the oxide of interest. To quantify how the mass conservation evolves for each individual oxide and for each advection algorithm, the same model was performed at five different resolutions: 100×200, 200×400, 300×600, 400×800, and 500×1000. The values of the mass conservation of silica content $M_{SiO_2}$ for each resolution are shown in Fig. 10 for all the models. The values of the mass conservation of each oxide for all the algorithms are shown in Fig. 11. The total running time of each model is reported in Fig. 12.

# 6. Results and discussion

The numerical models produced allow a better understanding of the process of passive chemical transport in magma within porosity waves and the impact of each advection scheme on the magma composition over time. All models confirm two distinct composition domains at the top of the porosity waves at the end of the simulations (Fig. 9). It is effectively a mixing of the compositions from the initial background porosity and from the anomaly. This is because melt is incorporated by the waves as they rise. This is attributed to the fact that the velocity of the porosity waves is higher than the melt velocity and has also been reported in previous studies (e.g. Jordan et al., 2018).

Comparing the results of the four algorithms, it is clear that the upwind scheme has the highest amount of numerical diffusion, which increases chemical mixing for non-physical reasons. The WENO-5 and QMSL exhibit similar results in terms of numerical diffusion, while the MIC shows the lowest amount with almost purely advective behaviour (Fig. 9). This is consistent with the numerical tests (Figs. 6 and 7). In terms of mass conservation, the oxide content is not conserved in all four schemes (Figs. 10 and 11). The WENO-5 gives the best results, with a mass conservation ranging from 98.87 to 100.51% for the lowest resolution to 99.85 to 100.06% at the highest resolution for all the oxides. The MIC performs similarly at high resolution, ranging from 99.77 to 100.11% for all the oxides at the highest resolution and with a significant increase in mass conservation from the 200x400 resolution. An improvement in the mass conservation for a *Co* number of 1.5 compared to the value of 0.7 is also noticeable. The QMSL shows slightly lower mass conservation for a *Co* of 0.7, ranging from 99.52 to 100.22% at the highest resolution and 97.22 to 101.26% at the lowest. In contrast to the MIC, there is a significant decrease for the mass conservation for a *Co* number of 1.5, ranging from 97.22 to 102.81% at low resolution to up to 97.77 to 101.01% at high resolution. The upwind scheme shows the worst values for mass conservation, ranging from 92.14 to 103.55% at low resolution to values of 96.97 to 101.37% at the highest resolution (Figs. 10 and 11). The better mass conservation of the MIC for a higher *Co* number can be explained by less reseeding and removal of markers,

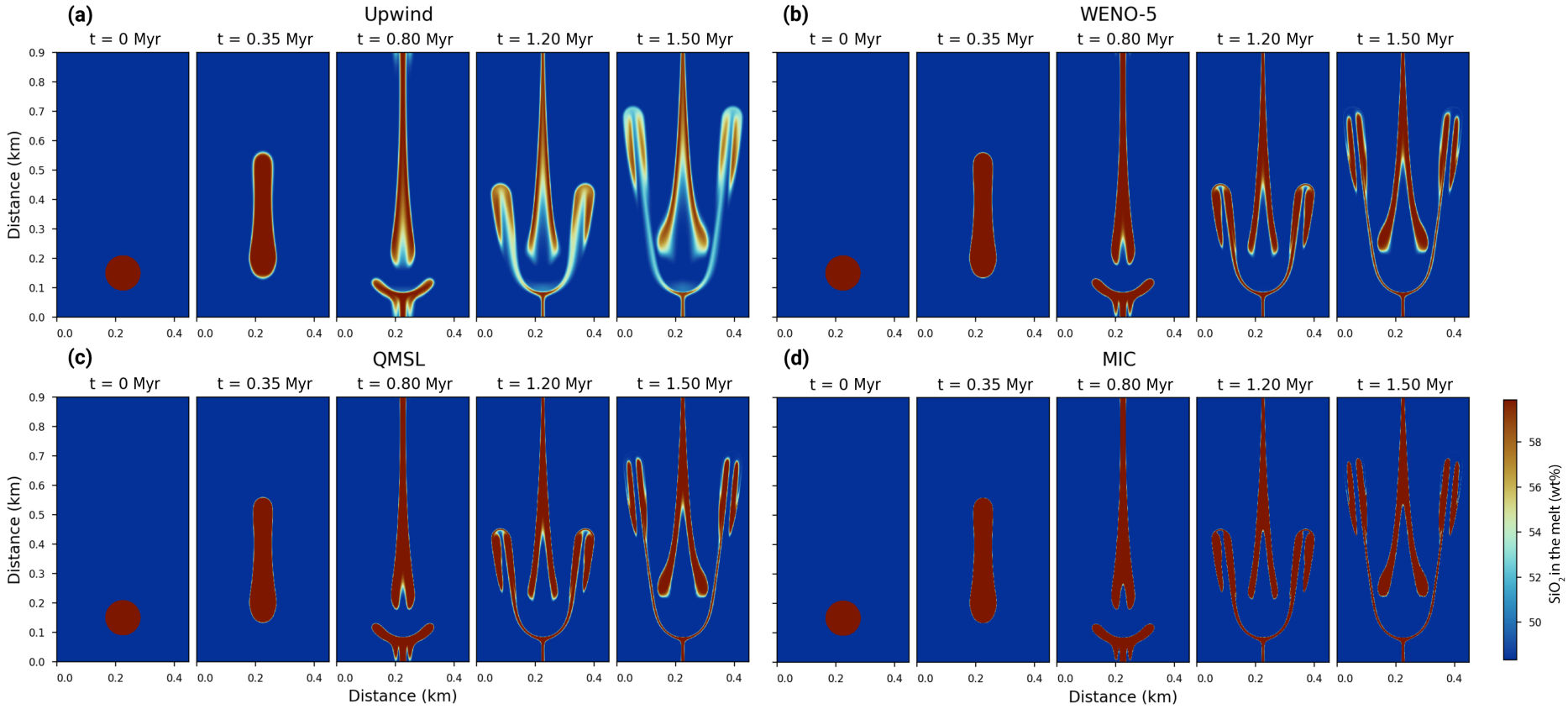


**Figure 9:** Evolution of the silica content in the melt for four different advection schemes: the upwind, the WENO-5, the QMSL, and the MIC (a)-(d) schemes. The Gaussian anomaly of porosity is associated with an andesitic composition, whereas the background porosity has a basaltic composition. The corresponding two-phase flow has an adaptive time step limited to a maximum value of a Courant number below 0.7 for all algorithms. The spatial resolution is 500×1000 nodes. The physical parameters used for the two-phase flow are reported in Table 3 and are identical for all models.

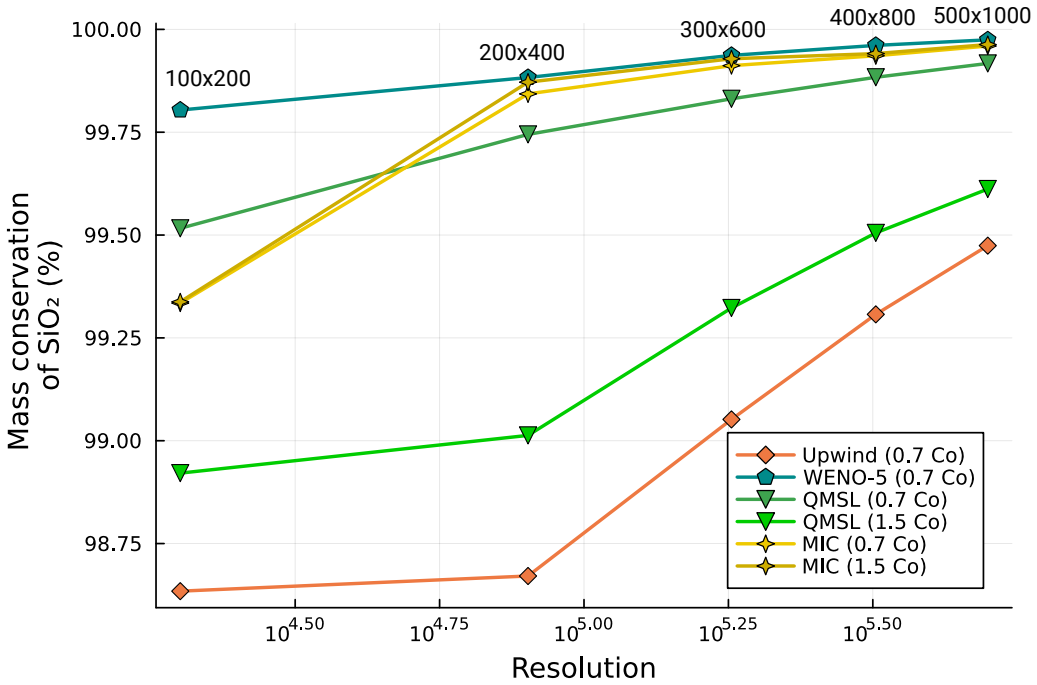


**Figure 10:** Mass conservation of silica content in the melt fraction for four different advection schemes and five different spatial resolutions at the end of each simulation. The Courant number used is 0.7 for the WENO-5 and the upwind schemes and 0.7 or 1.5 for the QMSL and the MIC schemes. The resolutions are 100×200, 200×400, 300×600, 400×800, and 500×1000. The physical parameters used are reported in Table 3.

as the approach used is not mass conservative. On the other hand, the poorer performance concerning the QMSL at higher *Co* number can be interpreted as showing the decrease in accuracy of the trajectory tracing with increasing time step. The differences in mass conservation observed in the different oxides through all the models show that the initial conditions play a role and that higher values in the anomaly at the beginning of the model leads to a loss of mass (e.g. $SiO_2$ or $Al_2O_3$), whereas the opposite leads to an excess of mass (e.g. CaO or $K_2O$). Also, the greater the relative difference between the composition of the oxide from the anomaly and the background melt fraction, the greater the mass conservation loss or gain (e.g. $H_2O$ or FeO). However, it is observed that the mass conservation of all the oxides appears to converge towards 1 with increasing resolution for all methods.

In terms of performance, all schemes, except the MIC, show a run time of the same order of magnitude for a *Co* number of 0.7 at all resolutions. This is explained by the multithreading approach, which allows high performance, even for more computationally expensive algorithms due to parallelism. The high computational cost of the MIC is mainly attributed to the reseeding and removal of the markers due to the highly divergent velocity field. This part was not fully parallelised due to race conditions caused by the removal and addition of memory at run time. Also, the MIC and QMSL perform better for a *Co* number of 1.5 compared to 0.7 (Fig. 12). This is explained by a larger adaptive time step used by the two-phase flow solver due to the extended stability domain, which means that fewer time steps are required to solve the system. All the calculations were performed on a single CPU, and the code could be further optimised, especially for the MIC. However, this result provides an idea of the cost of each method when parallelised and highlights the complexity of fully parallelising a MIC algorithm while dealing with a significant amount of reseeding and marker removal.

The upwind scheme is considered inadequate for this problem due to its high numerical diffusion, and its lack of mass conservation for highly divergent velocity fields. The MIC scheme shows very good results in terms of accuracy with the least amount of numerical diffusion and has no stability condition. It also demonstrates better mass conservation with a higher time-step. However, it is expensive in terms of computation and memory, as it needs to keep track of the markers. As the velocity field $\vec{v}_f$ is strongly divergent, it requires frequently regenerating and deleting markers, which adds complexity to the implementation and additional numerical cost. As a result, we

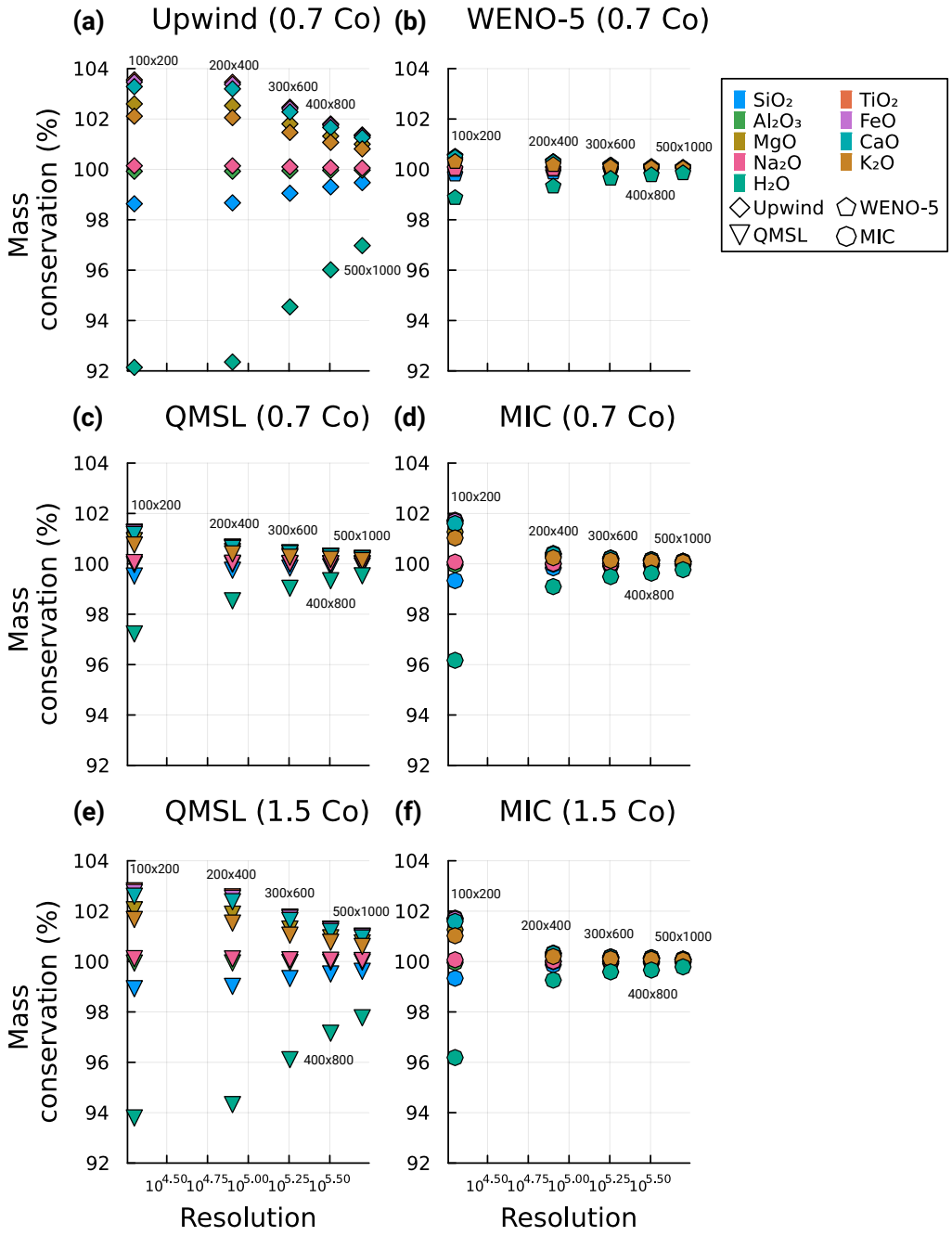


**Figure 11:** Mass conservation of each oxide in the melt fraction for four different advection schemes and five different spatial resolutions at the end of each simulation. The Courant number used is 0.7 for the WENO-5 and the upwind (a)-(b) schemes and 0.7 or 1.5 for the QMSL and the MIC (c)-(f) schemes. The resolutions are 100×200, 200×400, 300×600, 400×800, and 500×1000. The physical parameters used are reported in Table 3.

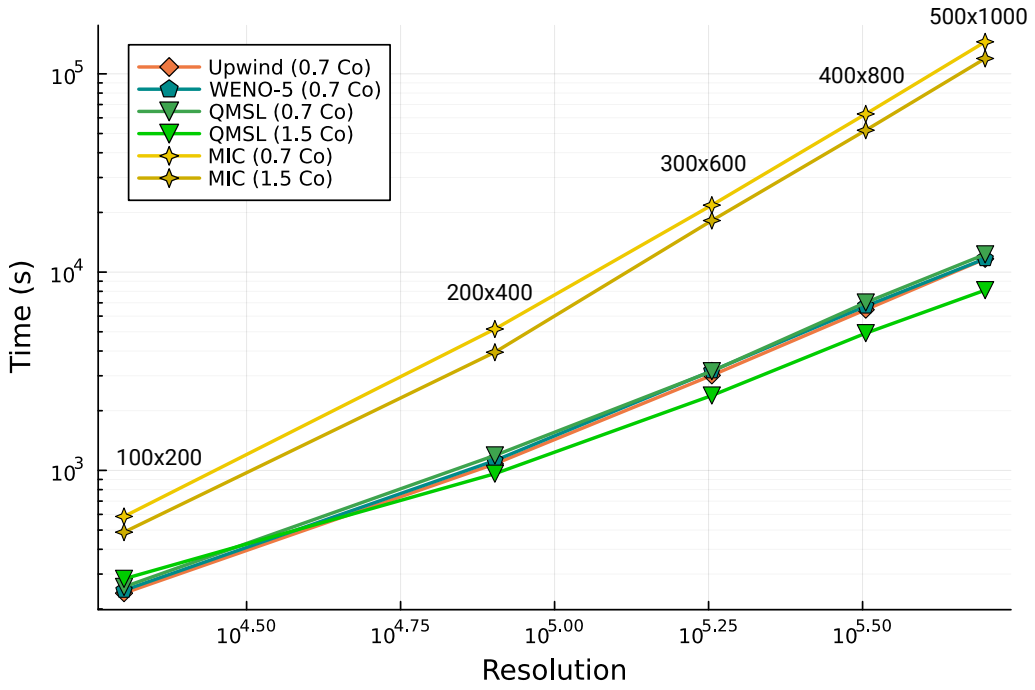


**Figure 12:** Total running time of the two-phase flow system coupled with four different advection schemes and five different resolutions. The Courant number used is 0.7 for the WENO-5 and the upwind schemes and both 0.7 and 1.5 for the QMSL and the MIC schemes. The resolutions are 100×200, 200×400, 300×600, 400×800, and 500×1000. The physical parameters used are reported in Table 3. All models were performed using a single computer with an Intel Xeon Gold 6128 processor and 128 GB of RAM using Julia version 1.10.2. All advection algorithms were computed on a CPU with multithreading using 24 threads.

consider this scheme to be too costly for this particular problem but recognise its robust qualities for other geodynamic problems where diffusion is not acceptable, such as thermomechanical deformation or mantle convection (e.g. Duretz et al., 2011; Trim et al., 2020; Ueda et al., 2015). On the other hand, the QMSL scheme shows very good performance with its extended stability field and good accuracy but has very poor mass conservation for a high $Co$, which contradicts the purpose of this scheme. A potential approach to improve the mass conservation would be to improve the trajectory tracing step, either by using higher-order multistep methods (e.g. Filbet & Prouveur, 2016) or by using Runge–Kutta schemes, similar to the one used for the MIC. On the basis of these results, the WENO-5 advection scheme appears to be the most appropriate for this problem. Mass conservation is a critical property for studying mass balance and mass transport problems associated with magma transport at different scales on Earth, and this algorithm obtains the best results. It also has good accuracy and reasonable performance and is easy to extend to higher dimensions and to parallelise.

## 7. Conclusions

In this study, a series of tests were carried out to determine which advection scheme is the most suitable for modelling the chemical transport of magma. Four of the most commonly used algorithms in the literature were compared: the upwind, WENO-5, MIC, and QMSL schemes. To test them, we combined a 2D two-phase flow model, which describes the evolution of the melt fraction of magma over time, with the chemical advection of its composition.

All algorithms, with the exception of the upwind scheme, are able to predict the melt composition with reasonable accuracy. However, mass conservation of each individual oxide in the melt is not fully achieved for any of the schemes. The MIC, while showing the least amount of numerical diffusion, requires a very large amount of reseeding and removal of markers due to the strongly divergent melt velocity field. This procedure is costly and requires reallocating memory at run time, complicating the implementation. The QMSL scheme has the worst mass conservation of the three algorithms, especially at high $Co$. This could potentially be improved by refining the trajectory tracing step to make it a more valuable alterna-

tive. The WENO-5 scheme shows the best results in mass conservation, even at low resolutions, is explicit, easy to implement, and extends in 3D, although it is constrained by the CFL condition. On the basis of these results, the WENO-5 scheme is the most suitable to use for transporting magma composition during magma ascent. This is also applicable to problems using similar formulations, such as chemical advection in aqueous fluids, and makes WENO-5 a suitable scheme for modelling reactive transport under crustal or mantle conditions.

## Code and data availability

The code used in this study allowing reproducibility of the data is available on GitHub (https://github.com/neoscalc/ChemicalAdvectionPorosityWave.jl) and at a permanent DOI repository (Zenodo): https://doi.org/10.5281/zenodo.8411354. The code is written in the Julia programming language. Refer to the repository's README for additional information. The code is distributed under the GPL-3.0 license. The data produced and used during this study are available at a permanent DOI repository (Zenodo): https://doi.org/10.5281/zenodo.13306073.

## Acknowledgements

Hugo Dominguez thanks Thibault Duretz and Ludovic Räss for discussion on the MIC implementation and the two-phase flow, respectively. The authors are grateful to Marcin Dabrowski and Albert de Montserrat Navarro for their thorough and constructive review of the original draft and Mauro Cacace for his editor handling. Funding was provided by the European Research Council (ERC) under the European Union's Horizon 2020 research and innovation programme (grant agreement No 850530).

## References


Aharonov, E., Spiegelman, M., & Kelemen, P. (1997). Three-dimensional flow and reaction in porous media: Implications for the Earth's mantle and sedimentary basins. *Journal of Geophysical Research: Solid Earth*, *102*(B7), 14821–14833. https://doi.org/10.1029/97JB00996 (cit. on pp. 18, 19).

Aharonov, E., Whitehead, J. A., Kelemen, P. B., & Spiegelman, M. (1995a). Channeling instability of upwelling melt in the mantle. *Journal of Geophysical Research: Solid Earth*, *100*(B10), 20433–20450. https://doi.org/10.1029/95JB01307 (cit. on p. 18).

Aharonov, E., Whitehead, J. A., Kelemen, P. B., & Spiegelman, M. (1995b). Channeling instability of upwelling melt in the mantle. *Journal of Geophysical Research: Solid Earth*, *100*(B10), 20433–20450. https://doi.org/10.1029/95JB01307 (cit. on p. 18).

Aitchison, J. (1982). The Statistical Analysis of Compositional Data. *Journal of the Royal Statistical Society Series B: Statistical Methodology*, *44*(2), 139–160. https://doi.org/10.1111/j.2517-6161.1982.tb01195.x (cit. on p. 31).

Bank, R., Coughran, W., Fichtner, W., Grosse, E., Rose, D., & Smith, R. (1985). Transient Simulation of Silicon Devices and Circuits. *IEEE Transactions on Computer-Aided Design of Integrated Circuits and Systems*, *4*(4), 436–451. https://doi.org/10.1109/TCAD.1985.1270142 (cit. on p. 29).

Barcilon, V., & Lovera, O. M. (1989). Solitary waves in magma dynamics. *Journal of Fluid Mechanics*, *204*, 121. https://doi.org/10.1017/S0022112089001680 (cit. on p. 18).

Bercovici, D., Ricard, Y., & Schubert, G. (2001). A two-phase model for compaction and damage: 1. General Theory. *Journal of Geophysical Research: Solid Earth*, *106*(B5), 8887–8906. https://doi.org/10.1029/2000JB900430 (cit. on p. 19).

Bermejo, R. (2001). Analysis of a class of quasi-monotone and conservative semi-Lagrangian advection schemes: *Numerische Mathematik*, *87*(4), 597–623. https://doi.org/10.1007/PL00005425 (cit. on p. 23).

Bermejo, R., & Staniforth, A. (1992). The Conversion of Semi-Lagrangian Advection Schemes to Quasi-Monotone Schemes. *Monthly Weather Review*, *120*(11), 2622–2632. https://doi.org/10.1175/1520-0493(1992)120<2622:TCOSLA>2.0.CO;2 (cit. on pp. 22, 23).

Bessat, A., Pilet, S., Podladchikov, Y. Y., & Schmalholz, S. M. (2022). Melt Migration and Chemical Differentiation by Reactive Porosity Waves. *Geochemistry, Geophysics, Geosystems*, *23*(2). https://doi.org/10.1029/2021GC009963 (cit. on p. 18).

Bouilhol, P., Connolly, J. A., & Burg, J.-P. (2011). Geological evidence and modeling of melt migration by porosity waves in the sub-arc mantle of Kohistan (Pakistan). *Geology*, *39*(12), 1091–1094. https://doi.org/10.1130/G32219.1 (cit. on p. 18).

Brown, M. (2013). Granite: From genesis to emplacement. *Geological Society of America Bulletin*, *125*(7–8), 1079–1113. https://doi.org/10.1130/B30877.1 (cit. on p. 18).

Carman, P. C. (1939). Permeability of saturated sands, soils and clays. *The Journal of Agricultural Science*, *29*(2), 262–273. https://doi.org/10.1017/S0021859600051789 (cit. on p. 28).

Carrera, J., Saaltink, M. W., Soler-Sagarra, J., Wang, J., & Valhondo, C. (2022). Reactive Transport: A Review of Basic Concepts with Emphasis on Biochemical Processes. *Energies*, *15*(3), 925. https://doi.org/10.3390/en15030925 (cit. on p. 19).

Chandrasekar, A. (2022, March 31). *Numerical Methods for Atmospheric and Oceanic Sciences* (1st ed.). Cambridge University Press. https://doi.org/10.1017/9781009119238 (cit. on pp. 20, 23).

Clemens, J., Bryan, S. E., Stevens, G., Mayne, M. J., & Petford, N. (2022). How are silicic volcanic and plutonic systems related? Part 2: Insights from phase-equilibria, thermodynamic modelling and textural evidence. *Earth-Science Reviews*, *235*, 104250. https://doi.org/10.1016/j.earscirev.2022.104250 (cit. on p. 18).

Connolly, J. A. D., & Podladchikov, Y. Y. (2007a). Decompaction weakening and channeling instability in ductile porous media: Implications for asthenospheric melt segregation. *Journal of Geophysical Research*, *112*(B10), B10205. https://doi.org/10.1029/2005JB004213 (cit. on p. 18).

Connolly, J. A. D., & Podladchikov, Y. Y. (2007b). Decompaction weakening and channeling instability in ductile porous media: Implications for asthenospheric melt segregation. *Journal of Geophysical Research*, *112*(B10), B10205. https:

//doi.org/10.1029/2005JB004213 (cit. on p. 28).

Connolly, J. A. D., & Podladchikov, Yu. Yu. (1998). Compaction-driven fluid flow in viscoelastic rock. *Geodinamica Acta*, *11*(2–3), 55–84. https://doi.org/10.1080/09853111.1998.11105311 (cit. on p. 30).

Costa, A. (2006). Permeability-porosity relationship: A reexamination of the Kozeny-Carman equation based on a fractal pore-space geometry assumption. *Geophysical Research Letters*, *33*(2), L02318. https://doi.org/10.1029/2005GL025134 (cit. on p. 28).

Courant, R., Isaacson, E., & Rees, M. (1952). On the solution of nonlinear hyperbolic differential equations by finite differences. *Communications on Pure and Applied Mathematics*, *5*(3), 243–255. https://doi.org/10.1002/cpa.3160050303 (cit. on p. 19).

Duretz, T., May, D. A., Gerya, T. V., & Tackley, P. J. (2011). Discretization errors and free surface stabilization in the finite difference and marker-in-cell method for applied geodynamics: A numerical study. *Geochemistry, Geophysics, Geosystems*, *12*(7), n/a–n/a. https://doi.org/10.1029/2011GC003567 (cit. on pp. 20, 35).

Filbet, F., & Prouveur, C. (2016). High order time discretization for backward semi-Lagrangian methods. *Journal of Computational and Applied Mathematics*, *303*, 171–188. https://doi.org/10.1016/j.cam.2016.01.024 (cit. on p. 35).

Gerya, T. V. (2019, May 23). *Introduction to Numerical Geodynamic Modelling* (2nd ed.). Cambridge University Press. https://doi.org/10.1017/9781316534243 (cit. on pp. 20, 23, 24).

Gerya, T. V., & Yuen, D. A. (2003a). Characteristics-based marker-in-cell method with conservative finite-differences schemes for modeling geological flows with strongly variable transport properties. *Physics of the Earth and Planetary Interiors*, *140*(4), 293–318. https://doi.org/10.1016/j.pepi.2003.09.006 (cit. on p. 20).

Gerya, T. V., & Yuen, D. A. (2003b). Characteristics-based marker-in-cell method with conservative finite-differences schemes for modeling geological flows with strongly variable transport properties. *Physics of the Earth and Planetary Interiors*, *140*(4), 293–318. https://doi.org/10.1016/j.pepi.2003.09.006 (cit. on p. 24).

Ghosh, D., & Baeder, J. D. (2012). Compact Reconstruction Schemes with Weighted ENO Limiting for Hyperbolic Conservation Laws. *SIAM Journal on Scientific Computing*, *34*(3), A1678–A1706. https://doi.org/10.1137/110857659 (cit. on p. 21).

Giordano, D., & Dingwell, D. B. (2003). Non-Arrhenian multicomponent melt viscosity: A model. *Earth and Planetary Science Letters*, *208*(3–4), 337–349. https://doi.org/10.1016/S0012-821X(03)00042-6 (cit. on p. 31).

Godunov, S. K., & Bohachevsky, I. (1959). Finite difference method for numerical computation of discontinuous solutions of the equations of fluid dynamics. *Matematičeskij sbornik*, *47(89)*(3), 271–306. Retrieved July 21, 2023, from https://hal.science/hal-01620642 (cit. on p. 19).

Gottlieb, S., Shu, C.-W., & Tadmor, E. (2001). Strong Stability-Preserving High-Order Time Discretization Methods. *SIAM Review*, *43*(1), 89–112. https://doi.org/10.1137/S003614450036757X (cit. on p. 21).

Grasso, F., & Pirozzoli, S. (2000). Shock-Wave-Vortex Interactions: Shock and Vortex Deformations, and Sound Production. *Theoretical and Computational Fluid Dynamics*, *13*(6), 421–456. https://doi.org/10.1007/s001620050121 (cit. on p. 20).

Harlow, F. H., Evans, M., & Richtmyer, R. D. (1955). *A machine calculation method for hydrodynamic problems*. Los Alamos Scientific Laboratory of the University of California. (Cit. on p. 20).

Harten, A., Engquist, B., Osher, S., & Chakravarthy, S. R. (1987). Uniformly High Order Accurate Essentially Non-oscillatory Schemes, III. In M. Y. Hussaini, B. van Leer, & J. Van Rosendale (Eds.), *Upwind and High-Resolution Schemes* (pp. 218–290). Springer. https://doi.org/10.1007/978-3-642-60543-7_12 (cit. on p. 19).

Hirsch, C. (2007). *Numerical computation of internal and external flows: Fundamentals of computational fluid dynamics* (2nd ed). Elsevier/Butterworth-Heinemann. (Cit. on p. 20).
OCLC: ocn148277909.

Jackson, M., Gallagher, K., Petford, N., & Cheadle, M. (2005). Towards a coupled physical and chemical model for tonalite–trondhjemite–granodiorite magma formation. *Lithos*, *79*(1–2), 43–60. https:

//doi.org/10.1016/j.lithos.2004.05.004 (cit. on p. 18).

Jha, K., Parmentier, E. M., & Phipps Morgan, J. (1994). The role of mantle-depletion and melt-retention buoyancy in spreading-center segmentation. *Earth and Planetary Science Letters*, *125*(1), 221–234. https://doi.org/10.1016/0012-821X(94)90217-8 (cit. on p. 18).

Jiang, G.-S., & Peng, D. (2000). Weighted ENO Schemes for Hamilton–Jacobi Equations. *SIAM Journal on Scientific Computing*, *21*(6), 2126–2143. https://doi.org/10.1137/S106482759732455X (cit. on p. 20).

Jiang, G.-S., & Shu, C.-W. (1996). Efficient Implementation of Weighted ENO Schemes. *Journal of Computational Physics*, *126*(1), 202–228. https://doi.org/10.1006/jcph.1996.0130 (cit. on p. 21).

Johnson, T., Yakymchuk, C., & Brown, M. (2021). Crustal melting and suprasolidus phase equilibria: From first principles to the state-of-the-art. *Earth-Science Reviews*, *221*, 103778. https://doi.org/10.1016/j.earscirev.2021.103778 (cit. on p. 18).

Jordan, J. S., Hesse, M. A., & Rudge, J. F. (2018). On mass transport in porosity waves. *Earth and Planetary Science Letters*, *485*, 65–78. https://doi.org/10.1016/j.epsl.2017.12.024 (cit. on pp. 19, 31).

Katz, R. F. (2008). Magma Dynamics with the Enthalpy Method: Benchmark Solutions and Magmatic Focusing at Mid-ocean Ridges. *Journal of Petrology*, *49*(12), 2099–2121. https://doi.org/10.1093/petrology/egn058 (cit. on p. 18).

Katz, R. F., Jones, D. W. R., Rudge, J. F., & Keller, T. (2022). Physics of Melt Extraction from the Mantle: Speed and Style. *Annual Review of Earth and Planetary Sciences*, *50*(1), 507–540. https://doi.org/10.1146/annurev-earth-032320-083704 (cit. on p. 18).

Katz, R. F., & Weatherley, S. M. (2012). Consequences of mantle heterogeneity for melt extraction at mid-ocean ridges. *Earth and Planetary Science Letters*, *335–336*, 226–237. https://doi.org/10.1016/j.epsl.2012.04.042 (cit. on p. 18).

Kelemen, P. B., Hirth, G., Shimizu, N., Spiegelman, M., & Dick, H. J. (1997). A review of melt migration processes in the adiabatically upwelling mantle beneath oceanic spreading ridges. *Philosophical Transactions of the Royal Society of London. Series A: Mathematical, Physical and Engineering Sciences*, *355*(1723), 283–318 (cit. on p. 18).

Keller, T., & Katz, R. F. (2016). The Role of Volatiles in Reactive Melt Transport in the Asthenosphere. *Journal of Petrology*, *57*(6), 1073–1108. https://doi.org/10.1093/petrology/egw030 (cit. on p. 18).

Keller, T., May, D. A., & Kaus, B. J. P. (2013). Numerical modelling of magma dynamics coupled to tectonic deformation of lithosphere and crust. *Geophysical Journal International*, *195*(3), 1406–1442. https://doi.org/10.1093/gji/ggt306 (cit. on pp. 18, 24).

LeVeque, R. J. (1992). *Numerical methods for conservation laws* (2nd ed). Birkhäuser Verlag. (Cit. on pp. 18, 20).

LeVeque, R. J. (2002). *Finite Volume Methods for Hyperbolic Problems*. Cambridge University Press. https://doi.org/10.1017/CBO9780511791253 (cit. on p. 19).

Liu, X.-D., Osher, S., & Chan, T. (1994). Weighted Essentially Non-oscillatory Schemes. *Journal of Computational Physics*, *115*(1), 200–212. https://doi.org/10.1006/jcph.1994.1187 (cit. on pp. 19, 21).

McDonald, A. (1984). Accuracy of Multiply-Upstream, Semi-Lagrangian Advective Schemes. *Monthly Weather Review*, *112*(6), 1267–1275. https://doi.org/10.1175/1520-0493(1984)112<1267:AOMUSL>2.0.CO;2 (cit. on pp. 20, 22).

McKenzie, D. (1984). The Generation and Compaction of Partially Molten Rock. *Journal of Petrology*, *25*(3), 713–765. https://doi.org/10.1093/petrology/25.3.713 (cit. on pp. 18, 19, 30).

Neuville, D. R., Courtial, P., Dingwell, D. B., & Richet, P. (1993). Thermodynamic and rheological properties of rhyolite and andesite melts. *Contributions to Mineralogy and Petrology*, *113*(4), 572–581. https://doi.org/10.1007/BF00698324 (cit. on p. 31).

Omlin, S., Malvoisin, B., & Podladchikov, Y. Y. (2017). Pore Fluid Extraction by Reactive Solitary Waves in 3-D: Reactive Porosity Waves. *Geophysical Research Letters*, *44*(18), 9267–9275. https://doi.org/10.1002/2017GL074293 (cit. on p. 18).

Pawar, S., & San, O. (2019). CFD Julia: A Learning Module Structuring an Introductory Course on Computational Fluid Dynamics. *Fluids*,

*4*(3), 159. https://doi.org/10.3390/fluids4030159 (cit. on p. 21).

Pusok, A. E., Kaus, B. J. P., & Popov, A. A. (2017). On the Quality of Velocity Interpolation Schemes for Marker-in-Cell Method and Staggered Grids. *Pure and Applied Geophysics*, *174*(3), 1071–1089. https://doi.org/10.1007/s00024-016-1431-8 (cit. on p. 24).

Rackauckas, C., & Nie, Q. (2017). DifferentialEquations.jl – A Performant and Feature-Rich Ecosystem for Solving Differential Equations in Julia. *Journal of Open Research Software*, *5*(1), 15. https://doi.org/10.5334/jors.151 (cit. on p. 29).

Räss, L., Simon, N. S. C., & Podladchikov, Y. Y. (2018). Spontaneous formation of fluid escape pipes from subsurface reservoirs. *Scientific Reports*, *8*(1), 11116. https://doi.org/10.1038/s41598-018-29485-5 (cit. on p. 28).

Reiner, M. (1964). The Deborah Number. *Physics Today*, *17*(1), 62–62. https://doi.org/10.1063/1.3051374 (cit. on p. 29).

Revels, J., Lubin, M., & Papamarkou, T. (2016). *Forward-mode automatic differentiation in Julia*. https://arxiv.org/abs/1607.07892 (cit. on p. 29).

Riel, N., Bouilhol, P., van Hunen, J., Cornet, J., Magni, V., Grigorova, V., & Velic, M. (2019). Interaction between mantle-derived magma and lower arc crust: Quantitative reactive melt flow modelling using STyx. *Geological Society, London, Special Publications*, *478*(1), 65–87. https://doi.org/10.1144/SP478.6 (cit. on p. 18).

Robert, A. (1981). A stable numerical integration scheme for the primitive meteorological equations. *Atmosphere-Ocean*, *19*(1), 35–46. https://doi.org/10.1080/07055900.1981.9649098 (cit. on pp. 20, 22).

Scott, D. R., & Stevenson, D. J. (1984). Magma solitons. *Geophysical Research Letters*, *11*(11), 1161–1164. https://doi.org/10.1029/GL011i011p01161 (cit. on p. 18).

Shu, C.-W. (2009). High Order Weighted Essentially Nonoscillatory Schemes for Convection Dominated Problems. *SIAM Review*, *51*(1), 82–126. https://doi.org/10.1137/070679065 (cit. on p. 21).

Smith, C. J. (2000). *The Semi-Lagrangian Method in Atmospheric Modelling*. Retrieved June 16, 2022, from https://www.semanticscholar.org/paper/The-Semi-Lagrangian-Method-in-Atmospheric-Modelling-Smith/b87a041f3d46a3bafb37b5bb7963008fccfb1067 (cit. on p. 23).

Solano, J. M. S., Jackson, M. D., Sparks, R. S. J., Blundy, J. D., & Annen, C. (2012). Melt Segregation in Deep Crustal Hot Zones: A Mechanism for Chemical Differentiation, Crustal Assimilation and the Formation of Evolved Magmas. *Journal of Petrology*, *53*(10), 1999–2026. https://doi.org/10.1093/petrology/egs041 (cit. on p. 18).

Sonnendrücker, E., Roche, J., Bertrand, P., & Ghizzo, A. (1999). The Semi-Lagrangian Method for the Numerical Resolution of the Vlasov Equation. *Journal of Computational Physics*, *149*(2), 201–220. https://doi.org/10.1006/jcph.1998.6148 (cit. on p. 20).

Spiegelman, M., Kelemen, P. B., & Aharonov, E. (2001). Causes and consequences of flow organization during melt transport: The reaction infiltration instability in compactible media. *Journal of Geophysical Research: Solid Earth*, *106*(B2), 2061–2077. https://doi.org/10.1029/2000JB900240 (cit. on p. 18).

Spiegelman, M., & Kenyon, P. (1992). The requirements for chemical disequilibrium during magma migration. *Earth and Planetary Science Letters*, *109*(3–4), 611–620 (cit. on p. 18).

Staniforth, A., & Côté, J. (1991). Semi-Lagrangian Integration Schemes for Atmospheric Models—A Review. *Monthly weather review*, *119*(9), 2206–2223. https://doi.org/10.1175/1520-0493(1991)119<2206:SLISFA>2.0.CO;2 (cit. on p. 20).

Trim, S. J., Lowman, J. P., & Butler, S. L. (2020). Improving Mass Conservation With the Tracer Ratio Method: Application to Thermochemical Mantle Flows. *Geochemistry, Geophysics, Geosystems*, *21*(2), e2019GC008799. https://doi.org/10.1029/2019GC008799 (cit. on p. 35).

Ueda, K., Willett, S., Gerya, T., & Ruh, J. (2015). Geomorphological–thermo-mechanical modeling: Application to orogenic wedge dynamics. *Tectonophysics*, *659*, 12–30. https://doi.org/10.1016/j.tecto.2015.08.001 (cit. on p. 35).

van Keken, P. E., King, S. D., Schmeling, H., Christensen, U. R., Neumeister, D., & Doin, M.-P. (1997). A comparison of methods for the modeling of thermochemical convection. *Journal of Geophysical Research: Solid Earth*, *102*(B10),

22477–22495. https://doi.org/10.1029/97JB01353 (cit. on p. 20).

Vasilyev, O. V., Podladchikov, Y. Y., & Yuen, D. A. (1998). Modeling of compaction driven flow in poro-viscoelastic medium using adaptive wavelet collocation method. *Geophysical Research Letters*, *25*(17), 3239–3242. https://doi.org/10.1029/98GL52358 (cit. on p. 28).

Wang, R., & Spiteri, R. J. (2007). Linear Instability of the Fifth-Order WENO Method. *SIAM Journal on Numerical Analysis*, *45*(5), 1871–1901. https://doi.org/10.1137/050637868 (cit. on p. 21).

Yarushina, V. M., Podladchikov, Y. Y., & Connolly, J. A. D. (2015). (De)compaction of porous viscoelastoplastic media: Solitary porosity waves. *Journal of Geophysical Research: Solid Earth*, *120*(7), 4843–4862. https://doi.org/10.1002/2014JB011260 (cit. on p. 28).

# Melting dynamics and pluton formation in the continental crust: a zircon geochronology and trace element study of the El Oro complex, Ecuador

Hugo Dominguez[1], Renée Tamblyn[1], Pierre Lanari[1, 2], Nicolas Riel[3], Etienne Jaillard[4], Jacob Forshaw[1], Mahyra Tedeschi[5], Samuel Macías[6]

[1] Institute of Geological Sciences, University of Bern, Baltzerstrasse 3, 3012 Bern, Switzerland

[2] Institute of Earth Sciences, University of Lausanne, Géopolis, 1015 Lausanne, Switzerland

[3] Institute of Geosciences, Johannes Gutenberg University, 55099 Mainz, Germany

[4] Université Grenoble Alpes, ISterre, IRD UR 219, CNRS UMR 5275, CS 40700, Grenoble, Cedex 9 38058, France

[5] Universidade Federal de Minas Gerais, Programa de Pós-Graduação em Geologia, CPMTC-IGC, Campus Pampulha, Belo Horizonte, Brazil

[6] Escuela Superior Politécnica del Litoral, Guayaquil, Ecuador

# 1. Introduction

The processes of melt production, segregation, and emplacement of magmas are fundamental to understanding the evolution of the continental crust. These processes govern the formation of migmatites and granitoids, which are crucial to deciphering the history of crustal growth and reworking as well as understanding heat transfer in the crust (Hawkesworth et al., 2010; Jaupart & Mareschal, 2010; Korenaga, 2018; Vielzeuf et al., 1990). A current geological challenge is to clarify the time scales and conditions under which these processes occur in sediment-sourced settings (Brown, 2013). In these environments, the relationship between the source (metapelitic migmatites) and the end-product (S-type plutons) may provide insights into these processes, though it is important to recognize that these systems often include an igneous-derived component. Partial melting of the crust does not typically occur under normal geothermal gradients and is usually driven by tectonic processes such as crustal thinning, thickening, or mantle upwelling (e.g. Clark et al., 2011; Clemens, 2003; England & Thompson, 1984). Therefore, it is important to constrain the thermal and physical conditions of the geodynamic regime during the periods of melt production and crystallisation.

Zircon geochronology has emerged as a powerful tool in addressing this challenge, providing precise age constraints that help unravel the complex history of both magmatic and metamorphic events involving melting (e.g. Farina et al., 2018; Michel et al., 2008; Oliver et al., 1993; Samperton et al., 2015; Schoene et al., 2012; Wu et al., 2011). Isotope-dilution, thermal ionization mass (ID-TIMS) U–Pb ages from magmatic zircons have long been used as a way to understand the timeframes of pluton emplacement and crystallisation by dating a single or group of whole zircon grains, and has been improving significantly in precision over the decades (Krogh, 1982; Mattinson, 2005; Paces & Miller Jr, 1993; Parrish, 1987; Schoene & Baxter, 2017; Silver & Deutsch, 1963; Tilton et al., 1957). The development of in situ geochronology (sensitive high-resolution ion microprobe (SHRIMP) and later secondary-ion mass spectrometry (SIMS)) introduced a radical new way to target particular zones or textures in zircon, often imaged by CL, and gave further insights on the ages of different zircon growth zones, and the inheritance of xenocrysts and antecrysts in magmatic and metamorphic systems (C. A. Andersen & Hinthorne, 1972; Ireland & Williams, 2003; Liati et al., 2016; Rubatto & Gebauer, 2000; Williams, 1992, 1997). The use of in situ laser inductively coupled plasma mass spectrometry (LA-ICP-MS) added to this the possibility of obtaining trace element data such as Ti and rare earth elements (REEs) in zircon in conjunction with U–Pb data, with the caveat that U–Pb ages usually are less precise than other methods (Košler & Sylvester, 2003; Kylander-Clark et al., 2013; Viete et al., 2015). By combining in situ U–Pb, trace element data and CL images, it becomes possible to distinguish populations of zircons beyond the U–Pb age uncertainty that record different information about the melting source and/or the crystallisation history and the pluton emplacement.

Few studies report the studies of both crustal-derived granitoid plutons and migmatites, their potential source, from the same locality (e.g. Couzinié et al., 2021; Li et al., 2022; Reichardt & Weinberg, 2012). This is due to the fact that melting generally takes place deep within the continental crust, near the heat source, while most plutons are emplaced in the middle to upper crust, where the transition from ductile to brittle rheology occurs (Sawyer et al., 2011). The El Oro complex in southern Ecuador provides a direct access to migmatites and their associated granitoids on a kilometre scale and is therefore a good natural laboratory to study these processes. This massif is interpreted as a tilted crustal section of metasediments from the Ecuadorian fore-arc (e.g. Baldock, 1982; Feininger, 1978, 1982; Gabriele, 2002; Litherland, 1994). The lower segment of this complex has undergone partial melting triggered by crustal thinning and the intrusion of gabbroic magma during the Triassic (Riel et al., 2013). This event led to the formation of a series of S-type plutons in the middle to upper crust (Aspden et al., 1995; Vinasco Vallejo, 2004). A later Cretaceous event induced the tilting of the sequence, which allows for the direct sampling of both the source rocks and the resulting granitoids on a distance of $\sim$20 km, providing a great opportunity for understanding crustal-scale processes.

In this study, we present a detailed geochronology and trace element analysis of zircons from S-type granitoids and migmatites within the El Oro complex. Additionally, metamorphic titanites from a metagabbro, interpreted to be the heat source for the thermal event, were dated. While we confirm the previously established ages of the migmatites and granitoids, our findings reveal that these processes persisted for an extended period of time (up to ca. 25 Myr). The emplacement of the granitoids is interpreted to be as-

sociated with a series of pulses through this duration. We also show the potential of collecting a high number of analyses per sample and to collect both U–Pb and trace element data to discriminate population, and gaining insight into melt processes, such as open system behaviour in migmatites.

# 2. Geological settings and previous studies

The El Oro metamorphic province is a complex of around 2400 $km^2$ situated in the southern western part of Ecuador and North-East of Peru. It is located in the active forearc of the Andes subduction system, close to the deflection separating the central Andes to the northern Andes and is part of the Amotapes massif. The province is bordered to the south by the Cretaceous Celica-Lancones sedimentary basin, to the east by Tertiary volcano-detrital deposits and the Cordillera Real, the metamorphic basement of the northern Andes that extends as far as Colombia and to the north by oceanic terrain accreted during the Cretaceous. To the south, the Cretaceous sediments of the Celica-Lancones basin are unconformably underlain by the El Oro metamorphic province. The other contacts, to the north and east, with the Cordillera Real and with oceanic terrains accreted to the margin in the Cretaceous are not known as they are masked by Mesozoic volcano-sedimentary deposits.

The El Oro metamorphic province is comprised of units of both oceanic and continental affinities assembled in a fore-arc position since the Palaeozoic, with E-W sub-vertical structures, and has been subdivided into three main complexes separated by tectonic discontinuities. From south to north, these units are: the El Oro complex, composed of Triassic units of oceanic affinities and a metapelitic sequence comprising large bodies of granitoids, the Raspas complex, an ophiolite, and the Birón complex, consisting of metasediments, migmatitic paragneisses, granitoids, metadiorites and amphibolites with a N-MORB-type geochemical affinity (Aspden et al., 1995; Feininger, 1980; Gabriele, 2002; Riel et al., 2013). The metapelitic sequence of the El Oro complex is the main focus of this study.

## 2.1. The El Oro complex

### 2.1.1. Units

The El Oro complex can be separated in three major groups, from south to north: the metamorphic continental sequence of the Tahuín group, the amphibolitised metagabbro of the Piedras unit, and the blueschists of the Arenillas-Panupalí unit (Fig. 1). The Tahuín group is interpreted as being composed mainly of clastic sediments originally deposited in a passive margin setting, which are now exposed as a section of tilted continental crust preserving increasing degree of metamorphism from south to north (Feininger, 1982). The age of deposition of the sediments at the top of the sequence is not well constrained, but is estimated to be either Devonian or Carboniferous, based on scarce paleological evidence mostly found on the equivalent sequence on the Peruvian side of the Amotape massif (Aspden et al., 1995; Cózar et al., 2024; Iddings & Olsson, 1928; Martínez, 1970; Mourier, 1988). The Tahuín group is separated mainly by the gabbroic Piedras unit by a large-scale normal fault but a magmatic contact has been observed in some localities (Riel et al., 2013). Different nomenclatures have been used over the time to describe the Tahuín group (e.g. Aspden et al., 1995; Baldock, 1982; Feininger, 1978). We follow here the nomenclature defined in Riel et al. (2013), which is based on Aspden et al. (1995), but redefine La Bocana unit as being metamorphic and not magmatic.

Three sub-units are defined, following major isograds. The El Tigre unit consists of unmetamorphosed to greenschist facies sediments, predominantly composed of turbidites (Aspden et al., 1995). The La Victoria unit, here defined from El Tigre by the Bt-in isograd, is composed of a sequence of metapelites and metapsammites preserving increasing degrees of metamorphism up to amphibolite facies (Feininger, 1978). The La Bocana unit is characterised by the apparence of partial melting and is composed of migmatites. Riel et al. (2013) divide this unit in two parts, upper La Bocana, characterised by the presence of metatexites, and lower La Bocana, defined by the Grt-in isograd, composed mainly of diatexites and more homogeneous materials. All these units are intruded by granitoids, with three plutons of importance: the El Prado, the La Florida and the Marcabelí plutons, showing S-type affinity (Aspden et al., 1995; Vinasco Vallejo, 2004).

The geodynamic driver of this high geothermal

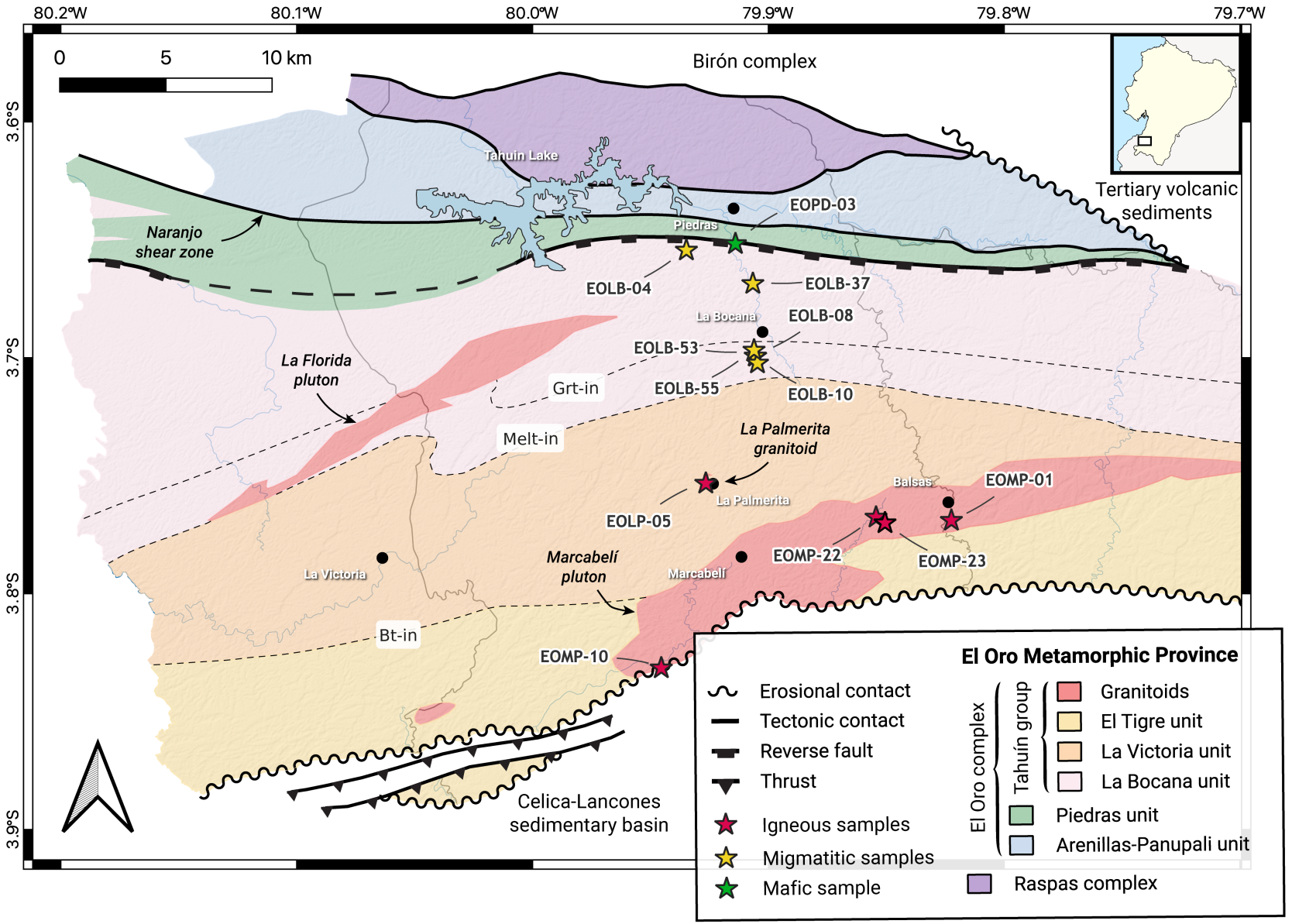


**Figure 1:** Simplified geological map of the western part of the El Oro metamorphic province. The stars represent the position of the samples used in this study. The El Prado pluton is on the East side of the map and not shown here. Based on field evidence and modified from Feininger (1978) and Riel et al. (2013).

gradient metamorphism of the Tahuín group is interpreted as the emplacement of the gabbro of the Piedras unit in the crustal root of the system (Riel et al., 2013). The gabbro itself is amphibolitised. It is suggested that the metamorphism and partial melting of the Tahuín group was rapidly ceased by the underthrusting of the comparatively cool blueschists of the Arenillas-Panupalí unit, which records peak *P–T* conditions of about 0.9 GPa and 300 °C (Gabriele, 2002).

### 2.1.2. Geochronological data from previous studies

Number of studies have provided temporal constraints on the metamorphic event responsible for the melting of the metasediments and the emplacement of granitoids in the Tahuín group and are reported below. When the mean squared weighted deviation (MSWD) was not reported in the original publication, it has been recalculated and is indicated by the letter R.

For the migmatites of La Bocana, Riel et al. (2013) reported two zircon $^{206}Pb/^{238}U$ ages: 225.7 ± 6.5 (MSWD = 2.6 (R), $n$ = 12) and 229.3 ± 2.4 Ma (MSWD = 0.96 (R), $n$ = 5), obtained using sensitive high mass-resolution ion microprobe (SHRIMP), and two monazite $^{208}Pb/^{232}Th$ ages at 226.0 ± 1.3 (MSWD = 2.44 (R), $n$ = 17) and 223.22 ± 2.2 Ma (MSWD = 1.71 (R), $n$ = 11), performed on LA-ICP-MS. Vinasco Vallejo (2004), using SHRIMP, reported a zircon $^{206}Pb/^{238}U$ age of 232.2 ± 5.1 (MSWD = 0.029, $n$ = 6) Ma. In the same study, Vinasco Vallejo (2004) obtained a zircon $^{206}Pb/^{238}U$ age of 234.9 ± 4.5 (MSWD = 0.64, $n$ = 6) Ma for the Marcabelí pluton, and two ages of 239.6 ± 7.3 Ma (MSWD = 1.3, $n$ = 9) and 215.5 ± 7.8 Ma (MSWD = 0.35, $n$ = 3) for the La Florida pluton. Noble et al. (1997) reported, using thermal ionization mass spectrometry (TIMS), a $^{207}Pb/^{235}U$ monazite age of 227.5 ± 0.8 (MSWD = 0.013 (R), $n$ = 3) Ma for the Marcabelí pluton.

Time constraints on the emplacement of the metagabbro protolith from the Piedras unit are provided by a zircon $^{206}Pb/^{238}U$ age from Noble et al. (1997) of $221^{+18}_{-16}$ Ma (MSWD = 0.015 (R), $n$ = 2) and from Cochrane et al. (2014), using LA-ICP-MS, yielding 222.7 ± 6.3 Ma (MSWD = 1.90, $n$ = 17). An integrated cooling $^{40}Ar/^{39}Ar$ age on hornblende from Gabriele (2002), obtained by stepped heating procedure, yields 226 ± 1.8 Ma, and was interpreted to date the metamorphism. The same study provided a $^{40}Ar/^{39}Ar$ age on hornblende of 225.3 ± 1.7 Ma from the blueschists of the Arenillas-Panupalí unit.

These ages all lead to a common event undergone by the El Oro complex during the middle to late Triassic from around 240 to 210 Ma. This includes the emplacement and metamorphism of the gabbroic Piedras unit, metamorphism and partial melting of the metasediments from the Tahuín group, migration and crystallisation of these melts in S-type plutons, and emplacement of the underlying blueschists. However, the direct links between the migmatites and plutons, and more specifically, the timing between melt formation and emplacement of the multiple plutons is not clear. These relationships can be resolved by in-situ U–Pb and trace element analyses of zircons throughout the Tahuín group.

## 3. Sampling strategy and samples description

The selection of representative samples involving melt processes is challenging as these processes inherently produce chemical heterogeneities in both migmatites and plutons. The strategy in this study was to select leucosomes from neosomes or diatexites in migmatites, as these are more likely to represent previous melt pathways. For the granitoids, diverse samples were collected to capture different magmatic phases, if present. To try to establish co-genetic links between the migmatites and the granitoids, the samples were collected along a general S-N trend, from the interpreted shallow to deep continental paleocrust in the Tahuín group. This was further complicated by the difficult outcrop conditions in the area and the majority of samples were collected along rivers to obtain fresher samples. For the granitoids, four samples were collected from the Marcabelí pluton and one sample was collected from a small isolated granitoid body, near the La Palmerita locality, hereafter referenced to as the La Palmerita granitoid. For the migmatites, two samples of leusocomes and two samples of diatexites were collected from the upper La Bocana unit and two samples of diatexites were obtained from the lower La Bocana unit. The upper La Bocana unit was specifically targeted because it is interpreted as the final melting front of the heat anomaly event (Riel et al., 2013). A brief description of the different samples and their petrography is presented below. The locations of the twelve different samples are shown in Fig. 1 and the exact GPS co-

ordinates are provided with the analytical data (see data availability section). Mineral abbreviations used in the following section and throughout this study follow the convention defined by Warr (2021). The terminology used for the description of migmatites is following Sawyer (2008).

## 3.1. Igneous samples

### 3.1.1. Marcabelí pluton

The Marcabelí pluton is not a homogeneous body and presents a variety of facies, from medium to coarse-grained monzogranites and granodiorites. It has an S-type affinity, but hornblende and mafic enclaves are also present in some localities (field evidence; Aspden et al., 1995; Vinasco Vallejo, 2004). In an attempt to capture this diversity, four different samples were selected. They are divided into three groups: medium-grained quartz-rich monzogranite, referred to as quartz monzonite (samples EOMP-01 and EOMP-23), coarse-grained monzogranite, referred to as monzogranite (sample EOMP-10), and coarse-grained granodiorite, referred to as granodiorite (sample EOMP-22) based on their occurrences of K-feldspar and quartz (Fig. 2A). The samples all contain Qz + Pl + Kfs + Bt. Chlorite is also often present. Samples EOMP-01 and EOMP-23 both also contains muscovite as major phase and sample EOMP-22 contains accessory hornblende. No titanium-bearing phases were observed directly in thin sections, except for EOMP-23, which contained titanite.

### 3.1.2. La Palmerita granitoid

The La Palmerita granitoid forms a decametric outcrop and is a homogeneous body with a few biotite-rich enclaves. The sample EOLP-05 has a medium grain size and the major minerals present are Qz + Pl + Kfs + Bt + Ms + Sil. The Ti-bearing accessory phases are Ilm + Ttn.

## 3.2. Migmatite samples

### 3.2.1. Upper La Bocana

The outcrops of the four samples (EOLB-08, EOLB-10, EOLB-53, EOLB-55) collected in upper La Bocana show a great variety in textures in migmatitic rocks on a scale of hundreds of metres. This ranges from less evolved metatexites with centimetric leucosomes and melanosomes to more evolved diatexites with dominant leucocratic neosomes and quasi-absence of paleosomes. An example of metatexite is shown in Fig. 2.B. Samples EOLB-08 and EOLB-10 are collected in decimetric large leucosomes in evolved metatexites, with centimetric patchy Bt-rich aggregates. The samples EOLB-53 and EOLB-55 are collected in homogeneous leucocratic diatexites. The major mineral assemblage of the four samples is Qz + Pl + Kfs + Bt + Ms + Ap. The Ti accessory phases are Ilm + Ttn with minor presence of rutile for all the samples and EOLB-55 also contains accessory garnet.

### 3.2.2. Lower La Bocana

The samples EOLB-04 and EOLB-37 were taken from two different localities but show a similar coarse-grained texture and major mineral assemblage with Qz + Pl + Kfs + Bt + Ms + Grt + Sil. The garnets in both samples are millimetric to centimetric poikiloblasts rimmed by biotite. The accessory Ti phases are Ilm + Rt with titanite also present in EOLB-04. Both samples also contain graphite. The samples show strong evidence of retrogression with the presence of chlorite and plagioclase alteration. The host rocks in both cases are diatexitic in texture with a homogeneous appearance (Fig. 2C).

## 3.3. Metagabbro sample

### 3.3.1. Piedras metagabbro

The sample EOPD-03 is a medium-grained amphibolite containing mainly hornblende and altered plagioclase. The main accessory Ti phase is titanite, which is present in large quantity, mostly in the hornblende. Quartz is present as a minor phase and rutile and zircon were found as inclusions in the titanite.

# 4. Analytical methods

## 4.1. Sample preparation and imaging

Samples were cut into small blocks and then disaggregated using a high-voltage SelFrag device at the University of Bern, followed by sieving. Zircon and titanite grains were extracted from the 65–250 and 250–500 µm fraction, respectively, using standard density and magnetic separation techniques, including a Frantz isodynamic magnetic separator and heavy

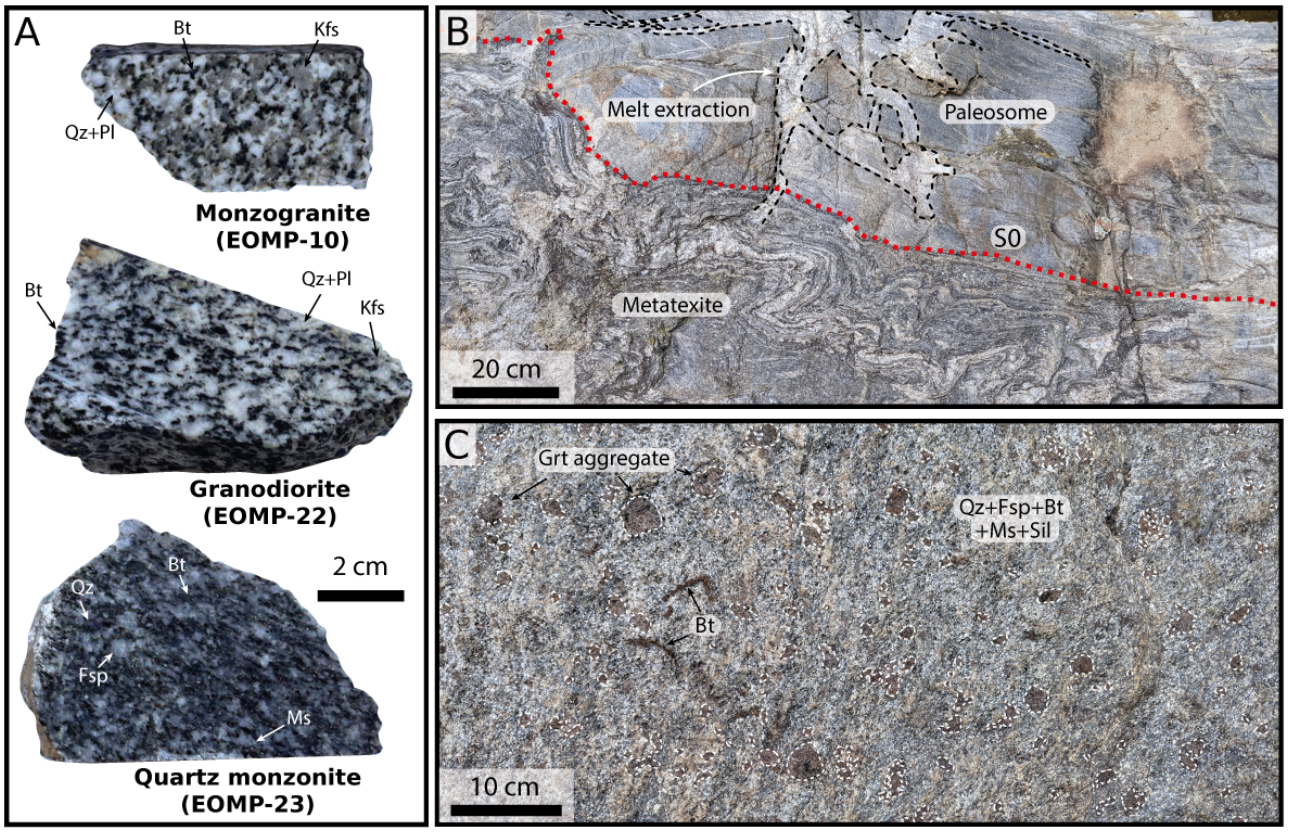


**Figure 2:** Granitic samples and field pictures of typical migmatites from La Bocana unit. A. Sample pictures of the granitic samples from the Marcabelí pluton showing their different textures. The sample EOMP-01 shows similar texture to EOMP-23. B. Outcrop picture of a typical metatexite in upper La Bocana unit. The paleosome is mainly formed by quarzitic layers whereas the metatexite is composed of millimetric to centimetric leucosomes and melanosomes. No garnet or silliminate is present in the rock. C. Outcrop picture of a representative diatexite in lower La Bocana unit. Garnet aggregates represent an important volume of the rock.

liquid methylene iodide. Hand-picked zircons and titanites were mounted in epoxy and polished to expose their mid-sections. Imaging was conducted on two different instruments: a ZEISS EVO50 scanning electron microscope (SEM) and a ZEISS SIGMA 560VP at the Institute of Geological Sciences, University of Bern. For zircon, charge contrast (CC) imaging was performed while using the ZEISS EVO50 under low vacuum conditions (18 Pa) with a 12 kV accelerating voltage, a beam current of 700–750 pA, and a working distance of 10–11 mm. Cathodoluminescence (CL) imagining was performed with the ZEISS SIGMA 560VP using 15 kV accelerating voltage and similar working distance. Charge contrast and CL images produced equivalent results. For titanite grains, back-scattered electrons (BSE) were performed on the ZEISS SIGMA 560VP using 15 kV accelerating voltage and a working distance of 10–11 mm.

## 4.2. Zircon and titanite U–Pb and trace element analyses

Zircon U–Pb and trace elements were collected simultaneously using a RESOlution-LR 193 nm excimer laser ablation system (Applied Spectra), with a S155 sample chamber (Laurin Technic), coupled to an Agilent 7900 ICP-MS housed at the University of Bern. Measurements were conducted across six sessions. Zircons were ablated at a surface energy density (or fluence) of 2.5 $J\,cm^{-2}$ at a repetition rate of 5 Hz, with laser spot diameters of 16 and 30 µm, with three pulses of pre-cleaning ablation. Analyses included 30 s of background, followed by 30 s of ablation, and 20 s of washout time. Titanite grains were ablated at a surface energy density (or fluence) of 3 $J\,cm^{-2}$ at a repetition rate of 5 Hz, and a laser spot diameter of 50 µm, with three pulses of pre-cleaning ablation. Analyses comprised 30 s of background, followed by 40 s of ablation, and 20 s of washout time. He was the carrier gas (at 400 $mL\,min^{-1}$) and N2 was added

(at 3.5 mL $min^{-1}$) to the carrier gas after the sample chamber to increase sensitivity. The measured masses and their corresponding dwell times are detailed in table 1 for each session.

**Table 1:** Dwell time used for each measurement session of zircon. Most of the rare eath elements were not measured during session 2, where additional zircon analyses for samples EOMP-01, EOMP-10, and EOMP-22 were conducted.

| Mass | Dwell time (ms) | Dwell time (ms) |
|---|---|---|
| | Sessions 1, 3, 4, 5, 6 | Session 2 |
| $^{29}Si$ | 5 | 5 |
| $^{31}P$ | 5 | 5 |
| $^{49}Ti$ | 10 | 30 |
| $^{89}Y$ | 5 | 5 |
| $^{90}Zr$, $^{91}Zr$ | 5 | 5 |
| $^{140}Ce$ | 10 | - |
| $^{146}Nd$ | 10 | - |
| $^{147}Sm$ | 10 | - |
| $^{151}Eu$ | 10 | - |
| $^{157}Gd$ | 10 | 10 |
| $^{159}Tb$ | 10 | - |
| $^{163}Dy$ | 5 | - |
| $^{165}Ho$ | 5 | - |
| $^{167}Er$ | 5 | - |
| $^{169}Tm$ | 5 | - |
| $^{172}Yb$ | 5 | - |
| $^{175}Lu$ | 5 | 5 |
| $^{202}Hg$ | 10 | 10 |
| $^{204}Pb$ | 20 | 10 |
| $^{206}Pb$ | 40 | 40 |
| $^{207}Pb$ | 40 | 40 |
| $^{208}Pb$ | 30 | 30 |
| $^{232}Th$ | 20 | 20 |
| $^{238}U$ | 30 | 30 |

All LA-ICP-MS data were processed using the software LADR (Norris & Danyushevsky, 2018) to correct for gas backgrounds, downhole fractionation and instrument mass bias and drift. Background measurements were subtracted from the analysis using a step function, while U–Pb isotopic ratios and trace elements were corrected for using polynomial fits. Downhole fractionation corrections were grouped by spot size.

The primary reference material (PRM) for zircon U–Pb calibration was GJ-1, which has a $^{206}Pb/^{238}U$ age of 600.7 ± 1.1 Ma (Jackson et al., 2004). Secondary reference materials included Plešovice, which has a $^{206}Pb/^{238}U$ age of 337.13 ± 0.37 Ma (Sláma et al., 2008) and 91500, which has a $^{206}Pb/^{238}U$ age of 1062.4 ± 0.4 Ma (Wiedenbeck et al., 1995). The Plešovice standard was used as a secondary reference standard for 16 µm spots only, as 30 µm spots produced high U counts, which often shifted the ICP-MS detector from pulse to analog mode, and had correspondingly high U/Pb ratios. This may have induced different downhole fractionation effects which could not be accounted by using the lower U content GJ-1 PRM. Plešovice was also monitored for across-session reproducibility, as discussed below. Over the course of the six sessions, Plešovice returned a weighted mean $^{206}Pb/^{238}U$ age of 339.46 ± 0.64/3.83 Ma (MSWD = 1.43, $n$ = 169) and 91500 returned a weighted mean $^{206}Pb/^{238}U$ age 1059.75 ± 1.51/11.27 Ma (MSWD = 0.91, $n$ = 246), where the reported uncertainties include without and with systematic uncertainty (see below). The PRM for trace elements was SRM NIST612 or SRM NIST610 (Jochum et al., 2011), and GSD-1G (Jochum et al., 2005) was used for a secondary standard correction in order to correct for spot size effects. Zr was used as the internal element standard for all zircon analyses with a value of 43.14 wt% .

Concerning titanite, only 1 session was conducted. The PRM used was MKDE1, which has a $^{206}Pb/^{238}U$ age of 600.7 ± 1.1 Ma (Spandler et al., 2016). The secondary reference materials included BLR, which returned a lower intercept discordia age of 1076 ± 34 Ma (MSWD = 5.7). The high uncertainty is attributed to the high U content of the reference material, which leads to low spread along the discordia line. By anchoring the discordia line to the common lead composition determined by the Stacey-Kramers model ($(^{207}Pb/^{206}Pb)_c$ = 0.912) (Stacey & Kramers, 1975), a lower intercept age of 1040.1 ± 10.3 Ma was obtained, which is within uncertainty of the reported TIMS age of 1047.1 ± 0.4 Ma (Aleinikoff et al., 2007). The PRM for trace elements was SRM NIST610, and GSD-1G (Jochum et al., 2005) was used for a secondary standard correction in order to correct for spot size effects.

## 4.3. Filtering, uncertainties and weighted means of zircon U–Pb dates

The programming language Julia (Bezanson et al., 2017) was used with Isoplot.jl (Keller, 2023) to compute dates, weighted means and propagate uncertainties. The guidelines and recommendations for uncertainty propagation and statistics from Horstwood et al. (2016) were used. All analyses in the samples older than 270 Ma were discarded as they can be attributed either to mixing with or inherited zircon cores. Additionally, only concordant data at a confidence level of 2σ were considered for the secondary standards

and the samples. As such, all data reported for the samples in this manuscript is concordant within 2σ and <270 Ma. Systematic uncertainties are propagated into the weighted mean date uncertainties presented in this study, and are obtained by combining in quadrature the random uncertainty, the excess variance ($\epsilon$), the uncertainty of the decay constant and the ratio uncertainty on GJ-1 for the isotopic ratio $^{206}Pb/^{238}U$. In order to enable comparison between dates obtained across multiple sessions, an estimation of $\epsilon$ is needed. This was achieved iteratively by computing a weighted mean from all the 16 µm analyses across the six analytical sessions of this study from Plešovice until the value of MSWD converges to 1 by varying $\epsilon$ (e.g. Sliwinski et al., 2022). The excess variance was estimated for the six sessions to be 1.12% at 2σ.

For each sample, weighted means were calculated using the median absolute deviation method. In this method, the median value of the population in each sample is determined, and the absolute deviation of each sample from this median is calculated. The median absolute deviation (MAD) is then found by taking the median of these absolute deviations. Any analysis with an absolute deviation exceedingly twice the MAD at 1σ is deemed an outlier and excluded from weighted mean calculations. This was done to obtain a consistent method to compute ages across samples and to remove bias from sample and signal selection. The values of MSWD obtained are often higher than the acceptable statistical range at 2σ, defined as $1 + \sqrt{\frac{1}{N}}$, where $N$ is the number of samples (Wendt & Carl, 1991), indicating overdispersion in the data. To estimate this statistical overdispersion ($\omega$), a similar approach was employed to that used for $\epsilon$. The overdispersion was computed iteratively until the value of MSWD converges towards $1 + \sqrt{\frac{1}{N}}$. This is done by assuming the total uncertainty on the analyses to be $\sqrt{\theta^2 + \epsilon^2 + \omega^2}$ where $\theta$ is the uncertainty of the individual analysis. This value of $\omega$ represents the sum of all processes contributing to statistical dispersion, such as Pb-loss, mixed ages or geological dispersion. This is further discussed in the discussion section. The dates and ages are reported with three uncertainties at 2σ: without systematic uncertainty propagation, with systematic uncertainty propagation, following the recommendations of Horstwood et al. (2016), and with systematic uncertainty propagation plus overdispersion when the MSWD value is higher than the acceptable statistical range at 2σ. This last uncertainty is referred as dispersion uncertainty and is the uncertainty needed to obtain a weighted mean with a statistically acceptable MSWD.

# 5. Results

## 5.1. Marcabelí pluton and La Palmerita granitoid

### 5.1.1. Zircon morphology

Zircon grains are colourless and mostly subrounded or euhedral, with a small portion being elongated. Small variations can be observed between samples, such as number and type of inclusions or sizes, but, overall, grains show the same characteristics. Their widths range from approximately 40 to 100 µm, with lengths varying from around 80 to 300 µm for elongation ratios ranging from 2 to 5. Charge contrast and CL images show complex zoning, with up to four or five distinct zones, composed mostly of inherited cores (Fig. 3). For the Marcabelí pluton, the CL zones with dates younger than ca. 270 Ma are characterised by oscillatory zoning and bright-CL, often overgrown by a slim CL-dark and homogeneous rim (Fig. 3A). The slim rim was observed on all samples but was particularly developed in EOMP-01. For La Palmerita granitoid, a distinct grey to dark CL-rim showing oscillation is present (Fig. 3B).

### 5.1.2. U–Pb and trace element zircon data

A total of 713 analyses were conducted on the four different samples from the Marcabelí pluton. Of these, 199 analyses were either older than 270 Ma or not concordant, leaving 514 valid analyses. These comprised 338 with a 16 µm spot size and 176 with a 30 µm spot size. With regard to the granitoid sample from La Palmerita, 195 analyses were performed. Following the filtering process, 30 analyses were retained, comprising 28 analyses of 16 µm spot size and 2 of 30 µm spot size. This high number of filtered analyses can be attributed to the presence of very thin rims, from which mixed analyses produced discordant ages, and a high portion of old inherited cores. The Terra-Wasserburg diagrams of the concordant dates of each granitoid sample are reported in the supplementary material (Fig. A.1.2).

The results of the $^{206}Pb/^{238}U$ dates are presented as KDEs for the four samples of the Marcabelí plu-

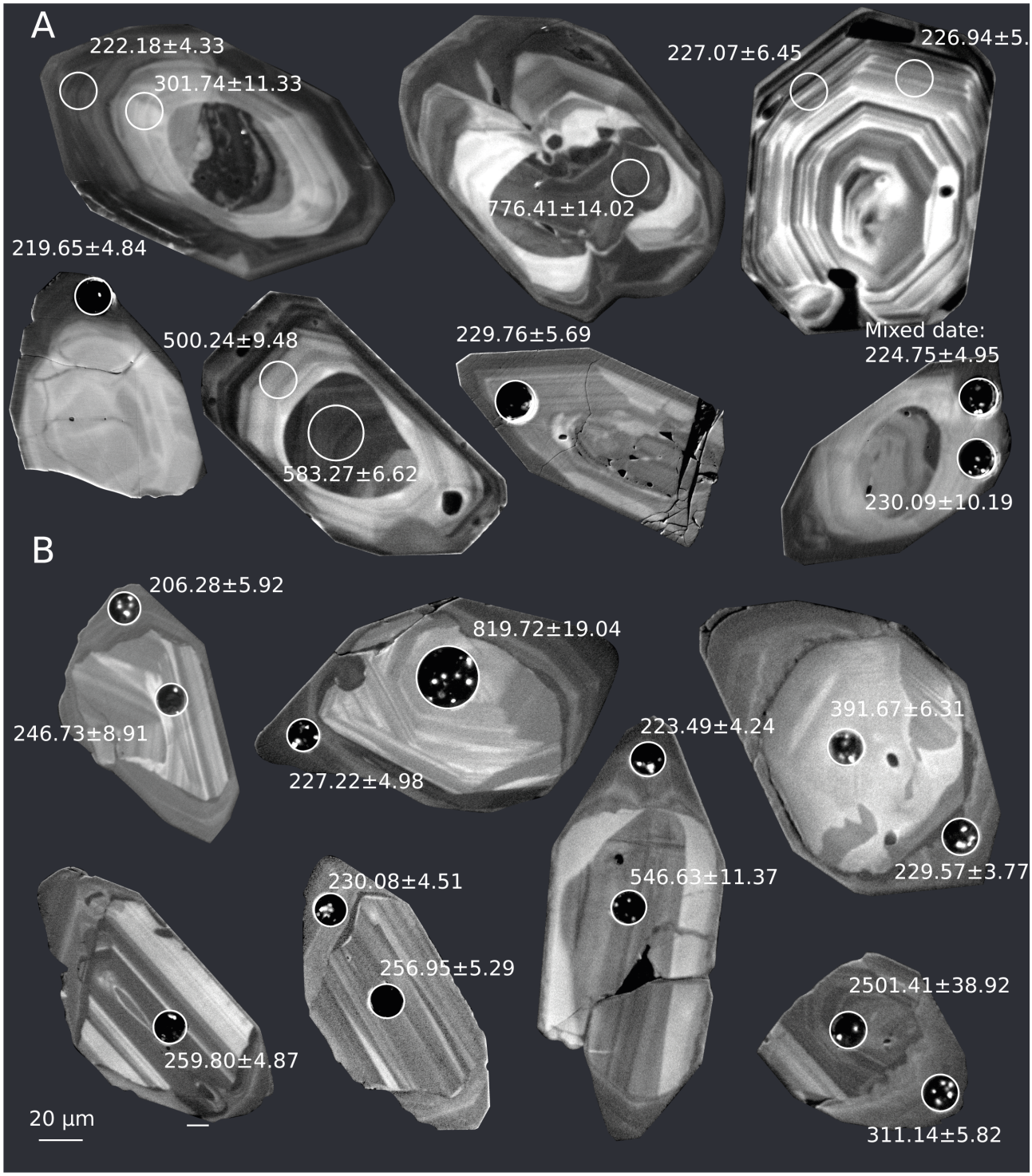


**Figure 3:** Representative zircon cathodoluminescence (CL) and charge contrast images of the igneous samples of the Marcabelí pluton (A) and La Palmerita granitoid (B). Zircons on all samples show multiple generations of inherited cores. Zircons from the Marcabelí pluton show bright to light CL rims with oscillatory zoning, sometimes rimmed by a dark-CL homogeneous overgrowth. Zircons from La Palmerita sometimes present cores with dates bellow 270 Ma, overgrown by a CL-grey rim.

ton in Fig. 4.A. The combined results for these four samples as a single population, as well as the results for the granitoid sample from La Palmerita, are presented in Fig. 4.B. In general, zircons show distinct populations which can be identified in their trace element patterns; those with high Th/U ratios (>0.1), higher rare earth element (REE) contents, and shallower REE slopes (i.e., low Ce/Lu ratios), and those with lower Th/U ratios (<0.1), slightly lower REE contents, and steeper REE slopes (higher Ce/Lu ratios). For samples with a high number of dark-rim analyses, age populations can be separated based on these geochemical characteristics, for example quartz monzonite sample EOMP-01 (for further details, see below and Figs. 5 and 6). The weighted mean calculated for this sample from the Marcabelí pluton are 226.40 ± 1.42/2.90/7.66 (MSWD = 4.97, $n$ = 59) and 230.41 ± 0.98/2.75/6.41 (MSWD = 2.79, $n$ = 107) Ma for Th/U ratio < and > 0.1, respectively. The other quartz monzonite sample, EOMP-23, yielded a weighted mean of 230.06 ± 1.43/2.94/6.6 Ma. The two other weighted means from the monzogranite and granodiorite samples are 226.61 ± 1.51/2.94/9.17 (MSWD = 7.65, $n$ = 69) and 228.51 ± 0.82/2.68/6.26 (MSWD = 3.84, $n$ = 144) Ma for EOMP-10 and EOMP-22, respectively. The combined weighted mean of all samples is 228.48 ± 0.71/2.65/7.93 (MSWD = 4.25, $n$ = 432) Ma for the Marcabelí pluton. The weighted mean of the sample of La Palmerita granitoid EOLP-05 is 231.94 ± 2.34/3.49/9.12 (MSWD = 6.29, $n$ = 24) Ma. Overall, the weighted means of the five samples are within uncertainty with each other and exhibit a very high dispersion-related uncertainty, ranging from 9.12 to 7.8 Myr, even for samples with a very high number of analyses.

The results of Ti-in-zircon thermometry using the calibration of Ferry and Watson (2007) are shown in Fig. 5.A for the Marcabelí and La Palmerita granitoids. Chondrite-normalised zircon REE patterns ($REE_N$) for the four samples of the Marcabelí pluton and EOLP-05 are shown in Fig. 6. The U/Th ratios vs $^{206}Pb/^{238}U$ for EOMP-01 and EOLP-05 is shown in Fig. 5.B. For Ti-in-zircon thermometry, $aSiO_2$ was fixed to 1 and $aTiO_2$ was assumed to be 0.5 for EOMP-01, EOMP-10, EOMP-22 and 0.4 for EOMP-23. The presence of Ti-bearing phases in EOMP-01, EOMP-10, EOMP-22 was not directly observed in the samples whereas titanite was found in EOMP-23. However, 0.5 is a recommanded value for $aTiO_2$ in S-type granitoids (e.g. Schiller & Finger, 2019) and ilmenite has been observed in other samples of the Marcabelí granitoids. Ilmenite was found in EOLP-05 and $aTiO_2$ was therefore fixed to 0.5 for La Palmerita granitoid.

Three samples of the Marcabelí pluton (EOMP-10, EOMP-22 and EOMP-23) show relatively uniform $REE_N$ and Ti-in-zircon temperature across the zircon analyses. They show a pronounced negative Eu anomaly and positive Ce anomaly, and a significant enrichment in HREEs relative to MREEs and LREEs. The temperature estimates range mostly between 650 and 850 °C, while the Th/U ratios are comprised between 0.2 and 0.5. The sample EOMP-01 also shows a population following a similar trend for the $REE_N$ but a second population can be distinguished. This population is characterised by a relative enrichment in HREEs, a relative depletion in MREEs and LREEs and a notable Th/U ratio below 0.1.

The temperature estimates show an important degree of variability, between 700 and 920 °C for zircon analyses with Th/U ratios > 0.1 and between 550 and 670 °C for Th/U ratios < 0.1. The zircons from the sample EOLP-05 from La Palmerita granitoid are characterised by a Th/U ratio below 0.1 and show a similar general trend for $REE_N$ with temperature estimates between 580 and 680 °C, approximately. Five analyses deviate from this trend, with enrichment in LREEs and MREEs, particularly Ce, a smaller Eu anomaly, and a Th/U ratio ranging from 0.7 to 1.5, approximately. The Ti-in-zircon temperature also records up to 800 °C, and $^{206}Pb/^{238}U$ dates are older than ca. 235 Ma, making them significantly older than the rest of the analyses.

Trace elements in zircon can also be used to gain information on the chemistry of the host magmas. The discrimination diagram for S-type granitoids from N. Roberts et al. (2024) is showed in Fig. 7 and is based on $\log_{10}$ ratios of Ce/U and Th/U. The zircon analyses from the two granitoids, Marcabelí and La Palmerita, as well as the inherited cores from the diatexites in upper La Bocana (see section below), are plotted. The four samples of the Marcabelí pluton show a pronounced clustering in the domain of hybrid S-types, with $\log_{10}$(Th/U) values between -0.9 and 0.2 and $\log_{10}$(Ce/U) values between -2.8 and -2.5. A significant number of analyses, especially from the sample EOMP-01, also show $\log_{10}$(Th/U) values bellow -1, with an important spread. The sample EOLP-05 from La Palmerita granitoid exhibits a notable clustering in the pure S-type field, with values ranging from -2 to -1.5 for $\log_{10}$(Th/U) and from -3.8 to -3 for $\log_{10}$(Ce/U). The five older analyses from La Palmerita cluster in the same field as the analyses

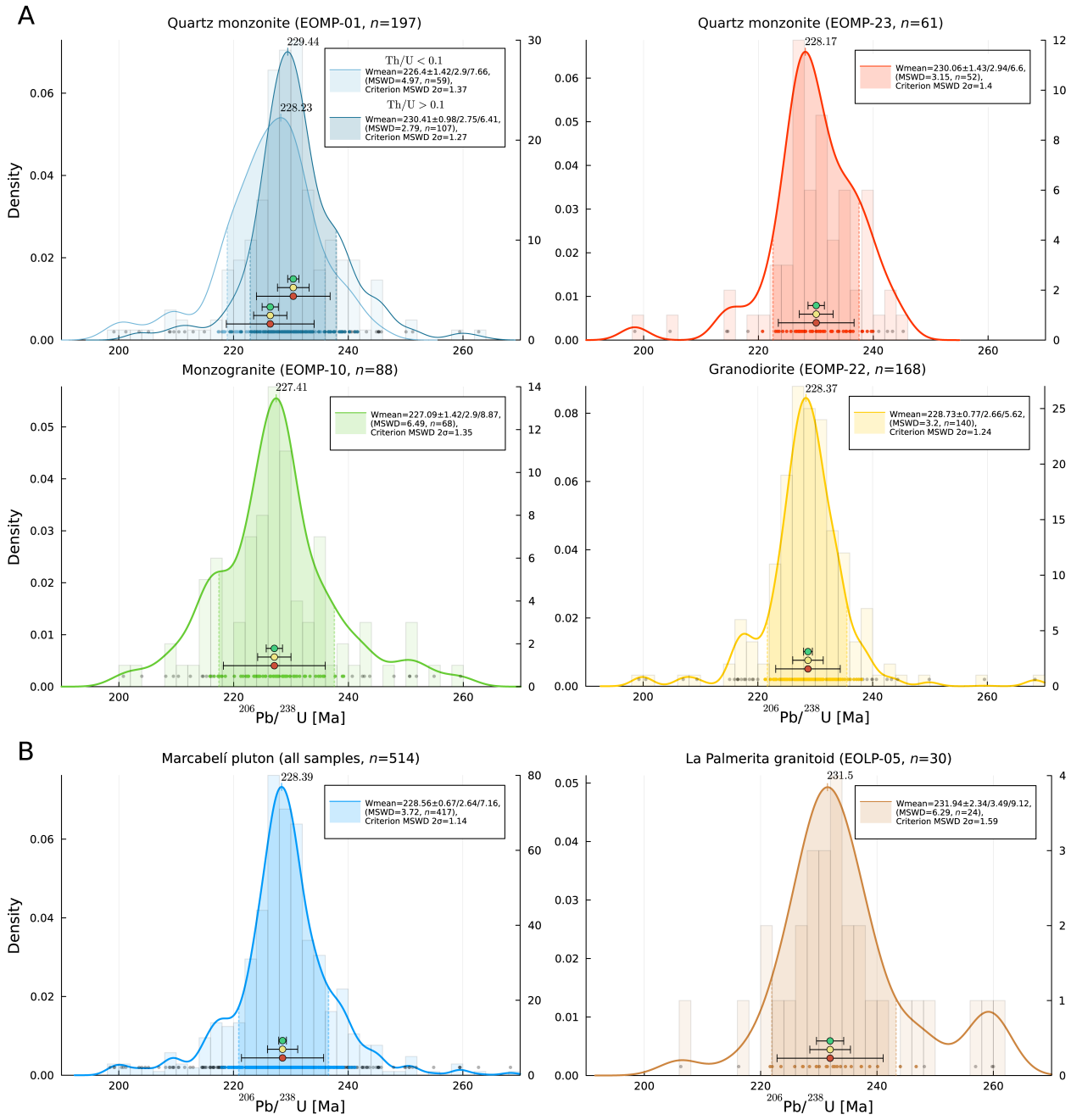


**Figure 4:** Kernel density estimates and histograms of the $^{206}Pb/^{238}U$ dates for the igneous samples. A) Four samples from the Marcabelí pluton. B) All samples from the Marcabelí pluton combined and sample from La Palmerita granitoid. The coloured areas represent the acceptable range at 1σ for the analyses to be included in the weighted mean calculation. These intervals are computed using the median absolute deviation method. Each age is reported with three uncertainties accounting for the contribution of random uncertainties, systematic uncertainties and for statistical dispersion (see Analytical methods part for more details). Uncertainties are reported at 2σ.

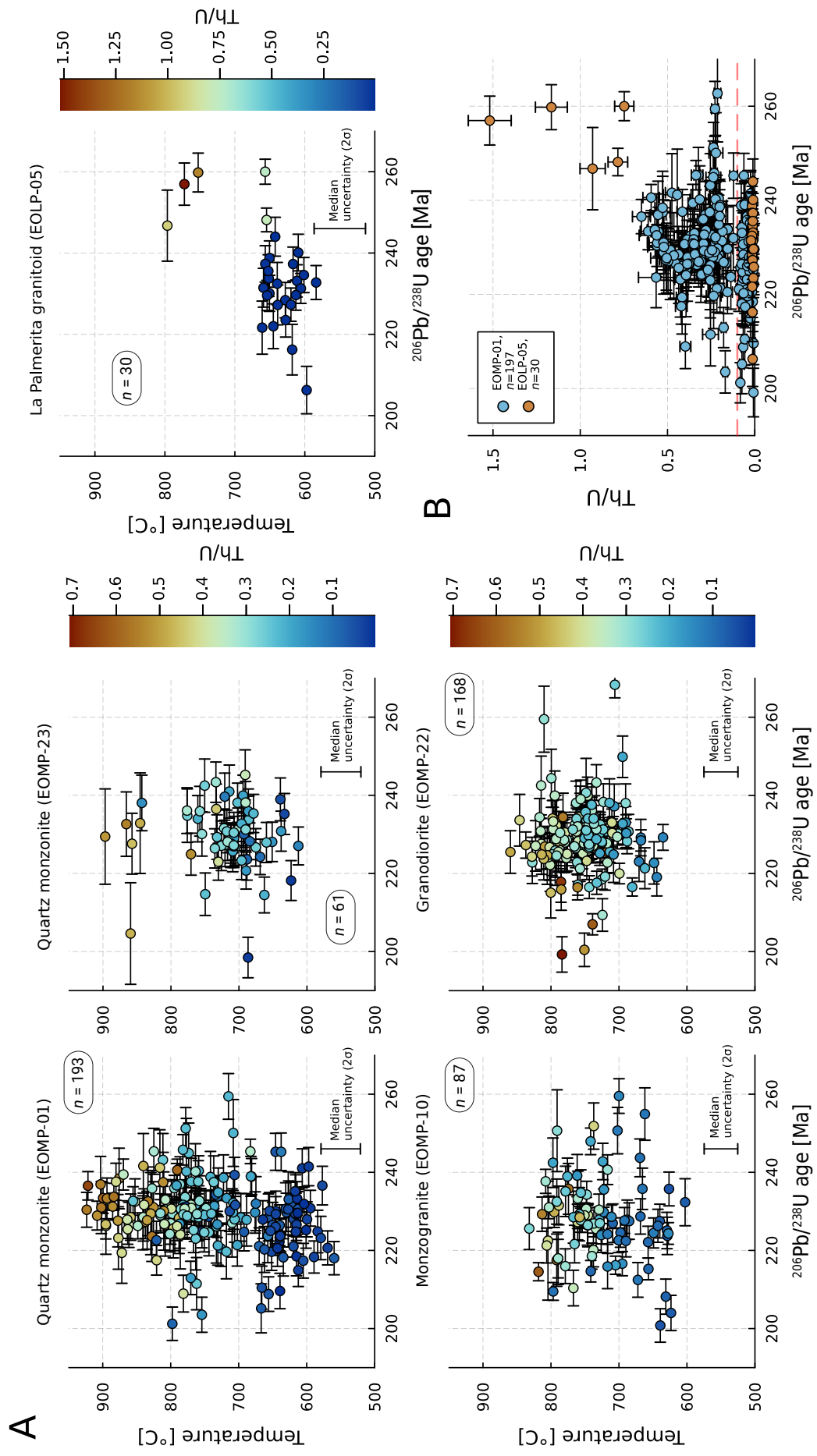


**Figure 5:** A) Ti-in-zircon thermometry vs $^{206}Pb/^{238}U$ dates from the zircon analyses of the igneous samples calculated using the formulation of Ferry and Watson (2007). The activities are assumed to be $aSiO_2 = 1$ and $aTiO_2 = 0.5$ for all samples except EOMP-23 where $aTiO_2$ was fixed to 0.4 due to the presence of Ttn in the sample. The colour bar represents the Th/U ratio. The median uncertainty for the temperature estimate is calculated by propagating the uncertainties from the Ti analyses and from the calibration of Ferry and Watson (2007). B) Th/U ratio vs $^{206}Pb/^{238}U$ dates for the sample of the Marcabelí pluton showing the most variability, and the sample of La Palmerita granitoid. The red vertical dotted line represents the value of Th/U ratio equal to 0.1. All uncertainties are reported at 2σ.

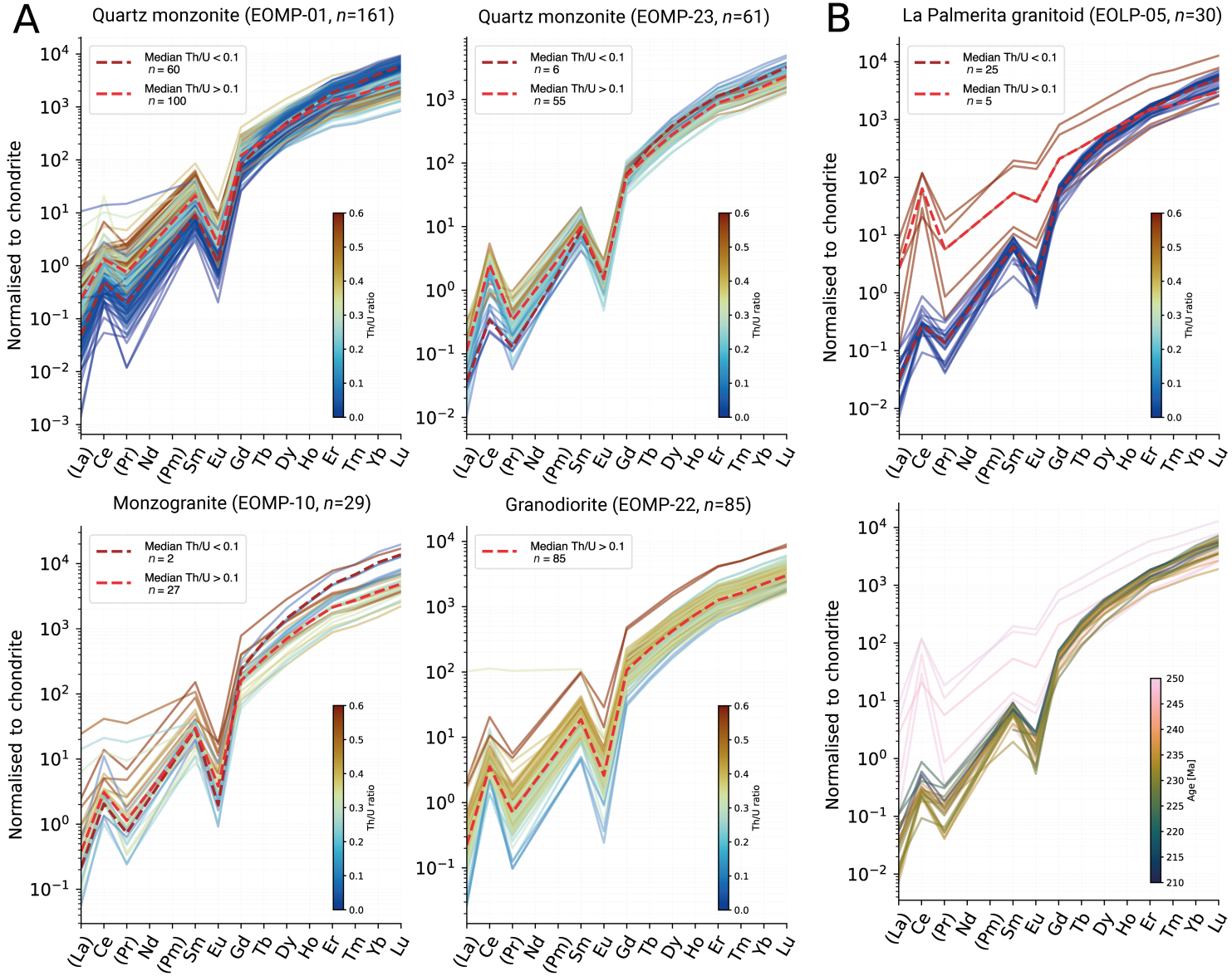


**Figure 6:** Chondrite-normalised REE diagrams of the zircon analyses from the igneous samples. A) Four samples of the Marcabelí pluton. B) Sample from La Palmerita granitoid. The dark and light red dotted lines represent the median calculated for analyses bellow and above 0.1 Th/U ratio, respectively and the colours represent either Th/U ratio or $^{206}Pb/^{238}U$ dates. The values of La, Pr and Pm were not measured and are estimated by extrapolation from the slope of Nd-Sm. These elements are written between brackets. Chondrite values are from McDonough and Sun (1995).

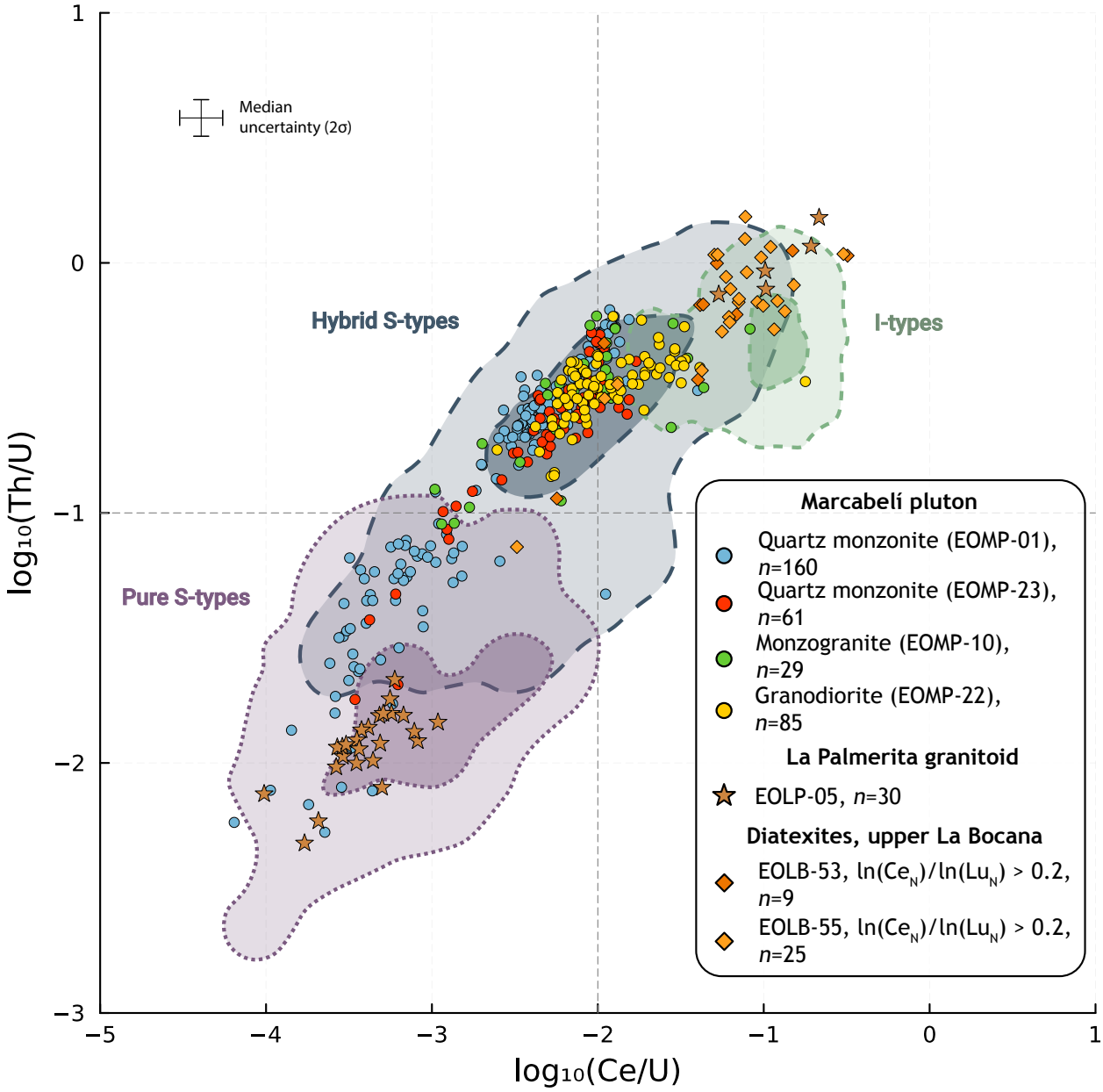


**Figure 7:** Granitoid discrimination diagram using $\log_{10}(Ce/U)$ vs $\log_{10}(Th/U)$ from zircon trace elements based on N. Roberts et al. (2024). The three groups of dark and lighter contours represent 2D KDE envelopes including 50 and 95% of their compiled data for each group, respectively. All the zircon analyses from the igneous samples with Ce measured and the analyses of the diatexites in the upper La Bocana with $\ln(Ce_N)/\ln(Lu_N)$ ratios above 0.2 are reported. The samples from the Marcabelí pluton show strong clustering in the hybrid S-type field, whereas La Palmerita granitoid cluster on the pure S-type field. One sample (EOMP-01) from the Marcabelí shows important dispersion for Th/U ratio bellow 0.1. The five oldest analyses of EOLP-05 and the analyses from EOLB-53 and EOLB-55 with similar ages show similar values, in the overlapping field between hybrid S-type and I-type, or fully in the I-type field.

from the two samples of diatexites that show similar dates and characteristics, within the overlapping field between hybrid S-type and I-type granitoids.

## 5.2. Migmatites from La Bocana

### 5.2.1. Zircon morphology

Zircon grains for the three groups of migmatitic samples from La Bocana show similar sizes and shapes, mostly subrounded or euhedral. Their lengths range between 40 and 300 µm with widths ranging between 20 and 180 µm. The elongation ratios are comprised between around 1.5 and 5. Noticeable differences and characteristics in CL images are observed between the three different groups of samples (Fig. 8). Zircons from upper La Bocana (EOLB-53, EOLB-55, EOLB-08, EOLB-10) often show a CL-dark homogeneous rims around bright cores (Figs. 8A and 8B), whereas zircons from lower La Bocana (EOLB-04, EOLB-37 in Fig. 8C) exhibit larger brighter rims with common oscillatory zoning and sometimes multiple rims recording the same or similar dates. Zircons from the migmatites in upper La Bocana preserve an important proportion of bright cores with dates < 270 Ma which range mostly between ca. 240 and 270 Ma for the diatexites (EOLB-53, EOLB-55) and between ca. 220 and 235 Ma for the leucosomes of metatexites (EOLB-08, EOLB-10).

### 5.2.2. U–Pb and trace element zircon data

The total number of analyses for all the migmatitic samples from La Bocana is 697, from which 338 were discarded due to discordance or dates older than 270 Ma. This represents after filtering 88 analyses for both samples of diatexite, 90 for both samples of the leucosomes from metatexites in upper La Bocana, and 181 analyses for the diatexite samples of lower La Bocana. The Terra-Wasserburg diagrams of the concordant dates of each migmatitic sample are reported in the supplementary material (Fig. A.1.3). The results of the $^{206}Pb/^{238}U$ dates are shown as KDEs for the six samples of migmatites in Fig. 9. Two populations are distinguished for the two samples EOLB-53 and EOLB-55 based on $\ln(Ce_N)/\ln(Lu_N)$ (Fig. 10A). These two populations show also distinguishable CL zoning, Th/U ratios and temperature estimates, supporting this distinction (see below and Figs 8.A and 12.A). The weighted means obtained are 248.21 ± 5.46/6.12/13.27 (MSWD = 15.3, $n$ = 9) and 250.07 ± 3.2/4.24/11.94 (MSWD = 14.72, $n$ = 23) for the oldest population and 226.96 ± 1.81/3.11/5.26 (MSWD = 4.28, $n$ = 20) and 230.98 ± 2.44/3.55/7.43 (MSWD = 6.64, $n$ = 20) Ma for the younger population for EOLB-53 and EOLB-55, respectively. The KDEs for the two samples of metatexite in upper La Bocana show only one population, with a weighted mean age of 227.01 ± 2.07/3.27/8.13 (MSWD = 6.37, $n$ = 32) and 223.87 ± 1.28/2.8/4.78 (MSWD = 3.29, $n$ = 36) Ma for EOLB-08 and EOLB-10, respectively. Similarly, the two samples of diatexite in lower La Bocana shows one population with a weighted mean of 223.6 ± 1.24/2.79/7.35 (MSWD = 3.17, $n$ = 78) and 224.52 ± 1.21/2.78/7.06 (MSWD = 2.86, $n$ = 73) Ma.

Chondrite-normalised zircon REE diagrams for the two samples of diatexite in upper La Bocana (EOLB-53, EOLB-55) are reported in Fig. 10 and $REE_N$ of the samples from the metatexites in upper La Bocana and the diatexites from lower La Bocana are shown in Fig. 11. The results of Ti-in-zircon thermometry using the calibration from Ferry and Watson (2007) are shown in Fig. 12 for the six samples. For Ti-in-zircon thermometry, $aSiO_2$ was fixed to unity due to the presence of quartz and $aTiO_2$ was assumed to be 0.5 for EOBL-08, EOLB-10, EOLB-53 and EOLB-55 and 1 for EOLB-04 and EOLB-37 due to the presence of ilmenite and coexistence of ilmenite and rutile in these samples, respectively.

The $REE_N$ in Fig. 10 for samples EOLB-53 and EOLB-55 show two groups of zircon analyses, both showing a relative enrichment in HREEs compared to MREEs and LREEs and a Ce and Eu anomaly. The first group is enriched in MREES and LREEs, especially Ce, compared to the second group, as shown by ln(CeN)/ln(LuN) > 0.2. This first group represents around 30% of the analyses from EOLB-53 and 50% from EOLB-55. This group also shows higher Ti-in-zircon temperature estimates with temperature ranging between 650 and 900 °C whereas the second group records temperature ranging from 600 to 750 °C (Fig. 12A).

The $REE_N$ from the metatexite samples (EOLB-08 and EOLB-10) show the same general trend of REEs. Two populations are present, with a relative enrichment in LREEs and MREEs but a relative depletion in HREEs which correlates with increasing values in Th/U. Defining the value 0.1 of Th/U as the discriminating factor between the two populations, analyses above 0.1 represents 15% and 44% of the analyses for EOLB-08 and EOLB-10, respectively. This also correlates with temperature estimates, with temperature

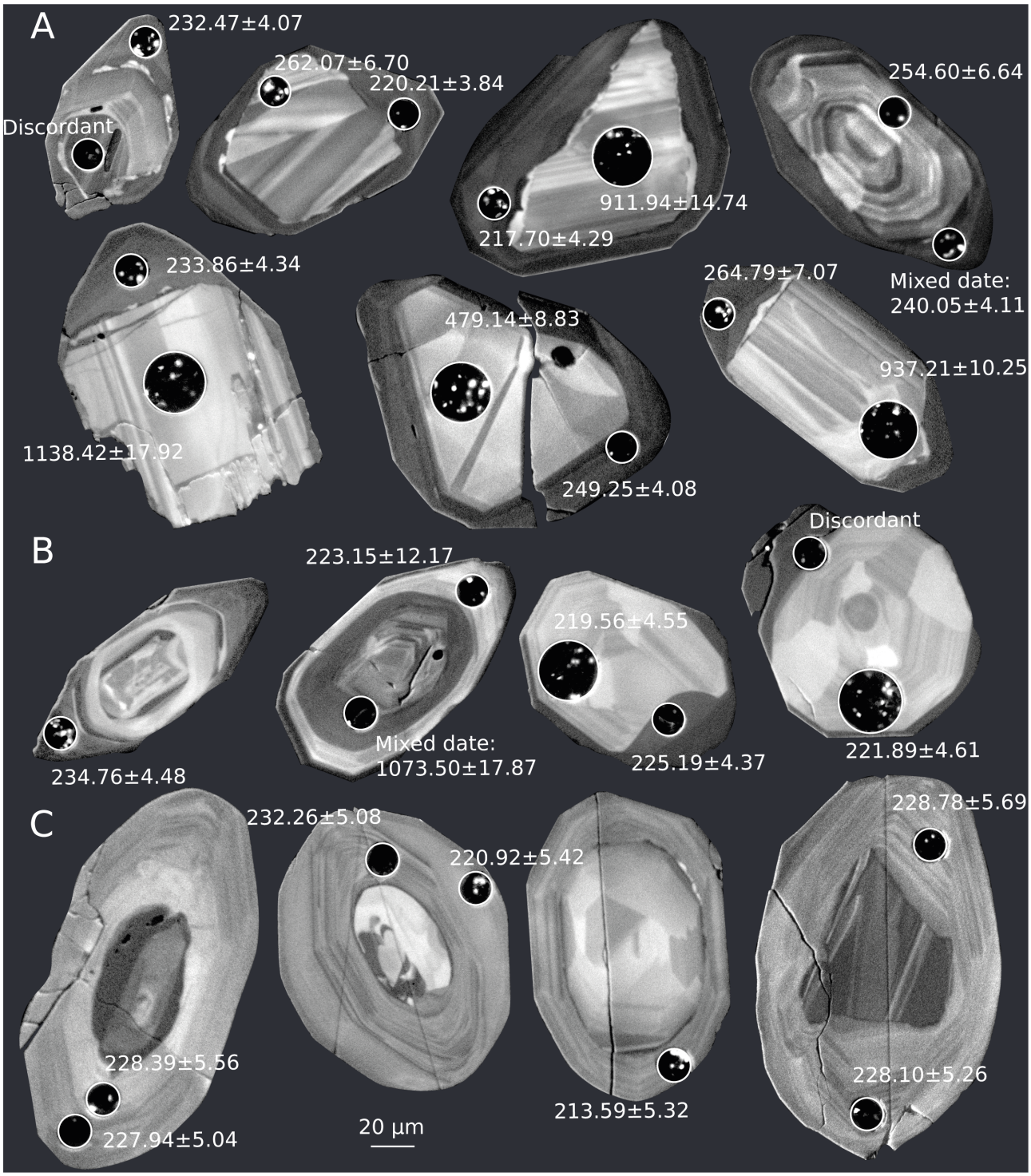


**Figure 8:** Representative zircon cathodoluminescence (CL) of the two samples of diatexites in upper La Bocana (EOLB-53, EOLB-55) (A), of leucosomes in metatexites in upper La Bocana (EOLB-08, EOLB-10) (B) and of diatexites in lower La Bocana (EOLB-04, EOLB-37) (C) with $^{206}Pb/^{238}U$ dates from ICP-MS analyses. Zircons on all samples often show multiple generations of inherited cores. Zircons in (A) present CL-bright cores with dates ca. 240-260 Ma, overgrown by thin CL-dark rims with ages ranging from ca. 220-240 Ma. Zircons in (B) show CL-bright cores with thin CL-dark rims with the same date within uncertainty, ranging from ca. 220-240 Ma. Zircons in (C) have large CL-grey rims showing often oscillatory zoning with dates between ca. 220-240 Ma. Young CL-bright cores and CL-dark rims correlate with Th/U ratio and temperature estimates for (A) and (B), see Fig. 12.

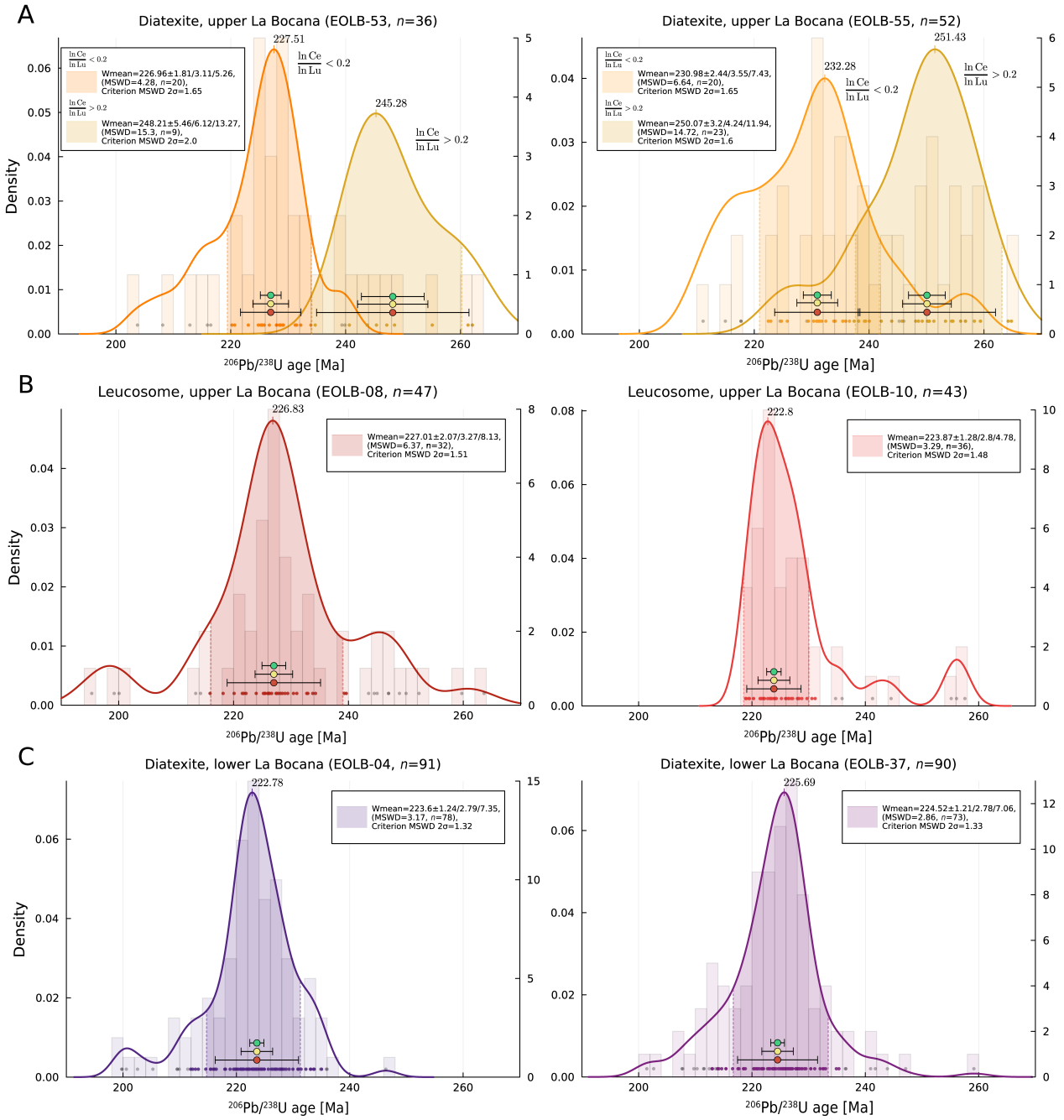


**Figure 9:** Kernel density estimates and histograms of the $^{206}Pb/^{238}U$ dates of the migmatitic samples. A) Two samples from diatexites in upper La Bocana. B) Two samples from leucosomes in metatexites in upper La Bocana. C) Two samples from diatexites in lower La Bocana. The coloured areas represent the acceptable range at 1σ for the analyses to be included in the weighted mean calculation. These intervals are computed using the median absolute deviation method. The colored dots represent the analyses included in that range. The ages are reported with three uncertainties at 2σ: without systematic uncertainty propagation, with systematic uncertainty propagation and with systematic uncertainty propagation plus overdispersion when the MSWD value is higher than the acceptable statistical range at 2σ (see Analytical methods for more details). Two populations are distinguished in A), based on ln(CeN)/ln(LuN) ratios. This also correlates with CL textures, Th/U ratios and temperature estimates (see Figs. 10 and 12).

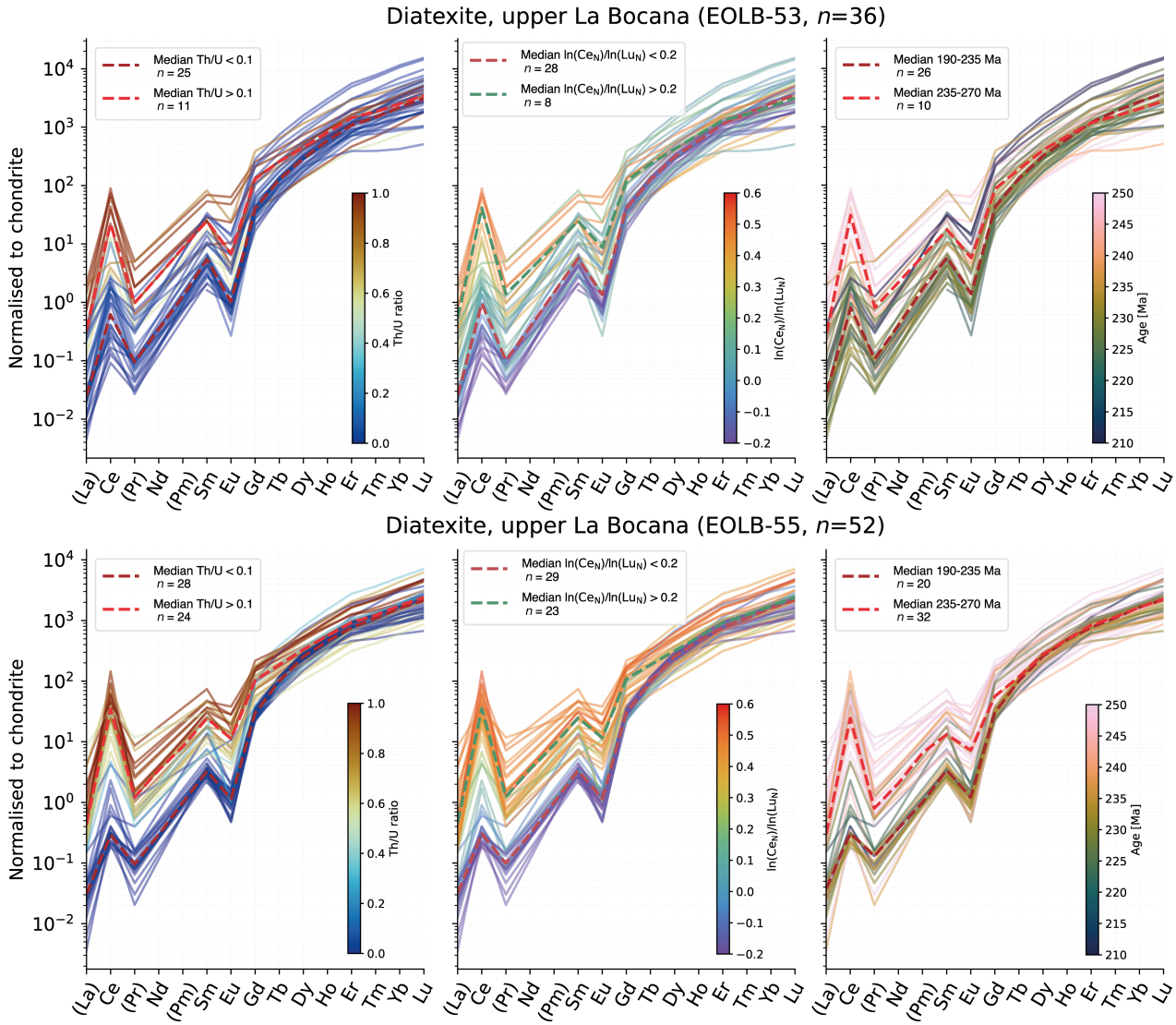


**Figure 10:** Chondrite-normalised REE diagrams of the samples of diatexites from upper La Bocana: EOLB-53 at the top and EOLB-55 at the bottom. Two populations of zircon across both samples show distinguishable $REE_N$ patterns which correlates with Th/U, ln(CeN)/ln(LuN) ratios and $^{206}Pb/^{238}U$ ages. The values of La, Pr and Pm were not measured and are estimated by extrapolation from the slope of Nd-Sm. These elements are written between brackets. Chondrite values are from McDonough and Sun (1995).

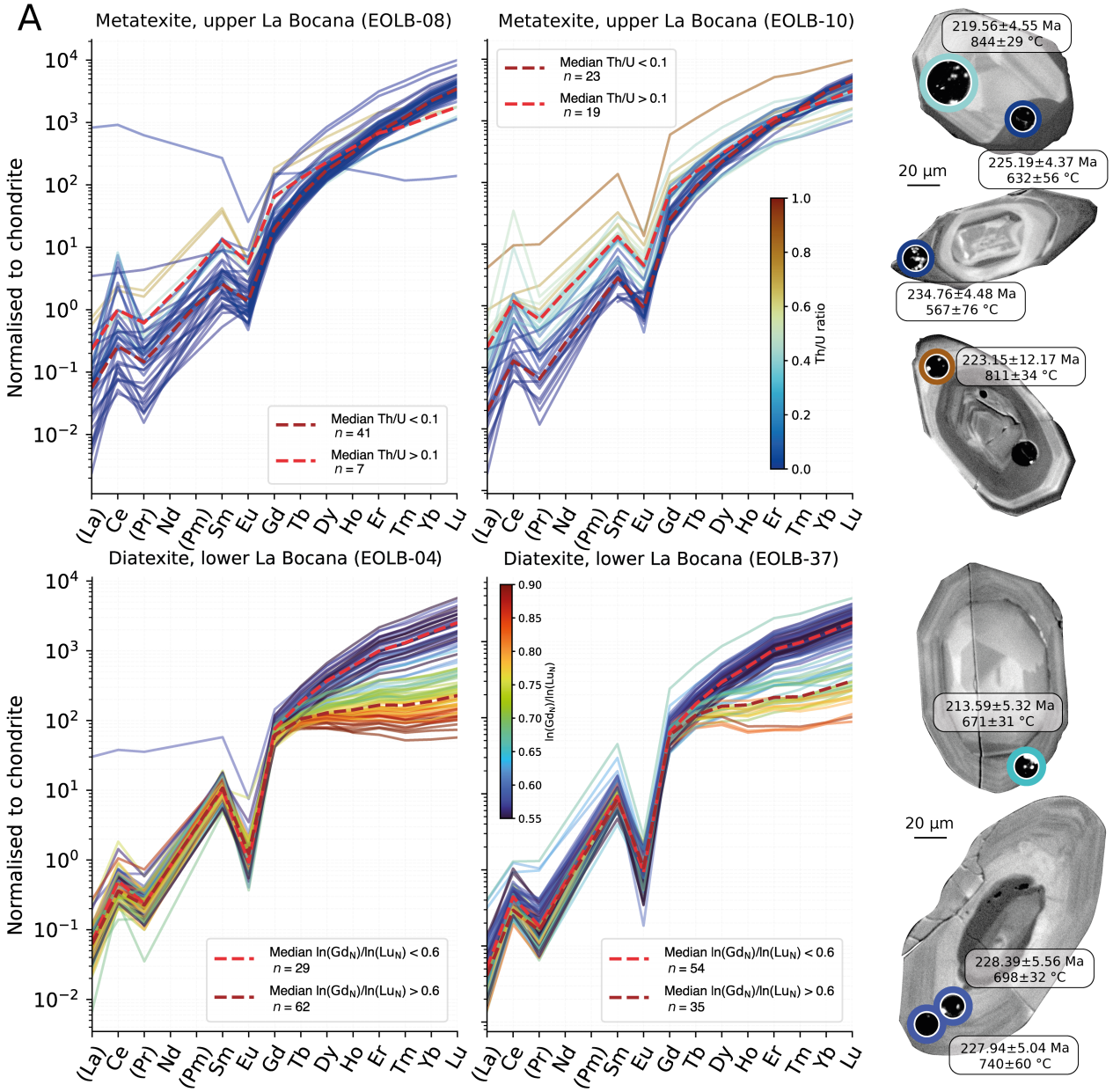


**Figure 11:** Chondrite-normalised REE diagrams of the zircon analyses and corresponding representative CL imaging from the leucosomes of metatexites from upper La Bocana (A) and from diatexites in lower La Bocana (B). (A) shows correlation between $REE_N$, Th/U ratio, temperature estimates and dark and bright CL domains. (B) shows depletion in the $HREE_N$ across the samples and no corresponding systematic in CL imaging, ages and temperature estimates. The values of La, Pr and Pm were not measured and are estimated by extrapolation from the slope of Nd-Sm. These elements are written between brackets. Colours in the CL images correspond to the value of Th/U or $\ln(Gd_N)/\ln(Lu_N)$ for the analyses following the colour bar in the REE diagrams, respectively. Chondrite values are from McDonough and Sun (1995).

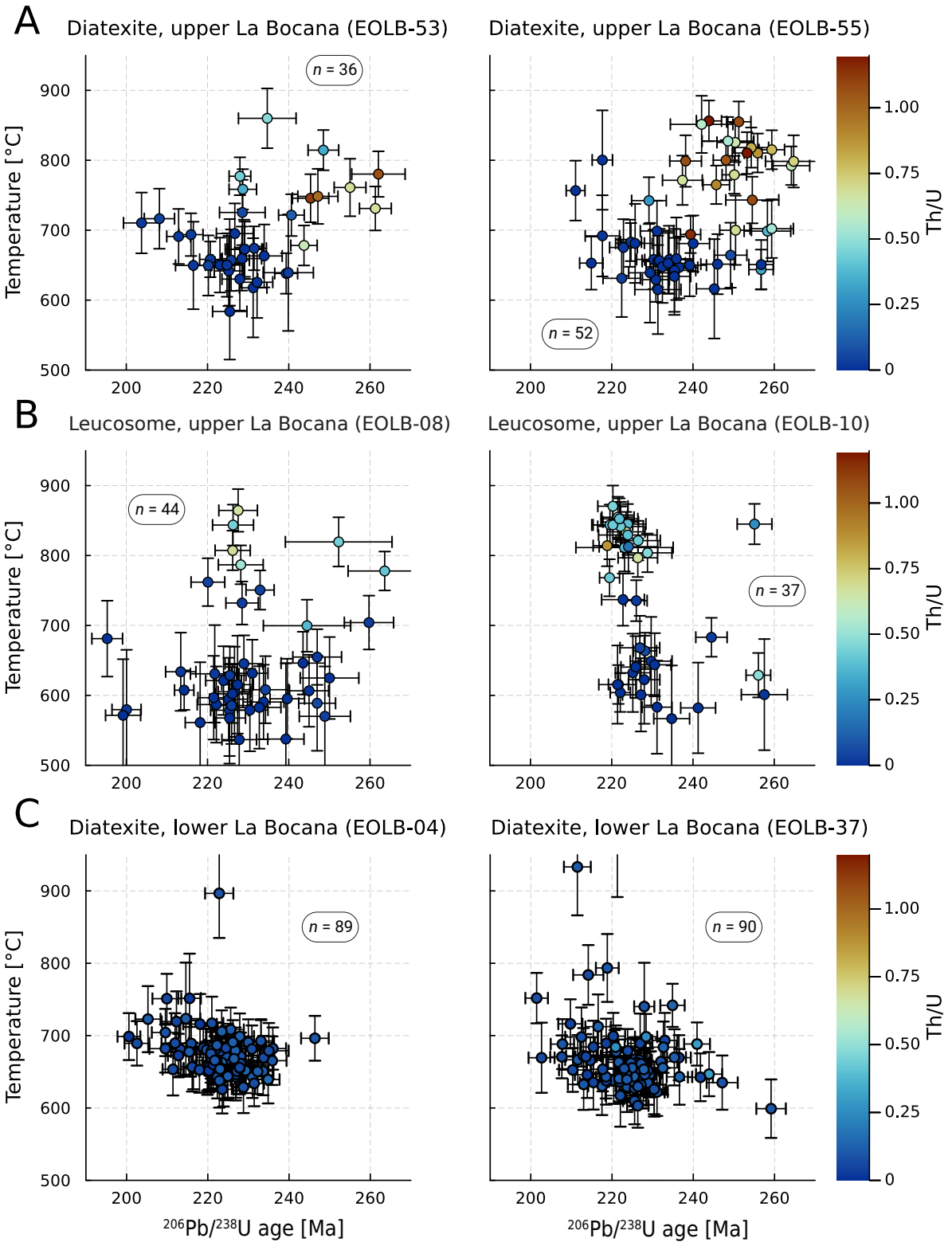


**Figure 12:** Ti-in-zircon thermometry vs $^{206}Pb/^{238}U$ dates from the zircon analyses of the migmatitic samples calculated using the formulation of Ferry and Watson (2007). A) Two samples from diatexites in upper La Bocana. B) Two samples from leucosomes in metatexites in upper La Bocana. C) Two samples from diatexites in lower La Bocana. The activities are assumed to be $aSiO_2 = 1$ for all samples and $aTiO_2 = 0.5$ for A) and B) and 1 for C) due to the presence ilmenite and rutile in the samples, respectively. The colour bar represents the Th/U ratio. The uncertainties for the temperature estimate are calculated by propagating the uncertainties from the Ti analyses and from the calibration of Ferry and Watson (2007). All uncertainties are reported at $2\sigma$.

ranging approximately from 750 to 900 °C and 550 to 700 °C for Th/U > 0.1 and Th/U < 0.1, respectively (Fig. 12B).

The $REE_N$ from the diatexite samples of lower La Bocana (EOLB-04, EOLB-37) show a relatively homogeneous composition of LREEs and MREEs but a range of composition on the HREEs for both samples, demonstrated by the $\ln(Gd_N)/\ln(Lu_N)$ ratio, with 97 over 180 analyses with value below 0.6 for both samples combined (Fig. 11B). This is commonly interpreted in metamorphic zircons as showing the influence of garnet growth concurrent or prior to zircon growth (e.g. Kohn & Kelly, 2018). The temperature estimates show a well-defined population ranging from 600 to mostly 750 °C for both samples (Fig. 12C).

The temperature estimates from Ti-in-zircon of all migmatitic samples are combined on a simplified *P–T* diagram showing the main melting reactions of a metapelitic composition (Fig. 13). The pressure is estimated by extrapolation from the localities of previous peak *P–T* estimates (Riel et al., 2013; Riel et al., 2016). The zircon analyses with Th/U ratios < 0.1 show temperature consistently bellow or within the lower uncertainty of the peak temperature of close samples, whereas analyses with Th/U ratios > 0.1 (with contour in red) are within the uncertainty or above the peak temperature estimates. The metatexites (samples EOLB-10 and EOLB-08) also show low temperature estimates around 550 and 600°C which are not within uncertainty above the wet solidus.

## 5.3. Metagabbro from Piedras

### 5.3.1. Titanite morphology

The selected titanite grains are mostly transparent and slightly yellow in colour with irregular and rounded shapes. Their sizes are ranging from 300 to 500 µm. The grains are homogeneous in composition without any observed sector zoning on back-scattered images (BSE) and sometimes contain zircon or rutile inclusions (Fig. 14C).

### 5.3.2. U–Pb and trace element titanite data

The total number of analyses after data reduction was 94 and no filtering was applied. The analyses for EOPD-03 yield an isochron age at 227.5 ± 4.5 (*n* = 94) Ma with a dispersion of 0.56 ± 0.23 Ma (Fig. 14A). Zr-in-titanite temperature estimates using the calibration of Hayden et al. (2008) show temperature ranging mostly between 710 and 750 °C assuming a pressure of 0.8 GPa and with activities $aSiO_2$, $aTiO_2$ and aZr set to unity due to the presence of quartz, rutile and zircon in the sample (Fig. 14B).

# 6. Discussion

## 6.1. Interpretation of zircon U–Pb and trace element data

The calculation and interpretation of zircon U–Pb ages from S-type granitoids and migmatitic systems can be challenging. Geological specificities, such as the high degree of detrital inheritance, increasing the risk of analytical mixing of different age zones during ablation of the grains, and the potentially long-lived nature of melting and (re)crystallisation processes need to be accounted for. Additionally, common issues with the U–Pb system in zircons, such as Pb-loss, also require consideration. In particular, concealed Pb-loss, where analyses show false concordance due to the positive correlation of the analytical uncertainties between $^{206}Pb/^{238}U$ and $^{207}Pb/^{235}U$, from which the slope follows the Concordia line, is of concern (e.g. T. Andersen et al., 2019). When calculating weighted mean ages from individual zircon analyses of a single event, it is possible to interpret the statistical dispersion in the dates as a combination of these processes (see Fig. 15). This dispersion can be estimated by the value of MSWD. Datasets with MSWD values higher than the acceptable statistical upper limit at 2σ indicate dispersion exceeding what is explainable by analytical uncertainties alone. Some of these processes only mainly contribute to decrease (e.g., Pb-loss) or increase (e.g., mixing with inherited cores) the date of individual analyses, hindering interpretation by adding meaningless dispersion relative to the geological processes of interest. On the other hand, some of these processes convey meaningful information, which can be termed as geological dispersion. Estimating the contribution of the analytical dispersion and the geological dispersion is challenging. There is increasing evidence that the geological dispersion in magmatic systems is beyond instrumental uncertainties and that it cannot be attributed to Pb-loss or inheritance alone, regardless of the analytical method applied (e.g. Miller et al., 2007; Schmitt et al., 2023). Based on this, the scatter in dates observed in granitic and migmatitic samples, when sufficient analyses are present, can be interpreted as containing meaningful

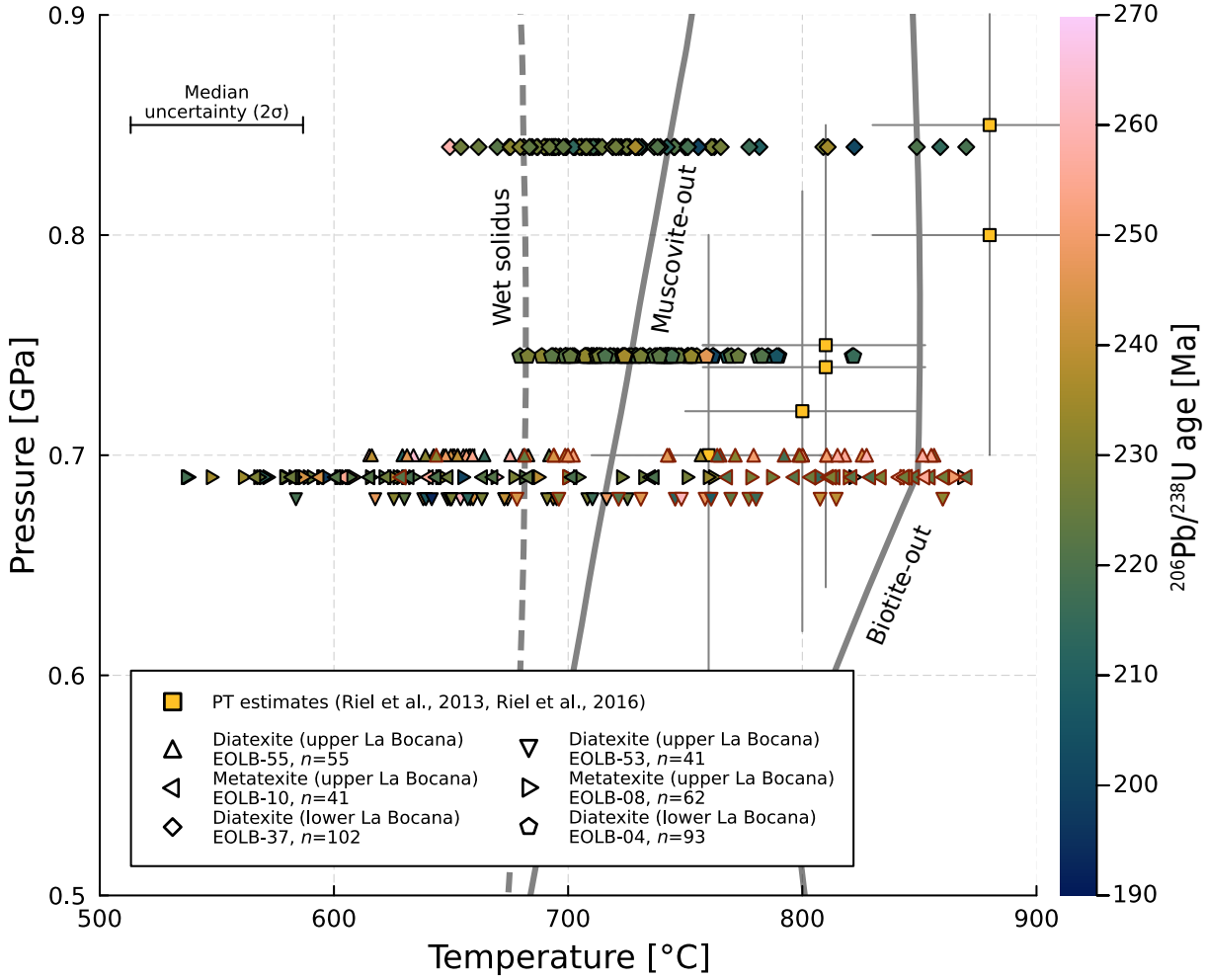


**Figure 13:** Zircon temperature record in migmatitic samples. Simplified pressure-temperature diagram showing the main melting reactions for a metapelitic composition from Johnson et al. (2021). Each point corresponds to the temperature estime from a concordant zircon analysis of a migmatitic sample using Ti-in-zircon (Ferry & Watson, 2007). Pressures for the zircon analyses are estimated by extrapolation from the *P–T* estimates of Riel et al. (2016) and Riel et al. (2013), based on the locations of the samples from the *P–T* estimates and hence have a similar uncertainty. The colour bar represents the corresponding $^{206}Pb/^{238}U$ dates of the analyses. Red contours of the analyses indicate Th/U ratios greater than 0.1.

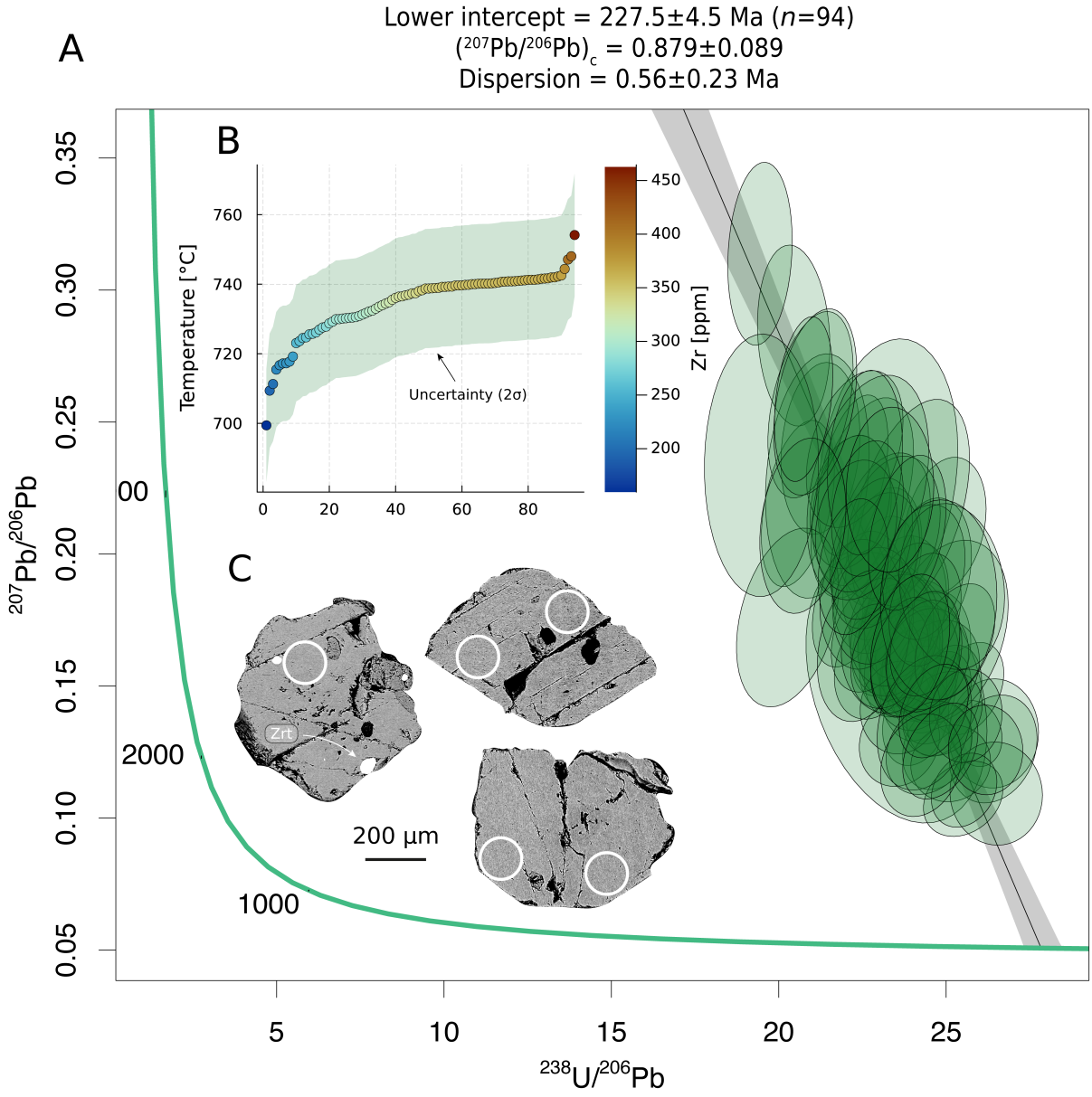


**Figure 14:** A) U–Pb titanite isochron age from the metagabbro sample EOPD-03 of the Piedras unit, calculated using IsoplotR (Vermeesch, 2018). Ellipse uncertainties are reported at 2σ. The lower intercept yields an age of 227.5 ± 4.5 Ma with a dispersion of 0.56 ± 0.23 Ma. B) Zr-in-titanite temperature estimates using the calibration from Hayden et al. (2008). The pressure is assumed to be 0.8 GPa. The activities $aSiO_2$, $aTiO_2$ and aZr set to unity due to the presence of quartz, rutile and zircon in the sample. C) Representative back scattered images of titanite grains analysed, with positions of spot sizes of 64 µm. Zircon and rutile are sometimes present as inclusions in the titanites.

geological information. The contribution of dispersion is quantified by adding an overdispersion term in the calculation of the third uncertainty reported for each weighted mean (see Analytical methods for more details). This uncertainty contains the contribution of both geological and non-geological dispersion and represents the total uncertainty needed for the weighted mean to reach an acceptable MSWD in the statistical sense.

Another key aspect for interpreting U–Pb ages is to understand at which stage zircons form. In metapelitic migmatites, zircon is expected to grow during the crystallisation of anatectic melt and not during the prograde metamorphic history (M. P. Roberts & Finger, 1997; Rubatto et al., 2006; Schaltegger et al., 1999). This is explained by the fact that the concentration of Zr needed in the melt to reach saturation increases with temperature, as predicted by zircon solubility models based on experiments (Boehnke et al., 2013; Crisp & Berry, 2022; Watson & Harrison, 1983). This effect is particularly important with increasing melt fraction as temperature increases in a partially molten rock, as more inherited or prograde zircons would be required to be dissolved to insure that Zr concentration in the melt stay in equilibrium with the rock, due to the relative proportion of melt compared to the rock (Kelsey et al., 2008; Kohn et al., 2015). Therefore, zircon growth during heating is difficult, and preservation would require entrapment within peritectic minerals (e.g. Yakymchuk, 2023). In granitoids, the same ideas apply, and zircon crystallisation occurs during the cooling phase of the intrusion. One additional factor that may play a more important role if different granitoids are compared, is the composition of the melt, as zircon solubility models also predict that the compositional parameter *M*, which is the cation ratio on anhydrous composition [Na + K + 2Ca] / [Al + Si], is an important variable (Boehnke et al., 2013; Watson & Harrison, 1983). As a result, the concentration of Zr required to achieve saturation is greater for intermediate melts (with high M values) compared to more felsic melts (with low M values). For felsic melts in granitoids, zircon growth has been shown to follow a continuous asymmetric distribution from temperatures between 900 and 600 °C (e.g. Keller et al., 2017; Samperton et al., 2017).

Spatially combining these data with trace elements allow populations to be distinguished on the basis of geochemical signatures and provide additional constraints on the conditions of zircon crystallisation. In particular, REEs elements have been used to infer the influence of other minerals during zircon growth, such as HREE depletion due to garnet (Rubatto, 2002), LREE depletion due to monozite, titanite or allanite (e.g. Rubatto et al., 2009) or the negative Eu anomaly (Eu*), linked to feldspar (Hinton & Upton, 1991; Schaltegger et al., 1999). The Eu* in conjunction with the positive Ce anomaly (Ce*) have also been used to infer the redox state of the magma from which zircon is crystallising, as $Eu^{2+}$ and $Ce^{4+}$ would be incompatible or preferably incorporated in the $Zr^{4+}$ site, respectively (e.g. Ballard et al., 2002; Murali et al., 1983; Trail et al., 2012). The U/Th ratio has also been used extensively to distinguish between magmatic (U/Th > 0.1) and metamorphic zircons (U/Th < 0.1), also because of the availability of U and Th data (e.g. Rubatto, 2017). It can be linked to multiple factors, such as presence of minerals with high or low Th/U ratio such as monazite, titanite, allanite, apatite or xenotime, equilibrium vs. disequilibrium behaviour, open system behaviour or aqueous fluid interaction (e.g. Rubatto, 2017; Yakymchuk et al., 2018). This distinction presents limitations with S-type granitoids, as their source is metasediments and they may also present low U/Th ratios (e.g. N. Roberts et al., 2024, and Fig. 7) but is mostly valid for metapelitic migmatites, except at UHT. Another trace element of interest in zircon is Ti with its use as a thermometer with Ti-in-zircon temperature estimates (e.g. Ferry & Watson, 2007). Titanium diffusion in zircon has recently been shown to be unlikely to occur below 800 °C (Bloch et al., 2022). The fact that maximum temperatures recorded of ca. 850–900 °C for several samples (Figs. 5A, 12A and B) may indicate a maximum closing temperature of Ti ca. 900 °C for this metamorphic sequence, supported by large zircon sizes between 200 and 300 µm, and may suggest a fast cooling rate. For REEs, their closure temperature is estimated to be above 1000 °C (Cherniak et al., 1997). Pb closure temperature is also generally estimated to be above 900 °C (Cherniak, 2010; Cherniak & Watson, 2001). This supports that temperature estimates, REEs patterns and $^{206}Pb/^{238}U$ dates can be interpreted together for each sample assuming no metamictisation, with caution for temperature estimates around 900 °C, as these could be cooling temperatures for Ti.

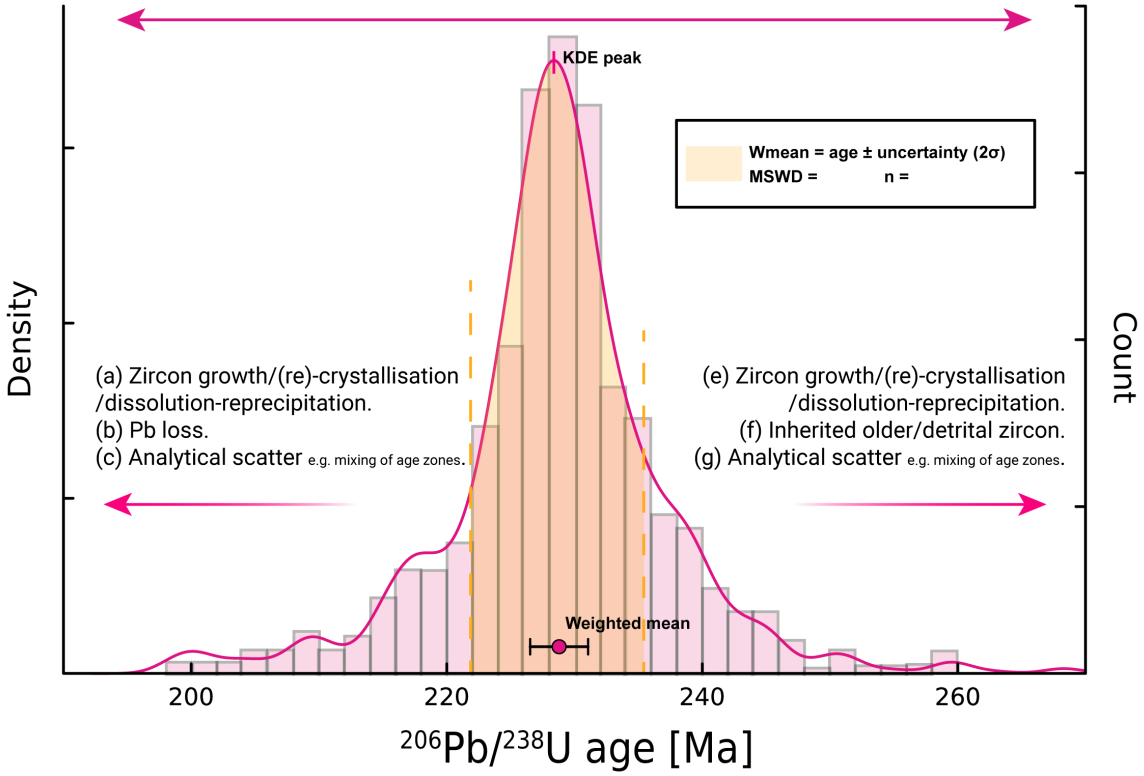


**Figure 15:** Conceptual kernel density estimate (KDE) and histogram of zircon analyses showing the possible contributions for the observed statistical dispersion on the right and on the left of the KDE peak.

## 6.2. Long-lived emplacement of plutons in the El Oro complex

The KDEs of the granitoid samples show a wide spread in $^{206}Pb/^{238}U$ ages, ranging from ca. 20 Myr. As a consequence, some of the calculated weighted means have high MSWDs with respect to the number of analyses, such as sample EOMP-10 with a MSWD of 6.49 for 68 analyses. These ages represent the peak of zircon crystallisation in each sample and are in good agreement with the peak of the KDEs (Fig. 4), but are not statistically compatible with a single population. Consequently, the age of 228.48 ± 0.71/2.65/7.93 (MSWD = 4.25, $n$ = 432) Ma, calculated by combining the four samples of the Marcabelí pluton can only be interpretated as the most probable zircon crystallisation time at the pluton scale based on four samples. The sample of quartz monzonite EOMP-01 shows the greatest variability, with two populations based on CL images and trace element data (Fig. 3A). Although there is an overlap in age between the two populations, the youngest population is interpreted to represent the final stage of crystallisation of zircon grains, based on the lowest temperature estimates recorded, between about 580 and 680 °C, and Th/U ratios < 0.1, whereas the older population, showing oscillatory zoning, is interpreted to have crystallised at a higher temperature, with a higher melt fraction, based on the higher temperature estimates, between about 700 and 900 °C, and the Th/U ratios > 0.1. Ti-in-zircon temperature estimates below the wet solidus (i.e. 680 °C, Fig. 5) are most likely the result of low Ti contents in the final vestiges of melt during zircon crystallisation, or as a result of poor equilibrium between the zircon and surrounding melts in the final cooling stages. Therefore, we propose that they reflect Ti-unbuffered conditions during cooling of the pluton. The overlap in dates between the two populations, the high MSWD compared to the statistically acceptable MSWD at 2σ, and the dispersion uncertainty calculated for each population, show that they are not statistically compatible as a single population based on age alone. This dispersion is interpreted as too high to be solely caused by non-geological dispersion. We propose that this dispersion represents multiple pulses of melt into the pluton, with several cooling stages, lasting for ca. 20 Myr. The range of dates in the zircons then represents different generations of zircons, i.e. antecrysts, preserved from previous magmatic pulses. The high

uncertainty of individual analyses and the fact that laser ablation sampling provides an integrated age are expected to mask the signal of individual pulses. Pulses of melt/crystal injection into the pluton would result in short heating and cooling events, rather than one large long-lived heating and cooling event. This is supported by the absence of a prominent contact aureole in the field, which would be expected if the Marcabelí pluton had been emplaced at high temperatures for 20 Myr. Furthermore, the fact that the four samples of the Marcabelí pluton show a similar spread in ages, which does not seem to be influenced by the sample type, show that these long-lived injections are recorded at the pluton scale. For the La Palmerita granitoid, the number of analyses does not allow to reach a definitive conclusion, but the obtained weighted mean of 231.94 ± 2.34/3.49/9.12 (MSWD = 6.29, $n$ = 24) Ma also shows a very high MSWD and dispersion uncertainty, suggesting a similar history. In addition, Vinasco Vallejo (2004) reports two ages for the La Florida pluton, located 15 km to the NW of the Marcabelí pluton (Fig. 1). These two ages, 239.6 ± 7.3 Ma (MSWD = 1.3, $n$ = 9) and 215.5 ± 7.8 Ma (MSWD = 0.35, $n$ = 3), are interpreted as being part of a same event with multiple pulses which is masked by under-sampling due to the small number of analyses. These two ages support the idea of a long-lived magmatic event of ca. 20 Myr on the scale of the El Oro complex, between ca. 220 and 240 Ma.

Regarding the chemistry of the melts responsible for the Marcabelí pluton and the La Palmerita granitoid, the trace element chemistry of the zircons suggests a slightly different source, with the Marcabelí pluton having a I-type component with an S-type signature, supported by the presence of hornblende in the field and multiple mafic enclaves, whereas the La Palmerita granitoid has a pure S-type composition, with no evidence of an I-type signature (Fig. 7).

If we compare the estimated duration of pluton emplacement with other systems, it appears than most plutons are emplaced on very short timescales, on the order of ca. 100 thousand years up to a few million years, based on TIMS analyses (Coleman et al., 2004; Matzel et al., 2006; Michel et al., 2008; Samperton et al., 2015; Schoene et al., 2012; Wotzlaw et al., 2013). The different timescales of different plutons, when compared, have shown a positive correlation with the size of the pluton considered, which has been interpreted to show that plutonic magmatic fluxes appear to be comparable from one geological context to another (De Saint Blanquat et al., 2011). As the Marcabelí pluton is probably an intermediate size pluton, based on the 2D exposed current surface, a lifetime of 20 Myr may be questionable. This observation is not irreconcilable with our interpretation. As such, individual pulses with significant amount of melt could be on the order of 100 thousand years, while periods of relatively low melt fluxes could be much longer. As the main melt source in this case is crustal, the amount and the duration of melt extraction is controlled by the advancement of melt producing dehydration-reactions. As no major deformation and tectonic phase is observed at the scale of the El Oro complex during the metamorphic event, it is likely that melt could continue to be emplaced in the same plutons. Thus, the major plutons could be reactivated throughout the duration of the anatexis during metamorphism, as long as melt extraction and transport occurs. Due to the high uncertainty of individual dates compared to TIMS analysis, it is expected that individual pulses would be masked, resulting in a dispersion in dates.

## 6.3. Evidence for an older magmatic event and open system behaviour in migmatites from upper La Bocana

The samples from upper La Bocana show similar weighted means for analyses with Th/U ratios < 0.1, with ages ranging from 230.98 ± 2.44/3.55/7.43 (MSWD = 6.64, $n$ = 20) to 223.87 ± 1.28/2.8/4.78 (MSWD = 3.29, $n$ = 36) Ma, indicating a melting event of ca. 15 Myr with a significant dispersion, between 220 and 235 Ma. The two diatexite samples (EOLB-53 and EOLB-55) from upper La Bocana show older zircon dates, which correlate with trace element data and temperature estimates (Figs. 9A, 10 and 12A). This population shows dates ranging from ca. 240 to 260 Ma with a very high dispersion and a similar signature compared to the older La Palmerita analyses (Figs. 5B and 6B). These analyses from both the La Palmerita granitoid and these migmatites both show a similar signature in the overlapping field between hybrid S-type and I-type (Fig. 7). The fact that no older inherited cores were observed in grains containing this signature support the I-type hypotheses (Figs. 3B and 8A). The dates recorded are younger than the depositional age estimated for the upper part of the sequence, El Tigre (maximum ca. 310 Ma), and are evidence of a past post-depositional event, further discussed in section 6.6. The fact that both the La

Palmerita granitoid and some migmatites from upper La Bocana show the same signature of zircons, unrelated to the melting event of their emplacement, indicates that part of the melt source of the La Palmerita granitoid comes from similar migmatites. This establishes a link between the upper La Bocana diatexites and the La Palmerita granitoid.

The two samples from leucosomes of metatexite, EOLB-08 and particularly EOLB-10, also show a population with a high Th/U ratio, distinct trace element signature and CL textures, but with similar dates to the other low Th/U analyses from these samples (Figs. 8B, 12B). These high Th/U analyses record temperature estimates between 800 and 900 °C, higher than what the local rocks are estimated to have experienced at peak conditions, due to the absence of peritectic garnet in the area and *P–T* estimates from previous studies (Fig. 13 and Riel et al., 2013; Riel et al., 2016). This absence of garnet has been interpreted as evidence that the main melting reaction in upper La Bocana is Ms break-down, which should occur below ca. 720 °C at these pressure conditions (Riel et al., 2013). These low temperature conditions are also unlikely to induce a resetting of the U–Pb isotopic system in zircon. Therefore, we interpret that the similar age but high temperature zircons have been derived from a hotter source, and therefore show open system behaviour and circulation of melt from different sources at the scale of a leucosome. Concerning the low temperatures bellow the wet solidus, it can be interpreted either as an underestimation of the activity of $aTiO_2$ in the melt, which would increase the temperature up to 70 °C or as a sign of disequilibrium crystallisation from melt or non-Henry's law substitution of Ti in zircons (e.g. Ferry & Watson, 2007).

## 6.4. Multiple melting events and garnet influence on zircon growth in migmatites from lower La Bocana

The zircon analyses of the two samples of migmatites from lower La Bocana (EOLB-04 and EOLB-37) sometimes show two distinct CL rims (Fig. 8C), indicating that some grains record multiple growth episodes. This is consistent with the dispersion observed in the calculated weighted means and the range of dates between ca. 215 and 235 Ma. This is interpreted as evidence for multiple partial-melting events, as zircon analyses give similar temperature estimates over a period of ca. 20 Myr. The HREEs data provide evidence that more than the majority of the combined analyses of the samples EOLB-04 and EOLB-37 grew in the presence of garnet (Fig. 11B). If these garnets are interpreted as metamorphic, this is evidence for the melting reaction of Bt break-down, which produces peritectic garnet.

## 6.5. Interpretation of titanite U–Pb and Zr-in-titanite temperature estimates

The closure temperature of Pb diffusion in titanite has been the subject of debate over the last decades. Based on natural data (e.g. Mezger et al., 1991; Spear & Parrish, 1996; Tucker et al., 2004) and experimental work (Cherniak, 1993), it has historically been thought that the closure temperature of Pb is quite low, between 500 and 600 °C. In a recent review, Kohn (2017) argues, based on more recent studies and evidence, that the closure temperature should be much higher, and that chronological resetting should be ineffective below 800 °C. Given that the natural intracrystalline gradient for Zr is at least as steep as that for Pb (Stearns et al., 2016), Zr should also not diffuse at temperatures below 800 °C. The fact that the titanite grains in this study are of significant size, mostly between 300 and 500 µm, supports the idea that the U–Pb age and the Zr-in-titanite temperature estimates, which are mostly between 700 and 760 °C within uncertainties, can be interpreted as a record of the crystallisation of the titanite grains. As the Zr-in-titanite thermometer of Hayden et al. (2008) was calibrated for the {111} sector chemistry and the analyses were carried out on unoriented grains, the temperature reported in this study can be overestimated by about 40 to 80 °C, further supporting that these are bellow closing temperatures of Zr and Pb.

## 6.6. Fast cooling of the gabbro emplacement

The homogeneous temperature estimates and well defined isochron age of 227.5 ± 4.5 Ma support the idea of a single generation of titanite, which is interpreted as metamorphic. This age is within uncertainty with the two zircon crystallisation ages, interpreted as magmatic, and the amphibole cooling age, interpreted as metamorphic, previously reported in the same unit (Cochrane et al., 2014; Gabriele, 2002; Noble et al., 1997). This confirms that the magmatism and the metamorphism linked to the cooling of the gabbro

occur in rapid succession. A more precise magmatic age would be helpful in the future, as Noble et al. (1997) report an age with only two analyses, whereas Cochrane et al. (2014) report very low U content in their analyses, producing high uncertainties.

## 6.7. Relationship between migmatites and granitoids

The main source of the Marcabelí pluton is interpreted to be migmatites from the lower La Bocana unit. However, it is also possible that they were also sourced from a deeper sedimentary source, which is not exposed but would form the granulite equivalent of the La Bocana unit. This could explain the mixed signature of the zircons from the Marcabelí pluton. The lower La Bocana migmatites have undergone the most partial melting in the preserved sequence, as evidenced by the presence of peritectic garnet. Texturally and geochronologically, two growth generations, sometimes separated by up to ca. 10 Myr, are resolved in the zircons of the 2 samples from this unit, supporting the idea of multiple generations of melting (Fig. 8C). This is in agreement with the ca. 20 Myr span in time of the emplacement of the Marcabelí pluton, and the hypothesis of multiple pulses of melt to build the pluton over this duration. Another observation is that dates in the granitoids seems to start at around ca. 240 Ma, whereas the zircons in the migmatites mainly record dates from ca. 235 Ma onwards (Figs 4B and 9). If this discrepancy is interpreted as geologically meaningful, i.e. that it cannot be explained by analytical uncertainties alone, it can be explained by the fact that zircons in migmatites would not record prograde metamorphism, whereas the melt extracted from them and be emplaced in plutons would crystallise. However, the peak metamorphism in the metamorphic sequence is estimated to be at around 228 Ma (Gabriele, 2002; Riel et al., 2014). Thus, we consider that 240 Ma is probably too early to have produced a significant amount in the La Bocana unit to emplaced it in the Marcabelí pluton. Therefore, we propose that the melt comes at that time from a deeper source than the La Bocana unit, currently not present anymore.

## 6.8. Geodynamic implications for the El Oro complex

Combining the geochronology of the different samples of this study allows a more accurate geological history of the Triassic event in the El Oro complex to be reconstructed. The main results of this study are reported in Fig. 16 with an interpretation of the main geological events on the scale of the El Oro complex. A new melting event between ca. 245 and 260 Ma is reported and is interpreted to have produced magmatism with an I-type signature, based on zircon trace element data (Fig. 7). The second magmatic event of the Tahuín group is shown to be long-lived, lasting for ca. 25 Myr, between ca. 215 and 240 Ma. This corresponds to the emplacement of the major S-type plutons in the El Oro complex. The duration of the prograde history of the metamorphic history is not well constrained, but the metamorphic peak is interpreted to be ca. 228 Ma and corresponds to the end of the emplacement of the Piedras gabbros and the beginning of the cooling of the sequence by the underplating of the blueschists of the Arenillas-Panupalí unit (Gabriele, 2002; Riel et al., 2014). This is supported by the new high temperature ($\sim$740 °C) titanite age obtained in this study. The zircon dates in the migmatites constrain the duration of the retrograde history and show multiple melt crystallisation events with a duration of ca. 20 Ma, between 215 and 235 Ma. Previous ages reported for the plutons and the migmatites from the La Bocana unit all fall within these ranges (Noble et al., 1997; Riel et al., 2013; Vinasco Vallejo, 2004), but the higher number of analyses in this study provides a better estimate of the total duration of these events and shows that they are long-lived processes.

These data are compatible with the geodynamic interpretation of the Triassic event in the El Oro complex proposed by Riel et al. (2014), with some adjustments. The new magmatic event recorded ca. 245 and 260 Ma, in the Late Permian to Early Triassic, is not well constrained. We suggest that it is either (i) remelting of a precursor igneous rock which formed part of the basement which the Tahuín Group were deposited into, in a forearc setting, or (ii) injection of a mantle-derived melt into the lower parts of the Tahuín Group at this time. Regardless, both geodynamic scenarios suggest some form of crustal thinning as early as ca. 260 Ma in the El Oro complex. This thinning either provided the heat to melt the basement in scenario

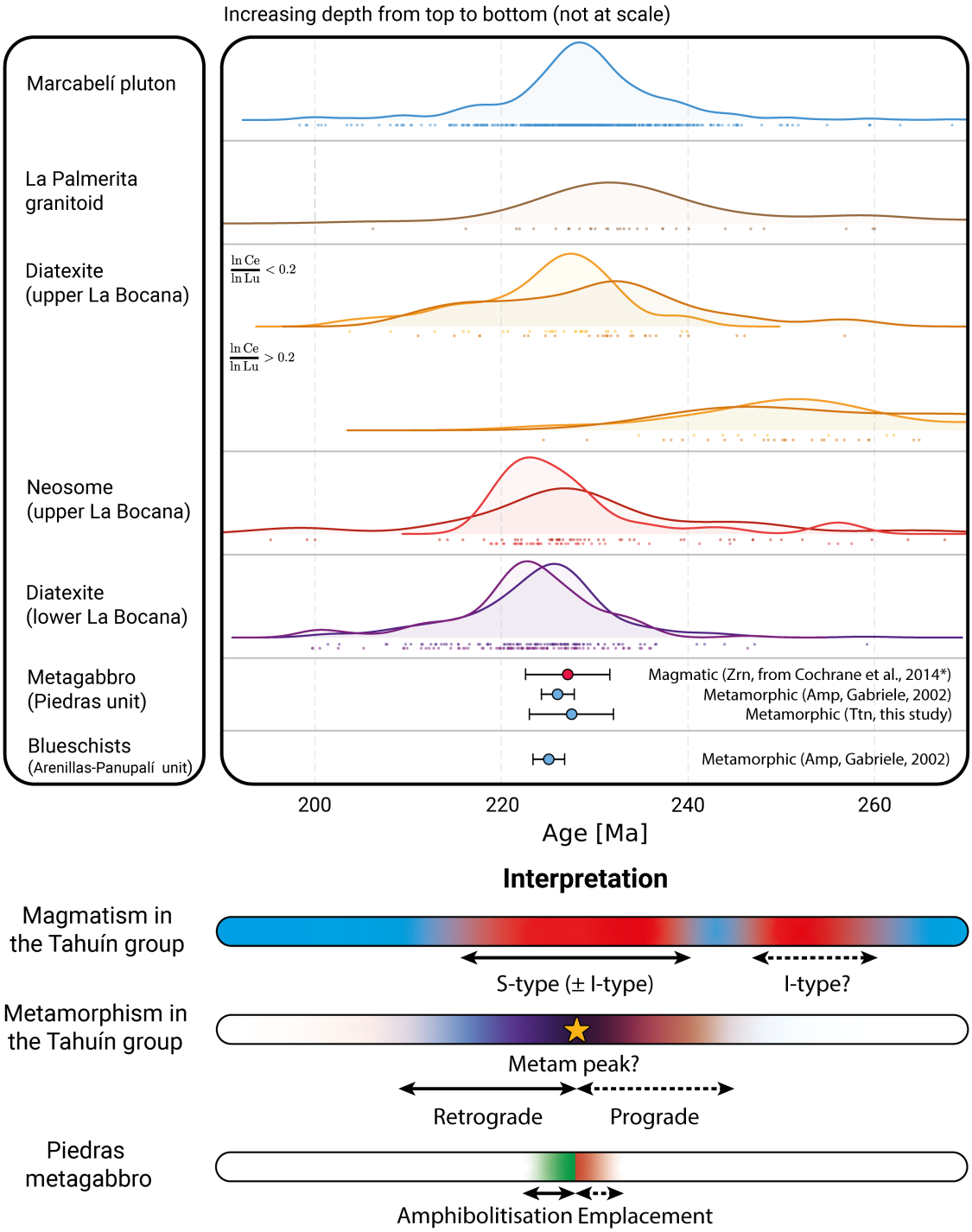


**Figure 16:** Summary figure of the geochronology data of the El Oro complex collected in this study and from Cochrane et al. (2014) and Gabriele (2002). Each kernel density estimates correspond to the analyses of one sample. The magmatic age of Cochrane et al. (2014) was recalculated by removing 4 analyses with dates bellow 220 Ma that were interpreted as metamorphic and therefore outlayers. An interpretation of the timing of the major events in the El Oro complex for the Triassic event are also provided.

(i), or allowed mantle decompression and melting in scenario (ii).

Concerning the later main Triassic event, the new geochronology data shows that the Marcabelí pluton likely started to be emplaced as early as ca. 240 Ma. The source at that time is interpreted as being deeper than La Bocana, since the metamorphic peak in the Tahuín group is estimated to be at ca. 228 Ma. This source appears to have been comprised of dominantly sedimentary materials. We suggest that this melting was driven by extension, crustal thinning and mantle upwelling. This residual part of the crust and the basement which was deposited onto were later delaminated and replaced by the mantle-derived mafic rocks of the Piedras unit. The subsequent history is similar to the one proposed by Riel et al. (2014): the underplating of the Arenillas-Panupalí blueschists bellow the Piedras unit occurred at ca. 226 Ma, as supported by $^{40}Ar/^{39}Ar$ ages on hornblende on both the Arenillas-Panupalí and the Piedras units (Gabriele, 2002), which allowed the quenching of the metamorphic sequence and the end of the heat source.

## 7. Conclusion

This study presents a detailed analysis of zircon U–Pb and trace element data, highlighting the complexities involved in interpreting the ages of S-type granitoids and migmatitic systems. The findings emphasise the challenges posed by geological factors such as inheritance, Pb-loss, and the long-lived nature of melting and crystallisation processes. Despite these challenges, the dispersion in zircon dates is interpreted as containing valuable geological information, which, when coupled with trace element data, provides insights into the conditions of zircon crystallisation and hence melting processes.

The analysis of the Marcabelí pluton suggests a long emplacement period with several pulses of melt injection over ca. 20 Myr, between 240 and 220 Ma. This interpretation is supported by the observed high MSWD values for some samples, suggesting episodic magmatic activity rather than a single, continuous event. Similarly, the La Palmerita granitoid, although with fewer analyses, shows a high MSWD and dispersion uncertainty in its zircon dates, suggesting a comparable history of prolonged magmatic activity. Trace element data and CL images of the older grains suggest that this granitoid shares a genetic link with the migmatites from upper La Bocana. In the La Bocana unit, trace element data and textural evidence indicate that some migmatitic samples exhibit open-system behaviour, while others record an older magmatic event, between ca. 260 and 250 Ma. Zircon growth in the deeper migmatitic samples occurs in equilibrium with garnets, consistent with the presence of peritectic garnets. Overall, the zircon dates indicate that the crystallisation of zircons in the La Bocana unit occurred between 235 and 215 Ma. The study also highlights the rapid cooling of the gabbro emplacement from the Piedras unit, supported by a titanite age of 227.5 ± 4.5 ($n$ = 94) Ma and temperature estimates around 740 °C.

These findings confirm that the main source of melt for the Marcabelí pluton and La Palmerita granitoid is the migmatites of the La Bocana unit. Overall, this work highlights the appeal of combining U–Pb and trace element data while analysing a large number of magmatic and metamorphic zircons. This approach provides valuable insights into the temporal and thermal evolution of these magmatic and metamorphic systems, emphasising the importance of prolonged and episodic processes in the development of complex plutonic bodies such as Marcabelí pluton. Finally, this study shows that studying systems where both the potential source and the final product of melting processes are accessible is a valuable approach to better constrain these processes.

## Data availability

The analytical data produced and used in this chapter, along with the GPS locations of each sample, are available at a permanent DOI repository https://boris-portal.unibe.ch/handle/20.500.12422/44675. This include the LA-ICP-MS data for both the zircon and titanite analyses alonside the spot positions of each individual analysis from CL (zircons) and backscattered (titanite) imaging.

## Acknowledgements

We thank C. Ganade for his help on the field and helpful discussions. Hugo Dominguez would like to thank D. Rubatto for discussions concerning zircon geochronology, L. Pacchiega and A. Berger for help on operating the different SEMs at the University of Bern and M. Lueder for discussions concerning closure temperature estimates. Funding was provided by the European Research Council (ERC) under the Eu-

ropean Union's Horizon 2020 research and innovation
programme (grant agreement No 850530).

## References


Aleinikoff, J. N., Wintsch, R. P., Tollo, R. P., Unruh, D. M., Fanning, C. M., & Schmitz, M. D. (2007). Ages and origins of rocks of the Killingworth dome, south-central Connecticut: Implications for the tectonic evolution of southern New England. *American Journal of Science*, *307*(1), 63–118. https://doi.org/10.2475/01.2007.04 (cit. on p. 50).

Andersen, C. A., & Hinthorne, J. R. (1972). U, Th, Pb and REE abundances and207Pb/206Pb ages of individual minerals in returned lunar material by ion microprobe mass analysis. *Earth and Planetary Science Letters*, *14*(2), 195–200. https://doi.org/10.1016/0012-821X(72)90006-4 (cit. on p. 44).

Andersen, T., Elburg, M. A., & Magwaza, B. N. (2019). Sources of bias in detrital zircon geochronology: Discordance, concealed lead loss and common lead correction. *Earth-Science Reviews*, *197*, 102899. https://doi.org/10.1016/j.earscirev.2019.102899 (cit. on p. 64).

Aspden, J. A., Bonilla, W., & Duque, P. (1995). *The El Oro metamorphic complex, Ecuador: Geology and economic mineral deposits*. British Geological Survey. Keyworth, Nottingham. (Cit. on pp. 44, 45).
OCLC: 36174214.

Baldock, J. W. (1982). *Geology of Ecuador: Explanatory bulletin of the national geological map of the Republic of Ecuador; 1: 1,000,000 scale 1982*. Ministerio de Recursos Naturales y Energéticos, Dirección General de Geología y Minas. (Cit. on pp. 44, 45).

Ballard, J. R., Palin, J. M., & Campbell, I. H. (2002). Relative oxidation states of magmas inferred from Ce(IV)/Ce(III) in zircon: Application to porphyry copper deposits of northern Chile. *Contributions to Mineralogy and Petrology*, *144*(3), 347–364. https://doi.org/10.1007/s00410-002-0402-5 (cit. on p. 67).

Bezanson, J., Edelman, A., Karpinski, S., & Shah, V. B. (2017). Julia: A Fresh Approach to Numerical Computing. *SIAM Review*, *59*(1), 65–98. https://doi.org/10.1137/141000671 (cit. on p. 50).

Bloch, E. M., Jollands, M. C., Tollan, P., Plane, F., Bouvier, A. .-., Hervig, R., Berry, A. J., Zaubitzer, C., Escrig, S., Müntener, O., Ibañez-Mejia, M., Alleon, J., Meibom, A., Baumgartner, L. P., Marin-Carbonne, J., & Newville, M. (2022). Diffusion anisotropy of Ti in zircon and implications for Ti-in-zircon thermometry. *Earth and Planetary Science Letters*, *578*, 117317. https://doi.org/10.1016/j.epsl.2021.117317 (cit. on p. 67).

Boehnke, P., Watson, E. B., Trail, D., Harrison, T. M., & Schmitt, A. K. (2013). Zircon saturation re-revisited. *Chemical Geology*, *351*, 324–334. https://doi.org/10.1016/j.chemgeo.2013.05.028 (cit. on p. 67).

Brown, M. (2013). Granite: From genesis to emplacement. *Geological Society of America Bulletin*, *125*(7–8), 1079–1113. https://doi.org/10.1130/B30877.1 (cit. on p. 44).

Cherniak, D. J. (1993). Lead diffusion in titanite and preliminary results on the effects of radiation damage on Pb transport. *Chemical Geology*, *110*(1–3), 177–194 (cit. on p. 70).

Cherniak, D. J. (2010). Diffusion in Accessory Minerals: Zircon, Titanite, Apatite, Monazite and Xenotime. *Reviews in Mineralogy and Geochemistry*, *72*(1), 827–869. https://doi.org/10.2138/rmg.2010.72.18 (cit. on p. 67).

Cherniak, D. J., Hanchar, J., & Watson, E. (1997). Rare-earth diffusion in zircon. *Chemical Geology*, *134*(4), 289–301. https://doi.org/10.1016/S0009-2541(96)00098-8 (cit. on p. 67).

Cherniak, D. J., & Watson, E. B. (2001). Pb diffusion in zircon. *Chemical Geology*, *172*(1), 5–24. https://doi.org/10.1016/S0009-2541(00)00233-3 (cit. on p. 67).

Clark, C., Fitzsimons, I. C. W., Healy, D., & Harley, S. L. (2011). How Does the Continental Crust Get Really Hot? *Elements*, *7*(4), 235–240. https://doi.org/10.2113/gselements.7.4.235 (cit. on p. 44).

Clemens, J. (2003). S-type granitic magmas—petrogenetic issues, models and evidence. *Earth-Science Reviews*, *61*(1), 1–18. https://doi.org/10.1016/S0012-8252(02)00107-1 (cit. on p. 44).

Cochrane, R., Spikings, R., Gerdes, A., Ulianov, A., Mora, A., Villagómez, D., Putlitz, B., & Chiaradia, M. (2014). Permo-Triassic anatexis, continental rifting and the disassembly of western Pangaea. *Lithos*, *190–191*, 383–402. https://doi.org/10.1016/j.lithos.2013.12.020 (cit. on pp. 47, 70–72).

Coleman, D. S., Gray, W., & Glazner, A. F. (2004). Rethinking the emplacement and evolution of zoned plutons: Geochronologic evidence

for incremental assembly of the Tuolumne Intrusive Suite, California. *Geology*, *32*(5), 433. https://doi.org/10.1130/G20220.1 (cit. on p. 69).

Couzinié, S., Bouilhol, P., Laurent, O., Marko, L., & Moyen, J.-F. (2021). When zircon drowns: Elusive geochronological record of water-fluxed orthogneiss melting in the Velay dome (Massif Central, France). *Lithos*, *384–385*, 105938. https://doi.org/10.1016/j.lithos.2020.105938 (cit. on p. 44).

Cózar, P., Díaz-Martínez, E., & Carlotto, V. (2024). Foraminiferal biostratigraphy of the pennsylvanian cerro prieto formation, amotape mountains, NW Peru: Correlation with the Central Andean basin. *Journal of South American Earth Sciences*, *146*, 105086. https://doi.org/10.1016/j.jsames.2024.105086 (cit. on p. 45).

Crisp, L. J., & Berry, A. J. (2022). A new model for zircon saturation in silicate melts. *Contributions to Mineralogy and Petrology*, *177*(7), 71. https://doi.org/10.1007/s00410-022-01925-6 (cit. on p. 67).

De Saint Blanquat, M., Horsman, E., Habert, G., Morgan, S., Vanderhaeghe, O., Law, R., & Tikoff, B. (2011). Multiscale magmatic cyclicity, duration of pluton construction, and the paradoxical relationship between tectonism and plutonism in continental arcs. *Tectonophysics*, *500*(1–4), 20–33. https://doi.org/10.1016/j.tecto.2009.12.009 (cit. on p. 69).

England, P., & Thompson, A. (1984). Pressure—Temperature—Time Paths of Regional Metamorphism I. Heat Transfer during the Evolution of Regions of Thickened Continental Crust. *Journal of Petrology*, *25*(4), 894–928. https://doi.org/10.1093/petrology/25.4.894 (cit. on p. 44).

Farina, F., Dini, A., Davies, J. H., Ovtcharova, M., Greber, N. D., Bouvier, A.-S., Baumgartner, L., Ulianov, A., & Schaltegger, U. (2018). Zircon petrochronology reveals the timescale and mechanism of anatectic magma formation. *Earth and Planetary Science Letters*, *495*, 213–223. https://doi.org/10.1016/j.epsl.2018.05.021 (cit. on p. 44).

Feininger, T. (1980). Eclogite and Related High-Pressure Regional Metamorphic Rocks from the Andes of Ecuador. *Journal of Petrology*, *21*(1), 107–140. https://doi.org/10.1093/petrology/21.1.107 (cit. on p. 45).

Feininger, T. (1978). Geologic map of western El Oro province. *Escuela Politecnica Nacional, Quito, Ecuador* (cit. on pp. 44–46).

Feininger, T. (1982). The metamorphic "basement" of Ecuador. *Geological Society of America Bulletin*, *93*(1), 87. https://doi.org/10.1130/0016-7606(1982)93<87:TMBOE>2.0.CO;2 (cit. on pp. 44, 45).

Ferry, J. M., & Watson, E. B. (2007). New thermodynamic models and revised calibrations for the Ti-in-zircon and Zr-in-rutile thermometers. *Contributions to Mineralogy and Petrology*, *154*(4), 429–437. https://doi.org/10.1007/s00410-007-0201-0 (cit. on pp. 53, 55, 58, 63, 65, 67, 70).

Gabriele, P. (2002, November 22). *HP terranes exhumation in active margin setting: Geology, petrology and geochemistry of the Raspas Complex in SW Ecuador* [Doctoral dissertation, Université de Lausanne (Suisse)]. Retrieved May 27, 2024, from https://hal.science/tel-04431244 (cit. on pp. 44, 45, 47, 70–73).

Hawkesworth, C., Dhuime, B., Pietranik, A., Cawood, P., Kemp, A., & Storey, C. (2010). The generation and evolution of the continental crust. *Journal of the Geological Society*, *167*(2), 229–248 (cit. on p. 44).

Hayden, L. A., Watson, E. B., & Wark, D. A. (2008). A thermobarometer for sphene (titanite). *Contributions to Mineralogy and Petrology*, *155*(4), 529–540. https://doi.org/10.1007/s00410-007-0256-y (cit. on pp. 64, 66, 70).

Hinton, R., & Upton, B. (1991). The chemistry of zircon: Variations within and between large crystals from syenite and alkali basalt xenoliths. *Geochimica et Cosmochimica Acta*, *55*(11), 3287–3302. https://doi.org/10.1016/0016-7037(91)90489-R (cit. on p. 67).

Horstwood, M. S. A., Košler, J., Gehrels, G., Jackson, S. E., McLean, N. M., Paton, C., Pearson, N. J., Sircombe, K., Sylvester, P., Vermeesch, P., Bowring, J. F., Condon, D. J., & Schoene, B. (2016). Community-Derived Standards for LA - ICP - MS U-(Th-)Pb Geochronology – Uncertainty Propagation, Age Interpretation and Data Reporting. *Geostandards and Geoanalytical Research*, *40*(3), 311–332. https://doi.org/10.1111/j.1751-908X.2016.00379.x (cit. on pp. 50, 51).

Iddings, A., & Olsson, A. A. (1928). Geology of Northwest Peru. *AAPG Bulletin*, *12*(1), 1–39. https:

//doi.org/10.1306/3D9327D7-16B1-11D7-8645000102C1865D (cit. on p. 45).

Ireland, T. R., & Williams, I. S. (2003). Considerations in zircon geochronology by SIMS. *Reviews in mineralogy and geochemistry*, *53*(1), 215–241 (cit. on p. 44).

Jackson, S. E., Pearson, N. J., Griffin, W. L., & Belousova, E. A. (2004). The application of laser ablation-inductively coupled plasma-mass spectrometry to in situ U–Pb zircon geochronology. *Chemical Geology*, *211*(1–2), 47–69. https://doi.org/10.1016/j.chemgeo.2004.06.017 (cit. on p. 50).

Jaupart, C., & Mareschal, J.-C. (Eds.). (2010). Global energy budget. Crust, mantle and core. *Heat Generation and Transport in the Earth*, 232–260. https://doi.org/10.1017/CBO9780511781773.009 (cit. on p. 44).

Jochum, K. P., Weis, U., Stoll, B., Kuzmin, D., Yang, Q., Raczek, I., Jacob, D. E., Stracke, A., Birbaum, K., Frick, D. A., Günther, D., & Enzweiler, J. (2011). Determination of Reference Values for NIST SRM 610–617 Glasses Following ISO Guidelines. *Geostandards and Geoanalytical Research*, *35*(4), 397–429. https://doi.org/10.1111/j.1751-908X.2011.00120.x (cit. on p. 50).

Jochum, K. P., Willbold, M., Raczek, I., Stoll, B., & Herwig, K. (2005). Chemical Characterisation of the USGS Reference Glasses GSA-1G, GSC-1G, GSD-1G, GSE-1G, BCR-2G, BHVO-2G and BIR-1G Using EPMA, ID-TIMS, ID-ICP-MS and LA-ICP-MS. *Geostandards and Geoanalytical Research*, *29*(3), 285–302. https://doi.org/10.1111/j.1751-908X.2005.tb00901.x (cit. on p. 50).

Johnson, T., Yakymchuk, C., & Brown, M. (2021). Crustal melting and suprasolidus phase equilibria: From first principles to the state-of-the-art. *Earth-Science Reviews*, *221*, 103778. https://doi.org/10.1016/j.earscirev.2021.103778 (cit. on p. 65).

Keller, C. (2023). Isoplot.jl. https://doi.org/10.17605/OSF.IO/Z37WE (cit. on p. 50).

Keller, C., Boehnke, P., & Schoene, B. (2017). Temporal variation in relative zircon abundance throughout Earth history. *Geochemical Perspectives Letters*, 179–189. https://doi.org/10.7185/geochemlet.1721 (cit. on p. 67).

Kelsey, D. E., Clark, C., & Hand, M. (2008). Thermobarometric modelling of zircon and monazite growth in melt-bearing systems: Examples using model metapelitic and metapsammitic granulites. *Journal of Metamorphic Geology*, *26*(2), 199–212. https://doi.org/10.1111/j.1525-1314.2007.00757.x (cit. on p. 67).

Kohn, M. J., Corrie, S. L., & Markley, C. (2015). The fall and rise of metamorphic zircon. *American Mineralogist*, *100*(4), 897–908. https://doi.org/10.2138/am-2015-5064 (cit. on p. 67).

Kohn, M. J. (2017). Titanite Petrochronology. *Reviews in Mineralogy and Geochemistry*, *83*(1), 419–441. https://doi.org/10.2138/rmg.2017.83.13 (cit. on p. 70).

Kohn, M. J., & Kelly, N. M. (2018, January 29). Petrology and Geochronology of Metamorphic Zircon. In D. E. Moser, F. Corfu, J. R. Darling, S. M. Reddy, & K. Tait (Eds.), *Geophysical Monograph Series* (1st ed., pp. 35–61). Wiley. https://doi.org/10.1002/9781119227250.ch2 (cit. on p. 64).

Korenaga, J. (2018). Crustal evolution and mantle dynamics through Earth history. *Philosophical Transactions of the Royal Society A: Mathematical, Physical and Engineering Sciences*, *376*(2132), 20170408 (cit. on p. 44).

Košler, J., & Sylvester, P. J. (2003). Present trends and the future of zircon in geochronology: Laser ablation ICPMS. *Reviews in mineralogy and geochemistry*, *53*(1), 243–275 (cit. on p. 44).

Krogh, T. (1982). Improved accuracy of U-Pb zircon ages by the creation of more concordant systems using an air abrasion technique. *Geochimica et Cosmochimica acta*, *46*(4), 637–649 (cit. on p. 44).

Kylander-Clark, A. R., Hacker, B. R., & Cottle, J. M. (2013). Laser-ablation split-stream ICP petrochronology. *Chemical Geology*, *345*, 99–112. https://doi.org/10.1016/j.chemgeo.2013.02.019 (cit. on p. 44).

Li, Y., Xie, H., Dong, C., Wang, S., & Wan, Y. (2022). Zircon evolution from migmatite to crustally-derived granite: A case study of late Neoarchean migmatite in the Yishan area, western Shandong, North China Craton. *Gondwana Research*, *112*, 82–104. https://doi.org/10.1016/j.gr.2022.09.008 (cit. on p. 44).

Liati, A., Theye, T., Fanning, C. M., Gebauer, D., & Rayner, N. (2016). Multiple subduction cycles in the Alpine orogeny, as recorded in single zircon crystals (Rhodope zone, Greece). *Gond-*

*wana Research*, *29*(1), 199–207. https://doi.org/10.1016/j.gr.2014.11.007 (cit. on p. 44).

Litherland, M. (1994). The metamorphic belts of Ecuador. *Overseas Mem Br Geol Surv*, *11*, 1–147 (cit. on p. 44).

Martínez, M. (1970). Geología del basamento Paleozóico en las Montañas de Amotape y posible origen del petróleo en las rocas Paleozóicas del noreste de Perú. *Primer Congr. Latinoam. Geol*, *2*, 105–138 (cit. on p. 45).

Mattinson, J. M. (2005). Zircon U–Pb chemical abrasion ("CA-TIMS") method: Combined annealing and multi-step partial dissolution analysis for improved precision and accuracy of zircon ages. *Chemical Geology*, *220*(1–2), 47–66 (cit. on p. 44).

Matzel, J. E., Bowring, S. A., & Miller, R. B. (2006). Time scales of pluton construction at differing crustal levels: Examples from the Mount Stuart and Tenpeak intrusions, North Cascades, Washington. *Geological Society of America Bulletin*, *118*(11–12), 1412–1430. https://doi.org/10.1130/B25923.1 (cit. on p. 69).

McDonough, W. F., & Sun, S. (1995). The composition of the Earth. *Chemical Geology*, *120*(3), 223–253. https://doi.org/10.1016/0009-2541(94)00140-4 (cit. on pp. 56, 61, 62).

Mezger, K., Rawnsley, C. M., Bohlen, S. R., & Hanson, G. N. (1991). U-Pb Garnet, Sphene, Monazite, and Rutile Ages: Implications for the Duration of High-Grade Metamorphism and Cooling Histories, Adirondack Mts., New York. *The Journal of Geology*, *99*(3), 415–428. https://doi.org/10.1086/629503 (cit. on p. 70).

Michel, J., Baumgartner, L., Putlitz, B., Schaltegger, U., & Ovtcharova, M. (2008). Incremental growth of the Patagonian Torres del Paine laccolith over 90 k.y. *Geology*, *36*(6), 459. https://doi.org/10.1130/G24546A.1 (cit. on pp. 44, 69).

Miller, J. S., Matzel, J. E., Miller, C. F., Burgess, S. D., & Miller, R. B. (2007). Zircon growth and recycling during the assembly of large, composite arc plutons. *Journal of Volcanology and Geothermal Research*, *167*(1–4), 282–299. https://doi.org/10.1016/j.jvolgeores.2007.04.019 (cit. on p. 64).

Mourier, T. (1988, January 1). *La transition entre Andes marginales et Andes cordilléraines à ophiolites : Évolution sédimentaire, magmatique et structurale du relais de Huancabamba (3 a 8 Lat. S ; Nord Pérou-Sud Équateur)* [These de doctorat]. Paris 11. Retrieved July 9, 2024, from https://theses.fr/1988PA112426 (cit. on p. 45).

Murali, A., Parthasarathy, R., Mahadevan, T., & Das, M. (1983). Trace element characteristics, REE patterns and partition coefficients of zircons from different geological environments—A case study on Indian zircons. *Geochimica et Cosmochimica Acta*, *47*(11), 2047–2052. https://doi.org/10.1016/0016-7037(83)90220-X (cit. on p. 67).

Noble, S. R., Aspden, J. A., & Jemielita, R. (1997). Northern Andean crustal evolution: New U-Pb geochronological constraints from Ecuador. *Geological Society of America Bulletin*, *109*(7), 789–798. https://doi.org/10.1130/0016-7606(1997)109<0789:NACENU>2.3.CO;2 (cit. on pp. 47, 70, 71).

Norris, A., & Danyushevsky, L. (2018). Towards estimating the complete uncertainty budget of quantified results measured by LA-ICP-MS. *Goldschmidt: Boston, MA, USA* (cit. on p. 50).

Oliver, G., Corfu, F., & Krogh, T. (1993). U-pb ages from SW poland: Evidence for a caledonian suture zone between baltica and gondwana. *Journal of the Geological Society*, *150*(2), 355–369 (cit. on p. 44).

Paces, J. B., & Miller Jr, J. D. (1993). Precise U-Pb ages of Duluth complex and related mafic intrusions, northeastern Minnesota: Geochronological insights to physical, petrogenetic, paleomagnetic, and tectonomagmatic processes associated with the 1.1 Ga midcontinent rift system. *Journal of Geophysical Research: Solid Earth*, *98*(B8), 13997–14013 (cit. on p. 44).

Parrish, R. R. (1987). An improved micro-capsule for zircon dissolution in U-Pb geochronology. *Chemical Geology: Isotope Geoscience Section*, *66*(1–2), 99–102 (cit. on p. 44).

Reichardt, H., & Weinberg, R. F. (2012). The dike swarm of the Karakoram shear zone, Ladakh, NW India: Linking granite source to batholith. *Geological Society of America Bulletin*, *124*(1–2), 89–103. https://doi.org/10.1130/B30394.1 (cit. on p. 44).

Riel, N., Guillot, S., Jaillard, E., Martelat, J.-E., Paquette, J.-L., Schwartz, S., Goncalves, P., Duclaux, G., Thebaud, N., Lanari, P., Janots, E., & Yuquilema, J. (2013). Metamorphic and geochronogical study of the Triassic El Oro metamorphic complex, Ecuador: Implications for high-temperature metamorphism in

a forearc zone. *Lithos*, *156–159*, 41–68. https://doi.org/10.1016/j.lithos.2012.10.005 (cit. on pp. 44–47, 64, 65, 70, 71).

Riel, N., Martelat, J.-E., Guillot, S., Jaillard, E., Monié, P., Yuquilema, J., Duclaux, G., & Mercier, J. (2014). Fore arc tectonothermal evolution of the El Oro metamorphic province (Ecuador) during the Mesozoic. *Tectonics*, *33*(10), 1989–2012. https://doi.org/10.1002/2014TC003618 (cit. on pp. 71, 73).

Riel, N., Mercier, J., & Weinberg, R. (2016). Convection in a partially molten metasedimentary crust? Insights from the El Oro complex (Ecuador). *Geology*, *44*(1), 31–34. https://doi.org/10.1130/G37208.1 (cit. on pp. 64, 65, 70).

Roberts, M. P., & Finger, F. (1997). Do U-Pb zircon ages from granulites reflect peak metamorphic conditions? *Geology*, *25*(4), 319. https://doi.org/10.1130/0091-7613(1997)025<0319:DUPZAF>2.3.CO;2 (cit. on p. 67).

Roberts, N., Yakymchuk, C., Spencer, C. J., Keller, C. B., & Tapster, S. R. (2024). Revisiting the discrimination and distribution of S-type granites from zircon trace element composition. *Earth and Planetary Science Letters*, *633*, 118638. https://doi.org/10.1016/j.epsl.2024.118638 (cit. on pp. 53, 57, 67).

Rubatto, D. (2002). Zircon trace element geochemistry: Partitioning with garnet and the link between U–Pb ages and metamorphism. *Chemical Geology*, *184*(1–2), 123–138. https://doi.org/10.1016/S0009-2541(01)00355-2 (cit. on p. 67).

Rubatto, D. (2017). Zircon: The Metamorphic Mineral. *Reviews in Mineralogy and Geochemistry*, *83*(1), 261–295. https://doi.org/10.2138/rmg.2017.83.9 (cit. on p. 67).

Rubatto, D., & Gebauer, D. (2000). Use of Cathodoluminescence for U-Pb Zircon Dating by Ion Microprobe: Some Examples from the Western Alps. In M. Pagel, V. Barbin, P. Blanc, & D. Ohnenstetter (Eds.), *Cathodoluminescence in Geosciences* (pp. 373–400). Springer. https://doi.org/10.1007/978-3-662-04086-7_15 (cit. on p. 44).

Rubatto, D., Hermann, J., Berger, A., & Engi, M. (2009). Protracted fluid-induced melting during Barrovian metamorphism in the Central Alps. *Contributions to Mineralogy and Petrology*, *158*(6), 703–722. https://doi.org/10.1007/s00410-009-0406-5 (cit. on p. 67).

Rubatto, D., Hermann, J., & Buick, I. S. (2006). Temperature and Bulk Composition Control on the Growth of Monazite and Zircon During Low-pressure Anatexis (Mount Stafford, Central Australia). *Journal of Petrology*, *47*(10), 1973–1996. https://doi.org/10.1093/petrology/egl033 (cit. on p. 67).

Samperton, K. M., Bell, E. A., Barboni, M., Keller, C. B., & Schoene, B. (2017). Zircon age-temperature-compositional spectra in plutonic rocks. *Geology*, *45*(11), 983–986. https://doi.org/10.1130/G38645.1 (cit. on p. 67).

Samperton, K. M., Schoene, B., Cottle, J. M., Brenhin Keller, C., Crowley, J. L., & Schmitz, M. D. (2015). Magma emplacement, differentiation and cooling in the middle crust: Integrated zircon geochronological–geochemical constraints from the Bergell Intrusion, Central Alps. *Chemical Geology*, *417*, 322–340. https://doi.org/10.1016/j.chemgeo.2015.10.024 (cit. on pp. 44, 69).

Sawyer, E. W., Cesare, B., & Brown, M. (2011). When the Continental Crust Melts. *Elements*, *7*(4), 229–234. https://doi.org/10.2113/gselements.7.4.229 (cit. on p. 44).

Sawyer, E. W. (2008). *Atlas of migmatites*. NRC research press. (Cit. on p. 48).

Schaltegger, U., Fanning, C. M., Günther, D., Maurin, J. C., Schulmann, K., & Gebauer, D. (1999). Growth, annealing and recrystallization of zircon and preservation of monazite in high-grade metamorphism: Conventional and in-situ U-Pb isotope, cathodoluminescence and microchemical evidence. *Contributions to Mineralogy and Petrology*, *134*(2–3), 186–201. https://doi.org/10.1007/s004100050478 (cit. on p. 67).

Schiller, D., & Finger, F. (2019). Application of Ti-in-zircon thermometry to granite studies: Problems and possible solutions. *Contributions to Mineralogy and Petrology*, *174*(6), 51. https://doi.org/10.1007/s00410-019-1585-3 (cit. on p. 53).

Schmitt, A., Sliwinski, J., Caricchi, L., Bachmann, O., Riel, N., Kaus, B., Cisneros De Léon, A., Cornet, J., Friedrichs, B., Lovera, O., Sheldrake, T., & Weber, G. (2023). Zircon age spectra to quantify magma evolution. *Geosphere*, *19*(4), 1006–1031. https://doi.org/10.1130/GES02563.1 (cit. on p. 64).

Schoene, B., & Baxter, E. F. (2017). Petrochronology and TIMS. *Reviews in Mineralogy and Geochemistry*, *83*(1), 231–260. https://doi.org/10.2138/rmg.2017.83.8 (cit. on p. 44).

Schoene, B., Schaltegger, U., Brack, P., Latkoczy, C., Stracke, A., & Günther, D. (2012). Rates of magma differentiation and emplacement in a ballooning pluton recorded by U–Pb TIMS-TEA, Adamello batholith, Italy. *Earth and Planetary Science Letters*, *355–356*, 162–173. https://doi.org/10.1016/j.epsl.2012.08.019 (cit. on pp. 44, 69).

Silver, L. T., & Deutsch, S. (1963). Uranium-Lead Isotopic Variations in Zircons: A Case Study. *The Journal of Geology*, *71*(6), 721–758. https://doi.org/10.1086/626951 (cit. on p. 44).

Sláma, J., Košler, J., Condon, D. J., Crowley, J. L., Gerdes, A., Hanchar, J. M., Horstwood, M. S., Morris, G. A., Nasdala, L., Norberg, N., Schaltegger, U., Schoene, B., Tubrett, M. N., & Whitehouse, M. J. (2008). Plešovice zircon — A new natural reference material for U–Pb and Hf isotopic microanalysis. *Chemical Geology*, *249*(1–2), 1–35. https://doi.org/10.1016/j.chemgeo.2007.11.005 (cit. on p. 50).

Sliwinski, J. T., Guillong, M., Horstwood, M. S. A., & Bachmann, O. (2022). Quantifying Long-Term Reproducibility of Zircon Reference Materials by U-Pb LA-ICP-MS Dating. *Geostandards and Geoanalytical Research*, *46*(3), 401–409. https://doi.org/10.1111/ggr.12442 (cit. on p. 51).

Spandler, C., Hammerli, J., Sha, P., Hilbert-Wolf, H., Hu, Y., Roberts, E., & Schmitz, M. (2016). MKED1: A new titanite standard for in situ analysis of Sm–Nd isotopes and U–Pb geochronology. *Chemical Geology*, *425*, 110–126. https://doi.org/10.1016/j.chemgeo.2016.01.002 (cit. on p. 50).

Spear, F. S., & Parrish, R. R. (1996). Petrology and Cooling Rates of the Valhalla Complex, British Columbia, Canada. *Journal of Petrology*, *37*(4), 733–765. https://doi.org/10.1093/petrology/37.4.733 (cit. on p. 70).

Stacey, J. S., & Kramers, J. D. (1975). Approximation of terrestrial lead isotope evolution by a two-stage model. *Earth and planetary science letters*, *26*(2), 207–221 (cit. on p. 50).

Stearns, M., Cottle, J., Hacker, B., & Kylander-Clark, A. (2016). Extracting thermal histories from the near-rim zoning in titanite using coupled U-Pb and trace-element depth profiles by single-shot laser-ablation split stream (SS-LASS) ICP-MS. *Chemical Geology*, *422*, 13–24. https://doi.org/10.1016/j.chemgeo.2015.12.011 (cit. on p. 70).

Tilton, G., Davis, G., Wetherill, G., & Aldrich, L. (1957). Isotopic ages of zircon from granites and pegmatites. *Eos, Transactions American Geophysical Union*, *38*(3), 360–371 (cit. on p. 44).

Trail, D., Bruce Watson, E., & Tailby, N. D. (2012). Ce and Eu anomalies in zircon as proxies for the oxidation state of magmas. *Geochimica et Cosmochimica Acta*, *97*, 70–87. https://doi.org/10.1016/j.gca.2012.08.032 (cit. on p. 67).

Tucker, R. D., Robinson, P., Solli, A., Gee, D. G., Thorsnes, T., Krogh, T. E., Nordgulen, Ø., & Bickford, M. (2004). Thrusting and extension in the Scandian hinterland, Norway: New U-Pb ages and tectonostratigraphic evidence. *American Journal of Science*, *304*(6), 477–532 (cit. on p. 70).

Vermeesch, P. (2018). IsoplotR: A free and open toolbox for geochronology. *Geoscience Frontiers*, *9*(5), 1479–1493. https://doi.org/10.1016/j.gsf.2018.04.001 (cit. on p. 66).

Vielzeuf, D., Clemens, J. D., Pin, C., & Moinet, E. (1990). Granites, Granulites, and Crustal Differentiation. In D. Vielzeuf & Ph. Vidal (Eds.), *Granulites and Crustal Evolution* (pp. 59–85). Springer Netherlands. https://doi.org/10.1007/978-94-009-2055-2_5 (cit. on p. 44).

Viete, D. R., Kylander-Clark, A. R., & Hacker, B. R. (2015). Single-shot laser ablation split stream (SS-LASS) petrochronology deciphers multiple, short-duration metamorphic events. *Chemical Geology*, *415*, 70–86. https://doi.org/10.1016/j.chemgeo.2015.09.013 (cit. on p. 44).

Vinasco Vallejo, C. J. (2004, December 22). *Evolução crustal e história tectônica dos granitóides permotriássicos dos Andes do Norte* [Doutorado em Geoquímica e Geotectônica]. Universidade de São Paulo. https://doi.org/10.11606/T.44.2004.tde-27102015-142142 (cit. on pp. 44, 45, 47, 69, 71).

Warr, L. N. (2021). IMA–CNMNC approved mineral symbols. *Mineralogical Magazine*, *85*(3), 291–320. https://doi.org/10.1180/mgm.2021.43 (cit. on p. 48).

Watson, E. B., & Harrison, T. M. (1983). Zircon saturation revisited: Temperature and composition effects in a variety of crustal magma

types. *Earth and Planetary Science Letters*, *64*(2), 295–304. https://doi.org/10.1016/0012-821X(83)90211-X (cit. on p. 67).

Wendt, I., & Carl, C. (1991). The statistical distribution of the mean squared weighted deviation. *Chemical Geology: Isotope Geoscience section*, *86*(4), 275–285. https://doi.org/10.1016/0168-9622(91)90010-T (cit. on p. 51).

Wiedenbeck, M., Alle, P., Corfu, F., Griffin, W., Meier, M., Oberli, F. v, Quadt, A. von, Roddick, J., & Spiegel, W. (1995). Three natural zircon standards for U-Th-Pb, Lu-Hf, trace element and REE analyses. *Geostandards newsletter*, *19*(1), 1–23 (cit. on p. 50).

Williams, I. S. (1992). Some observations on the use of zircon U-Pb geochronology in the study of granitic rocks. *Earth and Environmental Science Transactions of the Royal Society of Edinburgh*, *83*(1–2), 447–458 (cit. on p. 44).

Williams, I. S. (1997, January 1). U-Th-Pb Geochronology by Ion Microprobe. In M. A. McKibben, W. Shanks III, & W. I. Ridley (Eds.), *Applications of Microanalytical Techniques to Understanding Mineralizing Processes* (p. 0, Vol. 7). Society of Economic Geologists. https://doi.org/10.5382/Rev.07.01 (cit. on p. 44).

Wotzlaw, J.-F., Schaltegger, U., Frick, D. A., Dungan, M. A., Gerdes, A., & Günther, D. (2013). Tracking the evolution of large-volume silicic magma reservoirs from assembly to supereruption. *Geology*, *41*(8), 867–870. https://doi.org/10.1130/G34366.1 (cit. on p. 69).

Wu, F.-Y., Sun, D.-Y., Ge, W.-C., Zhang, Y.-B., Grant, M. L., Wilde, S. A., & Jahn, B.-M. (2011). Geochronology of the Phanerozoic granitoids in northeastern China. *Journal of Asian Earth Sciences*, *41*(1), 1–30. https://doi.org/10.1016/j.jseaes.2010.11.014 (cit. on p. 44).

Yakymchuk, C. (2023). Prograde zircon growth in migmatites. *Journal of Metamorphic Geology*, *41*(5), 719–743. https://doi.org/10.1111/jmg.12715 (cit. on p. 67).

Yakymchuk, C., Kirkland, C. L., & Clark, C. (2018). Th/U ratios in metamorphic zircon. *Journal of Metamorphic Geology*, *36*(6), 715–737. https://doi.org/10.1111/jmg.12307 (cit. on p. 67).

# Coupling thermal and phase equilibrium modelling to investigate time constraints in melting processes

Hugo Dominguez[1], Pierre Lanari[1, 2], Nicolas Riel[3], Jacob Forshaw[1]

[1] Institute of Geological Sciences, University of Bern, Baltzerstrasse 3, 3012 Bern, Switzerland
[2] Institute of Earth Sciences, University of Lausanne, Géopolis, 1015 Lausanne, Switzerland
[3] Institute of Geosciences, Johannes Gutenberg University, 55099 Mainz, Germany

# 1. Introduction

The definition of S-type granitoids and their link with metasediments have been proposed since 50 years, with the seminal work of Chappell and White (Chappell, 1984; Chappell & White, 1974, 2001; A. White & Chappell, 1977). In these studies, the high alumina saturation index (A/CNK, Shand, 1943), the K/Na molar ratio above unity, and the Sr and O isotopic ratios of the peraluminous granitoids of the Lachlan Fold Belt, in eastern Australia, were interpreted as evidence for melting of metasediments as the main source of the granitoids. In the following years, S-type granitoids have been shown to be the end product of mainly fluid-absent partial melting reactions that involve breakdown of micas in the deep crust (Breton & Thompson, 1988; Clemens & Vielzeuf, 1987; Powell, 1983; A. B. Thompson, 1983), although the role of water-fluxed melting has been underestimated in some settings and is still not well understood (e.g. Weinberg & Hasalová, 2015a). This S-type classification is part of the broader alphabetical (S-I-M-A) classification for granitoids (e.g. Chappell & White, 1974; Creaser et al., 1991; Eby, 1990; Loiselle et al., 1979), which is limited in its ability to separate certain igneous rocks. For example, it mixes source (S for sediments, I for metaigneous, M for mantle) and geotectonic setting (A for anorogenic). Moreover, the S/I discrimination is very strong, and does not leave space for intermediate compositions or mixed sources. Additionally, it heavily relies on the aluminosity of the rock (e.g. Bonin et al., 2020; D. B. Clarke, 1992; Frost et al., 2001). Despite these limitations, the term S-type remains relevant when used in a geological setting dominated by the melting of pelitic sequences and is used in this chapter in this context. This makes the formation and emplacement of S-type granitoids a key mechanism for understanding continental crust evolution, high-grade regional metamorphism and heat transport in the continental crust.

A persistent challenge in the study of S-type granitoids is to understand the chemical variation observed in major elements, trace elements, and isotopes at different scales within plutons (e.g. Brown, 2013; Brown & Pressley, 1999; Clemens & Stevens, 2012; Villaros, Stevens, Moyen, & Buick, 2009). This variation cannot be explained solely by differences in the chemical composition of melt produced from progressive melting reactions in a source rock (Montel & Vielzeuf, 1997; Patiño Douce & Johnston, 1991; Sawyer, 1996). Several hypotheses have been proposed to explain this variation and they can be broadly divided into three groups: fractional crystallisation, mixing, and unmixing models. Fractional crystallisation models explain the range in composition observed by the effect of different degrees of fractional crystallisation during the ascent and/or the emplacement of the magma (e.g. Breaks & Moore, 1992; Foden et al., 2002; Johannes et al., 2003). Mixing models explain the chemical variations by the mixing and mingling of different magmas, with a contribution from a more mafic source, either mantellic or from sediments with intermediate compositions (e.g. Collins, 1996; Gray, 1990). Finally, the unmixing models include the unmixing restite model (Chappell et al., 1987) or the entrapment of peritectic minerals and/or accessory minerals from the source (Clemens & Stevens, 2012; Stevens et al., 2007; Villaros, Stevens, & Buick, 2009). These models explain the chemical variation by different degrees of entrapment, which result in varying proportions of minerals being dissolved during the ascent of the magma.

Phase equilibrium modelling provides an opportunity to explore these hypotheses and to compare the results of numerical modelling with data extracted from natural observations. Although reproducing natural data with models does not guarantee the validity of the model — as very different models can produce similar results — this comparison is still valuable. It helps eliminate unlikely processes if they fail to replicate observed natural data. Modelling melting processes in the crust is challenging by essence, as they exhibit open system behaviour, with transport of mass and energy at the centimetre to crustal scale (Johnson et al., 2021; Mayne, Stevens, Moyen, & Johnson, 2020). It involves feedbacks between deformation, melt flow, chemical reactions, and heat flow. In this context, phase equilibrium modelling has been widely applied to try to better understand the melt composition, and its effect on and relation to the source (e.g. Diener & Fagereng, 2014; Nicoli & Dyck, 2018; Spear et al., 1999; R. W. White, 2003; Yakymchuk et al., 2015). Recent studies focusing on major element melt chemistry from metapelites have been exploring the effects of different bulk rock compositions, degrees of fractional crystallisation or entrapment from the source along $P$–$T$ paths (e.g. Koblinger & Pattison, 2017; Mayne, Stevens, & Moyen, 2020; Schwindinger et al., 2019). This approach aims to further develop the general understanding of the different variables on the melt and restite composition.

One important variable missing in phase equilibrium modelling is time. As equilibrium is by essence time invariant, this approach cannot provide time constraints. As such, recent approaches focus on *P–T* paths with constant increases in *T* and/or *P*, based, for instance, on linear or polynomial functions (e.g. Mayne, Stevens, Moyen, & Johnson, 2020). This is problematic because time provides a constraint on the feasibility of a physical process. This absence of time constraint can lead to unrealistic *P–T* paths. Additionally, comparing the total duration of a model with natural processes offers valuable insights into its plausibility. Timescales in crustal melting processes have been the topic of numerous studies, essentially relying on petrogeochronology (e.g. Farina et al., 2018; Gordon et al., 2008; Gordon et al., 2010; Harris et al., 2004) and have also been the topic of Chapter III. Combining these information, and using a *P–T–t* path with phase equilibrium modelling could potentially provide information on the duration of stability of a phase, or a melting reaction, while still operating within the limitations of the equilibrium paradigm.

In this chapter, we investigate this approach by bringing a time constraint based on a 1D crustal thermal model to ensure that the *P–T–t* paths used are physically realistic. This multi-layered model is composed of (meta-)sediments undergoing an isobaric thermal anomaly event causing partial melting at its base. The model geometry was designed based on the El Oro complex (southern Ecuador) and the modelling results were compared with natural observations from this metamorphic sequence. The El Oro sequence presents the particularity to show an exposed section through a paleo continental crust, providing an opportunity to study granitoids and migmatites, their potential sources. Geochemical data such as bulk rock compositions were produced in this study and two different thermal models were developed to reproduce the apparent thermal gradient of the El Oro the sequence. One of these thermal models was then coupled with thermodynamic calculations based on Gibbs energy minimisation to explore the evolution of the phase assemblages at different depths and the melt production at the scale of the crustal section. These predictions were then compared with the natural data from this sequence. By using this approach, it is possible to explore not only the composition but also the volume of melt produced and quantify the contribution of each layer along a 1D section. This approach provides mass balance assessments, to show, for example, that the volume of melt produced by the model is compatible with the observed occurrence of granitoids in the El Oro complex.

## 2. Geological settings

The El Oro complex represents a tilted portion of continental crust, containing three distinct units. From south to north, these units include the Tahuín group, a sequence of metamorphosed continental clastic sediments, the Piedras unit, composed of amphibolitised gabbro, and the Arenillas-Panupalí unit, which contains blueschist facies mafic rocks (Fig. 1).

The protolith of the Tahuín group is made of sediments deposited in a passive continental margin setting. This sedimentary sequence has undergone metamorphism with increasing grade from the southern to northern parts of the group (Feininger, 1982) during the late Triassic. Structurally, the Tahuín group is primarily separated from the adjacent Piedras unit by a large-scale normal fault, although localized magmatic contacts suggest the intrusive nature of the Piedras unit into the Tahuín group (Aspden et al., 1995; Riel et al., 2013). The Piedras unit, consisting of amphibolitised metagabbro, is interpreted to have acted as a heat source, driving the high-grade metamorphism of the Tahuín group (Riel et al., 2014). In contrast, the cooler blueschists of the Arenillas-Panupalí unit, which record peak metamorphic conditions of about 0.9 GPa and 300 °C, are interpreted to have contributed to the cooling of this high-temperature unit upon their underthrusting beneath the complex (Gabriele, 2002).

The Tahuín group is divided into three sub-units, each marked by major isograds. The El Tigre unit consists of largely unmetamorphosed to greenschist facies sediments, mainly turbidites (Aspden et al., 1995). The La Victoria unit, defined here by the Bt-in isograd from the El Tigre unit, is composed of metasediments, with the following mineral zones (mineral abbreviation after Warr (2021)): 1-Crd, 2-And, 3-fibrolitic Sil, 4-prismatic Sil and 5-Kfs (our field observations; Aspden et al., 1995; Feininger, 1978; Gabriele, 2002). The La Bocana unit is characterised by the prominent appearance of partial melting and is composed of migmatites. It is divided into two parts, following Riel et al. (2013): the upper La Bocana lacks garnet and interpreted to have retained a lower melt fraction at peak metamorphism, whilst the lower La Bocana contains garnet and a higher melt fraction. Representative field pictures of each unit of the Tahuín group

are shown in Fig. 2. Additionally, the units are intruded by three main S-type plutons: the El Prado, La Florida, and Marcabelí plutons (Aspden et al., 1995; Vinasco Vallejo, 2004). Representative field pictures of the Marcabelí and La Florida plutons are shown in Fig. 3.

The peak *P*–*T* conditions of the Tahuín group have been constrained by two studies (Riel et al., 2013; Riel et al., 2016), based mainly on phase equilibrium modelling. These studies show an important change in the metamorphic field gradient from the El Tigre and La Victoria units with ca. 45 °C km$^{-1}$ to the La Bocana unit, with 10–15 °C km$^{-1}$ (see Fig. 7A for the *P*–*T* estimates in a depth–*T* diagram). Consequently, peak metamorphic conditions in the La Bocana unit range from 0.4 ± 0.2 GPa and 650 ± 50 °C to 0.8 ± 0.2 GPa and 880 ± 50 °C. The sharp bend in the apparent geothermal gradient of peak metamorphic conditions, together with the lower gradient observed in the La Bocana unit, was found to be inconsistent with heat diffusion as the sole mechanism of heat transport (Riel et al., 2016). Instead, this geothermal gradient was interpreted to result from the formation and activation of a convection cell within the lower La Bocana unit, based on comparison with numerical models (Riel et al., 2016). This convection leads to heat advection by whole-rock flow in the partially molten crust. Another possible mechanism is heat advection by pervasive melt flow (e.g. Depine et al., 2008), which has not yet been explored for the El Oro complex.

The main source of the S-type plutons in the El Oro complex has been interpreted to be the migmatites from the La Bocana unit, based on geochronology, field evidence and geochemistry (Chapter III ; Riel et al., 2013; Riel et al., 2016). However, an evaluation of the total volume of melt produced by the La Bocana unit relative to the size of the plutons and its melt composition relative to their composition could help to quantify the contribution of the migmatites to the formation of the plutons.

# 3. Bulk rock chemistry

## 3.1. Methodology

Twenty-three samples from the Tahuín group were selected for bulk rock chemical analysis. The sampling strategy was to focus on the melt composition from the source in the migmatite to the emplacement in the plutons. Leucosomes were targeted in the migmatites as they represent the crystallisation of a melt derived from partial melting but also diatexites were selected, to see a potential difference between the two. Samples of granitoids without mafic enclaves or enclaves were targeted. From a large collection of samples (over 100), four samples of leucosomes were selected for the upper La Bocana, eleven samples for the Marcabelí pluton and two samples for the La Palmerita granitoid. This granitoid is a decametric outcrop located in the La Victoria unit, between the migmatites and the Marcabelí pluton (Fig. 1). In addition, 6 samples of shales were selected for the El Tigre unit from sediments. The goal was to obtain a representative composition of what could be the starting pelitic composition in the metapelitic sequence of the Tahuín group before metamorphism, assuming a similar depositional environment and sediment source though the sequence. The position of the samples is reported in Fig. 1.

The bulk rock chemical analyses were conducted at the Institute of Geological Sciences, University of Bern (Switzerland). Samples were disaggregated using a high-voltage SelFrag device, then dry-milled in an agate ring mill for 30 minutes, followed by a 15-minute milling of quartz sand to clean the equipment. Nanoparticulate pressed powder pellets (PPPs) were prepared using microcrystalline cellulose as a binder, following Peters and Pettke (2017). These PPPs were analysed using a laser ablation inductively coupled plasma mass spectrometer (LA-ICP-MS), comprising a GeoLas-Pro 193 nm ArF Excimer laser system and an ELAN DRC-e quadrupole mass spectrometer. Calibration was performed using GSD-1G reference material (Jochum et al., 2005), with GSP-2 as a secondary standard (Peters & Pettke, 2017; Pretorius et al., 2006). Accuracy was consistently better than 10%.

The PPPs were measured in single-spot mode with an energy density of 6 J cm$^{-2}$, a repetition rate of 10 Hz, and a beam size of 90 µm. Six analyses were conducted for each PPP, with pre-ablation cleaning using a larger spot size. Data were integrated over 50–60 seconds per analysis and reduced offline using SILLS software (Guillong et al., 2008). Detection limits were calculated according to Pettke et al. (2012), with internal standardization based on (i) assuming a fixed total of 100 wt% for major and trace elements, minus volatiles determined by loss on ignition, and (ii) assuming all Fe is present as FeO.

In addition to these analyses, bulk rock chemical data were collected from previous studies (Aspden et al., 1995; Riel et al., 2013; Riel et al., 2016; Vinasco

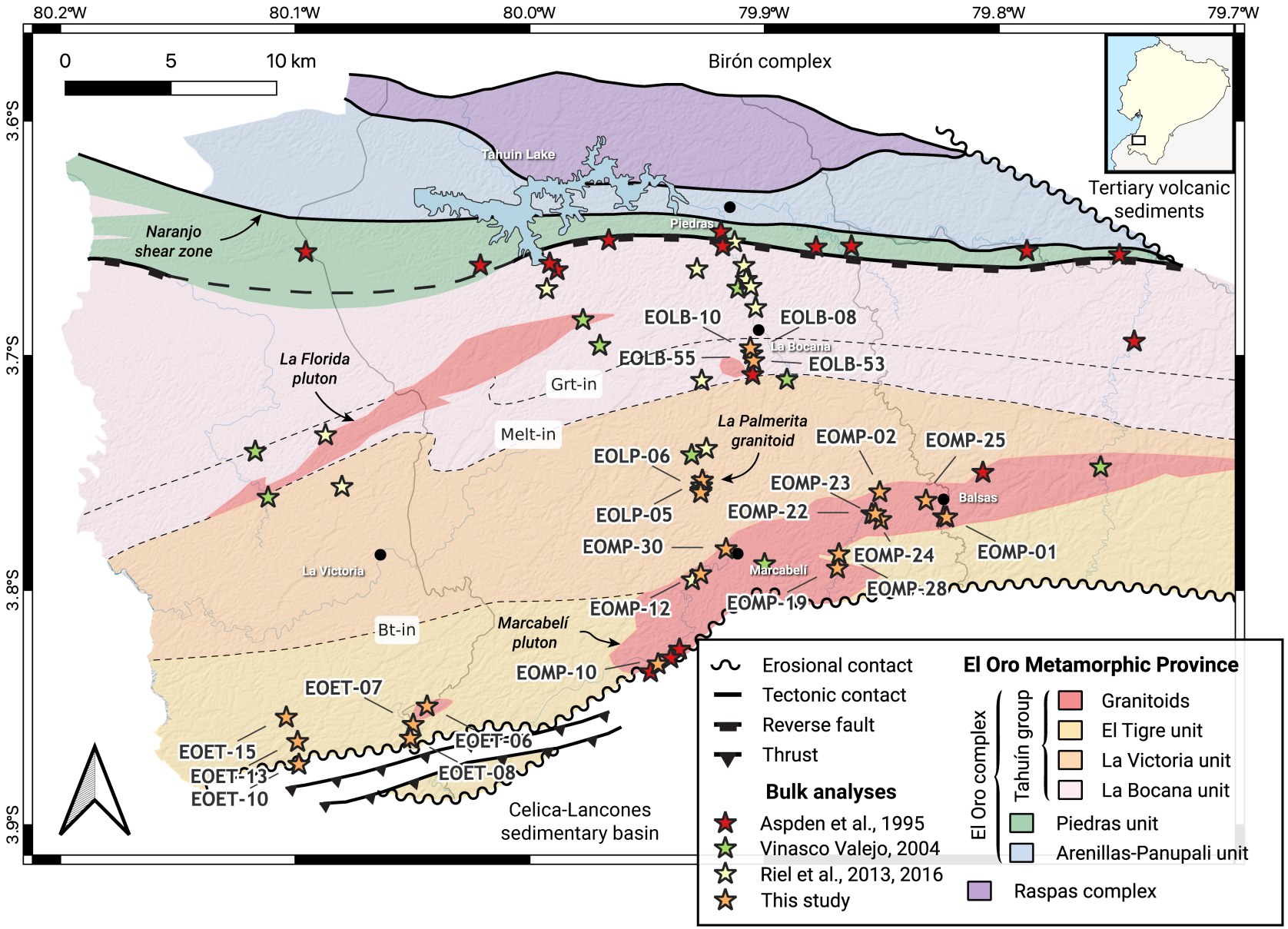


**Figure 1:** Simplified geological map of the western part of the El Oro metamorphic province. The stars represent the position of the samples used in this study. Orange stars are analyses produced in this study whereas other stars represent analyses from the literature (Aspden et al., 1995; Riel et al., 2013; Riel et al., 2016; Vinasco Vallejo, 2004). One analysis from the Piedras unit is located outside of the map on the East side of the massif, as well as the El Prado pluton. The map is based on field evidence and modified from Feininger (1978) and Riel et al. (2013).

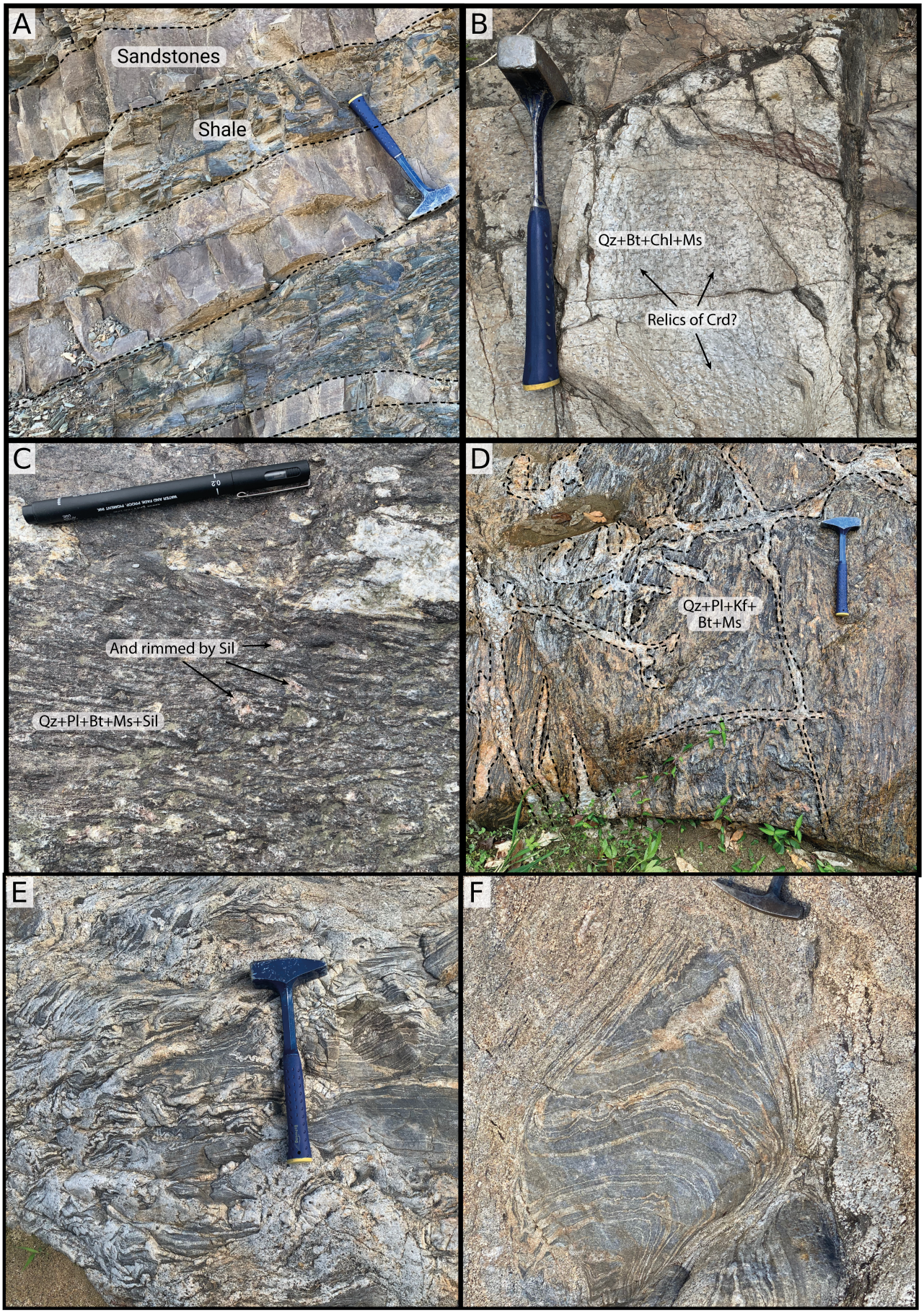
A
Sandstones
Shale
B
Qz+Bt+Chl+Ms
Relics of Crd?
C
And rimmed by Sil
Qz+Pl+Bt+Ms+Sil
D
Qz+Pl+Kf+
Bt+Ms
E
F

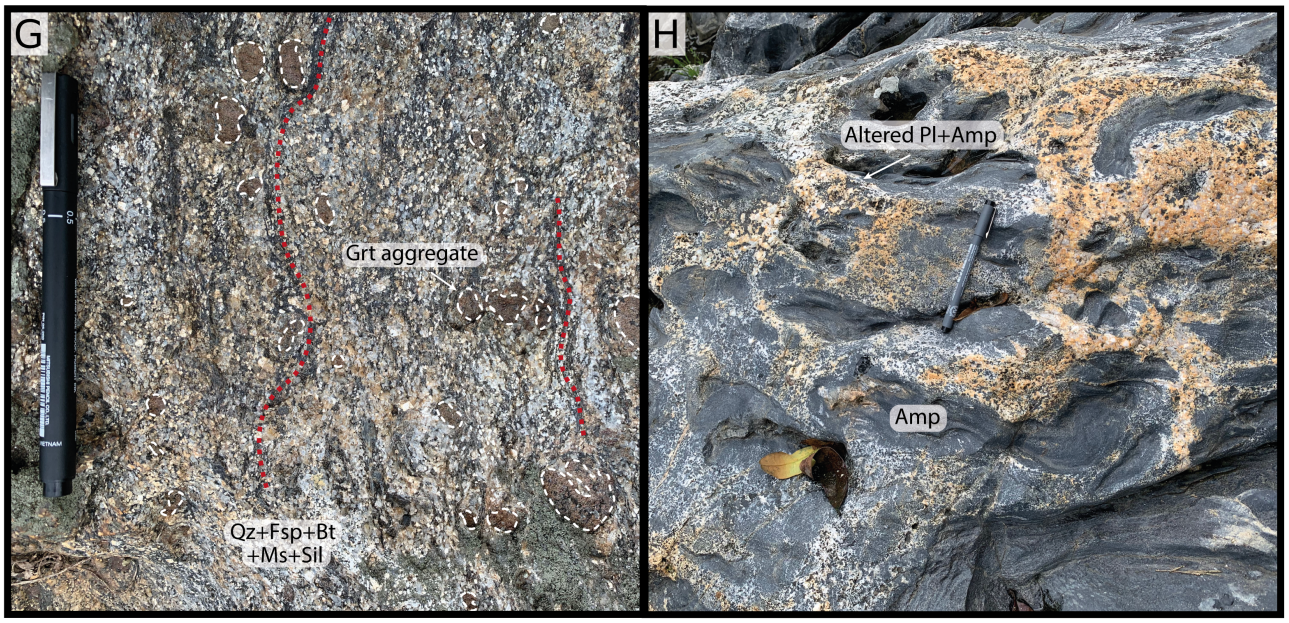


**Figure 2 :** Outcrop pictures of representative localities of the units of the Tahuín group, from low to high grades. A. Weakly metamorphosed sediments from the El Tigre unit showing an interbedded sequence of sandstones and shales. B. Spotted micaschist from the low grade of La Victoria unit. The porphyroblasts have been replaced by micas and chlorite but are interpreted as pseudomorphs of cordierite. C. Amphibolite facies metapelite from the La Victoria unit showing porphyroblasts of andalousite rimmed by sillimanite. D. Metatexite from the upper La Bocana unit showing net structure with leucosomes perpendicular to the main foliation. E. Schollen diatexite migmatite in the lower La Bocana unit. F Same locality as (E), showing evidence of flow foliation. G. Zoom on a diatexite from the lower La Bocana unit showing aggregate of peritectic garnets. H. Amphibolite showing diffuse contact with migmatites in the lower La Bocana unit, close to the contact with the metagabbro of the Piedras unit.

Vallejo, 2004), resulting in a total of 81 analyses, including 23 granitic and 31 migmatitic compositions. It is important to note that the La Bocana unit samples are migmatites, and the specific part sampled can greatly affect the whole-rock chemistry results. In this study, the four analyses for the upper La Bocana unit consist of 2 leucosomes and 2 diatexites, while the remaining analyses are from the literature. Consequently, accurately determining the specific portion of the migmatites analysed in these studies was not always feasible but the analyses selected are a majority of either diatexites or leucosomes.

## 3.2. Results

The results for the bulk analyses of the Tahuín group are shown in Figs. 4 and 5 for the major elements of the granitoids and metasediments, respectively. Spider diagrams of a selection of key trace and major elements of all the units is shown in Fig. 6.

Major element geochemistry of the pelitic sediments and metasediments shows that the low-grade sediments of El Tigre are slightly more Fe enriched than their metamorphic equivalent of the La Victoria and La Bocana units (Fig. 5). Most of the compositions of the upper La Bocana unit are outside the 80% percent volume contour of the kernel density estimate (KDE) of the worldwide metapelite database from Forshaw and Pattison (2023) for both the AFM and AKF diagrams, consistent with them being neosomes (or part of a neosome) and not restitic in composition. This is also the case, to a lesser extent, for the analyses of the lower La Bocana unit.

The geochemistry of the major elements of the granitoids shows that the majority of the analyses is moderately peraluminous (Fig. 4A and C) with low levels of alteration, as shown by the MFW (mafic, felsic, weathering) diagram from Ohta and Arai (2007) (Fig. 4B). This diagram allows the effects of differentiation and alteration on igneous rocks to be estimated by combining several indicators. They also have a low Mg# number of about 0.3 on average, and are part of a ferriferous association (Fig. 4D). There is no significant overlap between the migmatites of the upper La Bocana unit and the granitoids in terms of the aluminosity (Fig. 4A and C), whereas they show similar degree of maficity (Fe + Mg + Ti) (Fig. 4D).

Regarding the trace element data, the medians of

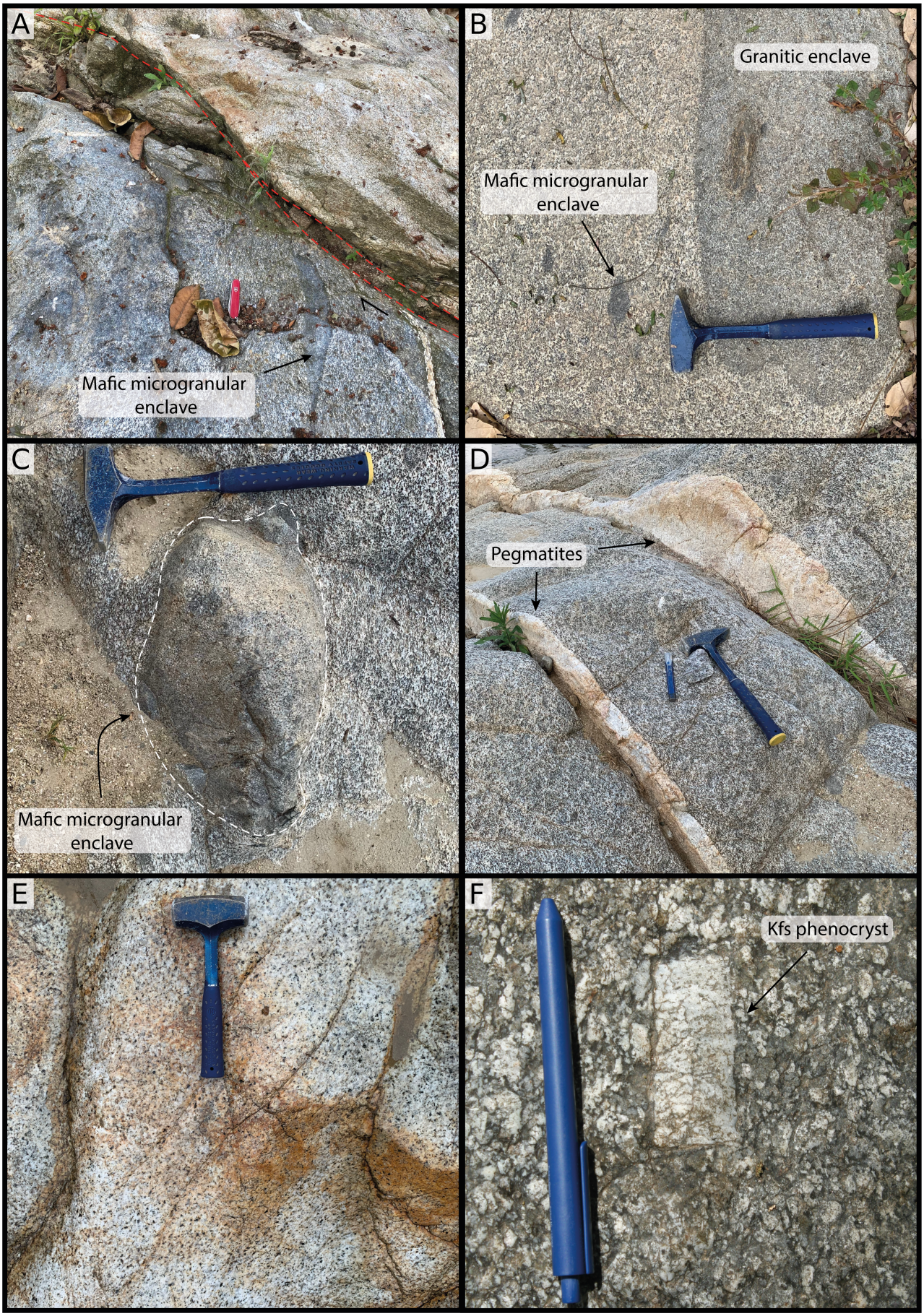
A
Mafic microgranular enclave
B
Granitic enclave
Mafic microgranular enclave
C
Mafic microgranular enclave
D
Pegmatites
E
F
Kfs phenocryst

**Figure 3 :** Outcrop pictures of representative localities of the Marcabelí pluton (A–D) and the La Florida pluton(E). A. Locality showing two types of granitoids in the Marcabelí pluton. The melanocratic granitoid shows kinematic indicators of deformation. The leucocratic granitoid is interpreted as posterior. Note the presence of a mafic microgranular enclave. B. Evidence of magma mingling. Locality close to (A). C. Large mafic microgranular enclave in the Marcabelí pluton. D. Presence of pegmatites in the Marcabelí pluton. Same locality as (C). E. Very leucocratic granitoid in the Marcabelí pluton. No presence of enclaves was found in the area. F. Large K-feldspar phenocryst in the La Florida pluton, characteristic of this pluton.

the sedimentary and metasedimentary samples from the El Tigre and La Victoria units show a relatively flat distribution when normalised to the upper continental crust (UCC) values (Rudnick & Gao, 2003), with a small depletion in Sr and Mo for both units and in Cu for the La Victoria unit relative to the other elements (Fig. 6A). Among the major elements, there is also a depletion in Ca and Na relative to UCC.

The trace element data of the granitoid samples show marked variation between samples, with the Marcabelí pluton providing enough samples to highlight the variation within the pluton itself (Fig. 6B), with variability Ba, Mo, Cu, . Two samples from the Marcabelí pluton show a similar trend to the sample from the La Palmerita granitoid, with similar depletion in V to Zn, with also a depletion in Mg. However, the median of the Marcabelí pluton shows a relatively flat distribution, with a stronger depletion in Cr, Ni, Sr, Mo, Sb and W.

The spider diagrams from the La Bocana unit are shown in Fig. 6C. Overall, the samples from the upper La Bocana unit show a stronger depletion relative to UCC compared to the lower La Bocana unit. The upper La Bocana samples show a positive Eu anomaly and a strong depletion in Mo and Sb. As the analyses from the lower La Bocana unit contain garnet, the proportion of garnet in the analysed rock may affect the bulk rock chemistry data, which may explain the observed variability in Mg compared to the upper La Bocana unit.

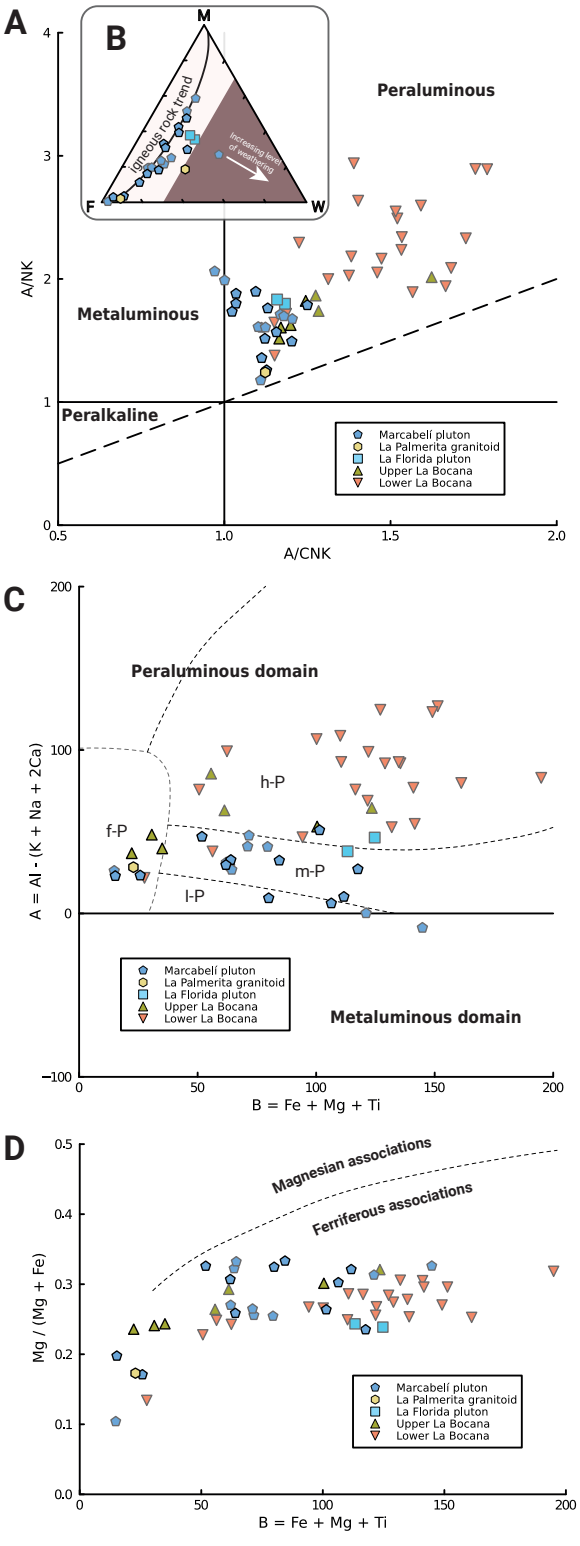


# 4. Thermal models for the El Oro complex

## 4.1. Methodology

To simulate a thermal history that is realistic with the petrological and geochronological data available for the El Oro complex, two 1D thermal models were created. These models explore two different mechanisms to reproduce the sharp change in the geothermal gradient observed in the peak P–T estimates occurring at

**Figure 4 :** Major elements geochemistry from the felsic rocks of the El Oro complex. A. A/CNK vs. A/NK diagram (Shand, 1943) [molar Al / (2Ca + Na + K) vs. molar Al / (Na + K)]. B. MFW diagram of Ohta and Arai (2007). This diagram is designed to show the effects of differentiation and alteration on magmatic rocks, by combining several indicators. M corresponds to mafic, F to felsic and W to weathering. The brown domain corresponds to W > 30%. The two analyses within this domain were deemed too weathered and discarded for the rest of this study. C. B–A diagram (Debon & Le Fort, 1983) [B = millications Fe + Mg + Ti vs. millications Al = Al - (K + Na + 2Ca)]. The subdivisions are from Villaseca et al. (1998): l-P, low peraluminous; m-P, moderately peraluminous; h-P, highly peraluminous; f-P, felsic peraluminous suites. D. B–Mg# diagram (Debon & Le Fort, 1988) [B = millications Fe + Mg + Ti vs. mole Mg / (Mg + Fe)]. Markers with black strokes are from this study whereas markers with grey strokes are data from the literature (Aspden et al., 1995; Riel et al., 2013; Riel et al., 2016; Vinasco Vallejo, 2004). The analyses from upper and lower La Bocana are not granitoids but migmatites, some of which are leucosomes, melanosomes or restites.

the transition between the upper amphibolite-facies crust (La Victoria unit) and the migmatite units (La Bocana unit). The geothermal gradient corresponding to peak metamorphic conditions changes from 45 °C/km to about 10–15 °C/km at a depth of 17 km (Riel et al., 2013; Riel et al., 2016).

The two geothermal models are solving the following heat equation:

$$\rho \left[ C_p(T) + \frac{\partial \phi}{\partial T} Q_L \right] \frac{\partial T}{\partial t} = \frac{\partial \left[ k(T) \frac{\partial T}{\partial x} \right]}{\partial x} + A, \qquad (28)$$

where $T$ is the temperature (K), $t$ is time (s), $\rho$ is the rock density ($\mathrm{kg\,m^{-3}}$), $C_p$ is the specific heat capacity ($\mathrm{J\,kg^{-1}\,K^{-1}}$), $\phi$ is the melt fraction, $Q_L$ is the latent heat ($\mathrm{Jkg^{-1}}$), $k$ is the thermal conductivity ($\mathrm{W\,m^{-1}\,K^{-1}}$) and $A$ is the radioactive heat ($\mathrm{Wm^{-3}}$).

Both models are using temperature-dependent thermal conductivity and specific heat capacity following Whittington et al. (2009), and constant latent heat and radiogenic heat production. The melt fraction is computed using a quadratic expression to compute the latent heat (e.g. Tierney et al., 2016). The common parameters of the models are shown in Table 1. The initial temperature is defined by the geothermal gradient of 25 °C/km and the temperature at the surface is fixed to 0 °C. This corresponds to an average geotherm for a continental crust (e.g. DiPietro, 2013). The bottom boundary is model and time dependent and is described in more details bellow.

The two models explore 2 different mechanisms of heat transport: (i) advection of melt from deep to middle crust, referred here-after as the advection model, and (ii) transport of heat through a convection cell in the middle crust, referred here-after as the convection model. The advection model is mainly following the formulation of Depine et al. (2008) and the convection model is based on the formulation from Riel et al. (2016), already applied to the El Oro complex.

The **advection model** consists of a 30 km thick continental crust. The total duration of this model is 15 Myr. The first 25 km are composed of a felsic crust and the last 5 km, of a mafic crust. At the beginning of the simulation, a heat flux of 150 $\mathrm{mW\,m^{-2}}$ is imposed at the base of the model. This corresponds to a very high Moho heat flux, used to account for mantle upwelling and decompression of the asthenosphere (e.g. Jaupart & Mareschal, 2007). Melt is extracted from the bottom of the model when the melt fraction exceeds 7 vol.% (e.g. Rosenberg & Handy, 2005) and is emplaced randomly at a crustal depth calculated using a normal distribution centred at km and with a standard deviation of 1 km ($\mathcal{N}(19,1)$) to simulate slightly depths of emplacement. Melt extraction is simulated by transporting the heat associated with it and by multiplying it by a melt focusing factor ($M$) equal to 10. This factor is defined to account for a 3D effect of melt emplacement to generate more heat than what can be produced from a 1D model (Depine et al., 2008). This parameter was fixed in the advection model such that the amount of melt emplaced during the simulation is around 5 km. This approach assumes that melt transport is both thermally efficient and instantaneous. The crust located beneath the emplacement depth is then displaced downward to maintain mass balance. After each extraction event, the temperature at the base of the model is reset to the solidus and no effect from melt-depletion is taken into account. This approach can be seen as considering continuous fluid replenishment at the base of the model or as accounting for 2- or 3D melt generated outside the 1D model (e.g. Connop et al., 2024). After 10 Myr, a thermal anomaly at 1250 °C is emplaced between 25 and 28 km to simulate the gabbro emplacement of the Piedras unit. At this stage, the deeper crust is assumed to have been delaminated and the melt extraction and emplacement is stopped. The temperature at the bottom of the model is fixed to 1250 °C for 0.3 Myr, after which the temperature is set to 300 °C to account for the underplating of the blueschists from the Arenillas-Panupalí unit and the

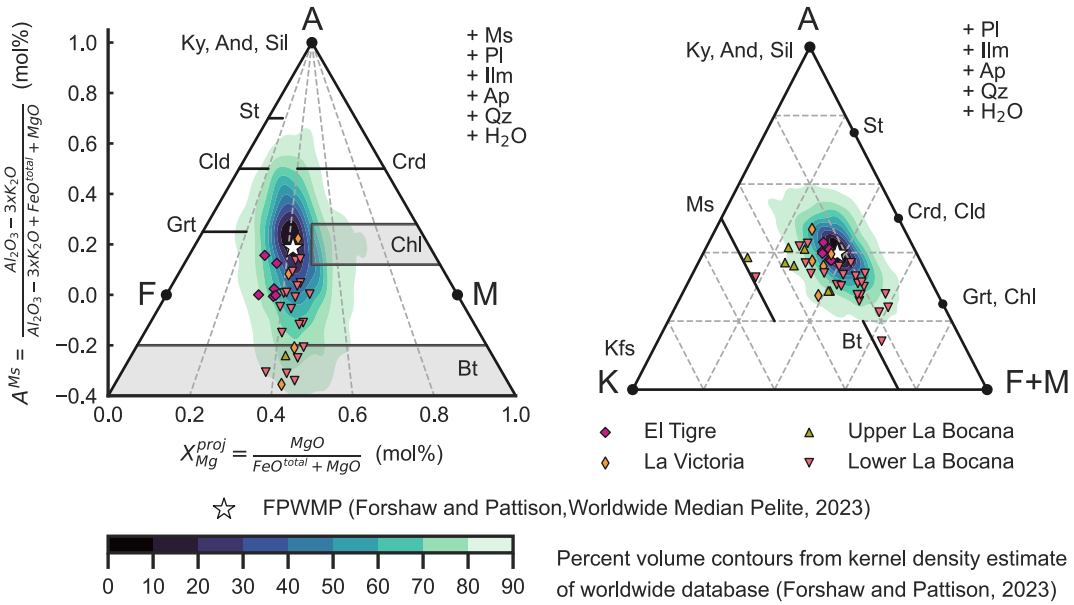


**Figure 5:** Distribution of the whole-rock analyses of the metasediments from the Tahuín group in the El Oro complex. Five analyses of the upper La Bocana are outside of the projection. A. AFM diagram from J. B. Thompson (1957). B. AKF diagram after Eskola (1915) with modifications from Spear (1993). The contours represent percentages of analyses from the global metapelite database, as determined through kernel density estimates based on the worldwide metapelite database from Forshaw and Pattison (2023).

**Table 1:** Parameters used in the thermal models

| Parameter | Symbol | Definition | Value | Unit |
|---|---|---|---|---|
| Rock density | $\rho$ | | felsic: 2700, mafic: 3300 | $\mathrm{kg\,m^{-3}}$ |
| Specific heat capacity | $C_p$ | Whittington et al. (2009) | T-dependent | $\mathrm{J\,kg^{-1}\,K^{-1}}$ |
| Thermal conductivity | $k$ | Whittington et al. (2009) | T-dependent | $\mathrm{W\,m^{-1}\,K^{-1}}$ |
| Latent heat | $Q_L$ | | $400 \times 10^3$ | $\mathrm{J\,kg^{-1}}$ |
| Radioactive heat | $A$ | | $2 \times 10^{-6}$ | $\mathrm{W\,m^{-3}}$ |
| Solidus temperature | $T_s$ | | felsic: 680, mafic: 820 | °C |
| Liquidus temperature | $T_l$ | | felsic: 1150, mafic: 1200 | °C |
| Melt fraction | $\phi$ | $\phi = 1.0 - \left(\frac{T_l - T}{T_l - T_s}\right)^2$, $\phi = 1.0$ if $T > T_l$, $\phi = 0.0$ if $T < T_s$. | T-dependent | - |

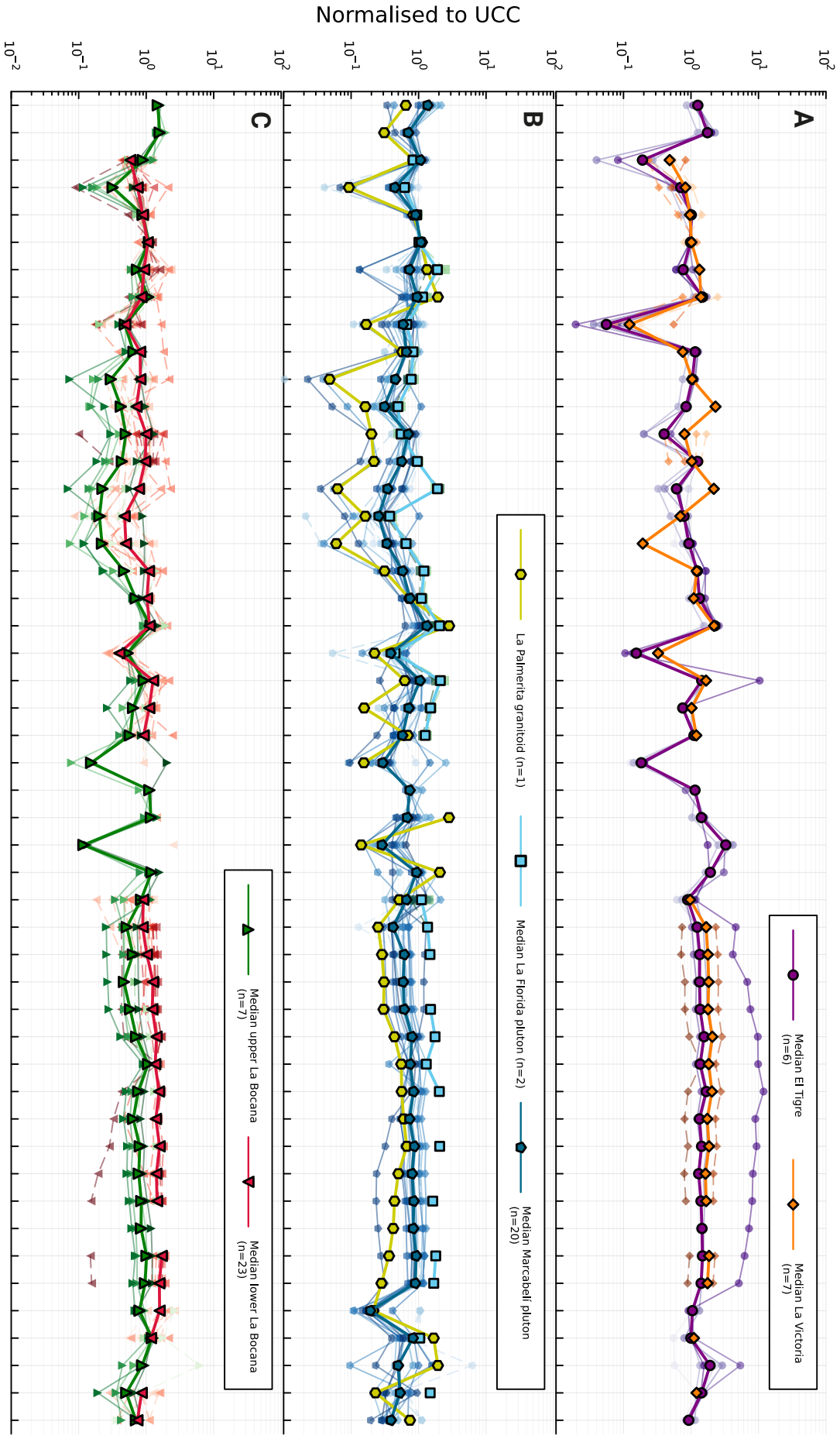


**Figure 6:** Whole-rock spider diagrams of trace elements and some major elements from the different units of the Tahuín group. Each element is normalised to the upper continental crust (UCC) estimate from Rudnick and Gao (2003). From top to bottom, low grade to medium grade metapelites and metapsamites from the El Tigre and La Victoria units (A), granitoids from the El Oro complex (B), migmatites from the La Bocana unit (C). Solid lines are analyses from this study, whereas dashed lines are data from the literature (Aspden et al., 1995; Riel et al., 2013; Riel et al., 2016; Vinasco Vallejo, 2004).

subsequent cooling of the sequence.

The **convection model** is based on the model and parameters from Riel et al. (2016) for the El Oro complex. The initial model was modified to include a prior heating phase before the activation of the convection cell, to incorporate the new geochronological data presented in Chapter III, which shows a longer heating event than previously estimated. The model is made of a 28 km thick continental crust for a total duration of 20 Myr. As with the advection model, the first 25 km are composed of a felsic crust whereas the bottom part is composed of a more mafic crust. The bottom boundary is similar to the advection model, with an elevated heat flux of 150 $\mathrm{mW\,m^{-2}}$. After 8 Myr, similarly to the advection model, a thermal anomaly at 1250 °C is emplaced between 25 and 28 km to simulate the gabbro emplacement of the Piedras unit and the bottom boundary is fixed to 1250 °C. At that point in time, the thermal effect of a convection cell is modelled between 17 and 25 km. This is done using the same approach as Riel et al. (2016), with a parametrisation based on the Nusselt-Rayleigh number relationship (see bellow). After 2 Myr, the temperature at the bottom is set to 300 °C to account for the underplating of the blueschists from the Arenillas-Panupalí, similarly to the advection model.

The Rayleigh number is a dimensionless number, which measures the driving force for convection relative to the damping effects of thermal diffusion and viscosity (e.g. Bunge et al., 1997):

$$Ra = \frac{\rho g \beta \Delta T h^3}{\eta \alpha}, \tag{29}$$

where $g$ is the gravity acceleration (9.81 $\mathrm{m\,s^{-2}}$), $\beta$ is the thermal expansivity ($3 \times 10^{-5}$ $\mathrm{K^{-1}}$), $\Delta T$ is the temperature variation across the convective layer (100 °C), $h$ is the thickness of the convection cell (8 km), $\eta$ is the viscosity ($1 \times 10^{15}$ Pa s) and $\alpha$ is the thermal diffusivity ($1 \times 10^{-6}$ $\mathrm{m^2\,s^{-1}}$). These values give $Ra \approx 40684$ for this model.

The Nusselt number is also a dimensionless number which represents the ratio of convective to conductive heat transfer across a boundary, here between the convection cell and the rest of the model (e.g. Jaupart & Mareschal, 2010):

$$Nu = \frac{q}{k\frac{\Delta T}{h}}, \tag{30}$$

where $k$ is the thermal conductivity and $q$ is the convective flux ($\mathrm{W\,m^{-2}}$), our unknown.

Both numbers can be linked with the following expression, assuming free-surface boundary conditions around the convection cell (Turcotte and Schubert (2014)):

$$Nu = 0.120 Ra^{\frac{1}{3}} \tag{31}$$

Using eq. (31) to obtain an expression for $Nu$, $q$ can be isolated in eq. (30). Combining the contribution of heat transport from the convection and the conduction (Riel et al., 2016), the hyperdiffusity (K) is defined as:

$$K = \frac{hq}{\Delta T} + k. \tag{32}$$

$K$ replaces the value of $k$ in eq. (28) between 25 and 28 km, at the emplacement of the convection cell.

Using these formulations for the advection and the convection models, eq. (28) is solved numerically. It is first discretised in space using finite differences and the resulting system of ordinary differential equations (ODEs) is then solved using the second order orthogonal-Runge-Kutta-Chebyshev method (ROCK2), a stabilised explicit method (Abdulle & Medovikov, 2001). This is done using DifferentialEquations.jl (Rackauckas & Nie, 2017), an ODE solver written in the Julia programming language (Bezanson et al., 2017). See Code availability section for more details.

## 4.2. Results

The results of both thermal models are shown in Fig. 7. Both models present a maximum temperature that is mostly within uncertainty with the profile observed in the $P$(depth)–$T$ estimates from Riel et al. (2013) and Riel et al. (2016) and the maximum temperature of the convection model is very close to the one obtained by Riel et al. (2016) (Fig. 7A). These models neglect the effect of the emplacement of granitoids in the upper crust, such as the Marcabelí pluton, which would help increasing the temperature in the upper part of the model to be close to the two shallow $P$–$T$ estimates of the sequence.

Even though both models satisfy the condition of reproducing the maximum $P$–$T$-$t$ estimates, they produce different ($P$)–$T$ paths as shown by Fig. 7B. In the advection model, the temperature increases in the middle crust results from melt injection associated with a hot mantle upwelling, leading to a steady increase over 5 Myr. The emplacement of the gabbroic intrusion representing the Piedras unit in this case is

not responsible for the sharp change in the geothermal gradient observed in the *P–T* estimates. In contrast, the convection model attributes the temperature increase to the activation of a convection cell triggered by the emplacement of a gabbroic intrusion, causing a more pronounced increase over a shorter duration of 2 Myr. The peak temperature recorded by both models are close to each other, both in time and temperature values, if the blueschist underplating event is used as a reference frame. Cooling history after this event is similar for both models. The differences in the duration of the gabbro intrusion of the Piedras unit satisfy in both cases the current geochronological constrains on the gabbroic magmatic emplacement, which record high uncertainty based on geochronology from two studies, as reported in Chapter III: $^{206}Pb/^{238}U$ age from Noble et al. (1997) of $221^{+18}_{-16}$ Ma (MSWD = 0.015 (R), $n$ = 2) and from Cochrane et al. (2014), using LA-ICP-MS, yielding 222.7 ± 6.3 Ma (MSWD = 1.90, $n$ = 17).

# 5. Coupling thermal modelling and phase equilibrium modelling

To study the link between the granitoids and the migmatites in the El Oro complex, the convection model was coupled to phase equilibrium modelling based on Gibbs free energy minimisation to simulate the prograde metamorphic history of a middle crust section undergoing partial melting. The choice of the thermal model is not trivial, because melt processes are *P–T* paths dependent in the case of open system (Mayne, Stevens, & Moyen, 2020). In this case, both thermal models have the same isobaric *P* conditions, and record similar peak *T*. As the focus of this study is on melt composition and melt volume, it is assumed that both thermal models should produce fairly similar results.

## 5.1. Methodology

In addition to the initial conditions and thermal parameters used in the convection model (see section 4.1 for more details), bulk rock compositions are required to allow the stable phases to be predicted at each node of the model using Gibbs free energy minimisation.

The rock model was designed based on field observations. The crustal section was composed of a repeated succession of three equally sized interbedded layers: a quartzitic, a semi-pelitic, and a pelitic layer. Each layer thickness was ∼140 m in the model, with a total number of layers corresponding to 200 nodes. Since the bulk compositions of the La Bocana unit represent the end-product after partial melting, and may have undergone melt extraction or addition, they are not suitable for modelling the prograde metamorphic history. Instead, pelitic and semi-pelitic compositions were selected based on the assumption that the depositional environment of the sediments from La Bocana unit was similar to these of the La Victoria and El Tigre units and thus had a similar composition before partial melting. The pelite composition was determined by calculating the median composition of each oxide from the El Tigre and La Victoria units. The semi-pelitic composition was obtained from sample EOET-08 from the El Tigre unit, which has a high $SiO_2$ content of 72.48 wt% and an intermediate composition between a pelite and a quartzite. For the quartzite composition, an average composition was used (F. W. Clarke, 1924). As this layer is expected to be non-reactive and mainly composed of quartz, an average composition outside of the El Oro complex was sufficient for the need of the models. For the pelite and semi-pelite, the $Fe^{3+}$ content was assumed to be 10% of the total molar iron. This value is based on estimates of Fe3+ in metapelitic minerals combined with their modal abundances given that previously reported titrimetric measurements should be considered maximums (Forshaw, unpublished data). The three compositions used are reported on table 2.

**Table 2:** Melt compositions (in mol) used in the models. 1: Median composition from the bulk compositions of the El Tigre and La Victoria units. 2: Semi-pelite from the El Tigre unit (sample EOET-08). 3: Quartzite from F. W. Clarke (1924).

| Oxide (mol) | Pelite[1] | Semi-pelite[2] | Quartzite[3] |
|---|---|---|---|
| $SiO_2$ | 75.15 | 81.42 | 93.09 |
| $TiO_2$ | 0.6 | 0.56 | 0.01 |
| $Al_2O_3$ | 10.58 | 7.58 | 1.9 |
| $Fe_2O_3$ | 0.6 | 0.5 | 0 |
| FeO | 5.44 | 4.95 | 2.91 |
| MnO | 0.04 | 0.01 | 0.01 |
| MgO | 3.35 | 2.06 | 0.26 |
| CaO | 0.36 | 0.20 | 0.01 |
| $Na_2O$ | 0.85 | 0.97 | 0.14 |
| $K_2O$ | 3.03 | 2.20 | 2.50 |
| $H_2O$ | 50 | 50 | 50 |

To predict the phase equilibrium for each layer, the Gibbs energy minimisation solver MAGEMin was used (Riel et al., 2022) with the

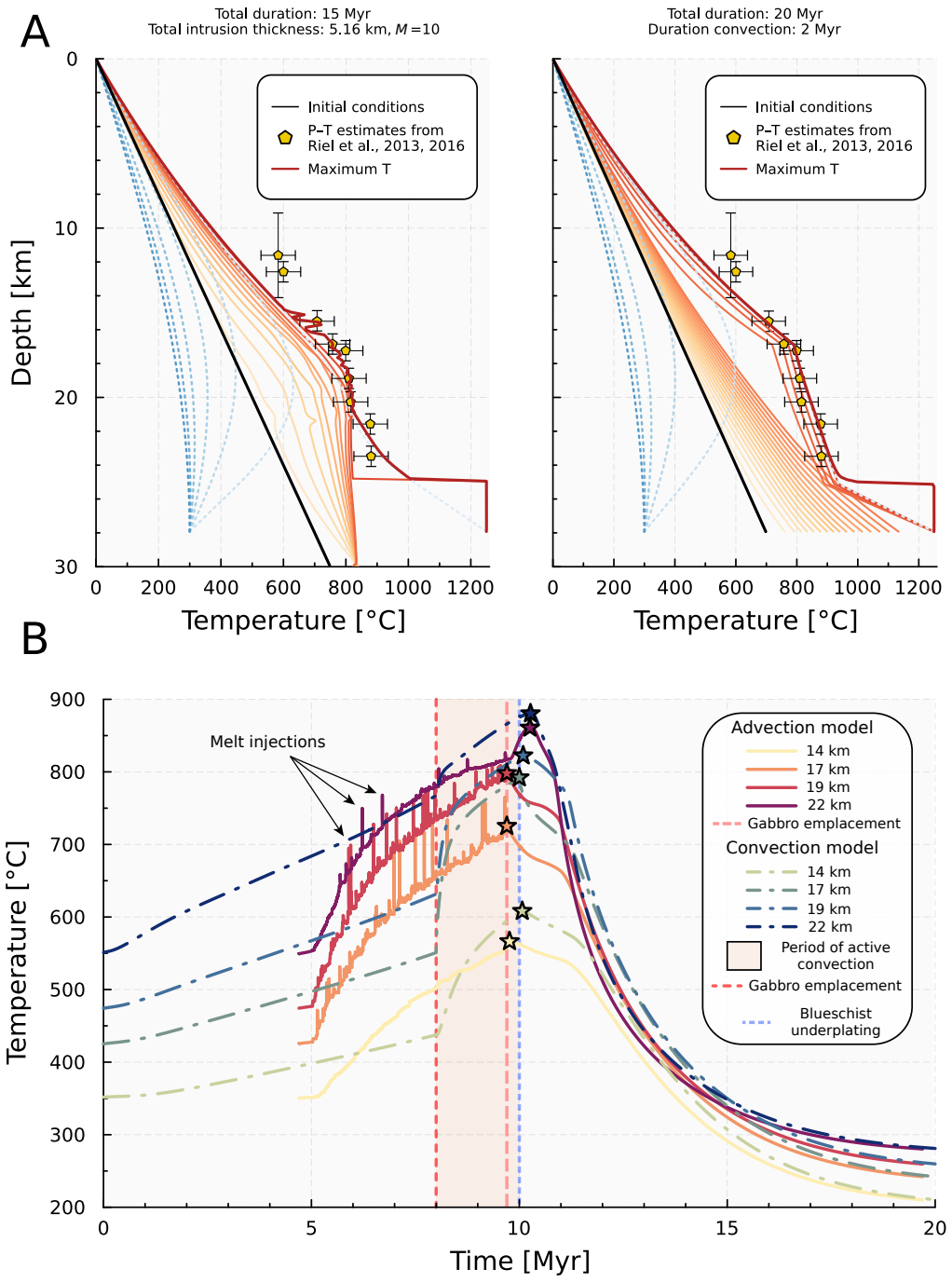


**Figure 7:** Thermal models for the El Oro complex. A. On the left, an advection dominated model for a total duration of 15 Myr, where melt produced at the bottom of the model is extracted when 7 vol% of melt is reached, and emplaced randomly following a normal distribution centred at 19 km ($\mathcal{N}(19,1)$) using a melt focusing factor of 10. On the right, a convection dominated model running for 20 Myr, where a convection cell is active between 25 and 28 during 2 Myr. Orange to red lines represent temperature at one timestep before the cooling of the sequence, whereas light to dark blue dotted lines are temperature during the cooling. Each orange to red lines are separated by 0.5 Myr whereas light blue to dark blue doted lines are separated by 1.5 Myr. Black lines are the initial conditions and correspond to an initial geotherm of 25 °C/km. Bold dark red lines correspond to the maximum temperature reached during the model and are compared to the peak temperatures recorded by the *P–T* estimates from Riel et al. (2013) and Riel et al. (2016). As the distance from each sample is known, the reported uncertainty on the depth of the *P–T* estimates are only 1 km, which can be considered as a relative uncertainty with respect to the total uncertainty of around 3 km per *P–T*. B. Time evolution of temperature of both models at specific depths. Since the models have different total durations, the starting time of the advection model is shifted so that the blueschist underplating event occurs at the same time in both models. Each line represents the temperature at a particular depth within the models. Stars indicate peak temperature condition for each depth, excluding spikes caused by melt injections in the advection model. See section 4.1 for more details on the settings of both models.

$MnO–Na_2O–CaO–K_2O–FeO–MgO–Al_2O_3–SiO_2–H_2O–TiO_2–O_2$ (MnNCKFMASHTO) system along with the internally consistent database of Holland and Powell (2011), and the set of solution solid models for metapelites (R. W. White, Powell, Holland, et al., 2014; R. W. White, Powell, & Johnson, 2014).

The coupled model was written in Julia (see Code availability section for access to the code). The strategy to couple phase equilibrium modelling and the convection thermal model, was to call the Gibbs energy minimizer only if an increase of 5 °C or more in the layer was reached since the previous minimisation. This value represents a small overstep which introduces a delay in the reactivity of the system to reach chemical equilibrium. This was done both to limit the number of calls per layer and to mimic a possible threshold needed to reach equilibrium. In that way, MAGEMin was called only during the prograde history, when $T$ is increasing. MAGEMin was called only for nodes with a depth between 8.5 and 25 km, to avoid low-grade metamorphic conditions and to focus on the preserved sequence of the Tahuín group, given that part of the crust that was supposedly located at the current emplacement of the Piedras and Arenillas-Panupalí units is currently unknown. The pressure used in the model is considered constant and to be entirely lithostatic. It was calculated by integrating the 1D profile based on a constant density of 2700 ($kg\,m^{-3}$). In addition to that, 0.1 GPa was added to take into account the increase in density in the crust with depth. No prograde mineral fractionation was considered in the model, although it can affect significantly the modal phase predictions (Lanari & Engi, 2017). After each minimisation, if a water phase is predicted stable, it was fractionated from the system to prevent melting in presence of water in excess. If melt was predicted with more than 7 vol% relative to the total volume of the layer, 6 vol% was extracted and removed from the system, effectively keeping 1 vol% of melt in the layer. The value of 7 vol% represents the volume of melt needed to reach the melt connectivity transition, as defined by Rosenberg and Handy (2005). The exact value of melt connectivity has been shown to not be critical for this type of modelling, as long as melt is extracted (Mayne, Stevens, & Moyen, 2020). The amount of melt staying in the rock represents the melt remaining on grain boundaries after each drainage event (e.g. Korhonen et al., 2013; Yakymchuk & Brown, 2014). After each time that MAGEMin is called, the stable phase assemblage, its composition, and the composition of the melt if it was extracted is stored, and the volume of the layer is adjusted to take into account for the melt loss. This change in volume is necessary to accurately calculate the volume of melt extracted if the layer encounter another melting extraction event. However, there was no feedback between phase equilibrium model and the thermal model. For simplicity, the density variations and the thermal properties such as heat capacity and latent heat of the reactions were not taken into account in the thermal model. The change in lithostatic pressure after extraction was also neglected, as it was considered that the extracted melt is emplaced in the upper crust maintaining the layer at the same depth. This assumption is debatable for layers that are situated on top of the layer where the melt is extracted. However, melting processes are $T$ dominated, with steep $dP/dT$ slopes, as described by Clapeyron equation (e.g. Johnson et al., 2021). As melting processes are the focus of this study, the lithostatic pressure was considered constant for each layer through the duration of the model. For the same reason, the potential whole-rock displacement induced by the convection cell was not taken into account, and the change in $P$, or the possible mixing with different layers induced, was neglected. The coupling between the thermal model and the Gibbs free energy minimiser MAGEMin is summarised in Fig. 8.

Different scenarios were tested to assess the impact of melt producing reactions and segregation of melt volume and composition. The two primary melting reactions in water-undersaturated metapelites involve the breakdown of muscovite and biotite (e.g. Breton & Thompson, 1988; Gardien et al., 1995; Pickering & Johnston, 1998). To explore the impact of both reactions on melt production and composition, one model was performed with only the extraction of melt produced by the Ms-breakdown reaction, referred to as the muscovite model, whereas a second model did not discriminate between the type of melting reaction for the extraction and is referred to as the biotite model. To also test the effect of excess water on melting, each of these two models were additionally also performed while introducing 5 moles of $H_2O$ at each minimisation. As free water is still removed at the end of each minimisation, this corresponds to adding 5 moles of $H_2O$ above the water-saturation level if water was predicted stable at the previous minimisation step, or adding water in an undersaturated system if water was not predicted at the previous step. This is done to explore intermediate scenarios of melt production between pure water-flux melting

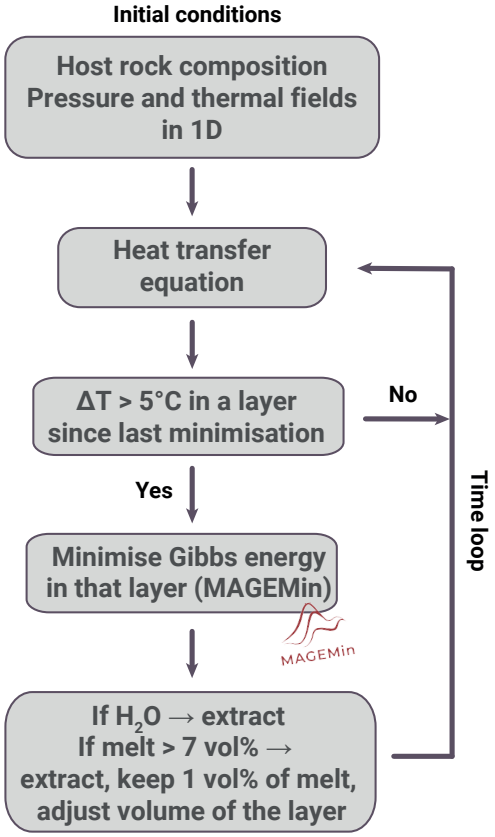


**Figure 8:** Summary of the steps of the coupling between the thermal model and thermodynamics using MAGEMin.

and pure dehydration-reaction melting, as it has been shown that a small amount of excess water can lead to an important increase on the amount of volume produced while still be in a dehydration-reaction melting dominated system (Schwindinger et al., 2019). The two models are referred to as the excess water muscovite and excess water biotite models. In addition to these four models, the effect of fractional crystallisation was explored, using the biotite model. This involved removing varying proportions of plagioclase, K-feldspar, or quartz from the crystallized melt at an intermediate depth of 13 km, with the temperature at that depth defined by the thermal model at the time of melt extraction. These minerals and proportions were chosen based on Bowen's crystallisation sequence for felsic melts (Bowen, 1928). Lastly, the effect of garnet entrapment was explored in one model where 70% of the garnet present in the phase assemblage of the layer of interest was retained in the melt during extraction using the biotite model. The contribution to the melt volume of the mineral entrapment was neglected in this case. These eight models, representing various scenarios, were designed to explore different processes associated with the production of melt by partial melting and the transport towards the pluton. The details of each model are summarised in Table 3.

## 5.2. Results

The integrated volume of melt extracted from the eight different models is reported in Fig. 9A. The number of melt extraction step per layer, with their relative volume is reported in Fig. 9B. Modebox diagrams of the three different lithologies, pelitic, semi-pelitic and quartzitic, for three different depths, are shown in Fig. 10 for the biotite model, in Fig. 11 for the muscovite model, in Fig. 12 for the excess water biotite model and in Fig. 13 for the excess water muscovite model. The depths chosen are about 15, 18 and 21.5 km, and correspond to layers reaching a maximum temperature of about 660 °C, 800 °C and 870 °C, respectively. The variation in the composition of the melt extracted in the eight different models are shown on an A/CNK vs. A/NK and on a B-Mg# diagram (similar to Fig. 4) on Fig. 14. Finally, the composition of the predicted melt composition is reported on a total alkali-silica (TAS) diagram (Bas et al., 1986; Le Maitre, 1989) in Fig. 15A and is compared to the whole-rock chemistry data of the granitoids of the El Oro complex. The same diagram is used to compare the final composition of the layers in the models, with the compositions from the migmatites of the La Bocana unit (Fig. 15B).

Concerning the volume of melt extracted, the models assume a rock column with a 1x1 metre base, so the volume corresponds to a melt thickness, and these terms are used interchangeably in the subsequent sections. The results show that the difference in volume produced from the four main models, the muscovite, the biotite and their equivalent with excess water, is significant. For a crustal section of approximately 15 km producing melt, the muscovite-breakdown reaction yields about 600 meters of melt thickness (Fig. 9). The melt volume generated from the biotite-breakdown reaction, estimated by the difference between the biotite and muscovite models, is slightly higher, with around 750 m. The excess water biotite melting model produces approximately 3450 meters of melt. In the fractionated crystallisation scenarios, up to one-third of the melt can crystallize before emplacement. In the model involving the entrapment of peritectic garnet, the volume change due to the addition or removal of the peritectic minerals from the melt and rock is neglected, but garnet entrapment has minimal impact on the fertility of the

**Table 3:** Summary table of the differences between the eight models obtained by coupling thermal and phase equilibrium modelling. The biotite model is the reference model used to highlight the additions of each model.

| Name of the model | Comparison to the biotite model | The specificity affects the composition of the layers compared to the biotite model |
|---|---|---|
| Biotite model | - | - |
| Muscovite model | Only extract melt from Ms dehydration reaction | Yes |
| Excess water biotite model | Add 5 mole of $H_2O$ before each minimisation | Yes |
| Excess water muscovite model | Only extract melt from Ms dehydration reaction Add 5 mole of $H_2O$ before each minimisation | Yes |
| Garnet entrapment model | Entrapment of 70% of Grt with melt extraction | Yes |
| Low fractional crystallisation model | Crystallise 30% of Pl and 10% of Kfs from the melt at 13 km of depth | No |
| Intermediate fractional crystallisation model | Crystallise 50% of Pl, 30% of Kfs and 10% of Qz from the melt at 13 km of depth | No |
| High fractional crystallisation model | Crystallise 80% of Pl, 50% of Kfs and 30% of Qz from the melt at 13 km of depth | No |

layer, producing a similar melt volume compared to the biotite model. In all models, the quartzitic layers failed to generate sufficient melt for extraction, rendering about one-third of the melting crust infertile—a likely overestimation. Therefore, the predicted melt volumes can be considered as lower-limit estimates.

With respect to the phase assemblages predicted for the different layers at different depths, the expected muscovite-breakdown and biotite-breakdown reactions are observed in the pelitic and semi-pelitic layers (Figs. 10, 11, 12, 13). Important differences between the muscovite and biotite with their excess water equivalents can be observed in the pelitic and semi-pelitic layers. The most important difference is the high proportion of melt predicted in the excess water models, which is an expected consequence (e.g. Schwindinger et al., 2019; Weinberg & Hasalová, 2015b). Consumption of K-feldspar is also observed in the excess water models during biotite destabilisation. Furthermore, the excess water biotite model predicts a significant amount of cordierite after the complete destabilisation of biotite, which is not observed in the excess water muscovite model. In addition, the fact that water as a phase is only stable with melt at a few stages in the excess water models shows that the melt is not often saturated with water, and is consistent with the aim of studying the effect of excess water and not water-flux melting. Finally, the quartzitic layers remain non-reactive in all models. Regarding the chemical composition of the different layers at the end of the models, they generally show a good compatibility with the whole-rock analyses of the La Bocana unit at the exception of the excess water biotite model, from which the consumption of K-feldspar and plagioclase produces a composition very poor in alkali (Fig. 15B). The muscovite and biotite models show that melt extraction doesn't reduce the overall silica content of the rock, as the melt has a similar content to the protolith, but reduces the alkali content. The garnet entrapment model shows a distinct trend from the protolith compositions, with an increase in silica and little effect on alkali. This is related to the composition of the garnet that is fractionated from the system during the melt extraction step along with the melt composition.

Regarding the composition of the extracted melt,

the results show that the melts are granitic and peraluminous in composition (Figs. 14 and 15A). Overall, the garnet entrapment model shows the most distinctive trend. This entrapment model shows 2 distinct populations, the melt extracted during muscovite-breakdown, when no garnet is stable, and the melt with actual garnet entrapment. This entrapment induces a significant increase in the Mg# and the maficity, as garnet contains significant amount of Mg and Fe (Fig. 14A and B). This is also observed by the decrease in alkali content in Fig. 15. The fractional crystallisation models show a different trend, with an increase in A/CNK (Fig. 14A) and a decrease in alkali content (Fig. 15A) compared to the biotite model, consistent with the fractional crystallisation of plagioclase and K-feldspar. The biotite, muscovite and excess water muscovite models all show similar compositions with very little variations whereas the excess water biotite model shows a wider range due to the important change in bulk chemistry of the layers induced by the important quantity of melt extracted. When compared with whole-rock analyses of granitoids from the El Oro complex, the models don't reproduce the chemistry of the natural data except for a few analyses. The models have a consistently higher alkali content, lower Mg# number and lower maficity compared to the natural igneous rocks, and show very little variation compared to what is observed in the granitoids (Figs. 14A and B and 15A). However, with the exception of the excess water biotite model, the predicted final composition of the layers is compatible with the range of compositions observed in the La Bocana unit (Fig. 15B).

Finally, the coupling with the thermal model allows the temporal evolution of the different models to be assessed. For example, in the muscovite and biotite models, biotite takes about 1.5 Myr to be consumed at about 21.5 km depth in the pelitic layer. In the excess water biotite model, biotite only takes only about 1 Myr to be consumed. On the other hand, the disappearance of muscovite is comparatively very fast, occurring in about 0.1 Myr in all models, for both pelitic and semi-pelitic layers (Figs. 10, 11, 12, 13). Thus, muscovite dehydration produces a melt extraction step in the short amount of time of 0.1 Myr for the layers at about 18 km of depth, whereas the next melt extraction step associated with biotite breakdown occurs after $\sim$1 Myr in the biotite model. This is also reflected in the evolution of the volume of melt extracted through time, with the sharp increase in melt volume after 8 Myr in the muscovite model (Fig. 9A), associated with the onset of the gabbro anomaly at the base of the 1D model. This shows a rapid consumption of muscovite in most layers.

# 6. Discussion

The coupling of crustal-scale thermal models with phase equilibrium modelling to study melt processes allows predictions to be compared with natural observations through four important variables: (i) the predicted melt volumes extracted by the different models (Fig. 9), (ii) the predicted phase assemblages in the source (Figs. 10, 11 and 12), (iii) the predicted composition of the extracted melt (Figs. 14 and 15), and (iv) time. The combination of these variables can provide insight into the relationship between melt source and granitoids, such as the migmatites of the La Bocana unit and the Marcabelí pluton (Fig. 1).

## 6.1. Limitations of the coupled thermal and phase equilibrium models

Before discussing the results presented in section 5.2, few of the limitations and uncertainties of the models presented in this study are examined here. Some limitations are due to uncertainties on the geological history of the El Oro complex. For example, the uncertainty on the *P–T-t* history of the metamorphic sequence. Furthermore, it is assumed that the chemical composition of the protolith forming the initial sedimentary sequence is similar at the crustal scale of the El Oro complex, and that the whole-rock analyses from the El Tigre and La Victoria units are representative of the protolith of the current migmatites of the La Bocana unit, assuming a similar depositional environment.

Other limitations are due to numerical constraints and assumptions made. Some of these are due to the constraints imposed by the compositional range of the existing thermodynamic data and the activity-composition models based on them (e.g. Gervais & Trapy, 2021; Lanari & Duesterhoeft, 2019). In addition, the specific applicability and limitations of the melt model to natural systems must be considered (e.g. Bartoli & Carvalho, 2021; R. W. White et al., 2011). Furthermore, the models are based on the assumption of equilibrium, which neglects any disequilibrium effects that can be observed for major, minor and trace elements (e.g. Guevara & Caddick, 2016; Markmann et al., 2024; Nicoli et al., 2017). Finally, granites can

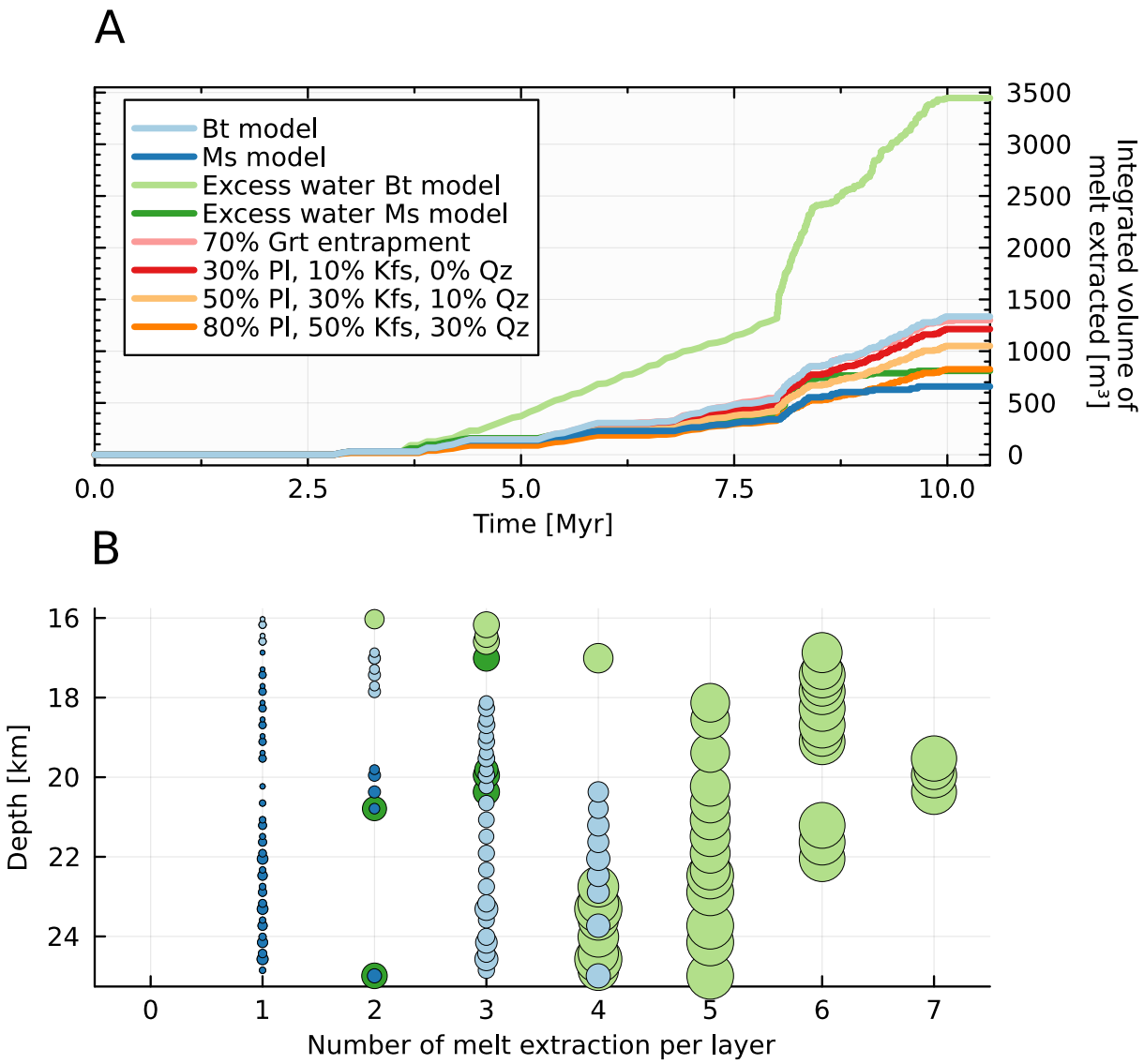


**Figure 9:** A. Time versus integrated volume of melt produced on a 1D sequence for 8 models with the same protoliths and using the convection model for the thermal evolution. The volume of melt produced can be related to the thickness of melt, as the 1D model is considered as a squared column with a width of 1 metre by 1 metre. Emplacement of the Piedras gabbro and the activation of the convection cell begins at 8 Myr and is characterised by a sharp increase in melt volume. The prograde metamorphic history ends at 10 Myr. B. Number of melt extraction steps versus depth for four models, the muscovite model, the biotite model and their equivalent with water in excess. The colours are the same as in (A). The size of the markers is proportional to the amount of volume extracted in a layer, and is normalised to the maximum volume produced in a layer in the three models. The excess water Ms model shows similar behaviour to the Ms model for most of the layers and is hidden by the muscovite model data points. Only the pelitic and semi-pelitic layers show melt extraction throughout the 1D sequence.

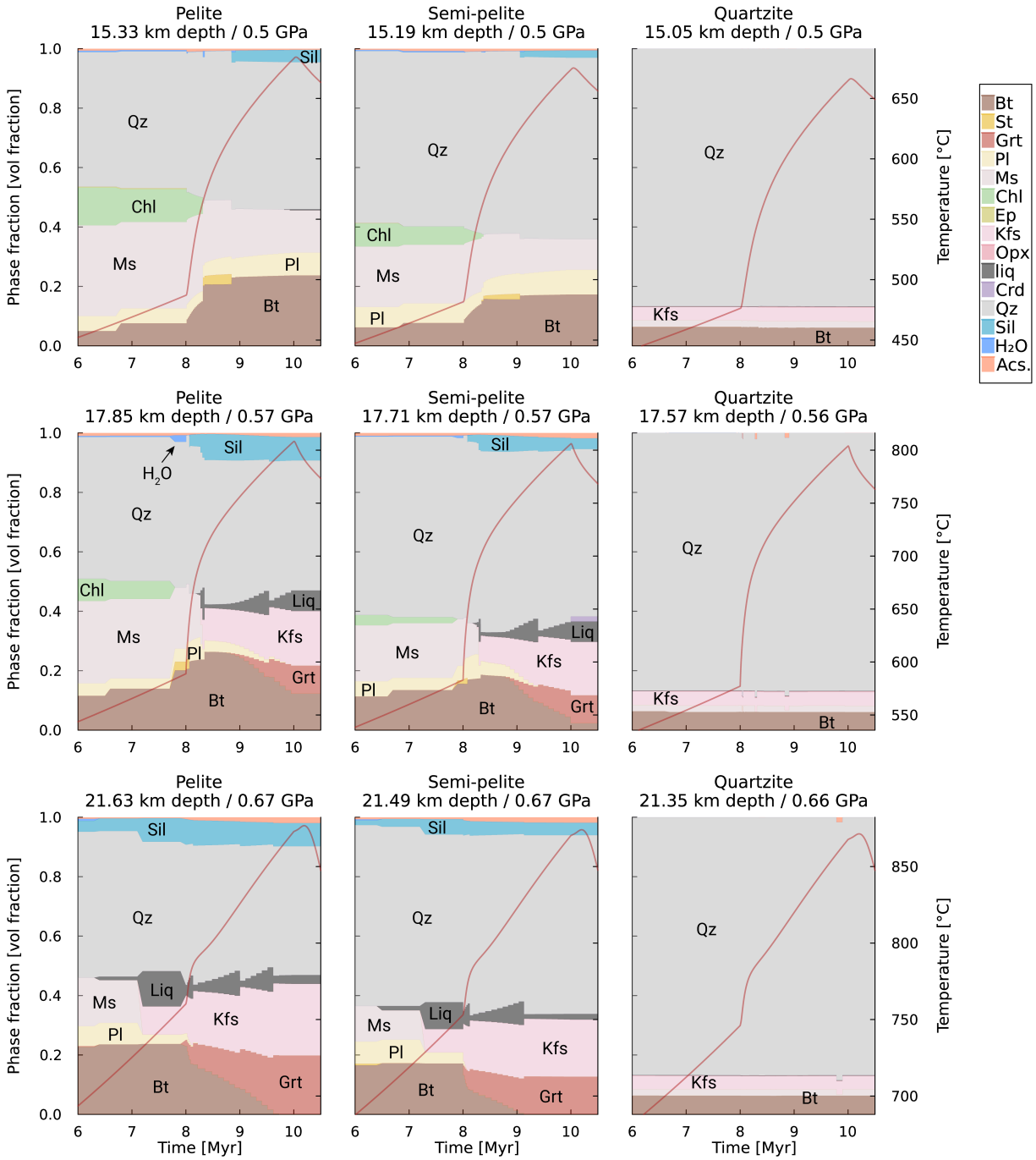


**Figure 10:** Evolution of phase assemblages for the biotite model. Modebox diagrams of the three different initial layers: pelite, semi-pelite and quartzite, at 3 different depths. Note that time is on the horizontal axis. The red line represents the temperature. Convection and emplacement of the Piedras gabbro starts at 8 Myr and the prograde metamorphic history ends at ca. 10 Myr. Melt is extracted when more 7 vol% is present, and 1 vol% of melt remains after extraction. The abbreviations are following Warr (2021) for the minerals, liq refers to liquid (melt), and Acs. to the accessory phases, which include e.g. titanium phases and magnetite.

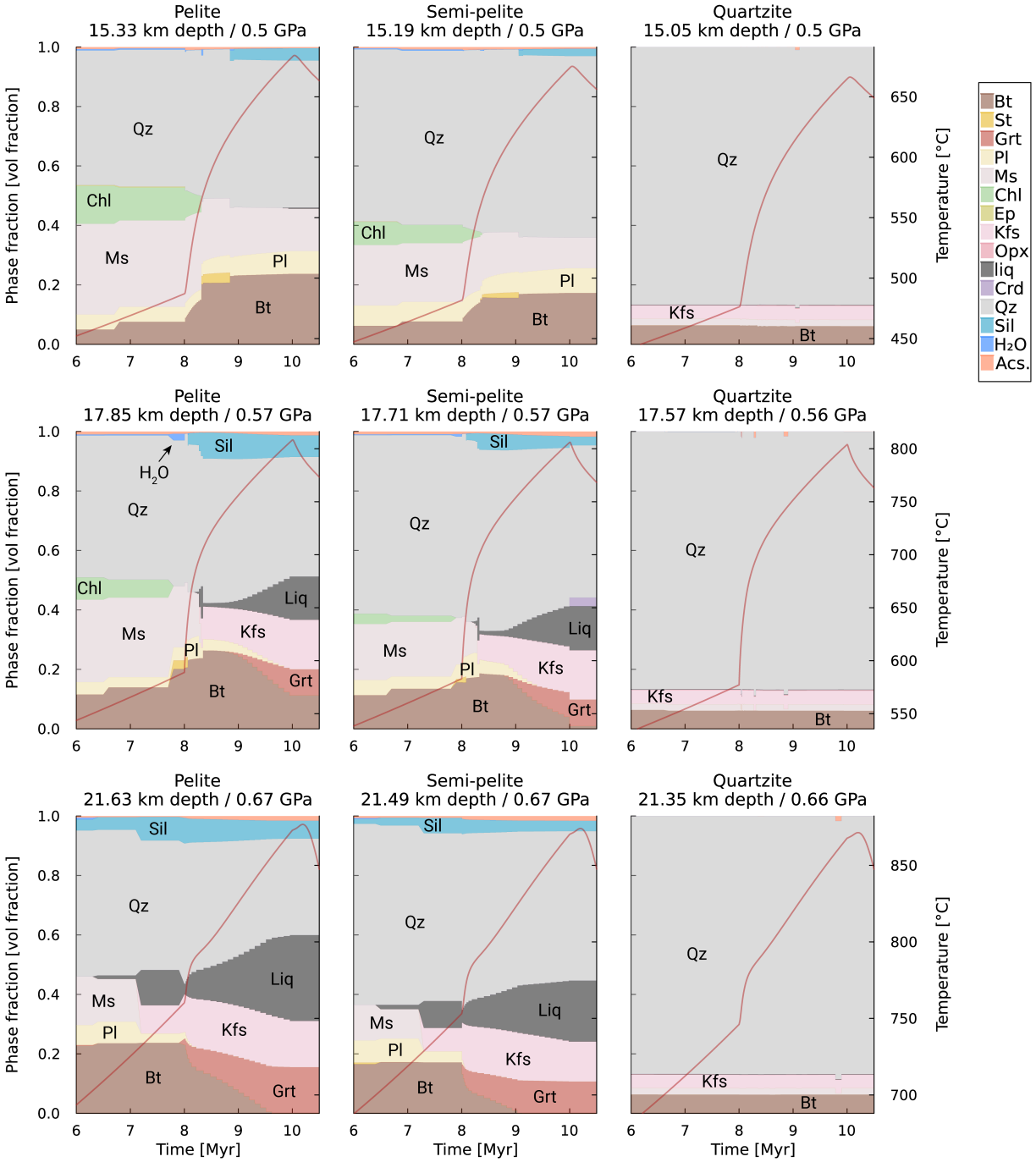


**Figure 11:** Evolution of phase assemblages for the muscovite model. Same legend as Fig. 10, but for a different model. In this model, only the melt produced by the muscovite-breakdown reaction is extracted when 7 vol% is present, and 1 vol% of melt remains after extraction.

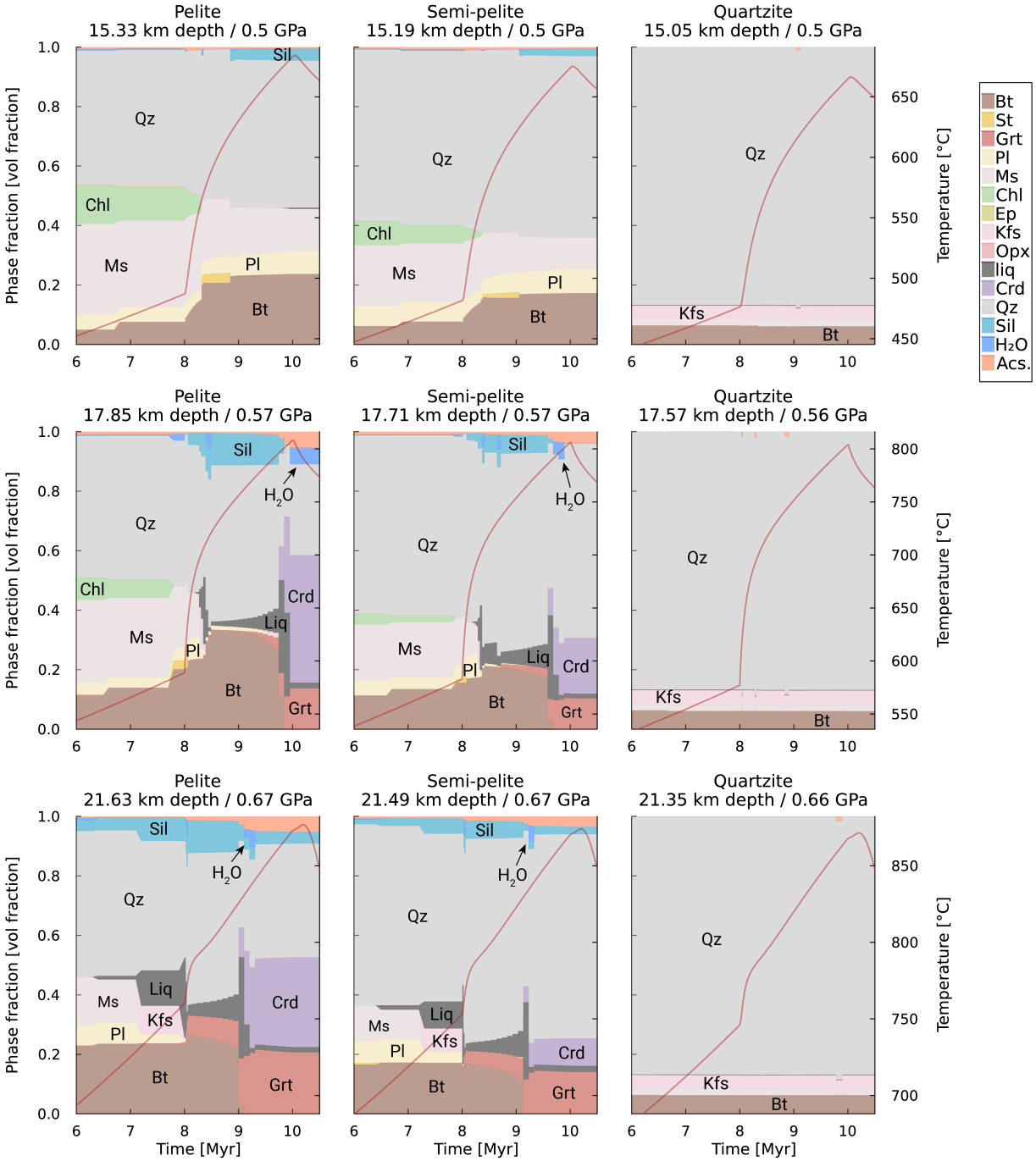


**Figure 12:** Evolution of phase assemblages for the excess water biotite model. Same legend as Fig. 10, but for a different model. In this model, 5 mole of water is added at each minimisation step. As in Fig. 10, the melt is extracted when more 7 vol% is present, and 1 vol% of melt remains after extraction.

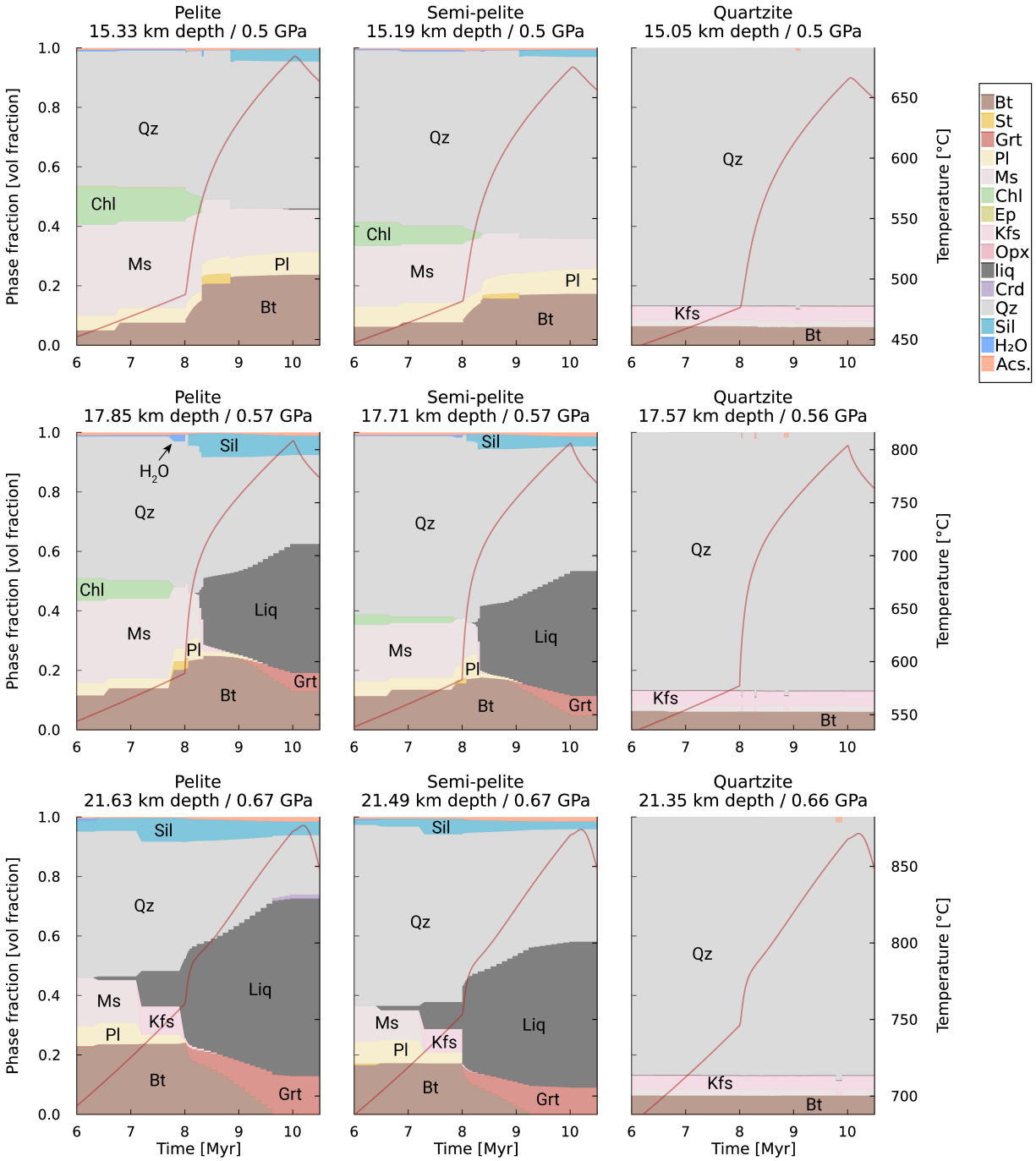


**Figure 13:** Evolution of phase assemblages for the excess water muscovite model. Same legend as Fig. 10, but for a different model. In this model, 5 mole of water is added at each minimisation step. As in Fig. 11, only the melt produced by the muscovite-breakdown reaction is extracted when 7 vol% is present, and 1 vol% of melt remains after extraction.

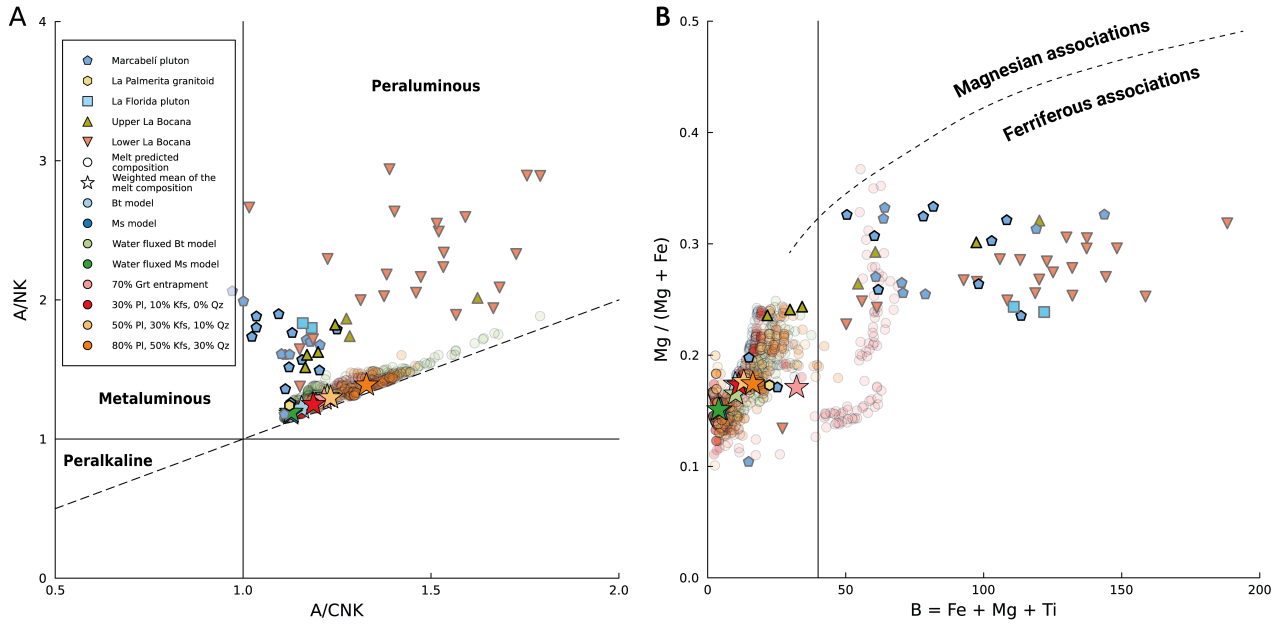


**Figure 14:** A. A/CNK vs. A/NK diagram (Shand, 1943) [molar Al / (2Ca + Na + K) vs. molar Al / (Na + K)]. Similar to Fig. 4A but with the addition of the predicted composition from the melt extracted from the 9 models. B. B-Mg# diagram (Debon & Le Fort, 1988) [B = millications Fe + Mg + Ti vs. molar Mg / (Mg + Fe)]. The legend is the same as in (A). Markers of the natural data with black strokes are from this study, while markers with grey strokes are data from the literature (Aspden et al., 1995; Riel et al., 2013; Riel et al., 2016; Vinasco Vallejo, 2004).

be more accurately viewed as mixtures of cumulus phases or even crystal mushes, from which liquids may have been extracted and subsequently erupted as dacites or rhyolites (e.g. Bachmann, 2004; Cashman et al., 2017). These limitations make direct comparison with natural migmatitic and igneous rocks complex; however, the results and the discussion presented in the following sections here demonstrate that modelling still allows insights into the general effect of melting reactions in the continental crust, and we argue that this approach is a powerful way of providing insights into the general effects of melt extraction on residual composition, volume produced and granitoid composition on crustal and geological time scales.

## 6.2. Relation between melt source and pluton emplacement

By comparing the results of the different models with the natural observations and the data collected in the El Oro complex in this study and the literature, it is possible to exclude unlikely scenarios and discuss on implications at the crustal scale.

By measuring the current average thickness of the Marcabelí pluton perpendicular to its structure on the geological map, the estimated thickness ranges from approximately 1000 to 3000 m (Fig. 1). This is assuming that the current exposure of the Marcabelí pluton is representative of its 3D structure. As such, this estimate could be underestimating or overestimating the real volume of the pluton. If it is assumed that the amount of melt extracted in the models has to correspond approximately to the current thickness of the Marcabelí pluton, it shows that the current results are in the same order of magnitude, with volumes of melt extracted ranging from around 500 to 3300 m (Fig. 9) and knowing than 1 third of the layers, composed of quartzite, are not producing any melt in the models. This result is limited by the fact that pluton emplacement and segregation of melt processes are ultimately part of a 3D problem but is consistent with the La Bocana unit being the main source of the Marcabelí pluton.

As these models also provide time, it is possible to compare not only the volumes produced but also the duration of melt extraction between models. For example, the muscovite and excess water muscovite models predict that most of the melt is extracted between 4 and 8.5 Myr, while the remaining models show that most of the extraction takes place between 4 and 10 Myr (Fig. 9). Based on the geochronological constraints on the duration of emplacement of the Marcabelí pluton in the El Oro complex by Chapter III, a steady extraction for a longer duration is more consistent with the current data. The extraction of the

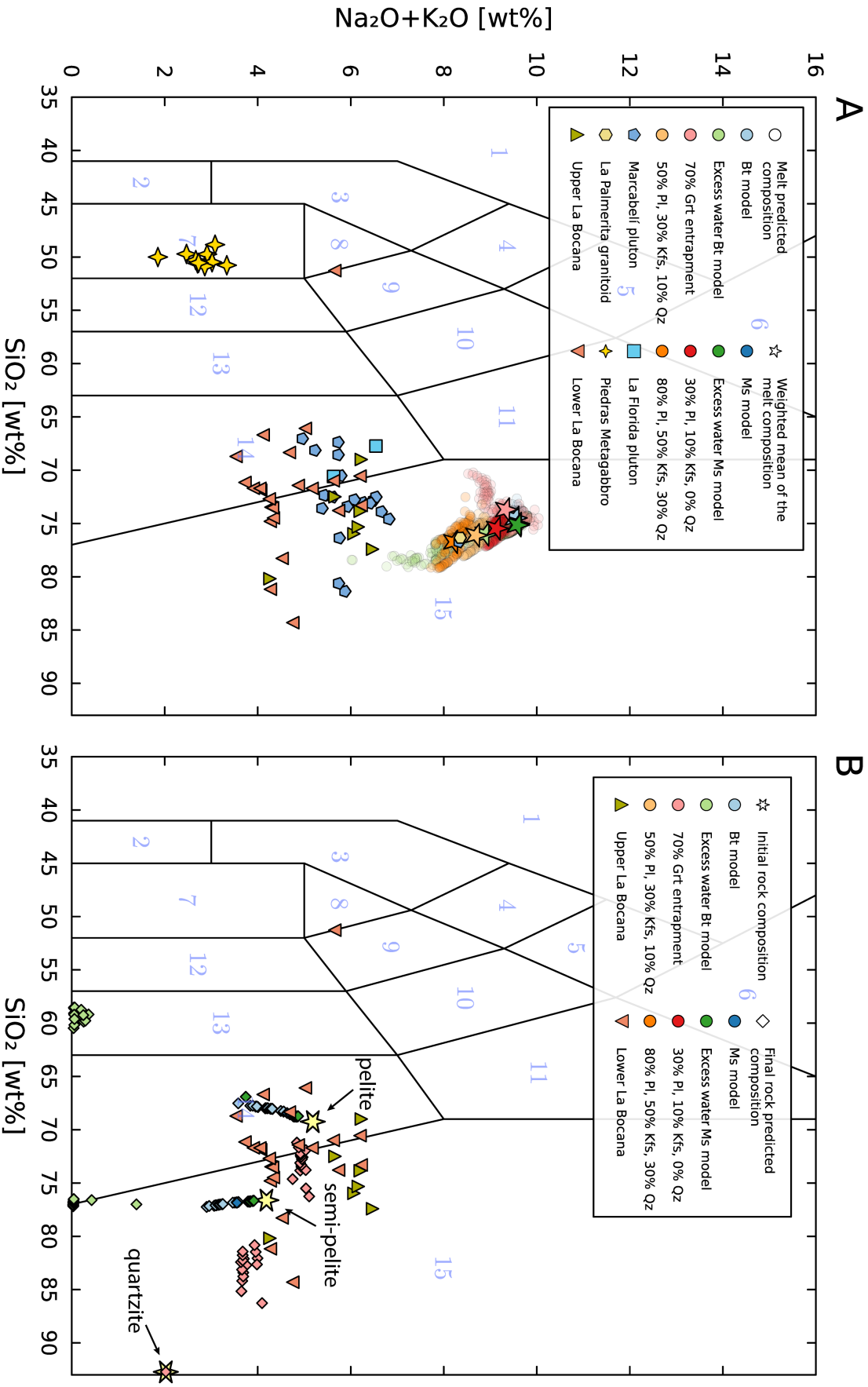


**Figure 15:** Total alkali–silica (TAS) diagrams (Bas et al., 1986; Le Maitre, 1989) of the prediction from the models and bulk rock analyses of the El Oro complex. All the compositions are renormalised to anhydrous compositions and without $P_2O_2$ for the natural data. A. TAS diagram of the composition of the melt extracted in 9 models with igneous bulk rock analyses and migmatites from the La Bocana unit. B. TAS diagram of the modelled final compositions of the different layers used in the 1D crustal models. Bulk rock analyses of migmatites from the La Bocana unit are also reported. 1: foidite, 2: peridot gabbro, 3: foid gabbro, 4: foid monzogabbro, 5: foid monzosyenite, 6: foid syenite, 7: gabbro, 8: monzogabbro, 9: monzodiorite, 10: monzonite, 11: syenite, 12: gabbroic diorite, 13: diorite, 14: granodiorite, 15: granite

melt from the biotite dehydration is therefore likely required based on time constraints.

In terms of the evolution of the phase assemblages, the excess water biotite model predicts the appearance of cordierite, while the other three models don't or only as a minor phase. No cordierite has been observed in the La Bocana unit samples and its absence was also reported by Riel et al. (2013). Moreover, the residual compositions in the layers show a very high depletion in alkali content at the end of the model due to the very high volume of melt extracted and the consumption of feldspars (Fig. 15B). This allows us to exclude this scenario from the others.

Therefore, based on the duration and volume of melt extracted, we propose that the biotite model best reproduces what is observed at the scale of the sequence. However, it is likely that the muscovite and excess water muscovite models are locally relevant, for some parts of the sequence. This is consistent with localities showing evidence of high melt fractions and diatexitic textures (e.g. Fig. 2). Distinguishing between the muscovite or the excess water muscovite models on the basis of residual composition and phase assemblage at the outcrop scale in migmatites would be difficult, as they predict similar assemblages, and K-feldspar is expected to crystallise from the high melt volume fraction predicted in the excess water model during cooling. This is consistent with recent investigations on excess water melting (Schwindinger et al., 2019) and this highlights the potential underestimation of the effect of excess water during partial melting.

## 6.3. Mixing with the metagabbro of the Piedras unit

The discrepancies observed between modelled melt chemistry and bulk rock analyses of the El Oro complex granitoids (Figs. 15A and 14) need to be addressed. None of the hypotheses explored in the models, such as fractional crystallisation or peritectic mineral entrapment, allow the trends and the values of the natural data to be reproduced, particularly in terms of alkali content, A/NK ratio, and maficity. This could be the result of limitations in the models, as discussed in section 6.1. However, the presence of hornblende and mafic enclaves in the Marcabelí pluton suggests a contamination from a more mafic source (Fig. 3; Aspden et al., 1995; Riel et al., 2013; Vinasco Vallejo, 2004). A potential source of this contamination is the (meta)gabbro of the Piedras unit. Mafic xenoliths and lenses are also present in the La Bocana unit (e.g. Fig. 2F) and the intrusive nature of the Piedras unit in the La Bocana unit has been suggested (Aspden et al., 1995; Riel et al., 2013). The lack of overlap between the modelled composition and the natural data is therefore interpreted to be mainly due to the absence of this mafic component in the modelling.

To test and to quantify this hypothesis of magma mingling, a simple mixing model, using the median composition of the bulk rock major element data from the metagabbro of the Piedras unit, and the volume-weighted mean of the composition of each model as two end-members, was conducted. The model follows the mixing test from Fourcade and Allègre (1981), and is based on this equation, following mass balance (e.g. Janoušek et al., 2016):

$$(\vec{C}_{\text{Marcabeli}} - \vec{C}_{\text{gabbro}}) = f(\vec{C}_{\text{model}} - \vec{C}_{\text{gabbro}}), \quad (33)$$

where $\vec{C}_{\text{gabbro}}$ is the vector containing the median composition of the metagabbro analyses from the Piedras unit, $\vec{C}_{\text{Marcabeli}}$ is the vector of the median composition of the Marcabelí pluton bulk rock analyses, $\vec{C}_{\text{model}}$ is the vector of the volume-weighted mean composition of the melt extracted from a model and $f$ is a linear function. All the compositions are expressed in wt%. The slope of $f$ corresponds to the ideal mixing fraction value considering all the components of the compositional vectors and is determined by finding the best fit to the data points.

The results are shown in Fig. 16. The models including fractional crystallisation were excluded, as they cannot be considered as a simple mixing model, since fractional crystallisation is a progressive process (e.g. Janoušek et al., 2016). The results show that all models predict a similar contribution of 85 to 93% from the crustal melts, with the entrapment garnet model showing the highest number. This is expected as all the models predict similar melt-extracted compositions. The contribution of the gabbroic composition is therefore estimated to be between 15 and 7 %. This estimate of the potential contribution of a gabbroic end member is considered to be a lower estimate as samples without mafic enclaves were selected for bulk rock analysis of the Marcabelí pluton. All mixing models show that the $K_2O$ content is quite far from the predicted mixing lines. This is consistent with the TAS diagram, which doesn't show a simple linear

relationship between the modelled melt composition, the felsic igneous samples, and the metagabbro from the Piedras unit (Fig. 15A). This is interpreted as a lack of another melt source, either from a deeper part of the crust that is no longer present, or from other protoliths not directly observed in the unit La Bocana unit, such as a meta-igneous or metagreywacke source. It is also a possible limitation of the numerical models, for example by underestimating the geological processes that occur between the melt extraction and the granitoid emplacement (e.g. Bachmann, 2004; Cashman et al., 2017).

## 6.4. Advection vs. convection: what controlled the thermal regime in the El Oro complex?

The results of the two thermal models presented in section 4.2 showed that they both satisfy the peak *P–T* estimates and the current geochronological constraints of the heat source (Fig. 7). This indicates that both advection and emplacement of melt, and whole-rock flow by to convection, are physically plausible mechanisms, based on the conservation of energy, for reproducing the geothermal gradient recorded by the metamorphic sequence of the El Oro complex in the middle to deep crust.

Both mechanisms have been proposed to explain quasi-isothermal gradients on other metamorphic sequences, especially migmatitic cores of gneiss domes, but melt advection as a mechanism has been favoured in most cases. For instance, heat advection induced by regional-scale magmatism has been proposed to explain the observations on the geothermal gradient of the Central Gneiss Complex of western British Columbia (Depine et al., 2008), the Variscan Montagne Noire gneiss dome (Trap et al., 2017), the Velay dome, in the French Massif Centrale (Barbey et al., 2015; Laurent et al., 2017), the Variscan Pyrenees (Connop et al., 2024; Siron et al., 2020) or the Higo metamorphic complex (Miyazaki, 2004). On the other hand, convection of lower crust has been proposed to generate large-scale crustal magmas during the Central Andes orogeny (Babeyko et al., 2002) or to explain the cyclicity in the zircon record of the Naxos dome (Vanderhaeghe et al., 2018).

For the El Oro complex, the advection model shows that a significant intrusion thickness of about 5 km and a high $M$ factor of 10 is required to reach the temperatures of the *P–T* estimates within 5 Myr. In the western part of the complex, the La Florida pluton may be evidence of this process (Fig. 1). However, no similar plutons have been observed in the western part of the La Bocana unit. Granitoids have been observed and reported in the migmatites near the town of La Bocana (field evidence; Aspden et al., 1995; Riel, 2012), but estimation of the size of these bodies is hampered by the outcrop conditions. In addition, the complexity of distinguishing between granitoids and diatexitic migmatites, the possible remelting of previous igneous rocks during prograde metamorphism, and the possibility that such plutons have been eroded or remain buried beneath the current surface, complicate the assessment. Finally, the emplacement of melt for 5 Ma suggests the need for both a significant heat and melt source. While mantle upwelling is thought to have provided the heat for this metamorphic event, ensuring a durable and steady supply of heat, the source of the melt is more challenging. Producing 5 km of melt thickness would require a thick and fertile crust. However, there is currently no evidence of such a body beneath the Tahuín group, largely due to the intrusion of the Piedras unit gabbro and subsequent tectonic processes. It is likely that a thicker crust once existed, but was subsequently delaminated, since only about 25 km of paleo-crust is currently preserved in the Tahuín group. Furthermore, no older basement was observed at the base of the sequence, on which the sediments of the La Bocana unit would have been deposited. This makes it difficult to exclude or validate this mechanism.

A similar conclusion can be reached for the convection hypothesis. One of the arguments in favour of convection from a field perspective would be the regional scale structure indicating whole-rock flow. No clear preferred orientation was observed at the unit scale. However, local folding structures at the multimeter scale have been interpreted as convection driven by Riel et al. (2016). These folds could also result from other ductile deformation mechanisms induced by the weakening of partially molten rock and extraction of melt (e.g. Brown et al., 1995; Weinberg et al., 2013). Finally, the model assumes a combined rock and melt viscosity of about $10^{15}$ Pa s to create a convection cell. Estimating the viscosity of partially molten rocks with increasing melt fraction is a complex issue and there are large uncertainties about the viability of this value under these conditions (**connollyViscosityCrystalMushes2022**; e.g. Hashim et al., 2013).

In conclusion, we estimate that the present ob-

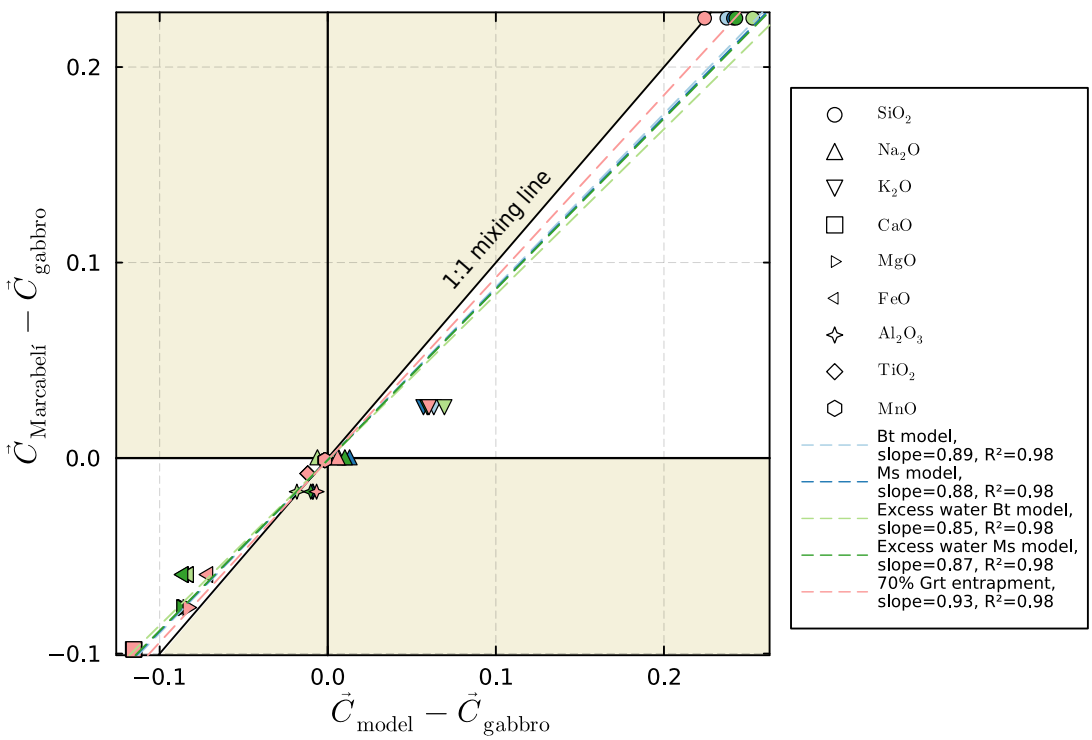


**Figure 16:** Results from the mixing test of Fourcade and Allègre (1981). This diagram compares the effects of 6 models on the theoretical mixing between the volume-weighted mean melt composition from each model ($C_{\text{model}}$) and the median composition of the metagabbro from the Piedras unit ($C_{\text{gabbro}}$). The targeted composition is the median of the whole-rock analyses from the Marcabelí pluton ($C_{\text{Marcabelí}}$). All three compositions are anhydrous and renormalised to 1 without $P_2O_5$. The lines correspond to the best fit for each model. The slope of each line corresponds to the estimated contribution between the two end-members, $C_{\text{model}}$ and $C_{\text{gabbro}}$, considering all major elements. The brown areas correspond to zones where the mixing ratio is inverted compared to the white areas.

servations and the 1D thermal models are currently insufficient to exclude one model from the other. Both mechanisms could also play a role on different timescales, with a single pulse of melt injection being much faster than whole-rock convection and we argue that both mechanisms could take place in the El Oro complex. We propose that the contribution of each mechanism to the overall heat budget could be estimated by developing more advanced 2D coupled thermo-mechanical models, which is beyond the scope of this study. However, the thermal models show that both mechanisms produce similar peak *P*–*T* conditions (Fig. 7). Although the choice of thermal mechanism has important implications for the geological history of the metamorphic sequence, we expect that the choice of one thermal model over the other for coupling with phase equilibrium modelling should not affect the main results presented in this study.

# 7. Conclusion

The integration of thermal and phase equilibrium models at the crustal scale provides an opportunity to evaluate the mass balance between the volume and composition of the melt produced and the occurrence and composition of granitoids at the crustal scale. This allows hypotheses to be tested to infer the contribution of different sources during a melting event. In particular, the ability to include time with phase equilibrium modelling brings new insights by allowing comparison with the timescales of melting processes provided by petrochronology. As time is constrained by the conservation of energy based on a thermal model, it is also important to have good constraints on the *P*–*T*–*t* path history of the metamorphic sequence before applying this type of modelling.

This model was applied to the El Oro complex, from which additional bulk rock compositions were produced during this study. The models showed, based on volume, that the amount of melt produced by partial melting in the La Bocana unit was compa-

rable to the observed volume of the Marcabelí pluton. This implies that the total time of emplacement of this pluton should be compatible with the timescale of the melting event occurring during prograde metamorphism in the crust, if the extraction of melt is progressive, and is in agreement with the results presented in Chapter III of a long-lived pluton. The total duration of melt extraction in the biotite model was ∼6 Myr. While this is comparatively shorter than the 20 Myr estimate based on geochronology from Chapter III, this duration does not include the retrograde metamorphic history which is recorded in zircons from migmatites.

The discrepancies between modelled melt compositions and bulk rock compositions were not resolved by fractional crystallisation or garnet entrapment. Therefore, we explored mixing ratios between granitoid melts and the Piedras gabbro to examine if this could explain the discrepancy. This showed that mixing of at least 7 to 15 % of the composition of the current metagabbro was required to reproduce the composition of the Marcabelí pluton, which is a conservative estimate. This mixing test showed that simple binary mixing is not sufficient to fully explain the discrepancy between the modelled compositions and the bulk composition of the granitoids, especially in terms of alkali content. Future work should vary the initial composition of the layers and testing different protoliths with more complex layering in the models could be investigated to see if the trends observed in the Marcabelí pluton can be explained in this way, or if some other processes are required to explain this discrepancy.

## Code and data availability

The code used in this study allowing reproducibility of the data is available on GitHub (https://github.com/Iddingsite/PhD2024CodeElOro) and at a permanent DOI repository (Zenodo): https://doi.org/10.5281/zenodo.13854597. The code is written in the Julia programming language. Refer to the repository's README for additional information. The code is distributed under the GPL-3.0 license. The bulk rock compositions produced in this chapter, alongside the compilation made from the literature, are also available at a permanent DOI repository: https://boris-portal.unibe.ch/handle/20.500.12422/44675.

## Acknowledgments

We thank Philip Hartmeier and Aiyana Diwa for their assistance on producing the bulk rock chemistry and Jean-François Moyen for useful discussions. Funding was provided by the European Research Council (ERC) under the European Union's Horizon 2020 research and innovation programme (grant agreement No 850530).

## References


Abdulle, A., & Medovikov, A. A. (2001). Second order Chebyshev methods based on orthogonal polynomials. *Numerische Mathematik*, *90*, 1–18 (cit. on p. 95).

Aspden, J. A., Bonilla, W., & Duque, P. (1995). *The El Oro metamorphic complex, Ecuador: Geology and economic mineral deposits*. British Geological Survey. Keyworth, Nottingham. (Cit. on pp. 85–87, 92, 94, 107, 109, 110).
OCLC: 36174214.

Babeyko, A., Sobolev, S., Trumbull, R., Oncken, O., & Lavier, L. (2002). Numerical models of crustal scale convection and partial melting beneath the Altiplano–Puna plateau. *Earth and Planetary Science Letters*, *199*(3–4), 373–388. https://doi.org/10.1016/S0012-821X(02)00597-6 (cit. on p. 110).

Bachmann, O. (2004). On the Origin of Crystal-poor Rhyolites: Extracted from Batholithic Crystal Mushes. *Journal of Petrology*, *45*(8), 1565–1582. https://doi.org/10.1093/petrology/egh019 (cit. on pp. 107, 110).

Barbey, P., Villaros, A., Marignac, C., & Montel, J.-M. (2015). Multiphase melting, magma emplacement and P-T-time path in late-collisional context: The Velay example (Massif Central, France). *Bulletin de la Société Géologique de France*, *186*(2–3), 93–116. https://doi.org/10.2113/gssgfbull.186.2-3.93 (cit. on p. 110).

Bartoli, O., & Carvalho, B. B. (2021). Anatectic granites in their source region: A comparison between experiments, thermodynamic modelling and nanogranitoids. *Lithos*, *402–403*, 106046. https://doi.org/10.1016/j.lithos.2021.106046 (cit. on p. 101).

Bas, M. J. L., Maitre, R. W. L., Streckeisen, A., Zanettin, B., & IUGS Subcommission on the Systematics of Igneous Rocks. (1986). A Chemical Classification of Volcanic Rocks Based on the Total Alkali-Silica Diagram. *Journal of Petrology*, *27*(3), 745–750. https://doi.org/10.1093/petrology/27.3.745 (cit. on pp. 99, 108).

Bezanson, J., Edelman, A., Karpinski, S., & Shah, V. B. (2017). Julia: A Fresh Approach to Numerical Computing. *SIAM Review*, *59*(1), 65–98. https://doi.org/10.1137/141000671 (cit. on p. 95).

Bonin, B., Janoušek, V., & Moyen, J.-F. (2020). Chemical variation, modal composition and classification of granitoids. *Geological Society, London, Special Publications*, *491*(1), 9–51. https://doi.org/10.1144/SP491-2019-138 (cit. on p. 84).

Bowen, N. L. (1928). *The evolution of the igneous rocks*. Princeton University Press. (Cit. on p. 99).

Breaks, F. W., & Moore, J. M. (1992). The Ghost Lake batholith, Superior Province of northwestern Ontario: A fertile, S-type, peraluminous granite-rare-element pegmatite system. *Canadian Mineralogist*, *30*, 835–835 (cit. on p. 84).

Breton, N. L., & Thompson, A. B. (1988). Fluid-absent (dehydration) melting of biotite in metapelites in the early stages of crustal anatexis. *Contributions to Mineralogy and Petrology*, *99*(2), 226–237. https://doi.org/10.1007/BF00371463 (cit. on pp. 84, 98).

Brown, M. (2013). Granite: From genesis to emplacement. *Geological Society of America Bulletin*, *125*(7–8), 1079–1113. https://doi.org/10.1130/B30877.1 (cit. on p. 84).

Brown, M., & Pressley, R. (1999). Crustal melting in nature: Prosecuting source processes. *Physics and Chemistry of the Earth, Part A: Solid Earth and Geodesy*, *24*(3), 305–316. https://doi.org/10.1016/S1464-1895(99)00034-4 (cit. on p. 84).

Brown, M., Averkin, Y. A., McLellan, E. L., & Sawyer, E. W. (1995). Melt segregation in migmatites. *Journal of Geophysical Research: Solid Earth*, *100*(B8), 15655–15679. https://doi.org/10.1029/95JB00517 (cit. on p. 110).

Bunge, H.-P., Richards, M. A., & Baumgardner, J. R. (1997). A sensitivity study of three-dimensional spherical mantle convection at $10^8$ Rayleigh number: Effects of depth-dependent viscosity, heating mode, and an endothermic phase change. *Journal of Geophysical Research: Solid Earth*, *102*(B6), 11991–12007. https://doi.org/10.1029/96JB03806 (cit. on p. 95).

Cashman, K. V., Sparks, R. S. J., & Blundy, J. D. (2017). Vertically extensive and unstable magmatic systems: A unified view of igneous processes. *Science*, *355*(6331), eaag3055. https://doi.org/10.1126/science.aag3055 (cit. on pp. 107, 110).

Chappell, B. (1984). Source rocks of i-and s-type granites in the lachlan fold belt, southeastern australia. *Philosophical Transactions of the Royal Society of London. Series A, Mathematical and Physical Sciences*, *310*(1514), 693–707 (cit. on p. 84).

Chappell, B., & White, A. (1974). Two contrasting granite types. *Pacific Geology*, *8*, 173–174 (cit. on p. 84).

Chappell, B., & White, A. (2001). Two contrasting granite types: 25 years later. *Australian Journal of Earth Sciences*, *48*(4), 489–499. https://doi.org/10.1046/j.1440-0952.2001.00882.x (cit. on p. 84).

Chappell, B., White, A., & Wyborn, D. (1987). The Importance of Residual Source Material (Restite) in Granite Petrogenesis. *Journal of Petrology*, *28*(6), 1111–1138. https://doi.org/10.1093/petrology/28.6.1111 (cit. on p. 84).

Clarke, D. B. (1992). *Granitoid rocks* (Vol. 7). Springer Science & Business Media. (Cit. on p. 84).

Clarke, F. W. (1924). *The data of geochemistry* (5th ed., Report No. 770). Washington, D.C. https://doi.org/10.3133/b770 (cit. on p. 96).

Clemens, J., & Stevens, G. (2012). What controls chemical variation in granitic magmas? *Lithos*, *134–135*, 317–329. https://doi.org/10.1016/j.lithos.2012.01.001 (cit. on p. 84).

Clemens, J., & Vielzeuf, D. (1987). Constraints on melting and magma production in the crust. *Earth and Planetary Science Letters*, *86*(2–4), 287–306. https://doi.org/10.1016/0012-821X(87)90227-5 (cit. on p. 84).

Cochrane, R., Spikings, R., Gerdes, A., Ulianov, A., Mora, A., Villagómez, D., Putlitz, B., & Chiaradia, M. (2014). Permo-Triassic anatexis, continental rifting and the disassembly of western Pangaea. *Lithos*, *190–191*, 383–402. https://doi.org/10.1016/j.lithos.2013.12.020 (cit. on p. 96).

Collins, W. (1996). Lachlan Fold Belt granitoids: Products of three-component mixing. *Earth and Environmental Science Transactions of the Royal Society of Edinburgh*, *87*(1–2), 171–181 (cit. on p. 84).

Connop, C. H., Smye, A. J., Garber, J. M., & Mittal, T. (2024). Heat sources for Variscan high-temperature–low-pressure metamorphism: Petrochronological constraints from the Trois Seigneurs massif, French Pyrenees. *Journal of Metamorphic Geology*, jmg.12775. https://doi.org/10.1111/jmg.12775 (cit. on pp. 92, 110).

Creaser, R. A., Price, R. C., & Wormald, R. J. (1991). A-type granites revisited: Assessment of a residual-source model. *Geology*, *19*(2), 163. https://doi.org/10.1130/0091-7613(1991)019<0163:ATGRAO>2.3.CO;2 (cit. on p. 84).

Debon, F., & Le Fort, P. (1983). A chemical–mineralogical classification of common plutonic rocks and associations. *Transactions of the Royal Society of Edinburgh: Earth Sciences*, *73*(3), 135–149. https://doi.org/10.1017/S0263593300010117 (cit. on p. 92).

Debon, F., & Le Fort, P. (1988). A cationic classification of common plutonic rocks and their magmatic associations : Principles, method, applications. *Bulletin de Minéralogie*, *111*(5), 493–510. https://doi.org/10.3406/bulmi.1988.8096 (cit. on pp. 92, 107).

Depine, G. V., Andronicos, C. L., & Phipps-Morgan, J. (2008). Near-isothermal conditions in the middle and lower crust induced by melt migration. *Nature*, *452*(7183), 80–83. https://doi.org/10.1038/nature06689 (cit. on pp. 86, 92, 110).

Diener, J. F. A., & Fagereng, Å. (2014). The influence of melting and melt drainage on crustal rheology during orogenesis. *Journal of Geophysical Research: Solid Earth*, *119*(8), 6193–6210. https://doi.org/10.1002/2014JB011088 (cit. on p. 84).

DiPietro, J. A. (2013). Keys to the Interpretation of Geological History. In *Landscape Evolution in the United States* (pp. 327–344). Elsevier. https://doi.org/10.1016/B978-0-12-397799-1.00020-8 (cit. on p. 92).

Eby, G. N. (1990). The A-type granitoids: A review of their occurrence and chemical characteristics and speculations on their petrogenesis. *Lithos*, *26*(1–2), 115–134 (cit. on p. 84).

Eskola, P. E. (1915). Om sambandet mellan kemisk och mineralogisk sammansattning hos Orijarvi traktens metamorfa bergarter. *Bull. Comm. Geol. Finl.*, *44*, S–1 (cit. on p. 93).

Farina, F., Dini, A., Davies, J. H., Ovtcharova, M., Greber, N. D., Bouvier, A.-S., Baumgartner, L., Ulianov, A., & Schaltegger, U. (2018). Zircon petrochronology reveals the timescale and mechanism of anatectic magma formation. *Earth and Planetary Science Letters*, *495*, 213–223. https://doi.org/10.1016/j.epsl.2018.05.021 (cit. on p. 85).

Feininger, T. (1978). Geologic map of western El Oro province. *Escuela Politecnica Nacional, Quito, Ecuador* (cit. on pp. 85, 87).

Feininger, T. (1982). The metamorphic "basement" of Ecuador. *Geological Society of America Bulletin*, *93*(1), 87. https://doi.org/10.1130/0016-

7606(1982)93<87:TMBOE>2.0.CO;2 (cit. on p. 85).

Foden, J., Elburg, M., Turner, S., Sandiford, M., O'Callaghan, J., & Mitchell, S. (2002). Granite production in the Delamerian Orogen, South Australia. *Journal of the Geological Society*, *159*(5), 557–575. https://doi.org/10.1144/0016-764901-099 (cit. on p. 84).

Forshaw, J. B., & Pattison, D. R. (2023). Major-element geochemistry of pelites. *Geology*, *51*(1), 39–43. https://doi.org/10.1130/G50542.1 (cit. on pp. 89, 93).

Fourcade, S., & Allègre, C. J. (1981). Trace elements behavior in granite genesis: A case study The calc-alkaline plutonic association from the Querigut complex (Pyrénées, France). *Contributions to Mineralogy and Petrology*, *76*(2), 177–195. https://doi.org/10.1007/bf00371958 (cit. on pp. 109, 111).

Frost, B. R., Barnes, C. G., Collins, W. J., Arculus, R. J., Ellis, D. J., & Frost, C. D. (2001). A Geochemical Classification for Granitic Rocks. *Journal of Petrology*, *42*(11), 2033–2048. https://doi.org/10.1093/petrology/42.11.2033 (cit. on p. 84).

Gabriele, P. (2002, November 22). *HP terranes exhumation in active margin setting: Geology, petrology and geochemistry of the Raspas Complex in SW Ecuador* [Doctoral dissertation, Université de Lausanne (Suisse)]. Retrieved May 27, 2024, from https://hal.science/tel-04431244 (cit. on p. 85).

Gardien, V., Thompson, A. B., Grujic, D., & Ulmer, P. (1995). Experimental melting of biotite + plagioclase + quartz ± muscovite assemblages and implications for crustal melting. *Journal of Geophysical Research: Solid Earth*, *100*(B8), 15581–15591. https://doi.org/10.1029/95JB00916 (cit. on p. 98).

Gervais, F., & Trapy, P.-H. (2021). Testing solution models for phase equilibrium (forward) modeling of partial melting experiments. *Contributions to Mineralogy and Petrology*, *176*(1), 4. https://doi.org/10.1007/s00410-020-01762-5 (cit. on p. 101).

Gordon, S. M., Whitney, D. L., Teyssier, C., Grove, M., & Dunlap, W. J. (2008). Timescales of migmatization, melt crystallization, and cooling in a Cordilleran gneiss dome: Valhalla complex, southeastern British Columbia. *Tectonics*, *27*(4), 2007TC002103. https://doi.org/10.1029/2007TC002103 (cit. on p. 85).

Gordon, S. M., Bowring, S. A., Whitney, D. L., Miller, R. B., & McLean, N. (2010). Time Scales of Metamorphism, Deformation, and Crustal Melting in a Continental Arc, North Cascades USA. *Geological Society of America Bulletin*, *122*(7–8), 1308–1330. https://doi.org/10.1130/B30060.1 (cit. on p. 85).

Gray, C. M. (1990). A strontium isotopic traverse across the granitic rocks of southeastern Australia: Petrogenetic and tectonic implications. *Australian Journal of Earth Sciences*. https://doi.org/10.1080/08120099008727931 (cit. on p. 84).

Guevara, V. E., & Caddick, M. J. (2016). Shooting at a moving target: Phase equilibria modelling of high-temperature metamorphism. *Journal of Metamorphic Geology*, *34*(3), 209–235. https://doi.org/10.1111/jmg.12179 (cit. on p. 101).

Guillong, M., Meier, D. L., Allan, M. M., Heinrich, C. A., Yardley, B., et al. (2008). Appendix A6: SILLS: A MATLAB-based program for the reduction of laser ablation ICP-MS data of homogeneous materials and inclusions. *Mineralogical Association of Canada Short Course*, *40*, 328–333 (cit. on p. 86).

Harris, N. B. W., Caddick, M., Kosler, J., Goswami, S., Vance, D., & Tindle, A. G. (2004). The pressure–temperature–time path of migmatites from the Sikkim Himalaya. *Journal of Metamorphic Geology*, *22*(3), 249–264. https://doi.org/10.1111/j.1525-1314.2004.00511.x (cit. on p. 85).

Hashim, L., Gaillard, F., Champallier, R., Le Breton, N., Arbaret, L., & Scaillet, B. (2013). Experimental assessment of the relationships between electrical resistivity, crustal melting and strain localization beneath the Himalayan–Tibetan Belt. *Earth and Planetary Science Letters*, *373*, 20–30. https://doi.org/10.1016/j.epsl.2013.04.026 (cit. on p. 110).

Holland, T. J. B., & Powell, R. (2011). An improved and extended internally consistent thermodynamic dataset for phases of petrological interest, involving a new equation of state for solids: THERMODYNAMIC DATASET FOR PHASES OF PETROLOGICAL INTEREST. *Journal of Metamorphic Geology*, *29*(3), 333–383. https://doi.org/10.1111/j.1525-1314.2010.00923.x (cit. on p. 98).

Janoušek, V., Moyen, J.-F., Martin, H., Erban, V., & Farrow, C. (2016). *Geochemical Modelling of Ig-*

*neous Processes – Principles And Recipes in R Language: Bringing the Power of R to a Geochemical Community*. Springer Berlin Heidelberg. https://doi.org/10.1007/978-3-662-46792-3 (cit. on p. 109).

Jaupart, C., & Mareschal, J.-C. (2007, January 1). *Heat Flow and Thermal Structure of the Lithosphere* (Vol. 6). https://doi.org/10.1016/B978-044452748-6.00104-8 (cit. on p. 92).
ADS Bibcode: 2007cld..book..217J.

Jaupart, C., & Mareschal, J.-C. (2010, November 11). *Heat Generation and Transport in the Earth*. Cambridge University Press. (Cit. on p. 95).

Jochum, K. P., Willbold, M., Raczek, I., Stoll, B., & Herwig, K. (2005). Chemical Characterisation of the USGS Reference Glasses GSA-1G, GSC-1G, GSD-1G, GSE-1G, BCR-2G, BHVO-2G and BIR-1G Using EPMA, ID-TIMS, ID-ICP-MS and LA-ICP-MS. *Geostandards and Geoanalytical Research*, *29*(3), 285–302. https://doi.org/10.1111/j.1751-908X.2005.tb00901.x (cit. on p. 86).

Johannes, W., Ehlers, C., Kriegsman, L. M., & Mengel, K. (2003). The link between migmatites and S-type granites in the Turku area, southern Finland. *Lithos*, *68*(3–4), 69–90. https://doi.org/10.1016/S0024-4937(03)00032-X (cit. on p. 84).

Johnson, T., Yakymchuk, C., & Brown, M. (2021). Crustal melting and suprasolidus phase equilibria: From first principles to the state-of-the-art. *Earth-Science Reviews*, *221*, 103778. https://doi.org/10.1016/j.earscirev.2021.103778 (cit. on pp. 84, 98).

Koblinger, B. M., & Pattison, D. R. M. (2017). Crystallization of Heterogeneous Pelitic Migmatites: Insights from Thermodynamic Modelling. *Journal of Petrology*, *58*(2), 297–326. https://doi.org/10.1093/petrology/egx017 (cit. on p. 84).

Korhonen, F., Brown, M., Clark, C., & Bhattacharya, S. (2013). Osumilite–melt interactions in ultrahigh temperature granulites: Phase equilibria modelling and implications for the *P–T–t* evolution of the Eastern Ghats Province, I ndia. *Journal of Metamorphic Geology*, *31*(8), 881–907. https://doi.org/10.1111/jmg.12049 (cit. on p. 98).

Lanari, P., & Duesterhoeft, E. (2019). Modeling Metamorphic Rocks Using Equilibrium Thermodynamics and Internally Consistent Databases: Past Achievements, Problems and Perspectives. *Journal of Petrology*, *60*(1), 19–56. https://doi.org/10.1093/petrology/egy105 (cit. on p. 101).

Lanari, P., & Engi, M. (2017). Local Bulk Composition Effects on Metamorphic Mineral Assemblages. *Reviews in Mineralogy and Geochemistry*, *83*(1), 55–102. https://doi.org/10.2138/rmg.2017.83.3 (cit. on p. 98).

Laurent, O., Couzinié, S., Zeh, A., Vanderhaeghe, O., Moyen, J.-F., Villaros, A., Gardien, V., & Chelle-Michou, C. (2017). Protracted, coeval crust and mantle melting during Variscan late-orogenic evolution: U–Pb dating in the eastern French Massif Central. *International Journal of Earth Sciences*, *106*(2), 421–451. https://doi.org/10.1007/s00531-016-1434-9 (cit. on p. 110).

Le Maitre, R. W. (1989). A classification of igneous rocks and glossary of terms. *Recommendations of the international union of geological sciences subcommission on the systematics of igneous rocks*, *193* (cit. on pp. 99, 108).

Loiselle, M. C., Wones, D. R., Loiselle, M. C., & Wones, D. R. (1979). Characteristics and origin of anorogenic granites. *Abstracts with Programs - Geological Society of America*, *11*(7), 468–468. Retrieved September 11, 2024, from https://eurekamag.com/research/018/535/018535699.php (cit. on p. 84).

Markmann, T. A., Lanari, P., Piccoli, F., Pettke, T., Tamblyn, R., Tedeschi, M., Lueder, M., Kunz, B. E., Riel, N., & Laughton, J. (2024). Multiphase quantitative compositional mapping by LA-ICP-MS: Analytical approach and data reduction protocol implemented in XMapTools. *Chemical Geology*, *646*, 121895. https://doi.org/10.1016/j.chemgeo.2023.121895 (cit. on p. 101).

Mayne, M. J., Stevens, G., & Moyen, J.-F. (2020). A phase equilibrium investigation of selected source controls on the composition of melt batches generated by sequential melting of an average metapelite. *Geological Society, London, Special Publications*, *491*(1), 223–241. https://doi.org/10.1144/SP491-2018-121 (cit. on pp. 84, 96, 98).

Mayne, M. J., Stevens, G., Moyen, J.-F., & Johnson, T. (2020). Performing process-oriented investigations involving mass transfer using Rcrust: A new phase equilibrium modelling tool. *Ge-*

*ological Society, London, Special Publications*, *491*(1), 209–221. https://doi.org/10.1144/SP491-2018-85 (cit. on pp. 84, 85).

Miyazaki, K. (2004). Low- *P* –high- *T* metamorphism and the role of heat transport by melt migration in the Higo Metamorphic Complex, Kyushu, Japan. *Journal of Metamorphic Geology*, *22*(9), 793–809. https://doi.org/10.1111/j.1525-1314.2004.00550.x (cit. on p. 110).

Montel, J.-M., & Vielzeuf, D. (1997). Partial melting of metagreywackes, Part II. Compositions of minerals and melts. *Contributions to Mineralogy and Petrology*, *128*(2–3), 176–196. https://doi.org/10.1007/s004100050302 (cit. on p. 84).

Nicoli, G., Stevens, G., Moyen, J.-F., Vezinet, A., & Mayne, M. (2017). Insights into the complexity of crustal differentiation: $K_2O$-poor leucosomes within metasedimentary migmatites from the Southern Marginal Zone of the Limpopo Belt, South Africa. *Journal of Metamorphic Geology*, *35*(9), 999–1022. https://doi.org/10.1111/jmg.12265 (cit. on p. 101).

Nicoli, G., & Dyck, B. (2018). Exploring the metamorphic consequences of secular change in the siliciclastic compositions of continental margins. *Geoscience Frontiers*, *9*(4), 967–975. https://doi.org/10.1016/j.gsf.2017.12.009 (cit. on p. 84).

Noble, S. R., Aspden, J. A., & Jemielita, R. (1997). Northern Andean crustal evolution: New U-Pb geochronological constraints from Ecuador. *Geological Society of America Bulletin*, *109*(7), 789–798. https://doi.org/10.1130/0016-7606(1997)109<0789:NACENU>2.3.CO;2 (cit. on p. 96).

Ohta, T., & Arai, H. (2007). Statistical empirical index of chemical weathering in igneous rocks: A new tool for evaluating the degree of weathering. *Chemical Geology*, *240*(3–4), 280–297. https://doi.org/10.1016/j.chemgeo.2007.02.017 (cit. on pp. 89, 92).

Patiño Douce, A. E., & Johnston, A. D. (1991). Phase equilibria and melt productivity in the pelitic system: Implications for the origin of peraluminous granitoids and aluminous granulites. *Contributions to Mineralogy and Petrology*, *107*(2), 202–218. https://doi.org/10.1007/BF00310707 (cit. on p. 84).

Peters, D., & Pettke, T. (2017). Evaluation of Major to Ultra Trace Element Bulk Rock Chemical Analysis of Nanoparticulate Pressed Powder Pellets by LA-ICP-MS. *Geostandards and Geoanalytical Research*, *41*(1), 5–28. https://doi.org/10.1111/ggr.12125 (cit. on p. 86).

Pettke, T., Oberli, F., Audétat, A., Guillong, M., Simon, A. C., Hanley, J. J., & Klemm, L. M. (2012). Recent developments in element concentration and isotope ratio analysis of individual fluid inclusions by laser ablation single and multiple collector ICP-MS. *Ore Geology Reviews*, *44*, 10–38. https://doi.org/10.1016/j.oregeorev.2011.11.001 (cit. on p. 86).

Pickering, J. M., & Johnston, A. D. (1998). Fluid-Absent Melting Behavior of a Two- Mica Metapelite: Experimental Constraints on the Origin of Black Hills Granite. *39*(10) (cit. on p. 98).

Powell, R. (1983). Processes in granulite-facies metamorphism. *High Grade Metamorphism, Migmatites and Melting. Meeting of the Geochemical Group of the Mineralogical Society*, 127–139 (cit. on p. 84).

Pretorius, W., Weis, D., Williams, G., Hanano, D., Kieffer, B., & Scoates, J. (2006). Complete Trace Elemental Characterisation of Granitoid (USGS G-2, GSP-2) Reference Materials by High Resolution Inductively Coupled Plasma-Mass Spectrometry. *Geostandards and Geoanalytical Research*, *30*(1), 39–54. https://doi.org/10.1111/j.1751-908X.2006.tb00910.x (cit. on p. 86).

Rackauckas, C., & Nie, Q. (2017). DifferentialEquations.jl – A Performant and Feature-Rich Ecosystem for Solving Differential Equations in Julia. *Journal of Open Research Software*, *5*(1), 15. https://doi.org/10.5334/jors.151 (cit. on p. 95).

Riel, N., Guillot, S., Jaillard, E., Martelat, J.-E., Paquette, J.-L., Schwartz, S., Goncalves, P., Duclaux, G., Thebaud, N., Lanari, P., Janots, E., & Yuquilema, J. (2013). Metamorphic and geochronogical study of the Triassic El Oro metamorphic complex, Ecuador: Implications for high-temperature metamorphism in a forearc zone. *Lithos*, *156–159*, 41–68. https://doi.org/10.1016/j.lithos.2012.10.005 (cit. on pp. 85–87, 92, 94, 95, 97, 107, 109).

Riel, N., Kaus, B. J. P., Green, E. C. R., & Berlie, N. (2022). MAGEMin, an Efficient Gibbs Energy Minimizer: Application to Igneous Systems. *Geochemistry, Geophysics, Geosystems*, *23*(7),

e2022GC010427. https://doi.org/10.1029/2022GC010427 (cit. on p. 96).

Riel, N. (2012, January 20). *Anomalie thermique et sous-placage en zone d'avant-arc : exemple du massif Triasique de El Oro, Equateur* [Doctoral dissertation, Université de Grenoble]. Retrieved September 16, 2024, from https://theses.hal.science/tel-00771736 (cit. on p. 110).

Riel, N., Martelat, J.-E., Guillot, S., Jaillard, E., Monié, P., Yuquilema, J., Duclaux, G., & Mercier, J. (2014). Fore arc tectonothermal evolution of the El Oro metamorphic province (Ecuador) during the Mesozoic. *Tectonics*, *33*(10), 1989–2012. https://doi.org/10.1002/2014TC003618 (cit. on p. 85).

Riel, N., Mercier, J., & Weinberg, R. (2016). Convection in a partially molten metasedimentary crust? Insights from the El Oro complex (Ecuador). *Geology*, *44*(1), 31–34. https://doi.org/10.1130/G37208.1 (cit. on pp. 86, 87, 92, 94, 95, 97, 107, 110).

Rosenberg, C. L., & Handy, M. R. (2005). Experimental deformation of partially melted granite revisited: Implications for the continental crust. *Journal of Metamorphic Geology*, *23*(1), 19–28. https://doi.org/10.1111/j.1525-1314.2005.00555.x (cit. on pp. 92, 98).

Rudnick, R. L., & Gao, S. (2003). Composition of the continental crust. *Treatise on Geochemistry*, *3*, 659. https://doi.org/10.1016/B0-08-043751-6/03016-4 (cit. on pp. 91, 94).

Sawyer, E. W. (1996). Melt segregation and magma flow in migmatites: Implications for the generation of granite magmas. *Earth and Environmental Science Transactions of The Royal Society of Edinburgh*, *87*(1–2), 85–94. https://doi.org/10.1017/S0263593300006507 (cit. on p. 84).

Schwindinger, M., Weinberg, R. F., & Clos, F. (2019). Wet or dry? The difficulty of identifying the presence of water during crustal melting. *Journal of Metamorphic Geology*, *37*(3), 339–358. https://doi.org/10.1111/jmg.12465 (cit. on pp. 84, 99, 100, 109).

Shand, S. J. (1943). *Eruptive Rocks: Their Genesis, Composition, and Classification, with a Chapter on Meteorites*. J. Wiley & sons, Incorporated. (Cit. on pp. 84, 92, 107).

Siron, G., Goncalves, P., Marquer, D., Pierre, T., Paquette, J.-L., & Vanardois, J. (2020). Contribution of magmatism, partial melting buffering and localized crustal thinning on the late Variscan thermal structure of the Agly massif (French Pyrenees). *Journal of Metamorphic Geology*, *38*(8), 799–829. https://doi.org/10.1111/jmg.12549 (cit. on p. 110).

Spear, F. S. (1993). Metamorphic phase equilibria and pressure–temperature–time paths. *Mineralogical Society of America Monograph.*, 352 (cit. on p. 93).

Spear, F. S., Kohn, M. J., & Cheney, J. T. (1999). P-T paths from anatectic pelites. *Contributions to mineralogy and petrology*, *134*, 17–32 (cit. on p. 84).

Stevens, G., Villaros, A., & Moyen, J.-F. (2007). Selective peritectic garnet entrainment as the origin of geochemical diversity in S-type granites. *Geology*, *35*(1), 9. https://doi.org/10.1130/G22959A.1 (cit. on p. 84).

Thompson, A. B. (1983). Fluid-absent metamorphism. *Journal of the Geological Society*, *140*(4), 533–547. https://doi.org/10.1144/gsjgs.140.4.0533 (cit. on p. 84).

Thompson, J. B., Jr. (1957). The Graphical Analysis of Mineral Assemblages in Pelitic Schists*. *American Mineralogist*, *42*(11–12), 842–858 (cit. on p. 93).

Tierney, C. R., Schmitt, A. K., Lovera, O. M., & De Silva, S. L. (2016). Voluminous plutonism during volcanic quiescence revealed by thermochemical modeling of zircon. *Geology*, *44*(8), 683–686. https://doi.org/10.1130/G37968.1 (cit. on p. 92).

Trap, P., Roger, F., Cenki-Tok, B., & Paquette, J.-L. (2017). Timing and duration of partial melting and magmatism in the Variscan Montagne Noire gneiss dome (French Massif Central). *International Journal of Earth Sciences*, *106*(2), 453–476. https://doi.org/10.1007/s00531-016-1417-x (cit. on p. 110).

Turcotte, D. L., & Schubert, G. (2014). *Geodynamics* (Third edition). Cambridge University Press. (Cit. on p. 95).

Vanderhaeghe, O., Kruckenberg, S., Gerbault, M., Martin, L., Duchêne, S., & Deloule, E. (2018). Crustal-scale convection and diapiric upwelling of a partially molten orogenic root (Naxos dome, Greece). *Tectonophysics*, *746*, 459–469. https://doi.org/10.1016/j.tecto.2018.03.007 (cit. on p. 110).

Villaros, A., Stevens, G., & Buick, I. S. (2009). Tracking S-type granite from source to emplacement: Clues from garnet in the Cape Granite Suite.

*Lithos*, *112*(3–4), 217–235. https://doi.org/10.1016/j.lithos.2009.02.011 (cit. on p. 84).

Villaros, A., Stevens, G., Moyen, J.-F., & Buick, I. S. (2009). The trace element compositions of S-type granites: Evidence for disequilibrium melting and accessory phase entrainment in the source. *Contributions to Mineralogy and Petrology*, *158*(4), 543–561. https://doi.org/10.1007/s00410-009-0396-3 (cit. on p. 84).

Villaseca, C., Barbero, L., & Herreros, V. (1998). A re-examination of the typology of peraluminous granite types in intracontinental orogenic belts. *Transactions of the Royal Society of Edinburgh: Earth Sciences*, *89*(2), 113–119. https://doi.org/10.1017/S0263593300007045 (cit. on p. 92).

Vinasco Vallejo, C. J. (2004, December 22). *Evolução crustal e história tectônica dos granitóides permotriássicos dos Andes do Norte* [Doutorado em Geoquímica e Geotectônica]. Universidade de São Paulo. https://doi.org/10.11606/T.44.2004.tde-27102015-142142 (cit. on pp. 86, 87, 92, 94, 107, 109).

Warr, L. N. (2021). IMA–CNMNC approved mineral symbols. *Mineralogical Magazine*, *85*(3), 291–320. https://doi.org/10.1180/mgm.2021.43 (cit. on pp. 85, 103).

Weinberg, R. F., Hasalova, P., Ward, L., & Fanning, C. M. (2013). Interaction between deformation and magma extraction in migmatites: Examples from Kangaroo Island, South Australia. *Geological Society of America Bulletin*, *125*(7–8), 1282–1300. https://doi.org/10.1130/B30781.1 (cit. on p. 110).

Weinberg, R. F., & Hasalová, P. (2015a). Water-fluxed melting of the continental crust: A review. *Lithos*, *212–215*, 158–188. https://doi.org/10.1016/j.lithos.2014.08.021 (cit. on p. 84).

Weinberg, R. F., & Hasalová, P. (2015b). Water-fluxed melting of the continental crust: A review. *Lithos*, *212–215*, 158–188. https://doi.org/10.1016/j.lithos.2014.08.021 (cit. on p. 100).

White, A., & Chappell, B. (1977). Ultrametamorphism and granitoid genesis. *Tectonophysics*, *43*(1–2), 7–22 (cit. on p. 84).

White, R. W. (2003). Prograde Metamorphic Assemblage Evolution during Partial Melting of Metasedimentary Rocks at Low Pressures: Migmatites from Mt Stafford, Central Australia. *Journal of Petrology*, *44*(11), 1937–1960. https://doi.org/10.1093/petrology/egg065 (cit. on p. 84).

White, R. W., Powell, R., Holland, T. J. B., Johnson, T. E., & Green, E. C. R. (2014). New mineral activity–composition relations for thermodynamic calculations in metapelitic systems. *Journal of Metamorphic Geology*, *32*(3), 261–286. https://doi.org/10.1111/jmg.12071 (cit. on p. 98).

White, R. W., Powell, R., & Johnson, T. E. (2014). The effect of Mn on mineral stability in metapelites revisited: New $a - x$ relations for manganese-bearing minerals. *Journal of Metamorphic Geology*, *32*(8), 809–828. https://doi.org/10.1111/jmg.12095 (cit. on p. 98).

White, R. W., Stevens, G., & Johnson, T. E. (2011). Is the Crucible Reproducible? Reconciling Melting Experiments with Thermodynamic Calculations. *Elements*, *7*(4), 241–246. https://doi.org/10.2113/gselements.7.4.241 (cit. on p. 101).

Whittington, A. G., Hofmeister, A. M., & Nabelek, P. I. (2009). Temperature-dependent thermal diffusivity of the Earth's crust and implications for magmatism. *Nature*, *458*(7236), 319–321. https://doi.org/10.1038/nature07818 (cit. on pp. 92, 93).

Yakymchuk, C., Brown, M., Clark, C., Korhonen, F. J., Piccoli, P. M., Siddoway, C. S., Taylor, R. J. M., & Vervoort, J. D. (2015). Decoding polyphase migmatites using geochronology and phase equilibria modelling. *Journal of Metamorphic Geology*, *33*(2), 203–230. https://doi.org/10.1111/jmg.12117 (cit. on p. 84).

Yakymchuk, C., & Brown, M. (2014). Consequences of open-system melting in tectonics. *Journal of the Geological Society*, *171*(1), 21–40. https://doi.org/10.1144/jgs2013-039 (cit. on p. 98).

Chapter V

# Conclusion

This thesis demonstrates that a multidisciplinary approach is required to improve our understanding of melting processes in the continental crust. This is necessary because of the complex interplay between melt producing metamorphic reactions, rheology, melt transport and extraction, and igneous processes associated with pluton emplacement. Emphasis was placed on numerical modeling, and the need to reconcile time constraints with these models. Time is a particularly important variable because systems involving melt are dynamic, with transport of matter and heat, and with complex interactions between rock and melt. Therefore, the plausibility of different models can be assessed if they occur on in similar timescales to those observed in real systems. Lastly, the main findings of each chapter of this thesis are summarised below.

In Chapter II, we made an important contribution to paving the way for more accurate and performant reactive transport modelling involving melt in the crust in the future. This chapter demonstrated the potential of using the WENO-5 algorithm to model the chemical advection of a melt during its ascent. This was assessed by coupling a two-phase flow solver with chemical advection in 2D, and the robustness of the WENO-5 scheme was tested against three other algorithms.

The focus of Chapter III was on reconciling the different timescales from melt source to pluton emplacement. This was done by collecting a large amount of geochronological and trace element data from zircons of the El Oro complex, from both migmatites and granitoids, using LA-ICP-MS. The results showed that zircon dates are spread over more than 20 Myr, both in migmatites and in granitoids. We proposed that this indicates the existence of multiple short magmatic pulses. The absence of major tectonic events and regional-scale deformation during the history of prograde metamorphism allowed the plutons to be long-lived in this metamorphic sequence. Trace elements were also used to show evidence of open system behaviour in low-melt fraction migmatites. This chapter has shown the appeal of collecting more zircon analyses per sample, along with trace element data, to try to constrain not only the age but also the duration of a melting/magmatic event.

Finally, Chapter IV explored a new modelling approach by combining a 1D crustal thermal model with phase equilibrium modelling . This approach allows the modelling of phase assemblages along $P$–$T$–$t$ paths, adding a time constraint compared to conventional phase equilibrium modelling. This approach was applied to the El Oro complex, using the new geochronological constraints obtained in Chapter III. Eight different models were tested to explore different processes associated with melt production by partial melting and transport towards the pluton. An assessment was made of the mass balance between the volume of melt produced at the crustal scale and the volume of pluton observed in reality was made. It was also used to compare melt-extracted compositions along the 1D crustal profile with migmatite and pluton bulk composition data. Melt production by the models lasted between 4.5 and 6 Myr, depending on the model, and produced a melt volume compatible with the size of the Marcabelí pluton. This is consistent with the idea that the La Bocana unit is the main source of this pluton. However, the predicted compositions of the melts were consistently different from the granitoid bulk rock analyses of the El Oro complex. Mixing with the gabbro of the Piedras unit was proposed to explain this discrepancy, and a mixing test predicted a contribution from the gabbro of between 7 and 15 %.

In conclusion, this thesis has demonstrated the value of developing and using numerical models to decipher melting processes in the continental crust. It also emphasised the need to constrain these models with observations, natural and analytical data. This work also highlights the potential of studying geological systems where both the melt source, such as migmatites, and the final product, granitoids, are accessible, such as the El Oro complex. Finally, an effort has been made to make all the codes used in the numerical models in this thesis available in public repositories. Further efforts should be made as a community to promote the systematic distribution of codes used in studies. Reproducibility and replicability are an important part of science so that results can be verified and validated.

# Appendices

# A.1. Supplementary material for chapter III

The following section includes the concordia diagrams of the different samples and analyses used in chapter III. In addition to that, the concordant inherited cores from the La Bocana unit are also used for provenance analyses. The complete dataset used in chapter III, containing the U–Pb and trace element analyses of zircon and titanite, is available at a permanent DOI repository: https://boris-portal.unibe.ch/handle/20.500.12422/44675.

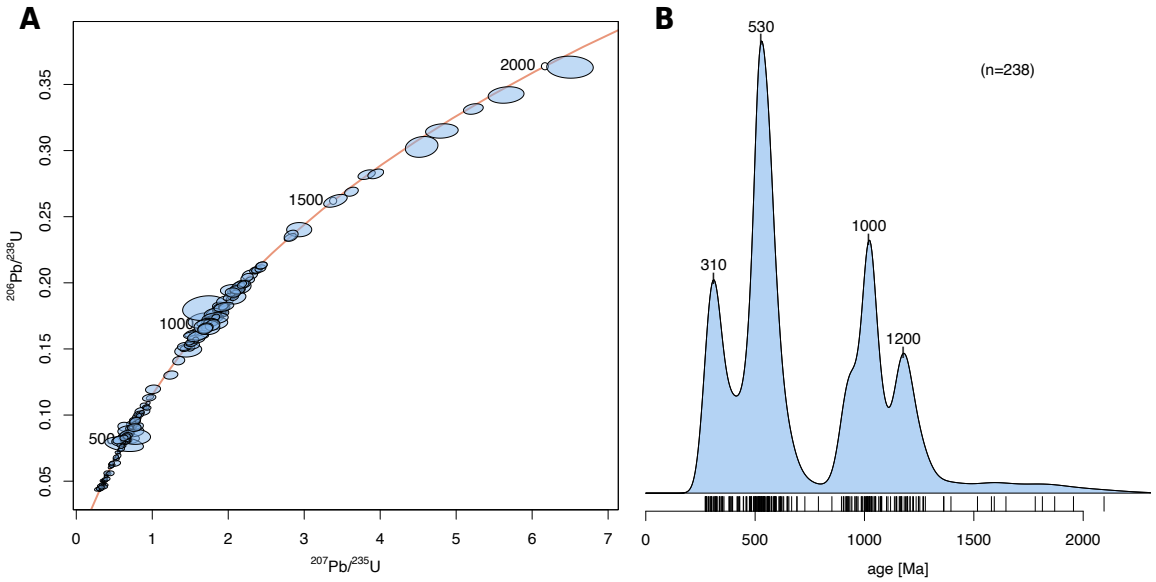


**Figure A.1.1:** Analyses from inherited zircon cores from the 6 samples of the La Bocana unit. A. Wheterill concordia diagram of analyses older than 300 Ma and concordant at 2σ, calculated using IsoplotR (Vermeesch, 2018). B. Kernel density estimate of the same analyses as in A. The dates older than 1100 Ma are calculated from the $^{207}Pb/^{206}Pb$ ratio and the younger dates are calculated from the $^{206}Pb/^{238}U$ ratio, calculated using IsoplotR (Vermeesch, 2018).

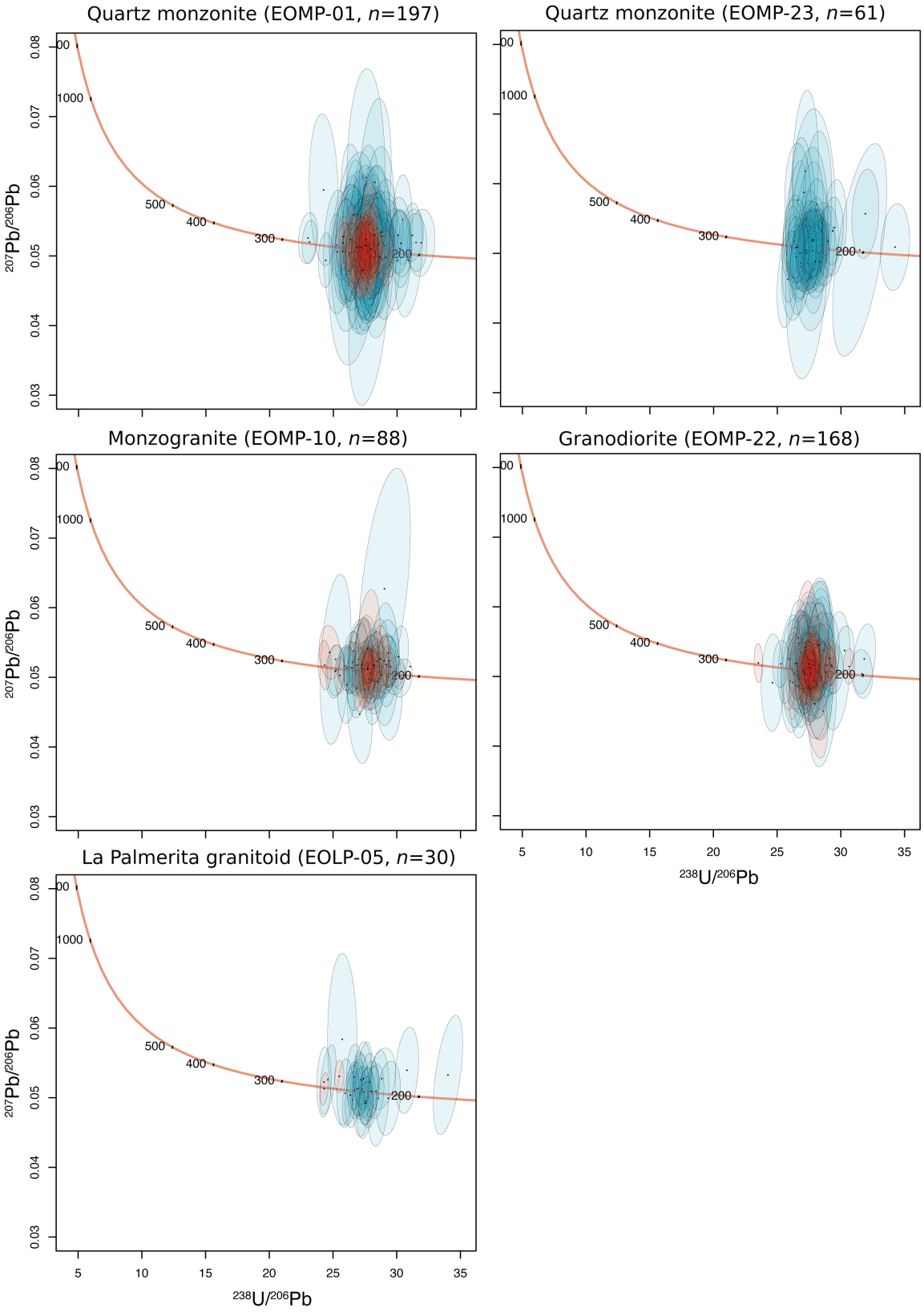


**Figure A.1.2:** Tera-Wasserburg concordia diagram of the zircon analyses from the granitic samples from the El Oro complex, calculated using IsoplotR (Vermeesch, 2018). Only dates younger than 270 Ma and concordant at 2σ are reported. Blue and red ellipses correspond to 16 and 30 µm laser spot size, respectively.

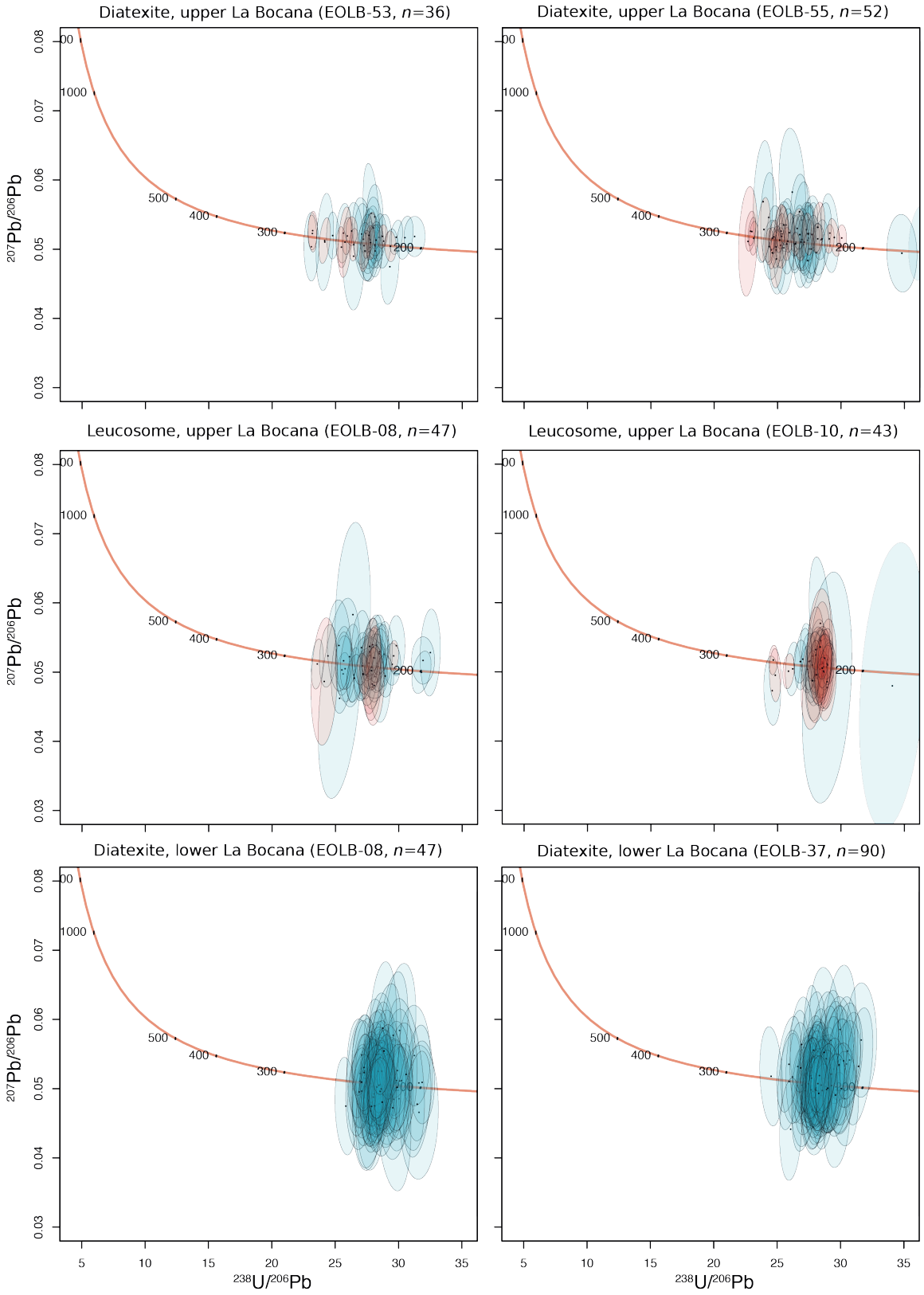


**Figure A.1.3:** Tera-Wasserburg concordia diagram of the zircon analyses from the migmatitic samples from the La Bocana unit, calculated using IsoplotR (Vermeesch, 2018). Only dates younger than 270 Ma and concordant at 2σ are reported. Blue and red ellipses correspond to 16 and 30 µm laser spot size, respectively.

# Declaration of consent

on the basis of Article 18 of the PromR Phil.-nat. 19

Name/First Name: Hugo Dominguez

Registration Number: 20-131-892

Study program: PhD of Science in Earth Sciences

Bachelor ☐ Master ☐ Dissertation ☑

Title of the thesis: From Migmatites to Granitoids: Transport Mechanisms, Timescales, and Melt Source

Supervisor: Prof. Pierre Lanari, Dr. Nicolas Riel

I declare herewith that this thesis is my own work and that I have not used any sources other than those stated. I have indicated the adoption of quotations as well as thoughts taken from other authors as such in the thesis. I am aware that the Senate pursuant to Article 36 paragraph 1 litera r of the University Act of September 5th, 1996 and Article 69 of the University Statute of June 7th, 2011 is authorized to revoke the doctoral degree awarded on the basis of this thesis.
For the purposes of evaluation and verification of compliance with the declaration of originality and the regulations governing plagiarism, I hereby grant the University of Bern the right to process my personal data and to perform the acts of use this requires, in particular, to reproduce the written thesis and to store it permanently in a database, and to use said database, or to make said database available, to enable comparison with theses submitted by others.

Bern, 03.10.2024

Place/Date

Signature